

This item was submitted to Loughborough University as a PhD thesis by the author and is made available in the Institutional Repository (<https://dspace.lboro.ac.uk/>) under the following Creative Commons Licence conditions.



For the full text of this licence, please go to:
<http://creativecommons.org/licenses/by-nc-nd/2.5/>



University Library

Author/Filing TitleTASCIOLV, Y.....

Class MarkT.....

Please note that fines are charged on ALL
overdue items.

FOR REFERENCE ONLY

0403270472



Profile Independent Wood-Moulding Machine


by

Yigit Taşcıoğlu
(BSc, MSc)

A Doctoral Thesis
submitted in partial fulfillment of the requirements
for the award of Doctor of Philosophy
of Loughborough University

April 2006

© by Yigit Taşcıoğlu (2006)

	Loughborough University Pilkington Library
Date	SEPT 2006
Class	T
Acc No.	0403270472

Abstract

Wood mouldings are long, narrow pieces of timber with ornamental profiles formed on one or more faces. They are used in furniture, architecture and joinery industries and typical applications include door/window frames, skirting boards and picture frames. Conventionally, wood mouldings are produced by planing/moulding machines, where cutting edges, attached to rotating cutterheads, sever chips from advancing workpieces. The cutting edges are shaped specifically for each individual moulding profile; hence, the raw material is transformed into the finished product with a single feed. When the production is to be changed from one profile to another, the conventional machines require new cutter knives that are manufactured for the profile to be machined. This requirement introduces tooling and machine set-up costs which cannot be compensated in shorter production runs.

In order to minimize the aforementioned costs in short production runs, this thesis aims at the holistic development of Profile Independent Wood-Moulding Machine (PIMM). In the PIMM concept, the profile geometry is supplied directly from CAD drawings, and the profile-specific cutter knives of the conventional process are emulated by position control of a single cutting tool along software generated trajectories.

This thesis approaches the PIMM from an integrated mechatronic design perspective. Alternative solutions for mechanical, electrical and software components of the system were generated and evaluated via mathematical modelling and simulation. Then, the selected solutions were realized in a proof-of concept PIMM system, and the effectiveness of the proposed method has been investigated through machining experiments.

Overall, this research proposes a new machining method and demonstrates an integrated design process that initiates from an idea and results in a fully functional, physical mechatronic system; via efficient use of software, simulation and rapid prototyping technologies.

Acknowledgements

The work described in this thesis was carried out in the Mechatronics Research Group (MRG), Wolfson School of Mech. & Manuf. Eng., Loughborough University, during the period 2002-2006. First of all, I wish to express my thanks to my supervisor Dr. Mike Jackson for his guidance and support throughout the investigation. I also wish to thank the staff and research students in the MRG, expecially Pavel Hynek, David Liddell and Terry, for their help and friendship.

I would like to thank Mark East and Phil Brindley from the Rapid Manufacturing Research Group, Jagpal Singh from Metrology Laboratory, and all the staff at the manufacturing workshop.

I am grateful to my friends in Loughborough who have made me feel like at home. Special thanks to my cousin Itir and friends William, Ozhan, Ozge, Volkan, Berna, Asan, Celine, Ozan, Selda, Fulya and Ozgur.

Finally, a great THANK YOU to my wife Ebru for her support and endless patience, and for the things she sacrificed just to be here with me.

Contents

<i>Abstract</i>	<i>i</i>
<i>Acknowledgements</i>	<i>ii</i>
<i>Contents</i>	<i>iii</i>
<i>Nomenclature</i>	<i>vii</i>
<i>List of Figures</i>	<i>x</i>
<i>List of Tables</i>	<i>xiv</i>
CHAPTER 1: INTRODUCTION	1
1.1 Background and Motivation	1
1.2 Proposed Machining Method	3
1.3 Research Objectives	4
1.4 Research Novelty	4
1.5 Method of Approach	5
1.6 Thesis Organization	7
CHAPTER 2: REVIEW OF PREVIOUS WORK.....	9
2.1 Introduction	9
2.2 Wood Machining	10
2.2.1 Definition and history of wood machining	10
2.2.2 Wood mouldings	12
2.2.3 Planing and moulding machines	13
2.2.4 Surface quality	15
2.2.5 Productivity in wood machining	17
2.3 Contouring Machinery	19
2.4 Profile Independent Wood-Moulding	22
2.5 Multi-Axis Drive System Control Structures and Software Mechanisms	22
2.5.1 Motion control coordination and error sources	23
2.5.2 Sophisticated axial controllers for independent drives	26
2.5.3 Dual-loop controllers	29
2.5.4 Cross-coupling controllers	31
2.5.5 Controllers with coordinate transformation	35
2.5.6 Scalar field control technique	38
2.6 Summary	42
CHAPTER 3: CUTTING FORCES	44
3.1 Introduction	44
3.2 Influencing Factors	45

3.2.1	Cutting direction	46
3.2.2	Width of cut	47
3.2.3	Cutting speed	47
3.2.4	Timber properties and condition	49
3.2.5	Cutter geometry and condition of the cutting edge	50
3.2.6	Chip thickness	53
3.2.7	Upcutting and downcutting	54
3.2.8	Chip formation	56
3.3	Theoretical Investigations	58
3.3.1	Cutting forces in PIMM process	58
3.3.2	Cutting power	63
3.4	Experimental Cutting Force Estimations	64
3.4.1	Test-rig	64
3.4.2	Measurement method	66
3.4.3	Test series	68
3.4.4	Test results and discussion	68
3.5	Summary	74
CHAPTER 4: SYSTEM MODELLING AND SIMULATION	75	
4.1	Introduction	75
4.2	Electro-Mechanical Hardware	77
4.2.1	Performance expectations from X and Y axis drives	77
4.2.2	Evaluation of hardware alternatives for X and Y axis drives	80
4.2.3	Mathematical modelling of X and Y axis drives	84
4.2.4	Expected performance and hardware of Z axis drive	90
4.3	Control Structure and Algorithms	92
4.3.1	Profile input	94
4.3.2	Input Translation	96
4.3.3	Reference Generator	99
4.3.4	Path Controller	101
4.4	Simulations	108
4.4.1	Actuator selection for the simulated system	108
4.4.2	Simulation parameters and inputs	109
4.4.3	Simulation Results	111
4.5	Summary	116
CHAPTER 5: PIMM TEST RIG	117	
5.1	Introduction	117
5.2	Mechanical Design	118
5.2.1	Cutter assembly (θ -Axis)	119
5.2.2	Horizontal drive (X-Axis)	120
5.2.3	Vertical drive (Y-Axis)	121
5.2.4	Timber feed drive (Z-Axis) and machine frame	122
5.3	Control Hardware	124

5.3.1	Control computer and multifunction I/O card	124
5.3.2	Driving amplifiers	126
5.4	Software Implementation in Simulink	128
5.5	Software Implementation in Visual Basic 6	129
5.5.1	Program structure	130
5.5.2	Data structure	132
5.5.3	Data capture and manipulation functions	134
5.5.4	Graphical User Interface	140
5.6	Future Plans	145
5.7	Summary	145
CHAPTER 6: SYSTEM IDENTIFICATION AND MODEL VALIDATION		147
6.1	Introduction	147
6.2	Validation of the Simulink RTWT Model	148
6.3	Identification of Amplifier and DC Motor Parameters	149
6.4	Identification of Disturbances on X and Y Axis Drives	153
6.4.1	Ideal drive model and performance	153
6.4.2	Friction identification, modeling and simulation	155
6.4.3	Validation of carriage weight in the Y-axis drive model	165
6.5	Summary	166
CHAPTER 7: MACHINING INVESTIGATIONS		168
7.1	Introduction	168
7.2	Machining Investigations	168
7.2.1	Influence of the cutter thickness on the resultant profile	168
7.2.2	Path speed limitation due to the available cutting power	171
7.2.3	Experiment setup	171
7.2.4	Friction compensation	172
7.2.5	Effects of cutting forces on the performance	173
7.2.6	Comparison of the passes on different directions	176
7.2.7	Accuracy measurements on a Coordinate Measuring Machine	178
7.2.8	Accuracy measurements of a scanned profile image	181
7.3	Investigation of Design Improvements via Simulation	184
7.3.1	Comparison of the actual and simulated systems	184
7.3.2	Effects of increased drive weight on the performance	187
CHAPTER 8: CONCLUSIONS AND FURTHER WORK		191
8.1	Conclusions	191
8.2	Recommendations for Further Work	193
8.2.1	Cutter assembly	193
8.2.2	Timber feed mechanism	194
8.2.3	Surface roughness	194
8.2.4	Cutting materials other than wood	194

8.2.5	Processing with multiple PIMMs	194
8.2.6	Change of profile along the length	195
8.2.7	Processing with vertical spindle	195
8.2.8	Portable PIMM	195
REFERENCES.....		196
APPENDICES		204
Appendix A: Typical moulding profiles		205
Appendix B: Representation of geometric information in DXF script		206
Appendix C: Matlab Function “dx fread.m”		207
Appendix D: Previous PIMM test-rig designs		210
Appendix E: Cutter motor specifications		213
Appendix F: X and Y axis drives hardware specifications		214
Appendix G: X and Y axis drives speed, force, and inertia calculations		218
Appendix H: Z axis drive hardware specifications		219
Appendix I: Sensoray Model 626 PCI I/O card specifications		220
Appendix J: X and Y axis drives amplifier specifications		221
Appendix K: Cutter motor amplifier specification		222
Appendix L: Performance criteria (IAE, ITAE, P_{IAE}, P_{ITAE})		223
Appendix M: Accompanying CD		225
Appendix N: Design Alternatives for a Novel Wood Moulder		226
Appendix O: Mechatronic Design of a Novel Wood Moulder		234
Appendix P: Profile Independent Wood Moulding Machine		258

Nomenclature

B	total equivalent damping coefficient lumped at the rotor	Nms/rad
B_c	carriage damping coefficient	Ns/m
B_m	rotor viscous damping coefficient	Nms/rad
B_s	leadscrew viscous damping coefficient	Nms/rad
C_t, C_c	digital control signals on T and C axes	-
C_x, C_y	digital control signals on X and Y axes	-
C_{fx}, C_{fy}	friction compensation signals	-
c	chip width	mm
d	depth of cut	mm
e	leadscrew efficiency	-
F	total cutting force	N
F_e	external force on the carriage	N
F_L	lateral force	N
F_n	normal (radial) cutting force	N
F_t	tangential (main) cutting force	N
F_{s_n}	normal force acting on the side edge of the cutter	N
F_{s_t}	tangential force acting on the side edge of the cutter	N
F_{t_n}	normal force acting on the tip edge of the cutter	N
F_{t_t}	tangential force acting on the tip edge of the cutter	N
f	feed increment	mm
g	gravitational acceleration	m/s ²
h	surface wave height	mm
I_{lim}	amplifier current limit	A
J	total equivalent inertia lumped at the rotor	kgm ²
J_m	rotor inertia	kgm ²
J_s	leadscrew inertia	kgm ²
K_a	amplifier gain	V/V
K_d	D/A gain	V
K_e	motor back-emf constant	Vs/rad
$K_p T, K_p C$	position gains of T and C axis controllers	-
K_t	motor torque constant	-

$K_v T, K_v C$	velocity gains of T and C axis controllers	-
k	Stribeck empirical parameter	-
L	chip length	mm
L_m	armature inductance	H
M	carriage mass	kg
NOS	number of segments in a profile	-
n	number of cutter teeth	-
n'	number of cutter workpiece engagements in 1 second	-
n_p	number of cutter workpiece engagements per pass	-
n_t	number of cutter teeth cutting at the same time	-
P	cutting power	W
P_{idle}	power consumption of the idling cutter motor	W
P_{total}	total power consumption of the cutter motor	W
p	surface wave pitch	mm
R, θ	polar coordinates of cutter position	mm, °
R_A	arc radius	mm
R_m	armature resistance	Ohm
R_s	leadscrew gain	mm
r	cutter radius	mm
T_m	motor torque	Nm
T_{idle}	torque generated by the idling cutter motor	Nm
T_{total}	total torque generated by the cutter motor	Nm
t	pass time	s
t_c	cycle time	s
U_c	disturbance voltage due to Coulomb friction	V
U_e	disturbance voltage due to external force	V
U_f	disturbance voltage due to friction	V
U_s	stiction break-away voltage	V
u	applied armature voltage	V
W_c	cutting work	Nm
w	workpiece width	mm
w_p	profile width	mm
X, Y	Cartesian coordinates of cutter position	mm

X_1, Y_1, X_2, Y_2	segment end-point coordinates	mm
X_A, Y_A	centre point coordinates for arc segments	mm
V_{lim}	path speed limit	mm/s
V_t, V_c	cutter velocity on T and C axes	mm/s
V_x, V_y	cutter velocity on X and Y axes	mm/s
v	cutter tip speed	m/s
v_{mean}	mean path speed	mm/s
α	cutter rake angle	°
α_s	rake angle at the side edge of the cutter	°
α_t	rake angle at the tip edge of the cutter	°
β	cutter sharpness angle	°
γ	cutter clearance angle	°
γ_s	clearance angle at the side edge of the cutter	°
γ_t	clearance angle at the tip edge of the cutter	°
Δ	re-defined zero velocity limit	rad/s
δ	cutter thickness	mm
δ_m	mean chip thickness	mm
ε_c	contour error	mm
ε_t	tangential error	mm
ε_x	x-axis tracking error	mm
ε_y	y-axis tracking error	mm
θ_1, θ_2	polar coordinates of arc end-points	°
θ_m	rotor angular displacement	rad
τ	transformation matrix	-
ψ	inclination angle between X-Y and T-C frames	°
ω	cutter angular speed	rpm
ω_{idle}	angular speed of the idling cutter	rpm
ω_{str}	Stribeck velocity	rad/s

Other symbols are defined as they appear in the text.

List of Figures

Figure 1.1 Conventional moulding process	2
Figure 1.2 PIMM concept	3
Figure 1.3 Research phases	5
Figure 2.1 Selection of wood mouldings	12
Figure 2.2 Rotary machining process	13
Figure 2.3 Planing and moulding machine	13
Figure 2.4 Cutterhead configuration	14
Figure 2.5 Profile-specific cutting knife	14
Figure 2.6 Surface waviness concept	16
Figure 2.7 Some examples of CNC contouring machinery [13][14]	20
Figure 2.8 Contouring and tracking errors	24
Figure 2.9 Biaxial motion control system	26
Figure 2.10 Two principal types of feedforward controllers [18]	28
Figure 2.11 Biaxial dual-loop controller	30
Figure 2.12 The cross-coupling controller [24]	32
Figure 2.13 The axial and contour errors for different cutter locations	33
Figure 2.14 The variable-gain cross-coupling controller [24]	34
Figure 2.15 Tangential-contouring (T-C) coordinate frame and errors	36
Figure 2.16 Tangential-contouring controller	37
Figure 2.17 Principle of the scalar field controller [42]	38
Figure 2.18 Definition of the scalar field [42]	39
Figure 2.19 Definition of the terms relating to the mechanism characteristic [42]	41
Figure 3.1 Cutting force F and its components F_t and F_n	45
Figure 3.2 Rotary chip cutting	46
Figure 3.3 Main cutting directions in wood machining	47
Figure 3.4 Cutting forces F_t and F_n vs. cutter rake angle α in B direction [58]	50
Figure 3.5 Phases of normal cutting force F_n during chip formation	51
Figure 3.6 Cutting forces F_t and F_n vs. cutter clearance angle γ in B direction [58]	52
Figure 3.7 Cutting forces F_t and F_n vs. chip thickness δ_m in B direction [58]	53
Figure 3.8 Cutting forces on a guided saw (a) down-cutting, (b) up-cutting [70]	55
Figure 3.9 Types of chip formation	56
Figure 3.10 Forces acting on the tool edges	58

Figure 3.11 Cutter-workpiece interaction	59
Figure 3.12 Cutting force graphs for various δ_m and a [58]	62
Figure 3.13 Photo of the cutting force rig.	65
Figure 3.14 Cutting force rig schematic	66
Figure 3.15 Measured power for Series #1 to #5	73
Figure 3.16 Measured power for Series #6 to #14	73
Figure 4.1 PIMM System	76
Figure 4.2 Moulding Dimensions	77
Figure 4.3 Mean path speed vs. pass time for a 100mm wide moulding	78
Figure 4.4 Geometric errors	79
Figure 4.5 Drive mechanism (a) and dynamic model (b) of a single axis	84
Figure 4.6 DC motor block diagram	85
Figure 4.7 Block diagram from armature voltage to carriage position	87
Figure 4.9 Production rate vs. cycle time for a 100 mm wide moulding	90
Figure 4.10 Control Structure	92
Figure 4.11 Generalized block diagram of the simulated system	93
Figure 4.12 DXF input function “dxfreadd.m” flowchart	95
Figure 4.13 Raw DXF profile	96
Figure 4.14 Final profile	97
Figure 4.15 Block diagram of the <i>Reference Generator</i>	99
Figure 4.16 Reference generator flowchart	100
Figure 4.17 Error components for different cutter locations	101
Figure 4.18 Generalized block diagram of the <i>Path Controller</i>	102
Figure 4.19 Coordinate transformation for line segments	103
Figure 4.20 Coordinate transformation for arc segments	104
Figure 4.21 Block diagram for the application of the controller gains	106
Figure 4.22 Simulation inputs (a) test profile (b) real moulding profile	110
Figure 4.23 Simulation results: Initial performance (a) test profile (b) contour error vs. horizontal position (c) path speed vs. horizontal position	112
Figure 4.24 Simulation results: Cascaded controller and velocity limit (a) test profile (b) contour error vs. horizontal position (c) path speed vs. horizontal position	113
Figure 4.25 Simulation results: Cascaded controller, velocity limit, and split arcs (a) test profile (b) contour error vs. horizontal position (c) path speed vs. horizontal position	114

Figure 4.26 Simulation results for the real moulding profile (a) moulding profile (b) contour error vs. horizontal position (c) path speed vs. horizontal position	115
Figure 5.1 PIMM test-rig	118
Figure 5.2 Cutter assembly	119
Figure 5.3 Horizontal drive	120
Figure 5.4 Vertical drive	122
Figure 5.5 Timber feed drive and machine frame	123
Figure 5.6 System diagram	124
Figure 5.7 PIMM model for Real-Time Windows Target	129
Figure 5.8 Block diagram of the software hierarchy [98]	131
Figure 5.9 Flowchart – API timer	134
Figure 5.10 Flowchart - Outer control loop	135
Figure 5.11 Flowchart – <i>ControlTimer</i>	136
Figure 5.12 Flowchart – <i>Sample</i>	138
Figure 5.13 Main window	140
Figure 5.14 Segment List window	143
Figure 5.15 Analysis window	143
Figure 5.16 Settings window	144
Figure 6.1 Steady-state curves of the drive motors	148
Figure 6.2 Amplifier and DC motor model	149
Figure 6.3 Amplifiers and motors before identification	150
Figure 6.4 Amplifiers and motors after identification	152
Figure 6.5 Ideal single-axis drive model	153
Figure 6.6 Drive inputs for disturbance identification	154
Figure 6.7 Ideal vs. actual drives	155
Figure 6.8 Classical friction model [98]	156
Figure 6.9 Single-axis drive model with friction	157
Figure 6.10 Modified friction model	158
Figure 6.11 Steady-state curves of the horizontal (X) and vertical (Y) drives	159
Figure 6.12 Simulation results with the modified friction model; (a) general performance, (b) acceleration & deceleration performance	161
Figure 6.13 The friction-velocity relation observed in [104]	162
Figure 6.14 Final friction model	163

Figure 6.15 Simulation results with the final friction model; (a) general performance, (b) acceleration & deceleration performance	164
Figure 6.16 Effect of gravity on the vertical drive	165
Figure 7.1 Cutter thickness compensation (a) target profile (b) target and result without compensation (c) compensated profile (d) target and result with compensation	169
Figure 7.2 Effect of cutter thickness on concave features (a) target profile, (b) target and result without compensation, (c) compensated profile, (d) target and result with compensation, (e) result with compensation	170
Figure 7.3 Reference input for the experiments (a) target profile (b) compensated profile	172
Figure 7.4 Contour error plots for (a) air cutting (b) wood cutting	174
Figure 7.5 Contour error plots for (a) left-to-right passes (b) right-to-left passes	177
Figure 7.6 Measured specimen	179
Figure 7.7 Measurements of a scanned profile image (a) scanned image (b) processed image (c) measurements on the detected edges (d) reference curve vs. detected edges	182
Figure 7.8 A typical moulding machined by the PIMM test-rig	185
Figure 7.9 Experiment and simulation results (a) moulding profile (b) simulated error (c) measured error (d) simulated speed (e) measured speed	186
Figure 7.10 Simulation results: increased speed limit (a) profile (b) contour error vs. horizontal position (c) path speed vs. horizontal position	188
Figure 7.11 Simulation results: increased weight (a) moulding profile (b) left-to-right pass error (c) right-to-left pass error (d) left-to-right pass speed (e) right-to-left pass speed	189

List of Tables

Table 2.1 Some properties of the selected machines	21
Table 2.2 The evaluation of independent axis controllers [cited in 16]	29
Table 2.3 The evaluation of servo-controllers [18]	35
Table 3.1 Cutting forces at different cutting speeds [57]	48
Table 3.2 Example machining parameters	61
Table 3.3 Influence of the PIMM machining parameters on cutting forces	63
Table 3.4 Test series	68
Table 3.5 Cutting force test results	69
Table 3.6 Parameters of the produced chips	71
Table 3.7 Corrected cutting force test results	72
Table 4.1 Evaluation Matrix for the X and Y axes	81
Table 4.2 Raw segment array	96
Table 4.3 Processed segment array	97
Table 4.4 Profile array	98
Table 4.5 Miniature anti-backlash leadscrews from Reliance Ltd. [88]	108
Table 4.6 Shortlisted DC motors	109
Table 4.7 Simulation parameters	109
Table 5.1 Horizontal drive parameters	121
Table 5.2 Vertical drive parameters	122
Table 5.3 I/O card specification [92]	126
Table 5.4 Allocation of the I/O ports	126
Table 5.5 Driving amplifier properties for X and Y axis motors	127
Table 5.6 Driving amplifier properties for cutter motor	127
Table 5.7 Visual Basic files in the PIMM project	131
Table 5.8 Active segment variables	133
Table 5.9 Flowchart details - <i>ControlTimer</i>	137
Table 5.10 Flowchart details - <i>Sample</i>	139
Table 6.1 Amplifier and motor parameters before identification	149
Table 6.2 Causes of model variance	151
Table 6.3 Amplifier and motor parameters after identification	151
Table 6.4 Drive parameters	154
Table 6.5 Identified friction parameters	160

Table 6.6 Acceleration and deceleration zones	160
Table 6.7 Simulation performance with the modified friction model	162
Table 6.8 Simulation performance with the final friction model	163
Table 6.9 Final model parameters	167
Table 7.1 Machining parameters for the experiments	172
Table 7.2 Controller parameters for the experiments	172
Table 7.3 Friction compensation parameters	173
Table 7.4 Air cutting and wood cutting experiment results	175
Table 7.5 Pass direction experiment results	176
Table 7.6 Reference switch points for passes on different directions	178
Table 7.7 CMM Results: Intersection point coordinates (X, Y) in millimeters	179
Table 7.8 CMM results: Calculated distances (mm) between the intersection points	180
Table 7.9 CMM results: Arc centre points and diameters	181
Table 7.10 Image processing results: Intersection point coordinates (X, Y) and their calculated distances to the reference points	183
Table 7.11 Drive model parameters	185
Table 7.12 Comparison of the experiment and simulation results	187
Table 7.13 Modified simulation parameters	190
Table 7.14 Simulation results for left-to-right and right-to-left passes	190

Chapter 1

Introduction

1.1 Background and Motivation

Wood mouldings are long, narrow pieces of timber with ornamental profiles formed on one or more faces. They are used in furniture, architecture and joinery industries and typical applications include door/window frames, skirting boards and picture frames.

Conventionally, wood mouldings are produced by planing/moulding machines. Despite being widely used, the term “mouldings” is somewhat misleading since this is a material removal process and no material deformation as such takes place. The material removal phenomena is similar to that of milling of metals in up-cutting mode, where a cutterhead containing cutting edges is used to sever chips from the advancing workpiece (Figure 1.1) [1].

The cutterheads contain suitably shaped cutter knives for each individual profile; hence, the raw material is transformed into the finished product with a single feed. This process is characterized by high cutting tool tip velocities ranging from 30 to

125 m/s with correspondingly high workpiece feed speeds between 5 and 120 m/min [1][2].

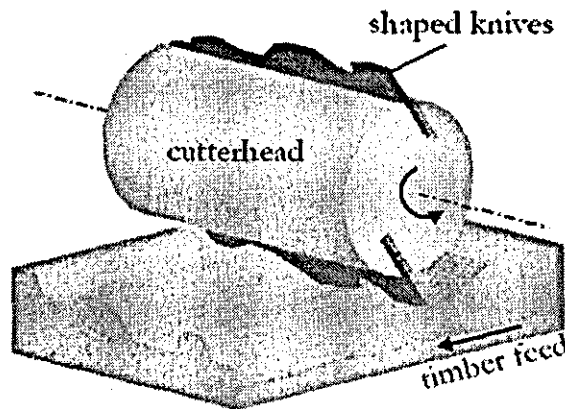


Figure 1.1 Conventional moulding process

When the production is to be changed from one profile to another, the conventional machines require new cutter knives that are manufactured for the profile to be machined. After the knives are changed, cutterhead balancing and machine set-up are needed to be performed before the production can start again. In mass production, high output capability of the conventional machines compensates the costs of manufacturing, mounting and maintenance of the profile-specific cutters as well as the downtime for machine set-up. Where just short production runs of particular type of moulding are required or even a few metres of a “one-off special” is needed, the aforementioned costs cannot be compensated.

It is intended to design a new moulding machine for short production runs in order to minimize the tooling and set-up costs. The proposed concept for a profile independent wood-moulding machine (PIMM) is described in the next section.

1.2 Proposed Machining Method

The essential part of the profile independent wood-moulding machine (PIMM) is a very thin (i.e. 1 mm) cutting disc, such as a circular saw, mounted on a two-axis positioning system (Figure 1.2). The moulding is produced by oscillating the rotating cutting disc along the width of the timber while following the desired profile geometry. The timber is fed in between two consecutive passes along the width.

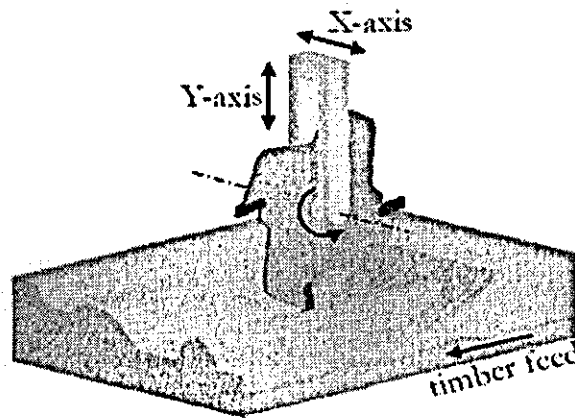


Figure 1.2 PIMM concept

In this concept, the profile geometry is supplied directly from CAD drawings, and the profile-specific cutter knives of the conventional process are emulated by position control of a single cutting tool along software generated trajectories. This introduces full manufacturing flexibility and enables the production of wood mouldings with minimum cost and machine set-up time. Also, within limits, the profile can be changed along the length of the timber, which is not possible with the conventional method.

It is clear that the production rate of the proposed method will be lower than the conventional method, but the PIMM is intended for smaller volumes of production where the conventional moulding machines are costly to operate.

1.3 Research Objectives

The overall objective of this research is the holistic development of profile independent wood-moulding machine (PIMM) through an integrated mechatronic design approach. In order to achieve the overall objective, the following secondary objectives were established:

- ◆ *To investigate material removal phenomena and cutting forces of the proposed machining method.*
- ◆ *To explore methods for extracting moulding profile geometry from CAD files.*
- ◆ *To form a mathematical modeling and simulation framework for the proposed machining method.*
- ◆ *To develop motion control and synchronization algorithms for cutter positioning.*
- ◆ *To build a test-rig for experimental verification.*

1.4 Research Novelty

The primary novelty of this research is the transformation of wood-moulding production from being hardware dependent to become software oriented. Before this work, the concept of using a single cutting tool for every moulding profile had never been experimented. Also, to the author's knowledge, the PIMM is the first example, where a circular disc cutter, such as a circular saw, is used to remove material while traversing along its axis of rotation.

This work is presented in the world's leading wood machining conference, 17th International Wood Machining Seminar, and the novelty is confirmed by the experts from academia and industry.

In addition, this research demonstrates an integrated design process that initiates from an idea and results in a fully functional, physical mechatronic system; via efficient use of software, simulation and rapid prototyping technologies.

1.5 Method of Approach

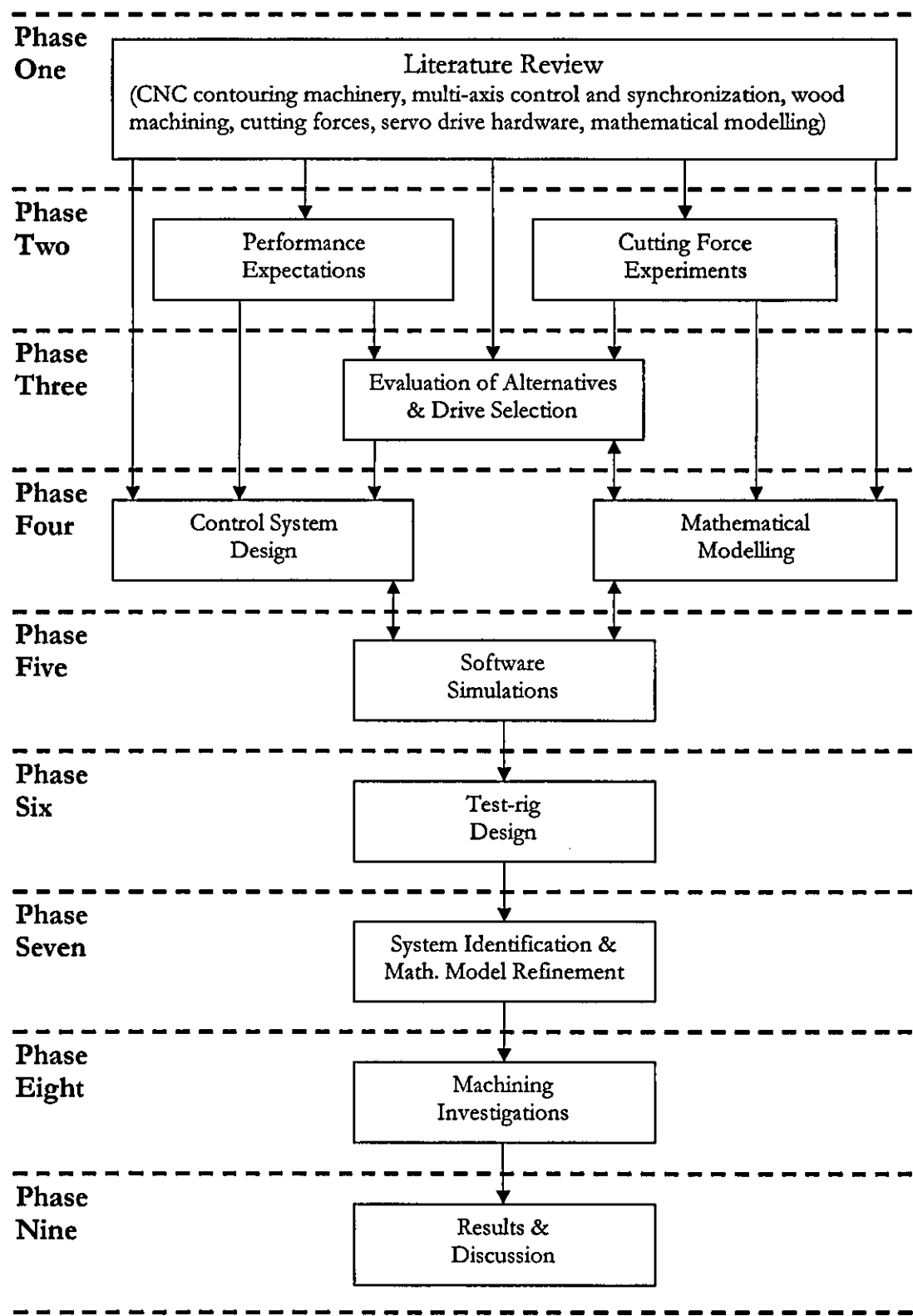


Figure 1.3 Research phases

Figure 1.3 depicts the nine phases of this research work and their interrelations. Brief descriptions of the phases are as follows:

Phase One consists of an extensive review of literature in related areas. The findings of this phase directly influenced the work carried out in the following three phases.

Phase Two: Performance targets are set for the PIMM system. Conceptual machining experiments were performed in order to investigate the material removal phenomena and cutting forces.

Phase Three evaluates actuator alternatives for the two-axis cutter positioning system. This phase results in a decision of the actuator type (i.e. timing belt drive, leadscrew drive, etc.).

Phase Four: The second stage of drive evaluation is supported by mathematical modeling. Available products are evaluated for the selected actuator type. Control system design is also performed in this phase.

Phase Five: Mathematical models and control system from the previous phase are refined and tuned via software simulations. The next phase is initiated when the simulation results meet the performance targets.

Phase Six: A test rig is designed for experimental verification.

Phase Seven: System identification is performed for refinement and validation of the mathematical models. Also, the unknown parameters of the test-rig are estimated.

Phase Eight includes experiments and testing. Limitations and performance of the concept, and its implementation, are analyzed.

Phase Nine discusses the results and identifies the areas for further research.

1.6 Thesis Organization

This thesis consists of eight chapters organized as follows:

Chapter 1 provides a general background on the production of wood mouldings, and introduces the proposed machining method. Objectives, novelty and methodology of this research work are also outlined.

Chapter 2 presents a literature review in various areas related to this research work.

Chapter 3 investigates the material removal phenomena and cutting forces in wood machining. Cutting forces occurring in the proposed machining method are estimated by a series of experiments. The experimental procedure is explained and the results are analyzed.

Chapter 4 describes the modeling and simulation framework. The PIMM system is studied in two parts as the electro-mechanical hardware and the control structure. In the first part; performance targets are set, actuators are selected, and mathematical models are derived. In the second part, algorithms for profile input and control system are explained. Finally, feasibility of the PIMM is verified via simulations.

Chapter 5 deals with some design aspects of the PIMM test-rig. Mechanical design, control hardware, and software implementations are presented.

Chapter 6 discusses the identification of system parameters for validation and refinement of the mathematical models. The employed procedures for friction modeling, identification, and simulation are explained.

Chapter 7 presents a discussion through machining experiments performed in the PIMM test-rig. The limitations and performance of the PIMM concept, in terms

of speed and accuracy, are investigated. Weak points of the current implementation are identified and potential improvements are proposed.

Chapter 8 outlines the conclusions of the research. Also, several areas of further research are recommended.

Appendices follow the main content.

Chapter 2

Review of Previous Work

2.1 Introduction

This chapter summarizes previous work done in the fields related to this research work. The reviewed literature is classified into four sections as follows:

- ♦ Wood machining: The areas of wood machining research, primarily related to planing and moulding:
- ♦ Contouring machinery: Capabilities and design features of the existing small-sized CNC contouring machinery.
- ♦ Profile Independent Wood-Moulding: Investigations on the concept prior to this research work.
- ♦ Multi-axis drive system control structures and software mechanisms: Review of the available multi-axis control algorithms and their evaluation in terms of performance, computational requirement and ease of implementation

2.2 Wood Machining

The previous work done in the areas of wood machining research, primarily related to planing and moulding, is reviewed in this section.

2.2.1 Definition and history of wood machining

Wood machining is a process of converting the wood feedstock into a value-added product, either by altering its geometric shape or improving its surface finish or the combination of both [3]. The challenge from a researcher point of view is to optimize the process in order to achieve manufacturing at the lowest cost within the shortest possible time with minimal waste and highest quality.

Wood was one of the first raw materials to be used by man and this use continues to the present day. In the beginning wood would be used in its raw state but, with the development of stone and metal tools, man began to use them to produce shapes that were more convenient to use. That was the beginning of woodworking industry [4].

The mechanization of woodworking starts with water wheel actuated sawmills. Such mills were in use in Europe since the 14th century and they would have used reciprocating saws. The cutting and shaping of wood by machine became widespread only after the late 18th century following series of important inventions.

The invention of steam engine made available a power source, which can be installed in any appropriate premises. Moreover, this new source was capable of delivering more power than water with controllability all year around. At this time, however, there were no machine tools, which could be used for cutting of wood.

The rotary machine cutting of timber started in 1777 with the invention of circular saw by Samuel Miller. Machine planing or moulding of wood became available

after the invention of rotating cutter block by Samuel Bentham in 1793. The origins of most of the types of woodworking machinery in use today can be tied to machines invented between about 1777 and 1850 [4].

The modern planers have developed initially from Malcolm Muir's patented invention in 1827. This machine was using an endless chain mechanism for automatic timber feed and tonguing and grooving saws for the planing operation. John McDowall modified the design of Muir in 1836 and converted machines to the planers that we know today. Feed rollers replaced the endless chain and rotating cutter blocks were employed instead of tonguing and grooving saws.

The end of the 19th century saw many engineering developments taking place in terms of machinery. Improvements like precision ball bearings, higher spindle speeds, better tooling materials and techniques have found their way into the woodworking industry.

Transmission of power from a single prime mover using lineshafts, belts and pulleys was causing a great deal of inefficiency due to significant power losses in the system and down-time for maintenance of numerous belts and bearings. Moreover, the positioning of the machines in the factory floor was dictated by the transmission mechanisms, resulting in a complicated workflow. In the beginning of 20th century, electric motors were first used in woodworking machinery for breaking down the complicated lineshaft transmissions. This new generation of machines offered much improved efficiency, flexibility and saving in floor space. Today's modern planers and moulders with their multiple cutterhead arrangements made the production more flexible and compact by replacing individual machines designed for particular operations.

Another set of improvements has been experienced in the tooling area of woodworking machinery. The square cutterblock has largely been superseded by round cutterblock tooling [2]. Due to the introduction of more durable cutting materials, solid profile cutting blocks are used less. Replaceable tungsten carbide

inserts offering improved tool life are used instead of high-speed steel cutter knives. Segmental cutterblocks are used for moulding.

2.2.2 Wood mouldings

Wood mouldings are long, narrow pieces of timber with ornamental profiles formed on one or more faces. Wood mouldings are used in furniture, architecture and joinery industries and typical applications include door/window frames, skirting boards and picture frames. They differ in the shape of the profile as well as the wood types used. A selection of wood mouldings can be seen in Figure 2.1.



Figure 2.1 Selection of wood mouldings

The raw material for the mouldings is in the form of rough sawn pieces with constant nominal rectangular cross section along the length. The section dimensions typically range from 10 to 100 mm thick and 20 to 300 mm wide. Timber lengths can be as small as 250 mm and as long as 6 metres depending on the customers' requirements and the incoming packs of timber. The lengths of run of any type of profile vary between several hundred metres to several hundred thousand metres in mass production [2]. The characteristics of the timber raw material, cutting tool parameters, spindle speed and feed rate are the four main factors affecting moulding process. All of them play an important role in the quality of the finished product.

After the moulding process the timber can go through intricate shape machining and sanding to produce components for assembly of furniture products. The final assembly is finished with stain and polish and the end product is produced.

2.2.3 Planing and moulding machines

Wood mouldings are produced in planing and moulding machines. The general name for this machining process is rotary machining of timber. Despite being widely used, the term 'mouldings' is somewhat misleading since this is a material removal process and no material deformation as such takes place. The material removal phenomena is similar to that of milling of metals in up-cutting mode, where a cutterhead containing cutting edges is used to sever chips from the advancing workpiece (Figure 2.2) [1].

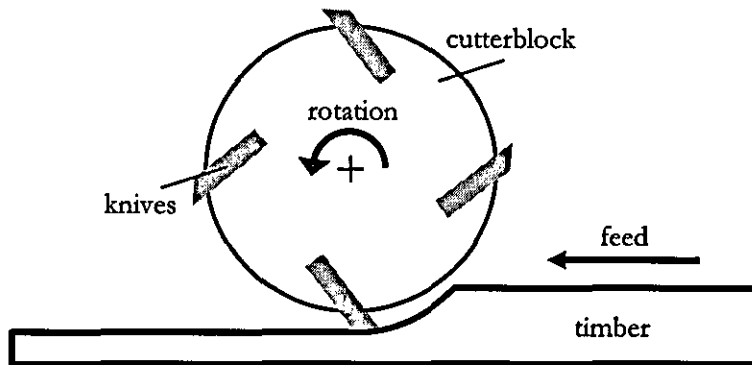


Figure 2.2 Rotary machining process

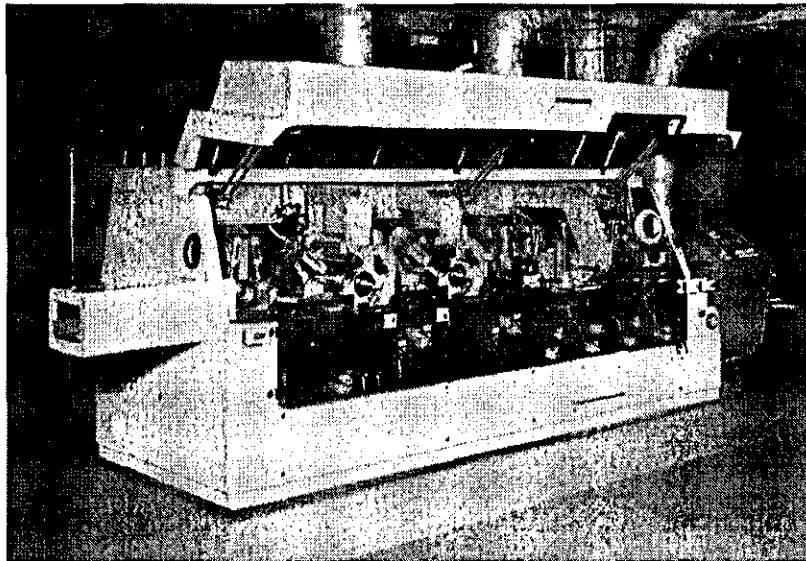


Figure 2.3 Planing and moulding machine

Rotary machining of timber is characterised by high cutting tool tip velocities ranging from 30 to 125 m/s with correspondingly high workpiece feed speeds between 5 to 120 m/min. Planing and moulding machines (Figure 2.3) comprise a number of horizontal and vertical cutterheads configured in position and type (Figure 2.4) to suit a particular market segment (e.g. saw milling, joinery, furniture). Consequently, high material removal rates are achievable.

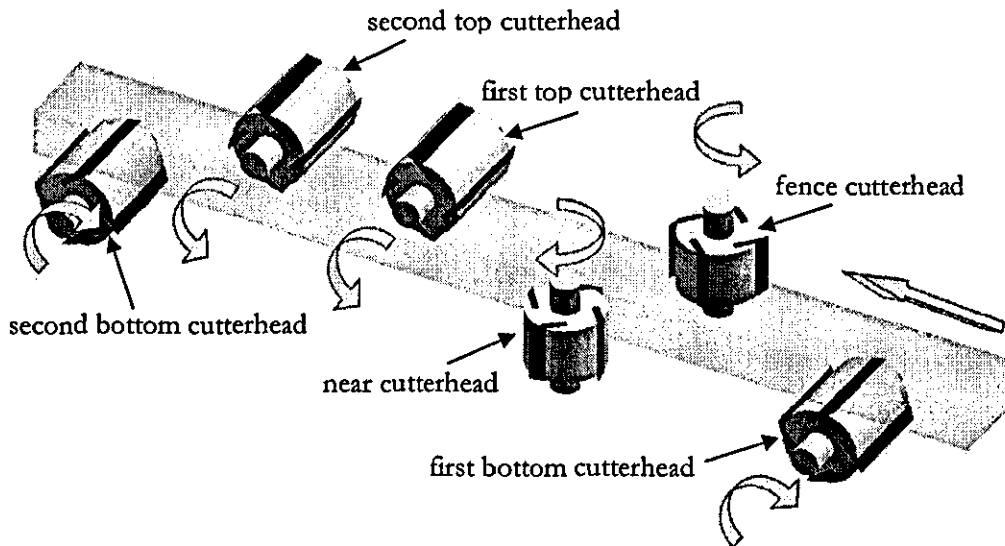


Figure 2.4 Cutterhead configuration

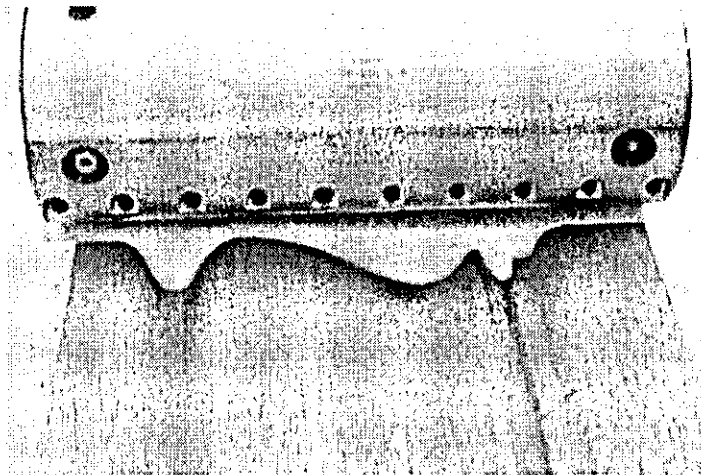


Figure 2.5 Profile-specific cutting knife

Planing and moulding machines are economical in mass production due to their high throughput capability and the possibility of machining all the faces in one feed. On the other hand, the need for using suitable shaped cutting knives (Figure 2.5) for each individual moulding profile makes the process inflexible to changes in production.

When the production is to be switched from one profile to another, first all the cutting knives are changed, then the cutterheads are balanced and then the machine set-up is performed in order to start machining the new profile. The high production rates of the machines compensate for the costs incurred in manufacturing, balancing and maintenance of the profile-specific cutting knives, as well as the set-up downtime. Where short production runs of a particular type of moulding are required, or even a few meters of a “one off special” is needed, the tooling and set-up costs cannot be compensated [5][6].

2.2.4 Surface quality

The quality of the machined timber surface determines the market sector in which the manufactured product can be used. It is characterized by three parameters.

- ◆ Geometric accuracy
- ◆ Surface roughness
- ◆ Surface waviness

In terms of geometric accuracy, the tolerances vary from $\pm 0.1\text{mm}$ to $\pm 0.5\text{mm}$ depending on the end-usage of the product. Surface roughness is described as texture effects due to the cellular structure of timber and also produced by cutting the timber with a knife edge. Surface waviness is defined as the longer-wavelength components produced by the rotary machining process, including any deviations from the ideal waviness profile [1]. The roughness and waviness quality of a timber surface is influenced by the following key factors [2]:

- ◆ Type and condition of the timber workpiece,
- ◆ Type and condition of the cutter equipment used,
- ◆ Machine configuration,
- ◆ Method of machine operation,
- ◆ Engineering quality of the machine.

Surface roughness is primarily influenced by workpiece and cutting tool properties whereas the surface waviness is primarily determined by type, operation and engineering quality of the machine.

Surface waviness is the inevitable result of the rotary machining process. Rotating cutterheads produce a regular series of waves that are perpendicular to the workpiece feed direction. An illustration of the ideal case for surface waviness is shown in Figure 2.6.

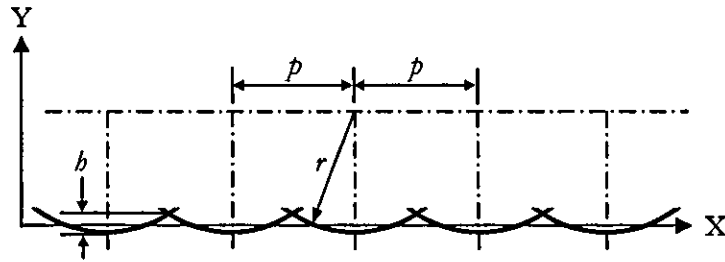


Figure 2.6 Surface waviness concept

The relationship between the parameters is well established and widely used [1][2][7][8] and is shown by equation (2.1).

$$p = \frac{V}{N \cdot n} \quad (2.1)$$

Where p is the surface wave pitch (mm), V is the workpiece feed velocity (mm/min), N is the number of cutting edges and n is the angular velocity of the cutterhead (rpm). A good quality surface is classified by a wave pitch of typically <1.5 mm and a lower quality surface by a wave pitch of typically >2.5 mm. The

wave height h of the idealized surface is defined by equation (2.2), where r is the cutter tracking radius, and is typically $2\text{ }\mu\text{m}$ for higher quality surfaces [1].

$$h = r - \sqrt{r^2 - \frac{p^2}{4}} \quad (2.2)$$

Surface waviness has no significant importance if the product is going to be coated or hidden by other materials. On the other hand; industries like furniture, joinery and high quality mouldings, where aesthetics is the main concern, demand the highest quality machined timber.

The equations above show that there is a trade off between quality and cost in rotary machining of timber. Increasing the feed speed on its own to achieve high throughput results in increased wave pitch therefore decreased quality. Also increasing the number of cutters and/or the spindle velocity preserves the quality but increases the power requirements and cost of production.

2.2.5 Productivity in wood machining

Woodworking industry deals with substantial amount of economic and technological complexity. However, in contrast to the vast amount of research and publication for metal machining, wood machining has received little attention. Due to the similarities with wood machining, researchers of the field often used widely studied metal milling and grinding literature [1].

Current productivity improvement initiatives in furniture production environments do not accord the necessary importance to wood machining processes. In most instances, efforts are targeted towards direct cost elements such as raw material and labour. A close examination of the product expenses however, reveals that machining related cost can account for 23% of the total production cost, and improvements in machining processes will inevitably lead to better production throughput and reduced unit cost [9]. Wood machining

research worldwide has traditionally focused on reducing cutting tool wear, improving tool design and optimizing spindle speed [10].

Productivity in wood machining processes has two essential dimensions, namely the resultant surface quality and the cost incurred [11]. The concept of quality in furniture must be approached from three different perspectives; structural, functional, and aesthetical. The influence of machining processes on aesthetical aspects of the furniture is perceived to be more far reaching than what it exerts on the structural and functional aspects [10].

The machining cost in the furniture industry is the sum total of four other cost elements [12] as defined in equation (2.3).

$$C_T = C_c + C_h + C_t + C_n \quad (2.3)$$

where, C_T is the total machining cost, C_c is the machining cost, C_h is the tool change cost, C_t is the tooling cost and C_n is the non-productive cost. The four cost elements contributing the total machining cost can be derived from equations (2.4) to (2.7).

$$C_c = \frac{R_c \cdot L \cdot \pi \cdot D}{F \cdot V} \quad (2.4)$$

$$C_h = \frac{R_c \cdot L \cdot \pi \cdot D \cdot t_1}{F \cdot V \cdot T} \quad (2.5)$$

$$C_t = \frac{C_e \cdot L \cdot \pi \cdot D}{F \cdot V \cdot T} \quad (2.6)$$

$$C_n = R_c \cdot t_n \quad (2.7)$$

Where R_c is the overhead charge rate (£/hour), L is the length of cut (m), D is the diameter of the cutter (mm), F is the feed rate (m/min), V is the cutting speed (mm/s), T is the tool life (min), t_l is the tool change time, t_n is the non-productive time, and C_t is the tool cost.

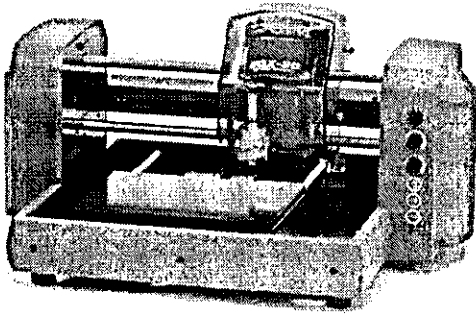
Increasing the cutting speed during the machining process, despite increasing the machining output, increases the tool change cost, tooling cost and unproductive cost as well. Therefore, an optimal cutting speed is not only preferable but also economically viable as well.

The R_c factor in the above equations constitute power consumption and machine depreciation rates. The relationships between power consumption and machining variables allow for a better estimation of energy requirements during the machining process. Coupled with the mathematical relationship for machining rate, tool wear and its related cost, the total machining cost can be determined more accurately [9].

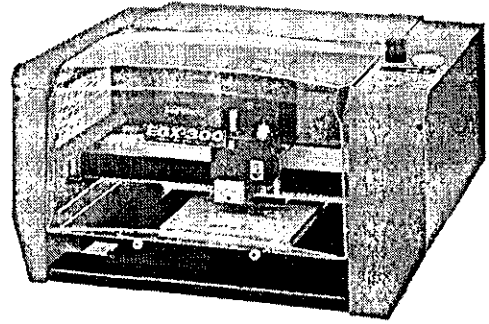
2.3 Contouring Machinery

As a part of the literature survey, the existing CNC contouring machinery for processing soft materials (i.e. wood, plastics, light metals etc.) have been researched. The following keywords were entered to scientific and www search engines:

- | | |
|---------------------------------------|-----------------------|
| ♦ miniature CNC machinery | ♦ CNC waterjet cutter |
| ♦ CNC contouring machinery | ♦ CNC laser cutter |
| ♦ CNC benchtop routing machine/router | ♦ vinyl cutter |
| ♦ CNC mini milling machine | ♦ contour cutter |
| ♦ CNC engraving machine/engraver | ♦ plotter |



1 – Roland EGX-20 Desktop Engraver



2 – Roland EGX-300 Desktop Engraver

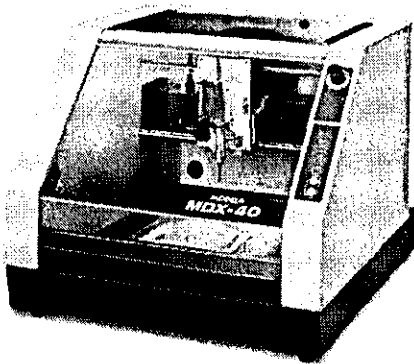
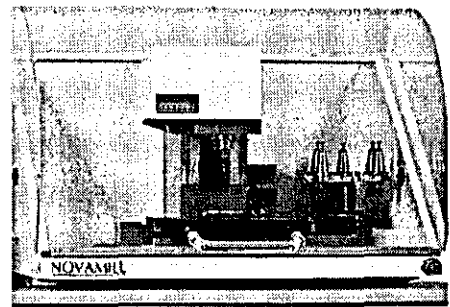
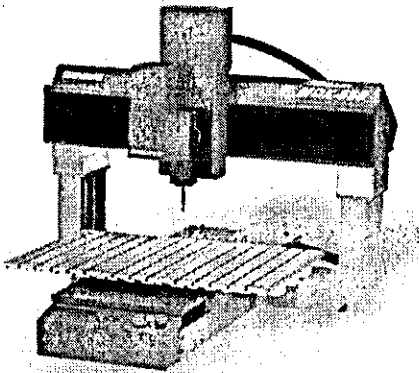
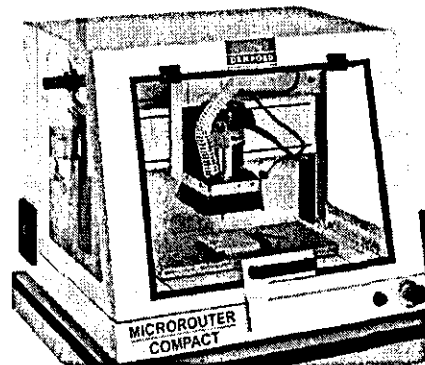
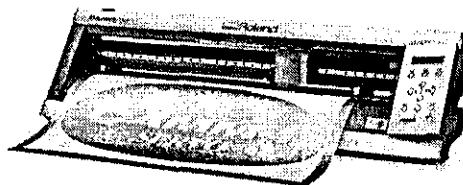
3 – Roland Modela MDX-20
CNC Desktop Milling Machine4 – Denford Novamill
CNC Desktop Milling Machine5 – Roland Modela MDX-650
CNC Desktop Milling Machine6 – Denford Microrouter Compact
CNC Desktop Router7 – Roland CAMM1 GX-24
Desktop Vinyl Cutter

Figure 2.7 Some examples of CNC contouring machinery [13][14]

The scientific search engines did not provide relevant information about the keywords. On the other hand, some examples are found from leading manufacturers of small-sized CNC processing machinery; such as Roland [13] and Denford [14]. Figure 2.7 shows photographs of these machines, and Table 2.1 lists their selected properties. The properties for the PIMM are approximated for comparison.

machine # (Figure 2.7)	operation area (XYZ) (mm)	max. drive speed (mm/s)	drive motor type	max. spindle speed (rpm)	spindle power (W)	selling price (£)
1	203x152x32	15 (XY), 6(Z)	step	15000	12	1500
2	305x230x30	60 (XY), 30(Z)	step	15000	30	3000
3	305x305x105	50 (XY), 30(Z)	step	15000	100	3000
4	229x152x114	25 (XY), 9(Z)	step	5000	370	12500
5	650x450x155	85	AC	12000	400	14000
6	400x200x100	37.5	step	24000	1300	7000
7	584x25 (XY)	10-500	DC	force on blade = 2.45N		1500
PIMM	$\approx 150 \times 30$ (XY)	≈ 300 (XY)	DC	> 15000	> 100	

Table 2.1 Some properties of the selected machines

Except the vinyl cutter (#7), the selected machines perform three-axis contouring, where X and Y are the horizontal axes and Z is the vertical. Whereas the PIMM performs two-axis contouring on the X- (horizontal) and Y- (vertical) axes, and the Z-axis (horizontal timber feed) thru-feeds the workpiece in one direction. In terms of operating area and spindle speed, the PIMM is near to the desktop engravers (#1 and #2). On the other hand, the required spindle power is in the range of milling machines (#3, #4, #5). However, the drive speeds in both types of machinery are much slower than the expected speed of the PIMM (i.e. ≈ 300 mm/s). The vinyl cutter (#7) operates at faster drive speeds, but the force acting on the vinyl cutter drives (i.e. force on blade) is very low compared to the ones expected to act on drives of the PIMM. Positioning accuracy and repeatability of the selected machines are ± 0.1 mm. This value is also expected from the PIMM.

As a result, the PIMM cannot be benchmarked directly against a certain type of machine, but it combines different features of various small-scale contouring machines.

2.4 Profile Independent Wood-Moulding

This section summarizes the previous work on the PIMM concept prior to this research work.

The initial effort on the concept [15] was concentrated on electro-mechanical design of a two-axis test-rig in order to experiment the feasibility of tracking moulding profiles. In a subsequent investigation [5][6][16], profile tracking was explored in more detail by applying various path control methods on the test-rig. Although, the results showed some evidence on the viability of the concept, the achieved tracking speed and accuracy were far from being satisfactory.

In the previous studies; possible options for cutter, spindle and timber-feed were not explored. The efforts were concentrated solely on the positioning along the X and Y axes under no-load (i.e. air cutting) conditions. However, the fact that the positioning is for a machining process was overlooked, and the real novelty, which is the method of material removal, had not been investigated. The priority of the X and Y axis drives is to accommodate a cutter and a spindle unit, which delivers sufficient power to remove material. Furthermore, this power requirement determines the weight and size of the spindle unit, and these are the most important factors that influence the design of the X and Y axis drives.

It can be concluded that, in order to achieve a successful PIMM system, a thorough investigation of the process requirements is essential in the initial stages of the design activity.

2.5 Multi-Axis Drive System Control Structures and Software Mechanisms

When compared to the conventional moulders, it is clear that the PIMM has a slower production rate. Whereas, the quality of the mouldings produced by the PIMM should match the ones produced by the conventional moulders utilizing

shaped cutters. Apart from the drive hardware with good dynamics, optimum control and synchronization of the drive motions are essential in order to achieve the required geometric accuracy. Therefore, the available multi-axis control algorithms have been investigated and evaluated in terms of their accuracy, computational requirement and ease of implementation.

2.5.1 Motion control coordination and error sources

Most of the machines and processes that are automated involve motion; therefore, they will require motion control and, quite often as in the case of PIMM, coordinated motion. From the motion control viewpoint, coordination and synchronization of any motions can only be obtained through some constraint. Mechanical systems achieve motion coordination and synchronization over a wide range of normal and abnormal operating conditions using cams, gears and linkages [17]. The mechanical coupling of motions is introduced by solid members. Any disturbance on one axis will transmit to all axes and the relative reactions will also reflect back to all axes. As long as the transmission parts are robust to withstand the disturbance and reactions, the synchronization of the motions can be maintained. When the mechanically linked systems are replaced by independent servo drives, the servo drives must be forced into coordination and synchronization by an appropriate control system.

The principle behind synchronization architecture is that independent intelligent drives perform in a dependent manner. This structure introduces reciprocal actions which provide the constraint. In the mechanical systems, the constraint is the direct restriction force, because of the rigid structure. In software mechanisms, the constraint which regulates the motions is control actions which are based on the feedback information of the states of the whole system. These real-time reciprocal actions between servo-drives can be provided by a closed-loop control [18].

There are two types of motion systems: (1) point-to-point (PTP), and (2) contouring (continuous path). For PTP systems, a good axial positioning accuracy at the target points is required, and usually, a conventional proportional (P) controller can satisfy this requirement [19][20]. PTP systems are used in pick-and-place machines, packaging machines and some machining operations like CNC drilling. However, most manufacturing machinery, including the PIMM, performs contouring operations, where the axes-of-motion trace a predetermined path of the “tool” relative to the workpiece. In contouring systems, the prime concern is the “contouring error” ε , which is the shortest distance from the actual position P to the desired contour, rather than the axial tracking errors E_x and E_y (Figure 2.8).

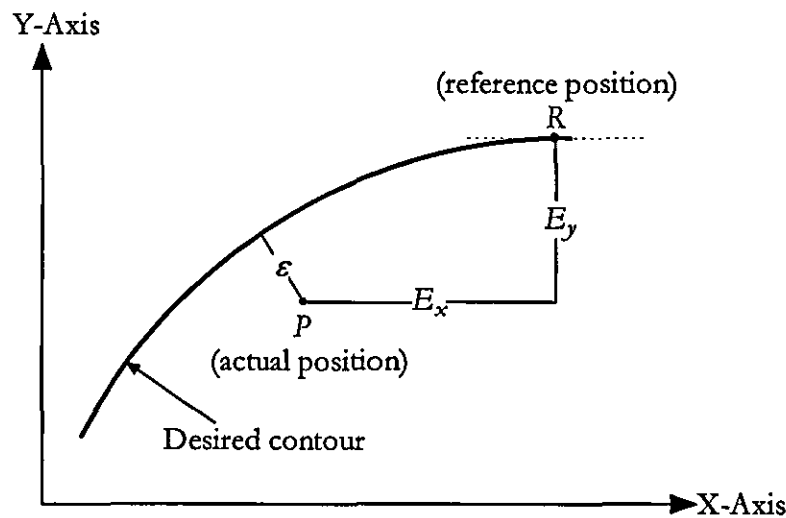


Figure 2.8 Contouring and tracking errors

Contour error sources in machining may be classified into three categories:

- ◆ mechanical hardware deficiencies (e.g. backlash, straightness error of the guideways, etc.) [21][22].
- ◆ cutting process effects (e.g. tool deflection, tool wear, vibration, etc.).
- ◆ controller and drive dynamics.

The total dimensional error is a combination of all errors from the above sources. The first and second sets of error sources can be reduced by improving the

mechanical hardware or utilizing compensation techniques but cannot be reduced by the control techniques discussed in this section [20][23]. However, the third set of error sources can be eliminated or reduced by utilizing properly designed multi-axis control and synchronization and they can be further classified into three categories [18][20][24].

(i) Mismatch in axial loop parameters

In case of mismatch axes, where the open-loop gains and the time constants of the axes of motion are not identical, each axis-of-motion has a different velocity transient and steady state position error. This causes contouring errors even without the presence of load disturbances [23].

(ii) External disturbances

Here a disturbance means an external action to the control loop which changes or disturbs the desired operation of the controlled variable. The controlled variable in this case is the position and the disturbances are the friction and the cutting forces.

(iii) Reference contour

For linear contours, each axis receives a position ramp input as a reference. The slope of the ramp is proportional to the required axial velocity. For ramp inputs, the control loop does not need special tracking abilities. However, when producing non-linear contours, the inputs to the control loops are also non-linear and this causes contour errors [20][25]. Contour errors also occur when cutting sharp corners. For example, if the table moves in the X-direction before the corner, and then in the Y-direction, the X-axis will still move when the motion in the Y-direction starts, which causes contour error [19].

The conventional controllers used in PTP systems result in significant contour errors in contouring systems. The approaches aimed at reduction of contour errors are discussed in five groups as follows:

- ◆ Sophisticated axial controllers for independent drives
- ◆ Dual-loop controllers
- ◆ Cross-coupling controllers
- ◆ Controllers with coordinate transformation
- ◆ Scalar field control technique

2.5.2 Sophisticated axial controllers for independent drives

Figure 2.9 shows the simplest biaxial control structure where two feedback controlled independent servo-drives receiving reference motion commands from a single microprocessor. The desired motion synchronization is defined by the reference position commands that are sent to individual axes and, none of the actual axis positions are used to generate a position demand from another axis. With this open-loop structure, the resulting motion synchronization is determined by the performance of individual servo-drives. The control algorithms in this section are aimed at individual drives to follow their command inputs as accurately as possible

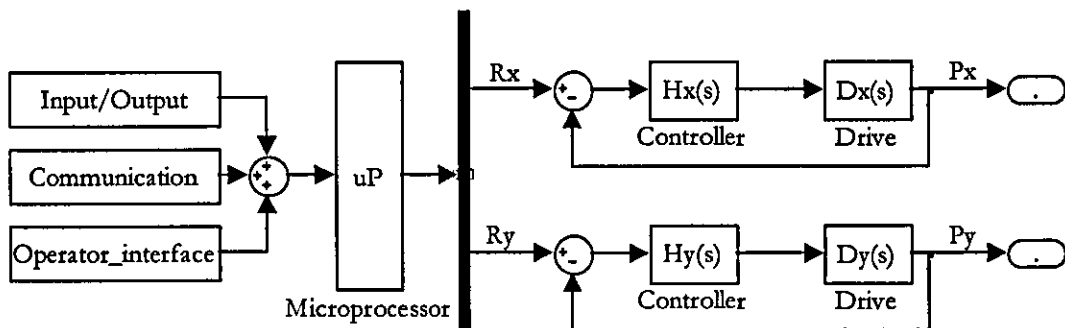


Figure 2.9 Biaxial motion control system

PID controller: It is the first solution that should be tried when feedback is used. The PID controller is by far the most dominating form of feedback controller used in the industry. More than 90% of all control loops is PID [26]. The correction signal is a combination of three components, namely, proportional (P), integral (I) and derivative (D). The controlled variable is corrected in a proportional manner to the error, steady-state errors and external disturbances are rejected with the integral term and using a derivative term the system damping is increased.

Design and tuning of PID controllers have been a large research area but these are not the focus of this work. Some recent examples can be found in [26][27][28] and [29].

Two main problems with PID controllers in contouring applications are: (1) poor tracking of corners and non-linear contours and (2) significant overshoots. To reduce the effect of these problems, the integral gain should be small and the implementation of the controller requires careful pre-programming of acceleration and deceleration periods [20].

Set-point gain scheduling (SPGS) method reported in [30] and [31] is another approach directed to remedying the corner tracking and overshoot problems. In this method, one high-gain and one low-gain controller is designed. The high-gain controller is used at the start in order to produce a rapid transient response. Then, the system switches to low-gain controller at a pre-defined point to ensure no overshoot. However, this method is only applicable to repetitive tasks and its use for stochastic systems is severely limited.

Feedforward controllers: Feedforward controllers have a feedforward term aimed at minimizing the position error during the move. The method is based on anticipating the required motion command signal and providing it as a bias signal [18]. Typically, the command signal is used in combination with an inverted plant model [32].

The two principal types of feedforward controllers are shown in Figure 2.10 where $H(s)$ and $D(s)$ represent the controller and drive units respectively.

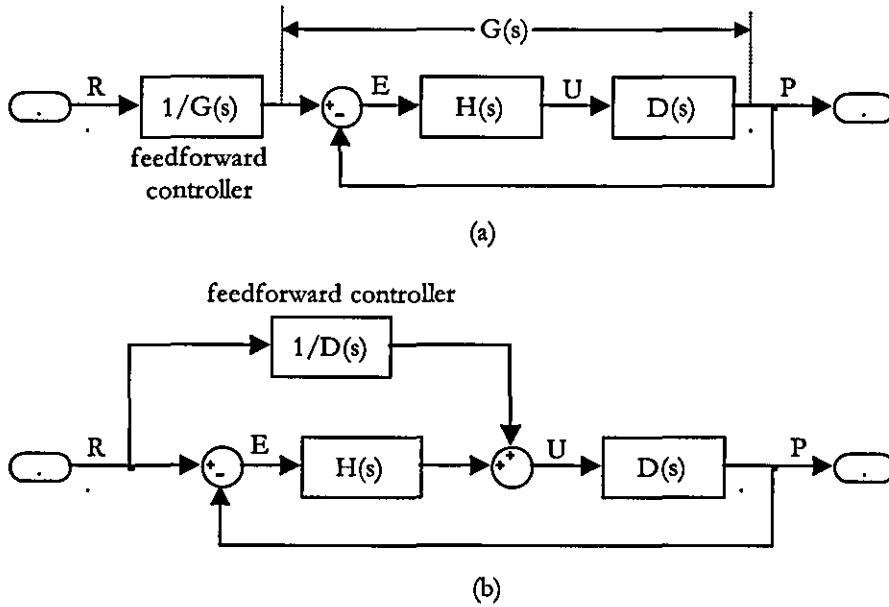


Figure 2.10 Two principal types of feedforward controllers [18]

The idea behind the design in Figure 2.10(a) is to implement in the control computer a transfer function, which is the exact inverse of the feedback control loop $G(s)$; and then the actual position becomes the required position. The design in Figure 2.10(b) has the same objective but the feedforward controller is the inverse transfer function of the drive unit only, and therefore it is independent from the design of the feedback controller [20].

A more advanced feedforward controller named "Zero Phase Error Tracking Controller (ZPETC)" was proposed in [33]. The concept of the ZPETC is based on pole-zero cancellation (i.e. $G^{-1}(z) \cdot G(z)=1$) and the design is similar to the one in Figure 2.10(a). The major disadvantage of the ZPETC is that it requires precise knowledge of the dynamic behavior of the drive system. However, there is usually a difference between the actual system and the model used in the computer, and this introduces another error source to the control system. Also, any external load perturbation or parameters varying in the position feedback loop may seriously degrade control performance [34]. In order to deal with the modeling errors and

plant parameter variations, adaptive ZPETC designs were proposed by many researchers [34][35][36].

Corner tracking problems also exist with ZPETC. To overcome this deficiency, the “Inverse Compensation Filter (IKF)” method was proposed [37]. This method adds a low-pass filter before the feedforward controller. The low-pass filter filters out the high-frequency signals needed in corner tracking, and consequently smoothes the resultant contouring path.

A basic comparison of the servo-controllers on dealing with the error sources described in the previous section is summarized in Table 2.2.

	P control	PID control	Feedforward (with P controllers)
Tracking non-linear trajectories	Fair	Fair (low speed) Poor (high speed)	Excellent (1) Fair (2)
Axis mismatch	Fair	Good	Excellent (1) Fair (2)
Disturbances	Poor	Good	Poor
Special Problems		Overshoot at stopping	Performance is sensitive to modeling error

Notes:

1. Assume no difference between theoretical model and real system
 2. Assume 2% difference between theoretical model and real system
- Grading: Excellent, Good, Fair, Poor.

Table 2.2 The evaluation of independent axis controllers [18]

2.5.3 Dual-loop controllers

Dual-loop controllers consist of two control loops, the inner loop embedding conventional motion controllers for each axis and the outer loop for synchronizing all axes. A schematic representation of biaxial dual-loop controller can be seen in Figure 2.11. Dual-loop design was firstly introduced for backlash compensation and slip couplers. Later, it has also been applied to feed systems for

packaging materials, high performance magnetic tape drives, and web tension control.

The design of a dual-loop controller is rather complex, since the control actions among the axes need to be well coordinated to avoid control action conflicts. There exist various designs for the outer loop controller. In [38] the outer loop controller dynamically modifies the interpolation process at each loop closing based upon the examination of the current actual and desired states of all axes. Depending on the examination, the controller determines whether or not the next increment of motion should be added to the inner control loop. A more improved version of this method is reported in [39]. The idea here is that, rather than simply deciding whether one should add the next increment of motion, one may choose to move forwards or backwards a set of increments determined by the consensus of all processes involved.

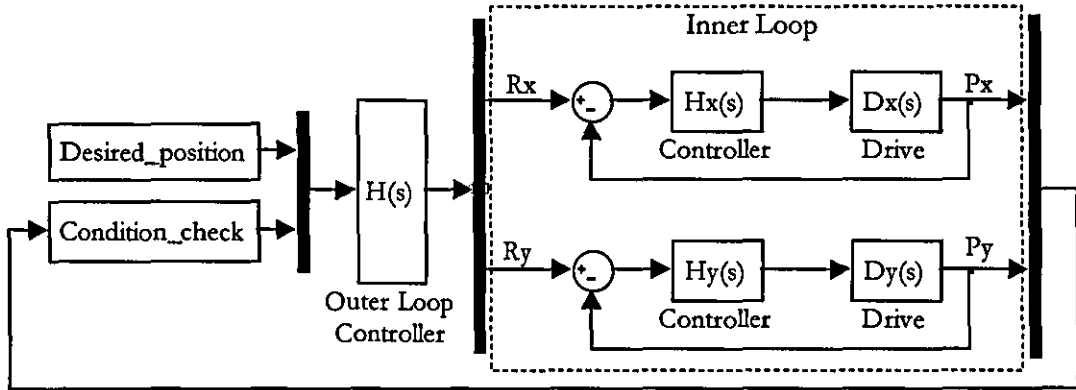


Figure 2.11 Biaxial dual-loop controller

Another design is presented in [40]. Given $x(k)$ and $x(k+1)$ are the desired outputs at k th and $(k+1)$ th time instances, the drive is required to move from $x(k)$ to $x(k+1)$ in a single step. If the required acceleration for this move is more than the drives capability, saturation occurs. In this design, the controller predicts the drive saturation and slows down the desired contour tracking speed to avoid it. The contour tracking speed is slowed down via an online trajectory planning algorithm. When the saturation is predicted, intermediate points are inserted between $x(k)$

and $x(k+1)$. Consequently, the distance from $x(k)$ to $x(k+1)$ is travelled in more than one step resulting in lower acceleration requirement and slower contour tracking speed. The same number of steps is also inserted to the other axis, even if it is not predicted to saturate, in order to preserve the motion coordination.

Compared to the independent drive controllers explained in the previous section, the dual-loop controllers result in better contouring accuracy due to the closed-loop nature of the motion synchronization.

2.5.4 Cross-coupling controllers

The cross-coupling control (CCC) architecture is concentrated on machine tool control. It was developed as a better alternative to conventional independent drive controllers for contouring applications. Also, some work in cross-coupling control can be found in the field of robotics, particularly in the domain of mobile robot control [41].

In a real (i.e. hardware) mechanism, there is inherent coupling between the various axes, and this ensures that a disturbance (load) applied to one axis will affect all axes in such a way that synchronization is maintained. In the basic software mechanism with independent drives, however, there is no coupling, so a disturbance affects only the axis to which it is applied. As no control system is ideal, the output position of the disturbed axis is bound to deviate from the reference position. The other axes are unaffected, so the output position state deviates from the desired contour [42].

The more primitive software mechanisms, that introduce coupling between independent axes, use master/slave topology. In this approach, the output position of one axis (the master) is fed through a transformation and used for the reference of another axis (the slave). When the master lags due to a disturbance or a demanding reference signal, the slave is restrained as well. This method is of

limited value because of the unidirectional nature of the coupling since no improvement is gained for disturbances applied to the slave axis [42].

The cross-coupling control architecture was first proposed in [43]. Unlike the master/slave techniques, it couples the axes in a symmetrical manner and grants equal-status to the axes. The main idea of cross-coupling control is to build in real time a contour error model based on the feedback information from all the axes as well as the interpolator, to find an optimal compensation law, and then to feed back correction signals to the individual axes. The cross-coupling controllers consist of two parts (1) the contour error model, and (2) the control law. All based on the original concept in [43], various CCCs were proposed by many other researchers. The differences lie either in the contour error model [44][45][46][47] or in the control law [24][48][49][50][51][52][53]. The block diagram of the cross coupled system is shown in Figure 2.12.

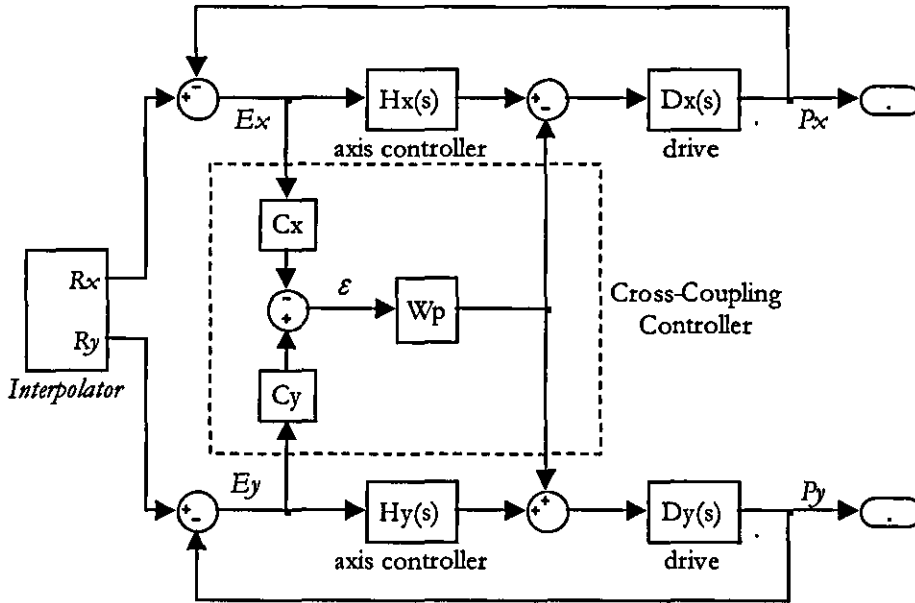


Figure 2.12 The cross-coupling controller [24]

The primary objective of the independent drive controllers is to reduce the individual axial tracking errors and thereby expect a reduction in the resultant contour error. However, reducing the axial errors does not necessarily reduce the

contour error in nonlinear cuts. Consider, for example, the case in Figure 2.13. Improvements in the axial control strategy shift the actual cutter location from point P to point P' . Although the axial errors E_x' and E_y' at point P' are smaller than E_x and E_y , the contour error at P' is larger than that at P [24].

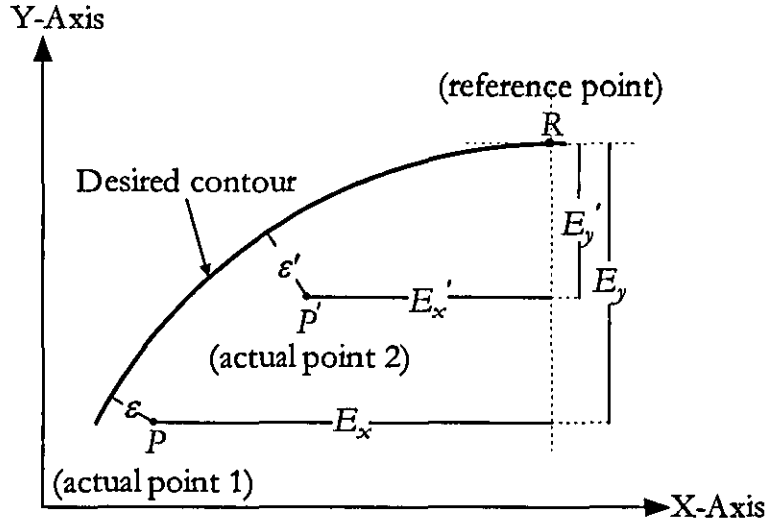


Figure 2.13 The axial and contour errors for different cutter locations

The philosophy of the cross-coupling control is that the elimination of the contour error ε is the controller objective. It considers the whole system as a single unit, rather than as individual loops. For a two axis system, the CCC responds to the difference between the two motion errors (i.e. synchronization error), to generate a coordination signal for the axes. The cross-coupled structure is suitable for systems where the time response of each individual controlled variable takes on a smaller role relative to the intervariable dependence $y=f(x)$ [43]. However, [48] and [49] report that the CCC, which was designed after the design of the individual axis controllers, improved the contouring response nearly independent of tracking response. Moreover, the design of the CCC was based on the linear model of the feed drive dynamics with significant non-linearities.

The Variable-Gain Cross-Coupling Controller, reported in [24], is an improved, non-linear CCC that is based on gains that vary in real-time according to the shape of the contour. This approach is superior to the basic CCC in dealing with non-

linear contours such as circles and parabolas. The structure of the variable-gain CCC is shown in Figure 2.14.

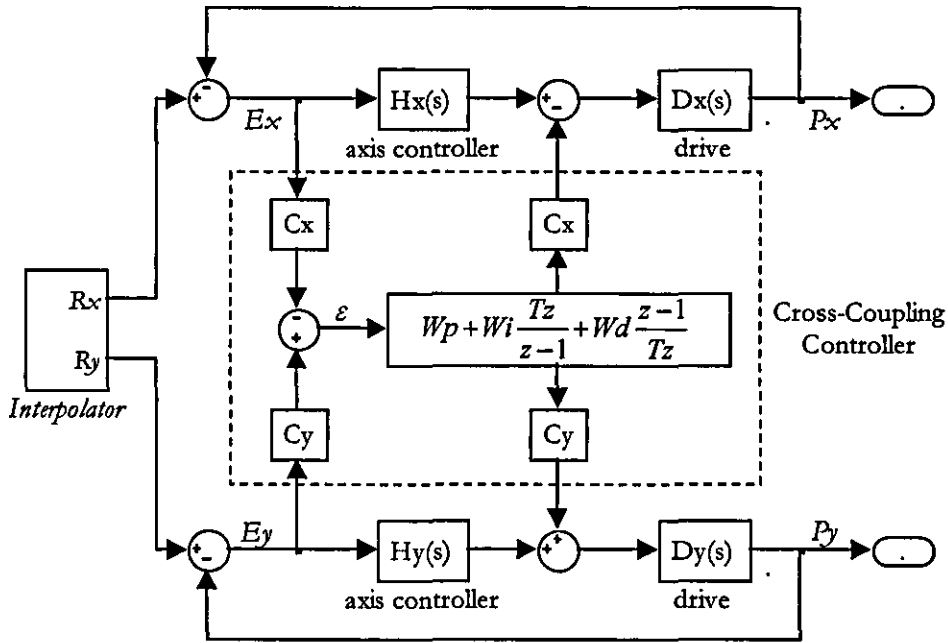


Figure 2.14 The variable-gain cross-coupling controller [24]

The PID controller gains W_p , W_i , and W_d (Figure 2.14) are fixed for a particular system. Typically, the cross-coupled control system is a multivariable system for a linear trajectory, and a multivariable, non-linear and time varying system for a circular trajectory. Hence, it is very difficult to select the controller parameters (gains). A trial and error approach for controller parameter selection is adopted in most applications [45]. The output of the PID controller is decomposed into two axial components by multiplying by C_x and C_y . The axial components are then injected to each of the corresponding loops with the appropriate sign. This scheme ensures that contour error correction is executed in the proper direction. For a cut of a linear segment, the gains C_x and C_y are adjusted at the beginning of the segment. For non-linear cuts they are adjusted continuously during the cut. Compared to the conventional uncoupled controllers, error reduction of 3:1 to 10:1 can be achieved depending on the resolution of the system. [24].

Table 2.3 given below is an extended version of the Table 2.2 and it shows a performance comparison between the cross-coupling controller and different uncoupled axial controllers.

	P control	PID control	Feedforward (with P controllers)	CCC
Tracking non-linear trajectories	Fair	Fair (low f) Poor (high f)	Excellent (1) Fair (2)	Good
Sharp corners	Fair	Poor	ZPETC: Fair (1, 2) IKF: Excellent (1) Fair (2)	Excellent
Axis mismatch	Fair	Good	Excellent (1) Fair (2)	Excellent
Disturbances				
a) friction	Poor	Good	Poor	Excellent
b) cutting forces	Poor	Good	Poor	Excellent
Special Problems		Overshoot at stopping	Performance is sensitive to modeling error	Requires a faster processor

Notes:

1. Assume no difference between theoretical model and real system
 2. Assume 2% difference between theoretical model and real system
- f = feedrate
Grading: Excellent, Good, Fair, Poor.

Table 2.3 The evaluation of servo-controllers [20]

2.5.5 Controllers with coordinate transformation

Various authors have proposed multi-axis contouring controllers which employ coordinate transformation [54][55][56][57]. Although their names are different, their idea is the same; to perform coordinate transformation from the machine axes to the trajectory (task) coordinate and design the controllers on the directions normal and tangential to the contour.

In biaxial contour tracking applications the major concerns are the tangential error ε_t and the contour error ε_c , which are, respectively, the error components tangent

and normal to the contour (Figure 2.15). Conventional motion controllers focus on the elimination of X- and Y-axis errors and expect a reduction in ε_t and ε_c . However, as mentioned earlier, the reduction of axial errors may not mean the reduction of the contour error ε_c [20]. To achieve an accurate contour tracking, many cross-coupling controllers have been developed and proven to be effective in elimination of the contour error. However, to minimise the contour error as well as the tangential error, proper designs for both the axial controllers and the cross-coupling controller are required. In practice, the coupled effect between the axial controllers and the cross-coupling controller may cause degradation in the tracking performance, and consequently bring a difficulty in the design of these controllers [54].

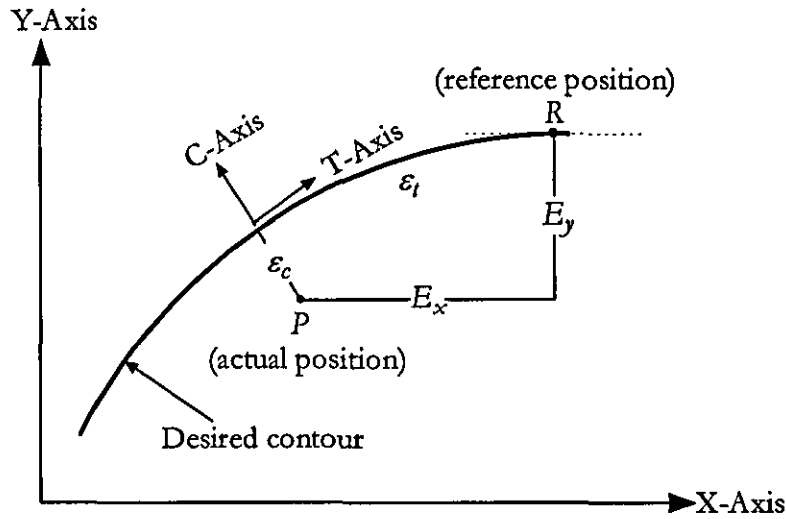


Figure 2.15 Tangential-contouring (T-C) coordinate frame and errors

To cope with the above problems, the controllers with coordinate transformation concentrate on direct and decoupled control of the concerned error components ε_t and ε_c through transformation between the machine (X-Y) and tangential-contouring (T-C) coordinate frames. As shown in Figure 2.15, T and C axes are, respectively, tangent and normal to the contour, so that ε_t and ε_c are the axial error components of this frame [55].

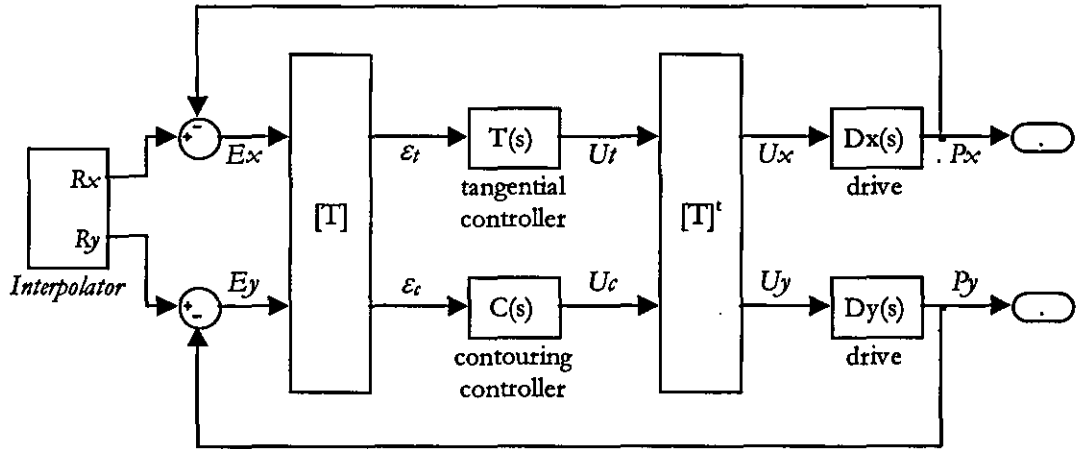


Figure 2.16 Tangential-contouring controller

Figure 2.16 shows the block diagram of the biaxial tangential-contouring controller proposed in [55]. Here, the coordinate transformation is represented by a matrix $[T]$ and its transpose $[T]^t$. Let θ be the inclination angle between the X-Y and T-C frames, then the transformation matrix is defined as:

$$[T] = \begin{bmatrix} \cos(\theta) & \sin(\theta) \\ -\sin(\theta) & \cos(\theta) \end{bmatrix} \quad (2.8)$$

If (R_t, R_c) and (P_t, P_c) are the incremental reference and output positions in the T-C basis, respectively. Then, we have

$$\begin{bmatrix} R_x \\ R_y \end{bmatrix} = [T]^t \begin{bmatrix} R_t \\ R_c \end{bmatrix} \quad (2.9)$$

$$\begin{bmatrix} P_t \\ P_c \end{bmatrix} = [T] \begin{bmatrix} P_x \\ P_y \end{bmatrix} \quad (2.10)$$

It should be noted that the incremental reference command in the contouring (C) direction is zero, i.e., $R_c=0$. Ideally, the contouring controller reduces the contour error; and the tangential controller maintains the desired feed rate, or cutting speed. Together, they achieve contouring accuracy.

This controller can be regarded as a modification to the cross-coupling controller. While maintaining the advantages of the CCC, it clearly identifies the control effort to drive the tool along the desired trajectory [56]. The coordinate transformation controllers decouple the error dynamics into tangential and normal directions, and enable the design of the respective controllers independently of each other [54][55][56][57].

2.5.6 Scalar field control technique

Scalar field control technique, proposed in [42], is another axis coupling strategy created through a more physical appreciation of requirements. Let M be the set of points that make up the desired position characteristic (i.e. desired curve) of a mechanism. If the output position of axis i of an n -axis mechanism is y_i , then $p(y_1, \dots, y_n)$ may be called the output position state of the mechanism. This may be viewed as a state vector comprising the positions of the axes. It is equally valid to refer p as a point in n -space that is described by the (y_1, \dots, y_n) co-ordinate system. The nature of mechanism constrains p to lie within M . The task of replacing a real mechanism with controlled servomotors can therefore be regarded as one of controlling the output positions of the servomotors to lie in M .

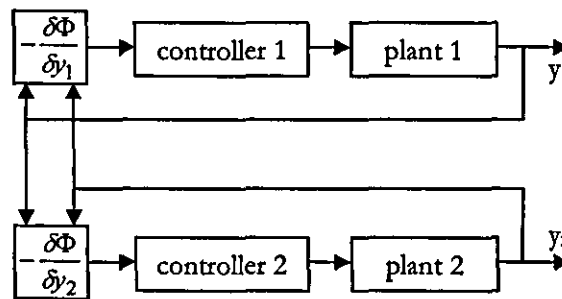


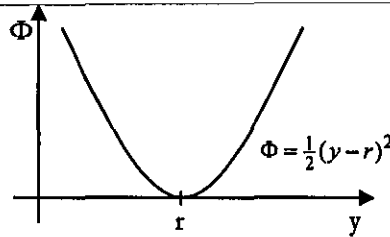
Figure 2.17 Principle of the scalar field controller [42]

A potential energy function (a function of y_1, \dots, y_n), or more generally a scalar field, is defined which has at its minimum the set of points M . The field is arranged so that its gradient is everywhere directed towards M . Each component of the gradient is then used as the input to a controller for the corresponding

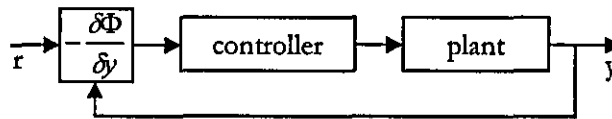
servomotor. This is shown in Figure 2.17 for a two axis case. The scalar field can be imagined as a surface on which a ball rolls under the influence of gravity. If the set of points M , all lie at the same level and are the lowest points on the surface, the ball will eventually settle to that set (if damping is present). It can be seen from this analogy that the coupling that is present in a real mechanism is also present here. A disturbance which acts to move the ball parallel to one of the co-ordinate axes will also cause movement in other directions in such a way that the ball remains close to M .



(a)



(b)



(c)

Figure 2.18 Definition of the scalar field [42]

In order to choose an appropriate scalar field, it is useful to examine a conventional single-axis servomechanism, like the one in Figure 2.18(a). The position error e in this system is given by:

$$e = r - y \quad (2.11)$$

The error signal forms the input to the controller, which, if correctly designed, tends to drive e to zero. An alternative approach would be to define a function Φ , such that

$$\Phi(y, r) = \frac{1}{2}(y - r)^2 \quad (2.12)$$

This is shown in Figure 2.18(b). The partial derivative of Φ with respect to y gives

$$\frac{\partial \Phi}{\partial y} = y - r \quad (2.13)$$

Hence, the single-axis controller can be implemented as shown in Figure 2.18(c), using a simple form of scalar-field control.

In a multi-axis system, there exist a whole set, M , of “target” position states, rather than a single reference position. Therefore logical choice would be to relate the scalar field to the distance between the output position state, p , and the nearest position state, q that lies in M . If this distance is denoted as d_{pq} , for an n -axis system, Φ_{pq} can be defined as:

$$\Phi_{pq}(y_1, \dots, y_n) = \frac{1}{2} d_{pq}^2 \quad (2.14)$$

This scalar field satisfies only the spatial requirements of the mechanism. In other words, it makes sure the output state p stays on M . However, the mechanism is also required to travel along M , and this introduces a temporal requirement. The conventional software mechanisms attempt to satisfy both the spatial and the temporal requirements through the same means, namely the reference signals. This is somewhat different to the situation in a real mechanism, where the spatial requirement, which is represented by the mechanism characteristic M , is met at all times, and any temporal requirement simply dictates the manner in which the state p travels within M . To achieve this with the scalar field controller, a second scalar field, Φ_{qr} , is introduced as:

$$\Phi_{qr}(y_1, \dots, y_n) = \frac{1}{2} d_{qr}^2 \quad (2.15)$$

The term d_{qr} is used to denote the distance, measured along the mechanism characteristic, between the reference position state $r(r_1, \dots, r_n)$ and the state q . This distance gives a measure of how far the output position state would have to travel along the characteristic M , to reach r .

The scalar field Φ is considered as a combination of the two fields, Φ_{pq} and Φ_{qr}

$$\Phi(y_1, \dots, y_n) = k_{pq} \Phi_{pq} + k_{qr} \Phi_{qr} \quad (2.16)$$

where, k_{pq} and k_{qr} are constants. The pq field gives the system a tendency to move towards the mechanism characteristic via the shortest route. The addition of the qr term also gives the system a tendency to move towards a particular position state r , within the characteristic. The two sets of efforts are therefore concerned with driving the output position state perpendicular and tangential to M , respectively. The constants k_{pq} and k_{qr} provide a relative weighting for the two tendencies. Generally, characteristic following is of greater importance to the reference tracking, therefore, k_{pq} would be apportioned a greater weighting.

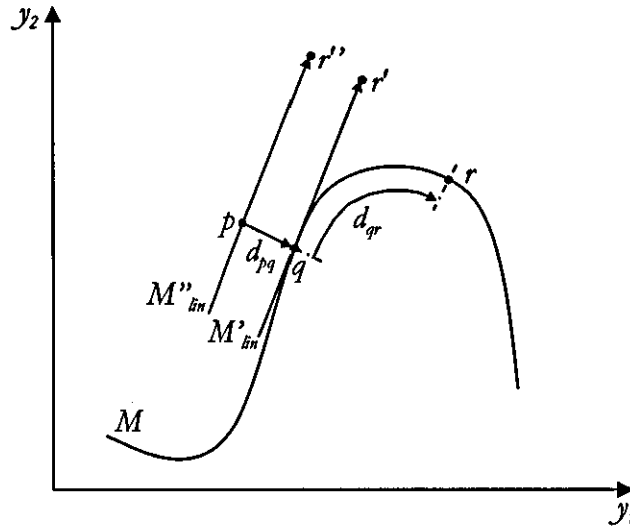


Figure 2.19 Definition of the terms relating to the mechanism characteristic [42]

Figure 2.19 shows a two-axis system with an arbitrary characteristic M , on which the above explained states and distances are shown. A relation M'_{lin} is generated by

linearising M about q . A state $r'(r'_1, \dots, r'_n)$ lies in M'_{lin} and is the image of $r(r_1, \dots, r_n)$ formed such that the distance qr' through M'_{lin} is equal to the distance through M from q to r . A relation M''_{lin} is then generated by shifting M'_{lin} in a direction normal to M until p lies in M''_{lin} . The controller generates character-seeking efforts which drive p towards q and reference-seeking efforts which drive p towards the state $r''(r''_1, \dots, r''_n)$ lying in M''_{lin} .

This technique introduces a form of coupling between the servo drives which closely emulates the type of coupling found in a real mechanism. Building a precise scalar field in real-time is crucial to the synchronization accuracy, particularly when nonlinearities exist in the system. It does, however, couple axes with reference to a logical analogy [18].

2.6 Summary

The previous work done in the fields related to this research are summarised. Firstly, the areas of wood machining research, which primarily relates to planning and moulding, are reviewed. Then, some examples of the existing small-scale CNC contouring machinery are presented and compared to the PIMM in terms of size, speed and power. It was seen that, the PIMM cannot be benchmarked directly against a certain type of machine, but it combines different features of various machines.

When compared to the conventional moulding machines, it is clear that the production rate of the PIMM will be lower. Whereas, the quality of the mouldings produced by the PIMM should match the ones produced by the conventional moulders utilizing shaped cutters. Apart from the drive hardware with good dynamics, optimum control and synchronization of the drive motions are essential in order to achieve the required geometric accuracy. Therefore, the available multi-axis control algorithms have been investigated and evaluated in terms of their accuracy, computational requirement and ease of implementation.

In order to achieve a successful PIMM system, a thorough investigation of the process requirements is essential in the initial stages of the design activity. The next chapter explores material removal phenomena, cutting forces and cutting power requirements.

Chapter 3

Cutting Forces

3.1 Introduction

In all of the dynamic machining processes, the nature of the cutting forces must be understood before accurate analysis of the production in terms of cost, quality and efficiency.

The metalworking industry has paid more attention to determination and modelling of the cutting forces than the woodworking industry. The reason is probably the relative difficulty with which metals can be machined. The nature of the rotary wood machining process is such that the cutting forces are impulsive in nature as in the milling of metals [2].

It is not intended for this thesis to present a wide view of the cutting forces encountered during wood machining. This has been treated in detail by [58], [59] and others over the last 50 years. Previous research by Kivimaa [58] reports the behaviour of cutting forces for various types of timbers and machining conditions. Although this work dates back more than fifty years, it is still the most

comprehensive investigation in woodworking forces and is referred by most, if not all, of the woodworking researchers dealing with the cutting forces.

The aim of this chapter is to investigate the nature of cutting forces and cutting power requirements in PIMM operation. For that, firstly, chip severing phenomena is described and the factors affecting the cutting forces in rotary wood machining are examined. Then, theoretical cutting force and power calculations are performed for PIMM operation mainly based on the results of Kivimaa [58]. Finally, purpose designed cutting force measurement test rig is explained and test results are discussed.

3.2 Influencing Factors

To separate a chip from a piece of wood, a certain force F must be applied to the tool. This force should be bigger than the cohesion of the wood material and it is the result of several forces. These are, force from the bending of fibres, shearing force and the friction force on the faces of the tool [60]. The total cutting force F can be divided into two components as shown in Figure 3.1. Tangential force component F_t (main cutting force) acts parallel to the movement direction of the cutting tool and the radial force component F_r is normal to this. F_t is considered to be the main component and it determines the energy consumption. Depending on the direction of the cutting force F , the F_r may be directed either towards or away from the wood surface. In the former case the component F_r is termed positive, and in the latter case negative (Figure 3.1).

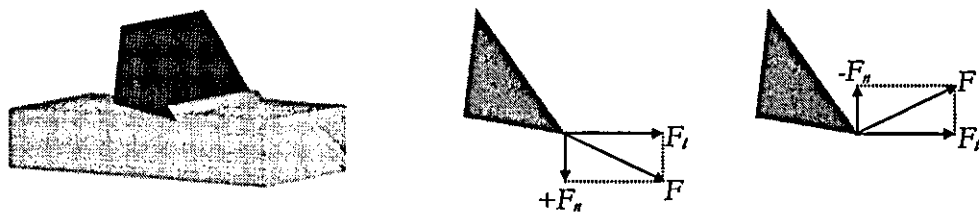


Figure 3.1 Cutting force F and its components F_t and F_r

Cutting forces are influenced by various machine and tooling parameters in rotary machining. These are illustrated in Figure 3.2.

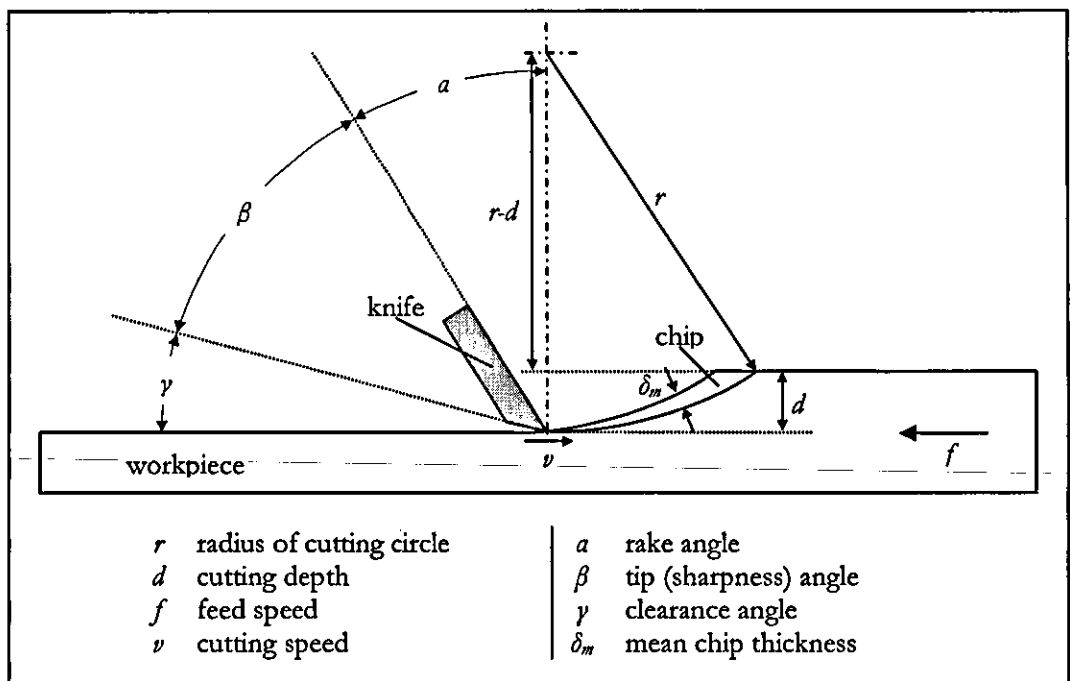


Figure 3.2 Rotary chip cutting

The following is a summary of the influence of machine, cutting tool and workpiece variables on cutting forces.

3.2.1 Cutting direction

Due to the anisotropic and cellular structure of wood, the cutting forces are influenced by the cutting direction. The cutting directions in the industry are determined by knife movement direction, cutting surface plane and direction of grain. The three main cutting directions are shown in Figure 3.3.

Generally, the magnitude of the main cutting force is the lowest in the *C* (veneer) direction. The *A* (crosscut) direction produce the highest main cutting forces because the wood is required to be failed in tension parallel to the grain [61]. In the *B* (planing) direction, both the cutting surface and knife movement are parallel to the grain and the magnitude of forces are in between the *A* and *C* directions.

The *B* direction is reported here after since this is the one where the planing and moulding processes are carried out.

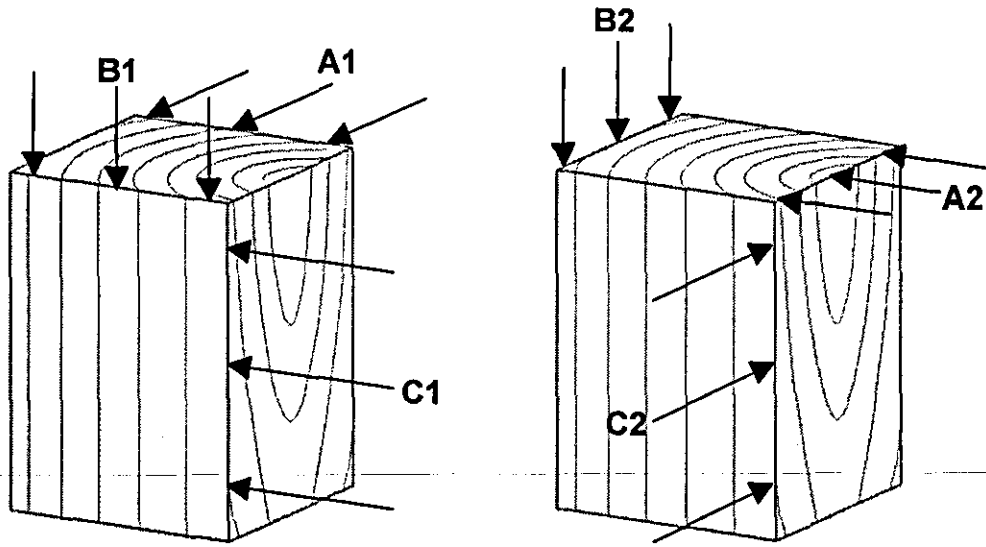


Figure 3.3 Main cutting directions in wood machining

3.2.2 Width of cut

It is well established that the cutting forces are directly proportional to the width of cut, provided the cutting edge always overlaps the workpiece. Most of the authors have reported the cutting forces per unit width of cutter/workpiece engagement.

3.2.3 Cutting speed

In practice the cutting speed of woodworking tools can be from less than 1 m/s to more than 125 m/s. However, there is no published work which investigates the whole range for cutting forces.

Kivimaa [58] carried out tests throughout the range 2.5 m/s – 50 m/s on a special purpose test rig, where 2 cm by 2 cm cross sectioned workpieces are fed radially into a rotating cutterhead. A work sharp knife having rake angle $\alpha=35^\circ$ and

clearance angle $\gamma=10^\circ$ was used to sever chips with an average thickness of $\delta_m=0.1$ mm from *Finnish Birch* (11% moisture content) workpieces.

It was reported that no change in tangential or normal cutting forces can be detected. The values obtained throughout the speed range are

$$F_t = 3 \text{ N/mm width of cut}$$

$$F_n = 0 \text{ N/mm width of cut}$$

Walker [59], reported on tests for a range of cutting speeds from 5 m/s to 35 m/s. The test rig consisted of a whirling arm which carried the timber sample and engaged with a stationary cutter mounted on a strain gauge arrangement. Chips with $\delta_m=0.125$ were severed from *Sycamore* and *Beech* specimens (12% moisture content). The cutter rake angle was $\alpha=30^\circ$. The results are averaged over five repeat tests and are as follows.

Cutting Speed (m/s)	Wood Type	F_t (N/mm width of cut)	F_n (N/mm width of cut)
5 m/s	<i>Sycamore</i>	6	0
5 m/s	<i>Beech</i>	5	0
35 m/s	<i>Sycamore</i>	5	0
35 m/s	<i>Beech</i>	5	0.7

Table 3.1 Cutting forces at different cutting speeds [59]

Comparison of two results from Kivimaa [58] and Walker [59] shows that, cutting speed has little influence on the magnitude of cutting forces between 2.5 m/s to 50 m/s.

McKenzie, according to [62], evaluated the force variation in cutting direction from a turning experiment, when cutting speed was increased from 15 m/s to 150 m/s. It was reported that, because of the speed changes, an additional amount of force due to acceleration has to be taken into account. This additional force is almost proportional to the square of the cutting speed and can be assimilated to an inertia force component of chip on the rake face. As a result, the higher the speed is, the greater the acceleration component. However, for turning and

sawing, cutting speed contribution on total forces seems to be low and, in any cases, is less than 10%.

In [63] and [64], oblique wood cutting is performed with a rotating disc cutter. It was reported that the specific cutting energy, which is the work required per unit volume of cut, tends to increase as the rotating speed of the disc cutter increases. This implies that the increase in the circumference speed of the cutter would increase the required energy, most of which would transform into heat and cause a rise in the temperature of the cutting knife.

In the light of the previous work, it can be concluded that the effect of the cutting speed on the cutting forces is negligible. On the other hand, many authors agree that higher cutting speed gives better surface quality. The common explanation is that the speed increase acts as if the wood fibers' inertia and stiffness have been increased. As a result fiber severance is cleaner and surface quality is better [2][62].

3.2.4 Timber properties and condition

Kivimaa [58] investigated the main cutting force on 21 different wood species ranging from *Balsa wood* at 0.15 specific gravity to *Indian Ebony* at 1.2 specific gravity. A cutter with a rake angle of $\alpha=35^\circ$ and clearance angle of $\gamma=10^\circ$ was used to severe 0.1 mm thick chips from specimens of 11% moisture content. The results show that the main cutting force increases with density and, one might expect times two increase in the magnitude of the cutting force depending on the wood species.

[65] and [66] reports cutting force tests on MDF boards having layers of different densities by using CNC routers and piezo-electric dynamometers. The results are in accordance with the ones obtained by Kivimaa [58]. Greater specific gravity substantially means less cell cavities and more cell walls in the wood; consequently, the force required to move the tool must also be greater [67].

Temperature and moisture content of the wood has little effect on the cutting forces. As the temperature of the timber increases, a slight decrease occurs in the cutting resistance. Also, increasing moisture content over 10% results in decreased cutting forces.

3.2.5 Cutter geometry and condition of the cutting edge

As in metal working, cutter geometry has a significant influence on the nature of the cutting forces developed during rotary woodworking. Cutter geometry parameters rake angle α , sharpness angle β and, clearance angle γ can be seen in Figure 3.2.

Kivimaa [58] reports on the influence of cutter rake angle α being varied from -3° to $+60^\circ$ while keeping all other factors constant, with the exception to the sharpness angle β which is clearly interrelated to α and γ (Figure 3.2).

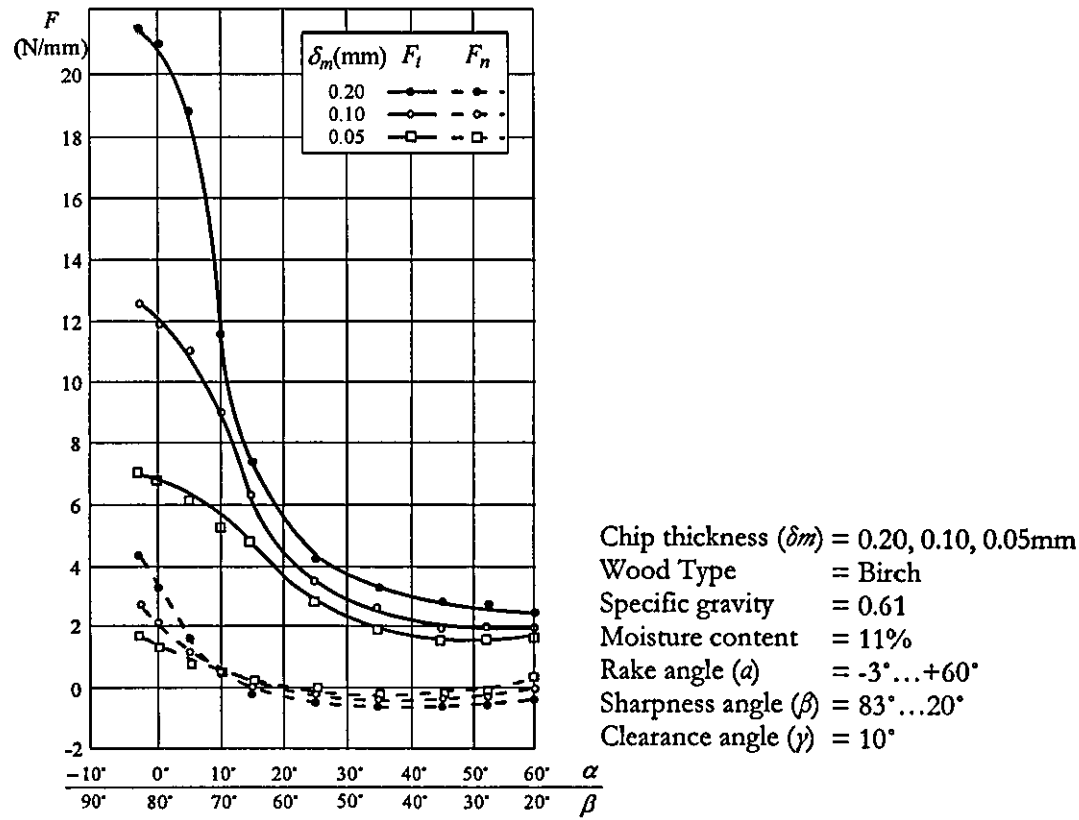


Figure 3.4 Cutting forces F_t and F_n vs. cutter rake angle α in B direction [58]

As can be seen from Figure 3.4, the rake angle has a significant effect on both the tangential and normal cutting forces. Rake angles smaller than 20° cause both cutting force components to increase. This is more significant at greater chip thicknesses.

It should be noted that the tangential cutting force F_t is always positive and increases with decreasing rake angle. Whereas, the normal force F_n is seen to be negative for rake angles between $\alpha=20^\circ$ and $\alpha=50^\circ$; and can be considered as pulling the workpiece into the cutterhead. This can be explained by examining the cutter-workpiece interaction (Figure 3.5).

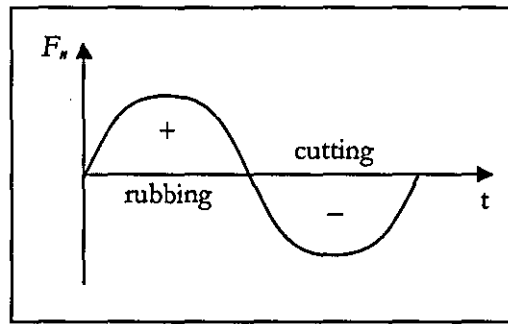


Figure 3.5 Phases of normal cutting force F_n during chip formation

When the cutter engages the workpiece, it pushes the workpiece away and rubs over the surface until it can “bite” and start to cut, at which point the normal force F_n becomes negative and the cutter starts pulling the workpiece into the cutterhead [2].

For smaller rake angles (i.e. $\alpha < 20^\circ$), it is more difficult for the cutter to “bite” the workpiece, and therefore, extended rubbing phase results in positive normal force. Increasing the rake angle further than $\alpha=50^\circ$, while keeping the clearance angle (γ) constant, results in very small sharpness angles (β) and the cutting edge gets duller due to its failure to stand the force directed to it. Dull cutting edge cannot “bite” the workpiece and positive normal forces occur due to extended rubbing.

Walker [59] found that reducing the rake angle from 30° to 15° increased the tangential force from 5 N/mm to 10 N/mm and the radial force from 0 N/mm to 3.5 N/mm. The cutting speed and chip thickness in the tests are 35 m/s and 0.125 mm respectively.

In another set of experiments, performed by Kivimaa [58], the clearance angle γ is varied between 2° and 35° while keeping all other factors constant, with the exception to the sharpness angle β . The obtained results are given in Figure 3.6.

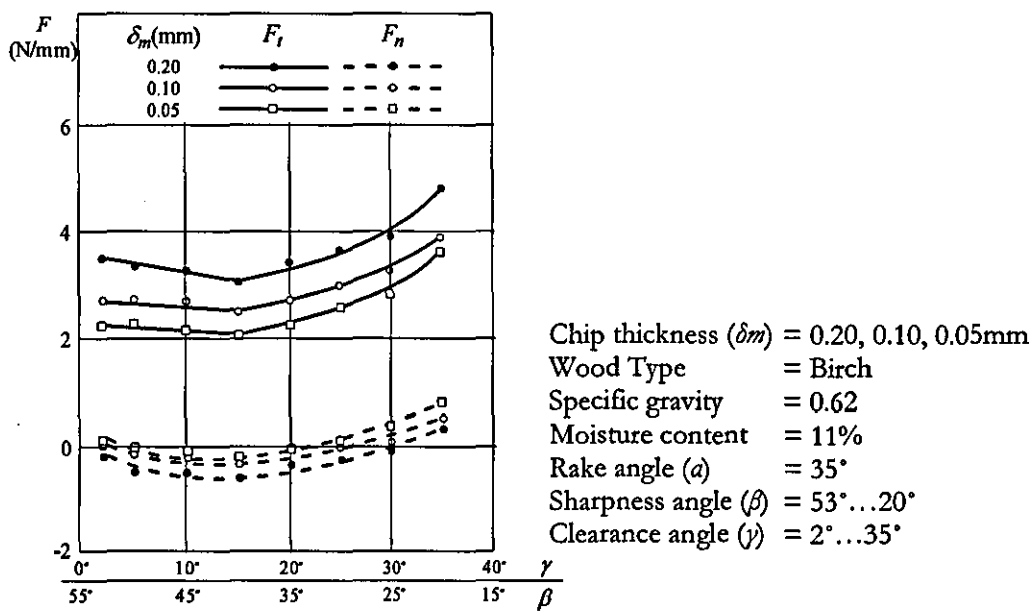


Figure 3.6 Cutting forces F_t and F_n vs. cutter clearance angle γ in B direction [58]

From Figure 3.6, as γ is increased, with constant α , the cutting forces are seen to decrease until a value of $\gamma=15^\circ$ is reached at which point a significant change occurs in the cutting force curves, and forces further increase with γ . Kivimaa [58] explains this by observing a critical sharpness angle β_{crit} below which microscopic chipping of the cutting edge occurs after a small number of engagements of the cutter with the workpiece.

With reference to Figure 3.2, one can see that the sum of α , γ and β is 90° . Consequently, there exists a compromise between large rake and clearance angles in order to keep the sharpness angle greater than β_{crit} .

At clearance angles less than 5° , interference may occur between the clearance face and the workpiece at large depths of cut at higher values of feed per tooth; this causes an increase in cutting forces and consequently power consumption [2].

It appears therefore, that a maximum rake angle of 35° , with sharpness angle of 45° and clearance angle of 10° is a reasonable compromise at this extreme. Clearly, as the rake angle is reduced the sharpness angle increases, thereby producing a stiffer and more durable cutting edge.

3.2.6 Chip thickness

Chip thickness, together with cutter geometry is the most significant parameter affecting the cutting forces. It can be seen in Figure 3.5 and Figure 3.6 that cutting forces, mainly the tangential force, increases with chip thickness. The greater rate of increase occurs at the small rake angles.

Kivimaa [58] studied the influence of chip thickness by using both work-sharp and dull cutters in order to form some kind of conception of the limits within which the force components vary when the tool gradually dulls during work. Nine different thicknesses from 0.0125 mm to 0.5 mm were employed. Figure 3.7 shows the obtained results.

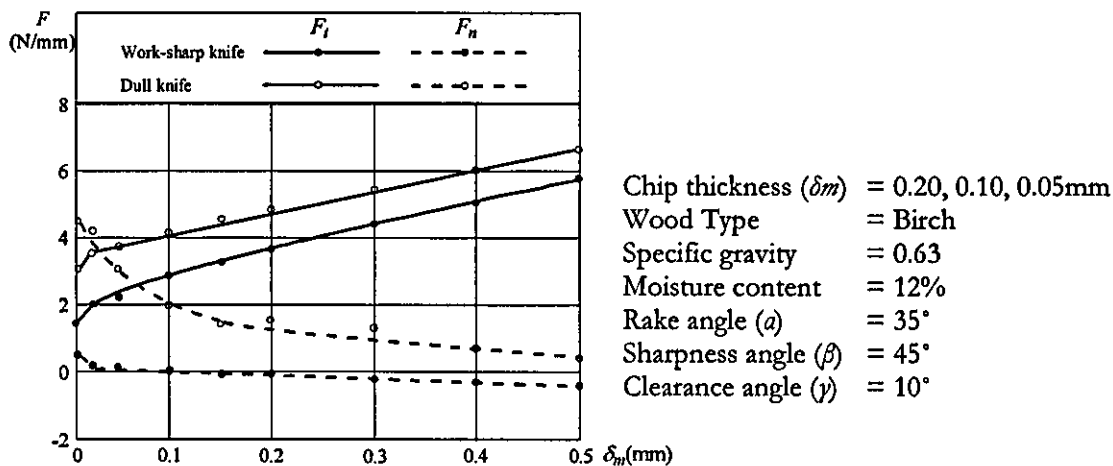


Figure 3.7 Cutting forces F_t and F_n vs. chip thickness δ_m in B direction [58]

First of all, it should be noted that dulling of the knife increases cutting forces irrespective of chip thickness. This increase is greater at thinner chips. Further, it is shown that within the chip thickness range from 0.025 mm to 0.5 mm, tangential force curves are almost linear.

Extensions of the F_t lines do not run through the origin but bisect the ordinate axis at a point above the origin. This indicates that the power required for cutting wood is needed for two different purposes. One part of the power is required for affecting the cutting proper (i.e. shearing) and remains constant while chip thickness varies. This part mainly depends on knife sharpness. The other part is needed for deforming the severed chips still resting against the knife face and, for this reason, depends largely on chip thickness and is, within a certain range, almost a linear function. Moreover, it also depends substantially on the rake angle of the knife, which determines the degree of deformation and type of injury done to the chips [58].

The tangential force value obtained for the thinnest chip thickness of 0.0125 mm lies clearly beneath the described F_t line. This is due to the fact that when test specimen feeds that small, not every knife impact will produce a separate perfect chip, some ride over the specimen compressing the wood slightly.

The high normal force values (i.e. even higher than the corresponding tangential force values) obtained with a dull knife cutting thin chips provide additional evidence in support of the tendency described above. Increasing chip thickness enables regular chip formation and causes F_n curves to drop rapidly.

3.2.7 Upcutting and downcutting

Over the years, the relative merits of up-cutting and down-cutting have been investigated by some researchers on different wood machining processes. Generally, down-cutting generates greater cutting forces and requires more power, up to 25%, due to increased average chip thickness [1][60][68].

The work presented in [69] and [70] discuss the influence of up- and down-cutting on circular saw cutting stability. In down-cutting arrangement (Figure 3.8), the saw applies cutting forces on the workpiece in the direction of saw rotation. In turn, the workpiece applies an equal reaction force on the saw in the opposite direction. This reaction force is shown by the solid arrows in Figure 3.8(a). When the saw is bent slightly to one side, the reaction force follows the slope of the saw and turns to the same side. This turning of the reaction force creates a sideways force component that augments the existing sideways deflection of the saw. This increase in saw deflection impairs cutting accuracy.

The opposite situation occurs with up-cutting saw shown in Figure 3.8(b). With a up-cutting saw, the rotation is reversed so that the tooth motion direction coincides with the feed direction in the cutting area. This change also reverses the direction of the reaction force. Thus, when the saw is bent to one side, the sideways component of the reaction force now opposes the existing saw bending deflection. The resulting reduction in saw deflection improves sawing accuracy.

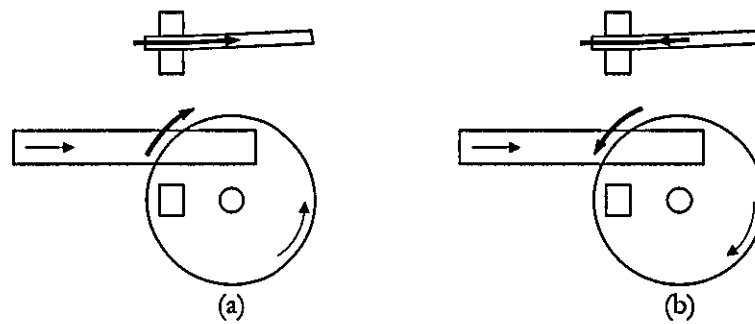


Figure 3.8 Cutting forces on a guided saw (a) down-cutting, (b) up-cutting [70]

Down-cutting also have a number of significant difficulties to overcome such as control of timber to prevent “snatch” occurring and extraction of wood chips which exit in the feed direction [2].

3.2.8 Chip formation

In wood machining, the type of chip formation influences the cutting forces, power consumption, cutting edge life and resultant surface quality. Chip formation is influenced by most of the previously discussed machine and timber parameters.

As recorded by Koch and enumerated by Franz [2][61][71] three basic chip types are observable when wood is machined parallel to the grain (i.e. *B* direction). These types are illustrated in Figure 3.9.

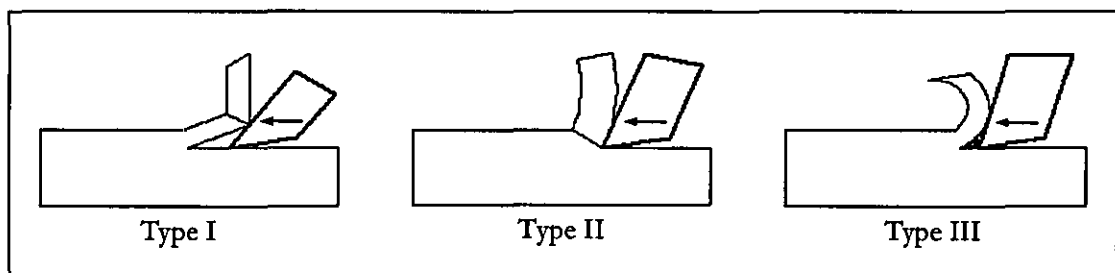


Figure 3.9 Types of chip formation

Type I chips are formed when cutting conditions are such that the wood splits ahead of the tool by cleavage until it fails in bending as a cantilever beam. Factors leading to formation of Type I chips are:

- ◆ Timber with high bending strength but low splitting strength.
- ◆ Machining conditions that produce chips having average to heavy thickness.
- ◆ Large rake angles.
- ◆ Low coefficient of friction between chip and tool face.
- ◆ Low moisture content.

The splitting that occurs ahead of the cutting edge frequently runs below the plane generated by the path of the cutting edge, and therefore produces a rough surface. This is termed as “chipped grain”. The Type I chip formation consumes minimum power and causes minimum tool wear.

Type II chips occur only under certain conditions; continuous wood failures that extent from the cutting edge to the work surface ahead of the tool must be induced. The movement of the tool strains the wood ahead of the tool in compression parallel to the grain and causes diagonal shearing stress; the wood fails and a continuous, smooth, spiral chip is formed. Factors which influence the formation of the Type II chips are:

- ◆ Small chip thickness.
- ◆ Average rake angles.
- ◆ Intermediate to high moisture content

Due to the cutting edge being in intimate contact with the wood at all times, cutter wear is greater than with a Type I chip. The resultant surface of the timber is exceptionally smooth and power demand is intermediate between that for Type I and Type III chips.

Type III chips tend to form in cycles. Wood is strained by compressive loading, and the particles of wood at the cutting edge become trapped due to poor chip flow conditions. This causes a built up edge of timber which effectively produces a new, softer cutting edge of greater rake angle which then promotes better chip flow and causes the trapped particles to be removed, and the process repeats. Factors which favour the production of Type III chips are:

- ◆ Small or negative rake angles.
- ◆ Dull cutting edges.
- ◆ Very low or very high moisture content.
- ◆ High coefficient of friction between chip and tool face.

This type of chip can cause a surface texture defect known as “fuzzy grain”, where the timber surface is effectively rubbed by the built up edge. Power consumption is high and dulling is rapid.

Koch, according to [2], goes on to say that it is possible for all three types of chip to occur sequentially at different points within the rotary milling cutter path. Ideally Type II chip should occur at the start of knife engagement with the workpiece, as this is the portion of the cutter path which determines the quality of the machined surface. Type I normally occurs towards the exit point of the cutter from the workpiece, where the effective rake angle is greater (see Figure 3.2).

3.3 Theoretical Investigations

The aim of this section is to predict the cutting forces and cutting power in the PIMM process. The experimental results obtained by Kivimaa [58] were adapted to the cutting conditions of the PIMM.

3.3.1 Cutting forces in PIMM process

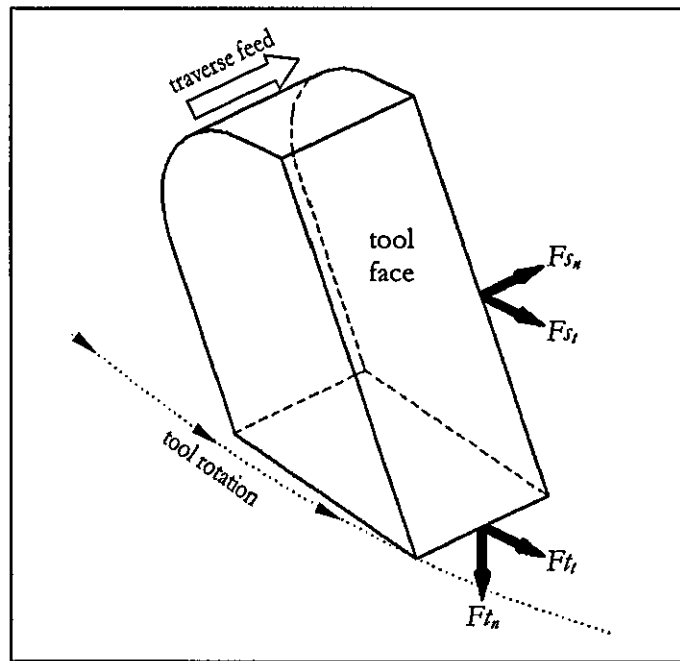


Figure 3.10 Forces acting on the tool edges

Due to the traverse motion of the cutting disc along the workpiece width, it is assumed that the side of the cutting tool as well as the tip perform cutting. Consequently, the cutting forces were estimated for two cutting edges (i.e. side

and tip) and then combined. Figure 3.10 illustrates the cutting force components acting on the cutting edges, where F_{s_t} and F_{s_n} are the tangential and normal components acting on the side of the tool and F_{t_t} and F_{t_n} are the forces acting on the tip of the tool.

Figure 3.11 shows the cutter-workpiece interaction and the important geometric parameters of the produced chips, where f is the feed increment, d is the depth of cut, c is the chip width and δ_m is the mean chip thickness. Another important parameter, chip length L is the length of the circular section at the bottom of the chip. Chip length L and the mean chip thickness δ_m are calculated by equations (3.1) and (3.2) respectively, where r is the cutter radius [58].

$$L = \frac{\cos^{-1}\left(\frac{r-d}{r}\right) \cdot 2 \cdot \pi \cdot r}{360} \quad (3.1)$$

$$\delta_m = f \cdot \frac{d}{L} \quad (3.2)$$

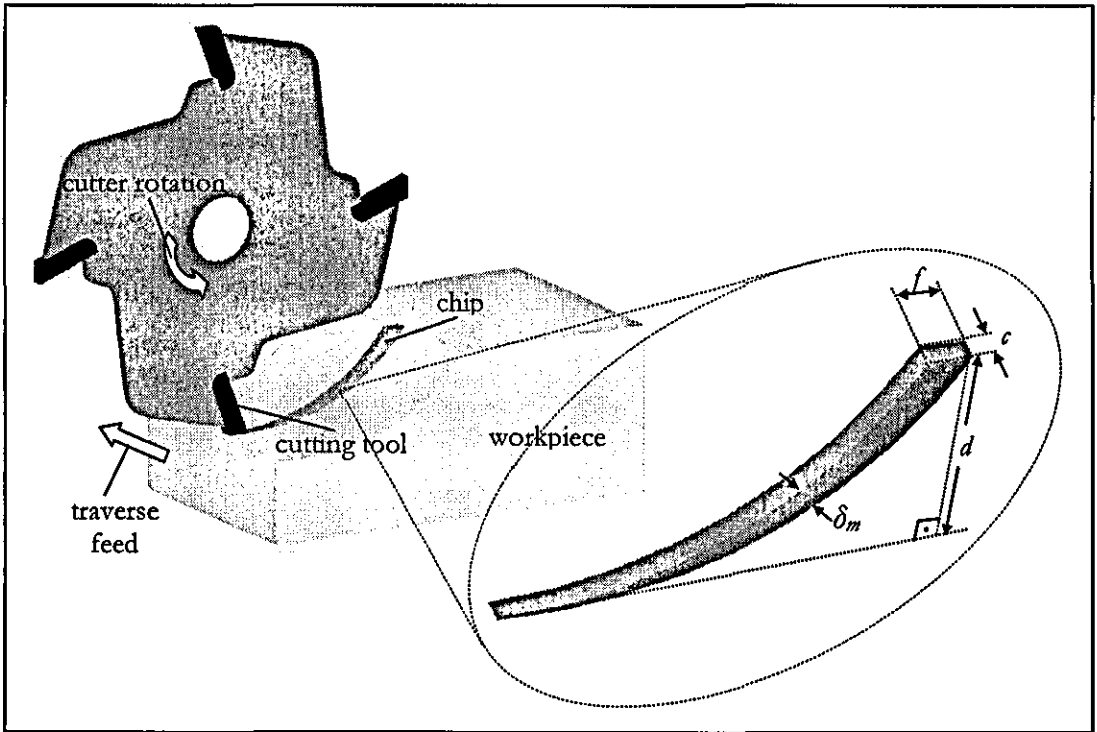


Figure 3.11 Cutter-workpiece interaction

At this point; some of the influencing factors, explained in the previous section, can be adapted to PIMM operation while keeping in mind the assumption that the two edges in Figure 3.10 are cutting at the same time.

Cutting direction: It can be understood from Figure 3.3 that when one of the edges (i.e. side or tip) is cutting on $B1$ direction, the other edge cuts on $B2$ direction and vice versa. Therefore, for both edges, the results of Kivimaa's work on B direction can be used.

Width of Cut and Chip Thickness: For the tip of the cutter, width of cut (i.e. width of cutter/workpiece engagement) at any given time is equal to the chip width c (Figure 3.11). The ratio of cutting speed to traverse speed is assumed to be great enough, such that, the chip width stays constant throughout the cutter workpiece engagement. On the other hand, chip thickness increases from 0 to f during a single cut and its mean value δ_m is used to characterize this parameter.

When the side of the cutter is considered, the chips have constant thickness which is equal to the dimension c . This time the width of cut increases from 0 to f and, δ_m value can be considered as the mean cutting width for the side of the cutter (Figure 3.11).

Cutting speed: In the previous section, it was concluded that the effect of the cutting speed on the cutting forces is negligible for conventional wood machining processes. However in PIMM, due to the traverse motion of the cutter, the cutting speed has an indirect, yet significant, influence on the cutting forces. Increasing the cutting speed, while keeping the traverse speed constant, increases the number of cutter-workpiece engagements (3.3) per unit length along the traverse direction. Consequently, teeth of the cutter sever chips with smaller width (3.4) and hence result in smaller forces.

$$n_p = \frac{\omega}{60} \cdot n \cdot t \quad (3.3)$$

$$c = \frac{w}{n_p} \quad (3.4)$$

n_p = number of chips per pass

w = workpiece width (mm)

n = number of cutter teeth

c = chip width (mm)

ω = cutting speed (rpm)

t = pass time (s).

The influences of the other machining parameters are studied on the following example (Table 3.2), where a single pass over the width of a stationary workpiece with constant depth of cut is considered. Assuming that a single chip is severed at each cutter-workpiece engagement, the mean chip thickness δ_m , the number of chips per pass n_p and the chip width c are calculated from equations (3.2), (3.3) and (3.4) respectively.

Parameter	Value	Parameter	Value
Cutter radius (mm)	r 50	Workpiece width (mm)	w 70
Number of teeth	n 12	Depth of cut (mm)	d 5
Cutting speed (rpm)	ω 15000	Feed increment (mm)	f 1
Cutter tip rake angle ($^\circ$)	α_t 10	Pass time (s)	t 2
Cutter tip clearance angle ($^\circ$)	γ_t 10	Mean chip thickness (mm)	δ_m 0.2
Cutter side rake angle ($^\circ$)	α_s 0	Chip width (mm)	c 0.012
Cutter side clearance angle ($^\circ$)	γ_s 10	Chips per pass	n_p 6000

Table 3.2 Example machining parameters

$$F_t = Ft_t \cdot c + Fs_t \cdot \delta_m \quad (3.5)$$

$$F_n = Ft_n \cdot c \quad (3.6)$$

$$F_L = Fs_n \cdot \delta_m \quad (3.7)$$

For the tip of the cutter, where $\alpha=10^\circ$ and $\delta_m=0.2$ mm, tangential and normal cutting force values per width of cut are obtained from Figure 3.12(a) as $Ft_t=11.5$ N/mm and $Ft_n= 0.5$ N/mm. For the side of the cutter, as explained before, the chips have constant thickness and it is equal to c . Consequently, tangential and normal force values are read from Figure 3.12(b), for $\alpha=0^\circ$ and $c=0.012$ mm, as $Fs_t=2$ N/mm and $Fs_n= 1$ N/mm. The total tangential force F_t , normal force F_n , and lateral force F_L are calculated by equations (3.5), (3.6) and (3.7) respectively. For the parameters in Table 3.2 these forces are $F_t= 0.538$ N, $F_n= 0.006$ N and $F_L= 0.2$ N.

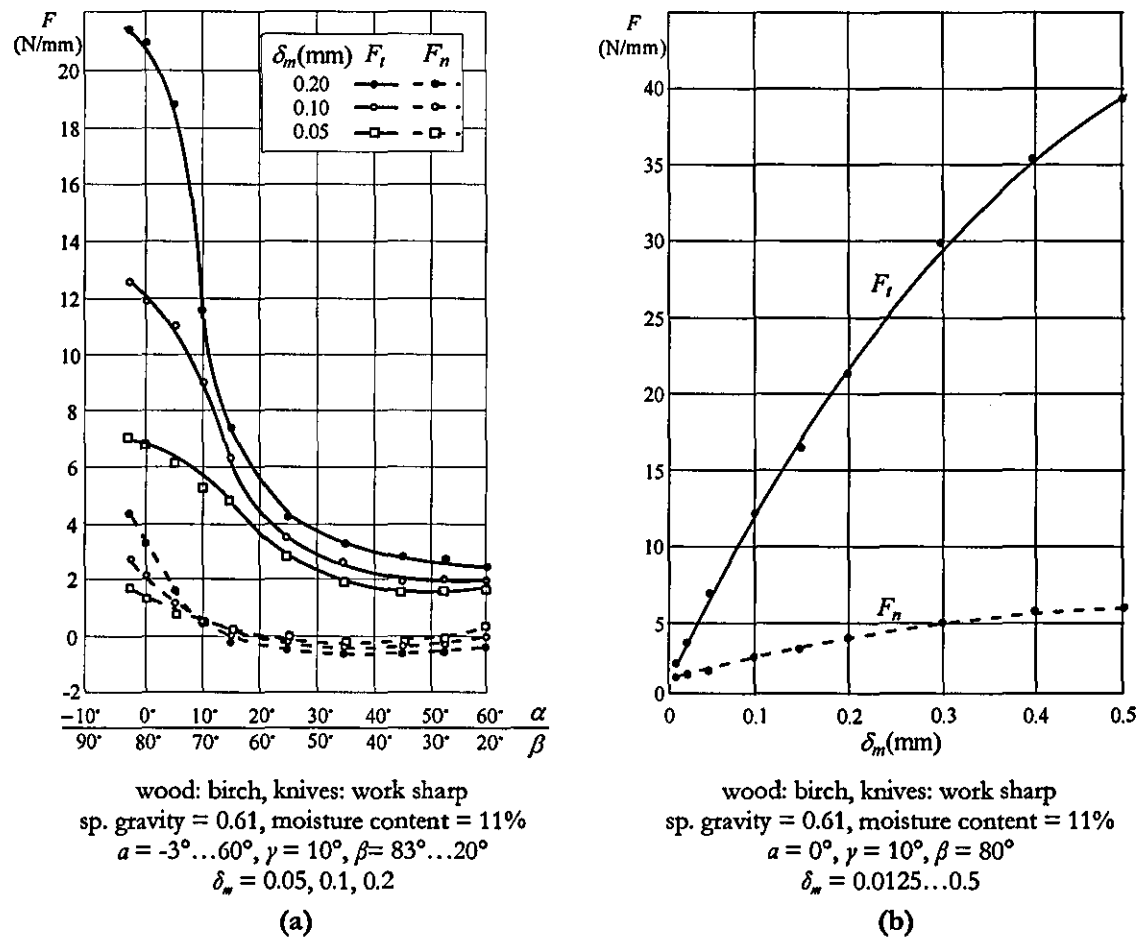


Figure 3.12 Cutting force graphs for various δ_m and α [58]

The following outlines the influences of some of the parameters in Table 3.2 on cutting forces. When considering a particular parameter, the other parameters are thought to remain unchanged.

Cutter radius (r): Increasing the cutter radius results in greater chip length L (3.1), smaller mean chip thickness δ_m (3.2) and hence smaller cutting forces (Figure 3.12).

Number of teeth (n): Increasing the number of cutter teeth causes more chips to be produced (3.3) but with smaller chip widths (3.4), and therefore, results in smaller cutting forces.

Depth of cut (d): Increasing the depth of cut increases the chip length L (3.1) as well as the mean chip thickness δ_m (3.2). Consequently, results in greater cutting forces (Figure 3.12).

Feed Increment (f): Feed increment is directly proportional to the mean chip thickness δ_m (3.2), therefore an increase results in greater cutting forces (Figure 3.12).

Pass time (t): Decreasing the pass time (i.e. increasing the traverse speed) causes smaller number of chips (3.3), having greater chip widths (3.4), to be produced. This results in greater cutting forces.

parameter		increase in parameter	decrease in parameter
cutter radius	r	low F	high F
number of teeth	n	low F	high F
rake angle	α	low F	high F
cutting speed	ω	low F	high F
workpiece width	w	no-change	no-change
depth of cut	d	high F	low F
feed increment	f	high F	low F
pass time	t	low F	high F

Table 3.3 Influence of the PIMM machining parameters on cutting forces

Table 3.3 summarizes the influence of the PIMM machining parameters on the cutting forces. The next section investigates cutting power requirements.

3.3.2 Cutting power

This section explains the theoretical method used for estimating the cutting power requirement. Firstly, the work W_c along the direction of motion in order to sever one chip is calculated (3.8) from the total tangential force F_t and the chip length L . Then, the number of cutter-workpiece engagements in one second n' is computed by equation (3.9), where ω is the cutting speed in rpm and n is the number of cutter teeth. Finally, assuming that a single chip is severed at each cutter-workpiece engagement, the required power P is estimated by multiplying W_c and n' (3.10).

$$W_c = F_t \cdot L \cdot 10^{-3} \quad (3.8)$$

$$n' = \frac{\omega}{60} \cdot n \quad (3.9)$$

$$P = W_c \cdot n' \quad (3.10)$$

For the machining parameters in Table 3.2, W_c , n' and P are as follows:

$$W_c = 0.013 \text{ J} \quad n' = 3000 \quad P = 39.4 \text{ W}$$

The estimated value only includes the power required for material removal and does not contain the effects of possible friction. Experimental investigations, presented in the next section, provide better understanding of the cutting power requirements.

3.4 Experimental Cutting Force Estimations

This section presents the experimental work carried out for the estimation of cutting forces from the measured cutting power.

3.4.1 Test-rig

Cutting force measurements were performed on a purpose designed test-rig (Figure 3.13), in which, timber specimens are fed towards a rotating cutter from the side and a single pass along the timber width is performed with a constant depth of cut. The test-rig comprises of three main parts: frame, feed drive and cutter assembly.

The feed drive features a DC motor driven ballscrew and precision linear guides, and it provides longitudinal movement up to 125 mm/s. Prior to cutting, the whole feed drive is moved towards the cutter assembly in order to set the feed increment f , and the motor speed is adjusted to achieve the desired pass time t .

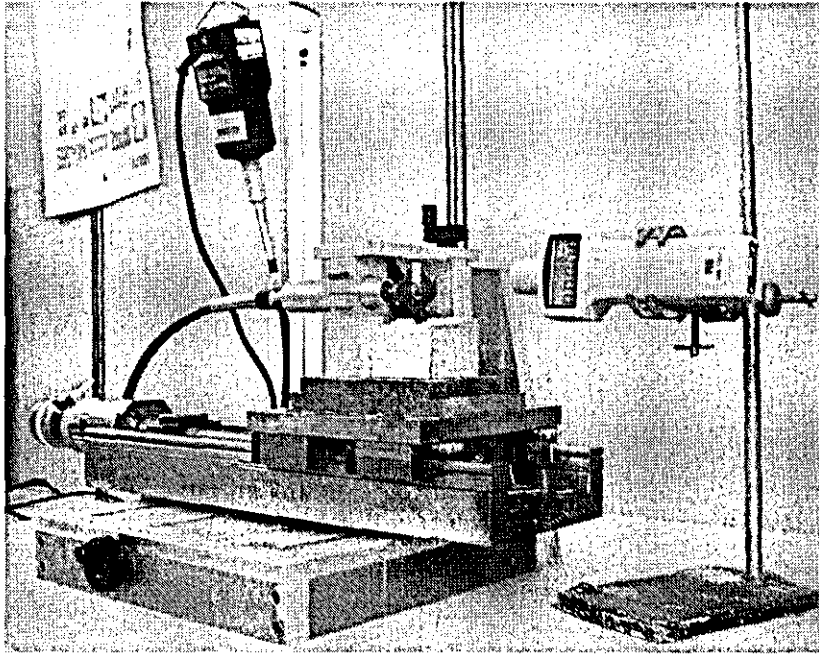


Figure 3.13 Photo of the cutting force rig.

The cutter, which is attached to a collet, is driven by a *Dremel Multi-Tool* via a flexible shaft. The *Dremel* motor is a 250 W, 220V AC motor and its speed can be adjusted manually in the range of 5000 – 22000 rpm. The cutting speed ω is measured with a non-contact optical tachometer having 1 s sampling rate. Prior to cutting, the cutter assembly can be moved in vertical direction to set the desired depth of cut d .

Initially the test-rig was designed to use with a three-axis load cell, attached to the feed table and carrying a timber specimen. Series of tests had been performed; however, meaningful cutting force data could not be acquired in any of the three directions. As it can be understood from the previous section, the magnitudes of the cutting forces are very small (i.e. in the order of a few newtons maximum). These small forces could not be detected among the vibration of the test-rig and the electrical noise of the available equipment (i.e. charge amplifiers). Design and manufacture of a special purpose load cell was outside the scope of this research work; consequently, the load cell arrangement was not used.

As an alternative approach, it was decided to derive the cutting power and forces from the power input to the cutter motor. Timber specimens were screwed directly to the feed table and an AC watt-meter, which is capable of measuring the average power in one second intervals, was connected between the cutter motor and the mains socket. Similar methods, utilizing a watt-meter, are reported in [60], [65] and [68]. The findings show that, very high correlation exists between the power calculated from measured cutting forces (3.9) and the power measured directly with a watt-meter; and this correlation permits estimation of cutting forces for given machining conditions. Figure 3.14 shows the schematic of the final cutting force test- rig.

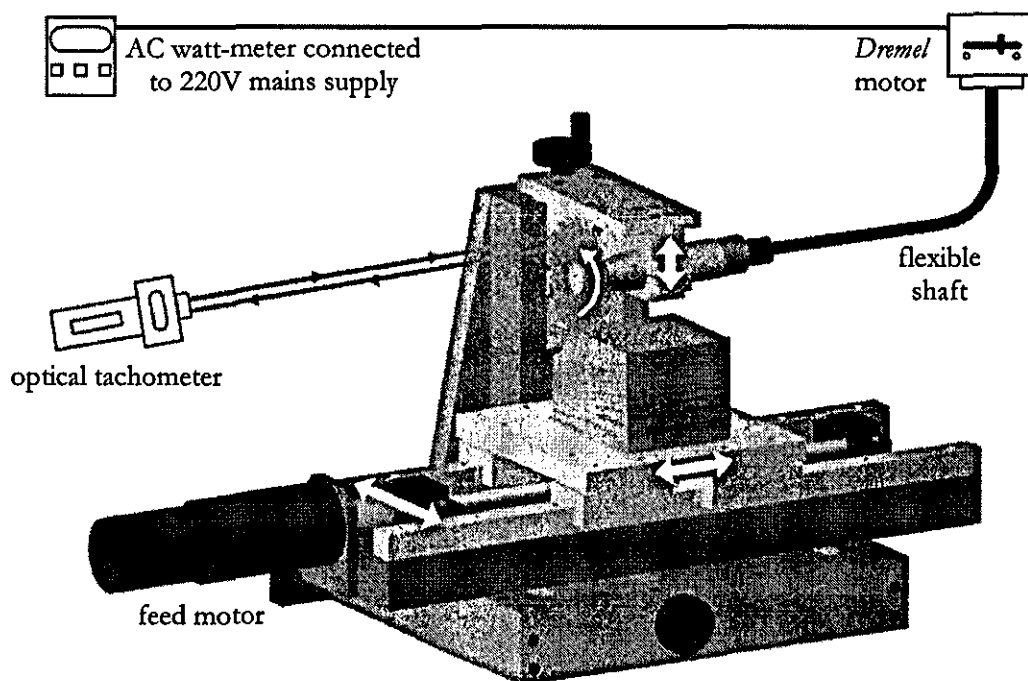


Figure 3.14 Cutting force rig schematic

3.4.2 Measurement method

This section presents the measurement procedure and explains the method used for calculating the cutting force and power.

The following steps show the procedure repeated for each test:

- Step 1: Set depth of cut d by adjusting the cutter assembly position.
- Step 2: Set feed increment f by adjusting the feed drive position.
- Step 3: Set pass time t by adjusting the feed motor speed.
- Step 4: Set cutter idling speed ω_{idle} .
- Step 5: Record power consumption of the idling cutter motor P_{idle} .
- Step 6: Switch on the feed motor.
- Step 7: While cutting, record cutter speed ω , and power consumption of the cutter motor P_{total} .
- Step 8: When cutting ends, switch off feed and cutter motors.

Before the timber is fed to the cutter, idling power consumption P_{idle} of the cutter motor, at the desired idling speed ω_{idle} , is read from the watt-meter. Consequently; the torque resulting from the rotating inertias (i.e. rotor, flexible shaft, and cutter) and friction, is figured out from equation (3.11).

$$T_{idle} = \frac{P_{idle}}{\omega_{idle}} \quad (3.11)$$

When the cutting starts, the cutter speed drops to a lower value and stays there until the cutting ends. This is due to the cutter motor having no means of real-time control to compensate the cutting torque. Therefore, the cutter speed ω and the total power consumption of the cutter motor P_{total} are read; and the total torque is calculated (3.12).

$$T_{total} = \frac{P_{total}}{\omega} \quad (3.12)$$

$$T = T_{total} - T_{idle} \quad (3.13)$$

To find the cutting torque (i.e. torque required for severing chips from workpiece), the idling torque T_{idle} is subtracted from the total torque T_{total} (3.13). From the cutting torque, cutting power P and cutting force F is calculated by equations (3.14) and (3.15) respectively, where r is the cutter radius.

$$P = \omega \cdot T \quad (3.14)$$

$$F = \frac{T}{r} \quad (3.15)$$

3.4.3 Test series

Series #	Cutter						Workpiece		Machine				
	r (mm)	n	α_r (°)	γ_r (°)	α_s (°)	γ_s (°)	w (mm)	s_{12}	f (mm)	d (mm)	t (s)	ω_{idle} (rpm)	P_{idle} (W)
1	42.5	20	10	10	0	10	70	0.55	1	5	3	13500	106.5
2	42.5	20	10	10	0	10	70	0.55	2	5	3	13500	106.5
3	42.5	20	10	10	0	10	70	0.55	1	10	3	13500	106.5
4	42.5	20	10	10	0	10	70	0.55	2	10	3	13500	106.5
5	42.5	20	10	10	0	10	70	0.55	1	15	3	15000	106.5
6	25.4	4	15	10	0	10	70	0.55	1	5	2	17000	105
7	25.4	4	15	10	0	10	70	0.55	2	5	2	17000	105
8	25.4	4	15	10	0	10	70	0.55	3	5	2	17000	105
9	25.4	4	15	10	0	10	70	0.55	1	5	3	17000	105
10	25.4	4	15	10	0	10	70	0.55	2	5	3	17000	105
11	25.4	4	15	10	0	10	70	0.55	3	5	3	17000	105
12	25.4	4	15	10	0	10	70	0.55	1	5	4	17000	105
13	25.4	4	15	10	0	10	70	0.55	2	5	4	17000	105
14	25.4	4	15	10	0	10	70	0.55	3	5	4	17000	105

Table 3.4 Test series

Measurements were carried out in 14 different series, each of which consisted of five identical tests. The arithmetic means of the obtained ω and P_{total} values were used in further calculations. 70 mm wide *Meranti* wood specimens having specific gravity $s_{12}=0.55$ were used as specimens. Two different cutters were employed with various machining parameter combinations. Cutter, workpiece and machine parameters of the test series are listed in Table 3.4.

3.4.4 Test results and discussion

Table 3.5 shows the measured (i.e. P_{total} and ω) and calculated (i.e. T , F and P) results for the test series. The validity analysis is done by comparison with the theoretical values (Section 3.3), which are based on the results of Kivimaa's [58] experiments.

Series #	P_{total} (W)	ω (rpm)	T (Nm)	F (N)	P (W)
1	123.76	12322	0.021	0.484	26.552
2	146.86	10795	0.055	1.284	61.696
3	142.80	11014	0.048	1.140	55.905
4	190.20	9883	0.108	2.551	112.229
5	173.80	9871	0.093	2.184	95.927
6	120.54	15440	0.016	0.613	25.175
7	132.40	14380	0.029	1.139	45.582
8	150.20	13804	0.045	1.769	64.941
9	118.56	15724	0.013	0.513	21.439
10	134.44	14613	0.029	1.137	44.183
11	146.76	13728	0.043	1.697	61.971
12	115.58	16007	0.010	0.392	16.711
13	130.12	14981	0.024	0.943	37.589
14	137.80	14413	0.032	1.272	48.777

Table 3.5 Cutting force test results

To find the theoretical cutting force and power for Series #1, firstly, the length L and mean chip thickness δ_m of the produced chips are calculated from equations (3.1) and (3.2).

$$L=20.8 \text{ mm} \quad \delta_m=0.2 \text{ mm}$$

Secondly, the number of cutter-workpiece engagements (3.3) is:

$$n_p=12322$$

Here, it is worth checking if a complete chip is severed at each engagement. This is done by calculating the number of teeth on the portion of the cutter circumference, which is equal to the chip length. In other words, number of teeth cutting at the same time n_t (3.16).

$$n_t = \frac{L}{2 \cdot \pi \cdot r} \cdot n \quad (3.16)$$

If $n_t \leq 1$ then a complete chip is severed at each engagement. On the other hand, when $n_t > 1$; although n_p teeth runs over the workpiece, only n_p/n_t full chips are severed.

For Series #1,

$$n_t = 1.56$$

Therefore, if it is assumed that only full chips are severed, the chip width is calculated as follows.

$$c = w / (n_p / n_t) = 0.009 \text{ mm}$$

Based on the δ_m and c values and the respective rake angles, F_{t_i} and F_{s_i} are found from Figure 3.12 and the total tangential force F_t is calculated (3.5).

$$F_{t_i} = 11.5 \text{ N/mm}$$

$$F_{s_i} = 1.8 \text{ N/mm}$$

$$F_t = 0.464 \text{ N}$$

Finally, the theoretical cutting power is calculated from equation (3.10), where n' is replaced by n'/n_t due to the reasons explained above, and it is:

$$P = 25.411 \text{ W}$$

The obtained theoretical force and power values are within 5% to the measured values in Table 3.5. Considering the assumptions taken in the calculations and the difference in timber species between Kivimaa's experiments (*Birch*) and the current ones (*Meranti*), the results are reasonably accurate and sufficient for the purpose of this investigation.

Table 3.6 lists the calculated parameters of the produced chips in all test series. For the tip rake angles of the used cutters (i.e. 10° and 15°), Kivimaa reports the cutting forces only up to $\delta_m = 0.2 \text{ mm}$ (Figure 3.12). Therefore, except Series #1, there is no data available to compare against the measured values. However, for $\delta_m = 0.3 \text{ mm}$, an approximation can be made. In Figure 3.12(a), from 0° to 15° rake angles, the cutting force value reduces by 30% for $\delta_m = 0.05 \text{ mm}$, 50% for $\delta_m = 0.1 \text{ mm}$ and 65% for $\delta_m = 0.2 \text{ mm}$. Also, from 0° to 10° rake angles, the cutting force reduction percentages are 20% for $\delta_m = 0.05 \text{ mm}$, 25% for $\delta_m = 0.1 \text{ mm}$ and 45% for $\delta_m = 0.2 \text{ mm}$. Consequently, the reduction percentage for $\delta_m = 0.3 \text{ mm}$ can be

approximated as 70% for 15° and 50% for 10° from the respective values at 0° rake angle, which are given in Figure 3.12(b).

Series #	L (mm)	δ_m (mm)	n_p	n_t	c (mm)
1	20.8	0.2	12322	1.56	0.009
2	20.8	0.5	10795	1.56	0.010
3	29.76	0.3	11015	2.23	0.014
4	29.76	0.7	9884	2.23	0.016
5	36.85	0.4	9871	2.76	0.020
6	16.21	0.3	2059	0.41	0.034
7	16.21	0.6	1917	0.41	0.037
8	16.21	0.9	1841	0.41	0.038
9	16.21	0.3	3145	0.41	0.022
10	16.21	0.6	2923	0.41	0.024
11	16.21	0.9	2746	0.41	0.025
12	16.21	0.3	4267	0.41	0.016
13	16.21	0.6	3995	0.41	0.018
14	16.21	0.9	3844	0.41	0.018

Table 3.6 Parameters of the produced chips

If, for example, Series #9 is considered, where $\delta_m=0.3$ mm and $c=0.022$ mm; the following values are obtained from Figure 3.12(b).

$$F_{t_i} = 29 - (29 * 70\%) = 8.7 \text{ N/mm} \qquad F_{s_i} = 3.5 \text{ N/mm}$$

Hence, from equations (3.5) and (3.10), the cutting force and power are calculated as;

$$F_t = 1.241 \text{ N} \qquad P = 21.089 \text{ W}$$

The theoretical power is very close (i.e. within 5%) to the measured value. On the other hand, the theoretical force is much higher than the force in Table 3.5. The reason for the difference can be explained by the n_t value, which is 0.41 in Series #9. This value can be interpreted as; in one revolution of the cutter, only 41% of the time the cutter is in contact with the workpiece (i.e. cutting). The rest of the time (i.e. 59%) the cutter is rotating freely, therefore, cutting force is 0 N. The actual cutting force and torque change periodically between zero and a maximum value. The values listed in Table 3.5, which are calculated by equations (3.13) and

(3.15), represent the average cutting force and torque over time. Consequently; the maximum force and torque values, which occur while the cutter is actually cutting, is found by dividing the average values in Table 3.5 by n_t . For Series #9 this gives,

$$F = 0.513 / 0.41 = 1.251 \text{ N.}$$

Table 3.7 lists the experimental and theoretical results for the applicable series. The thick frame indicates the corrected torque and force values due to $n_t < 1$.

Series #	P_{total} (W)	ω (rpm)	T (Nm)	Experimental		Theoretical	
				F (N)	P (W)	F_t (N)	P (W)
1	123.76	12322	0.021	0.484	26.552	0.464	25.411
2	146.86	10795	0.055	1.284	61.696	N/A	N/A
3	142.80	11014	0.048	1.140	55.905	1.103	54.046
4	190.20	9883	0.108	2.551	112.229	N/A	N/A
5	173.80	9871	0.093	2.184	95.927	N/A	N/A
6	120.54	15440	0.039	1.495	25.175	1.556	25.967
7	132.40	14380	0.071	2.778	45.582	N/A	N/A
8	150.20	13804	0.110	4.315	64.941	N/A	N/A
9	118.56	15724	0.032	1.251	21.439	1.241	21.089
10	134.44	14613	0.071	2.773	44.183	N/A	N/A
11	146.76	13728	0.105	4.139	61.971	N/A	N/A
12	115.58	16007	0.024	0.956	16.711	0.979	16.929
13	130.12	14981	0.059	2.300	37.589	N/A	N/A
14	137.80	14413	0.078	3.102	48.777	N/A	N/A

Table 3.7 Corrected cutting force test results

Figure 3.15 and Figure 3.16 show bar charts of measured cutting power for Series #1 to #5 and #6 to #14 respectively. As expected, more power is consumed at deeper cuts (Figure 3.15), higher feed increments (Figure 3.15(a), Figure 3.16) and lower pass times (Figure 3.16).

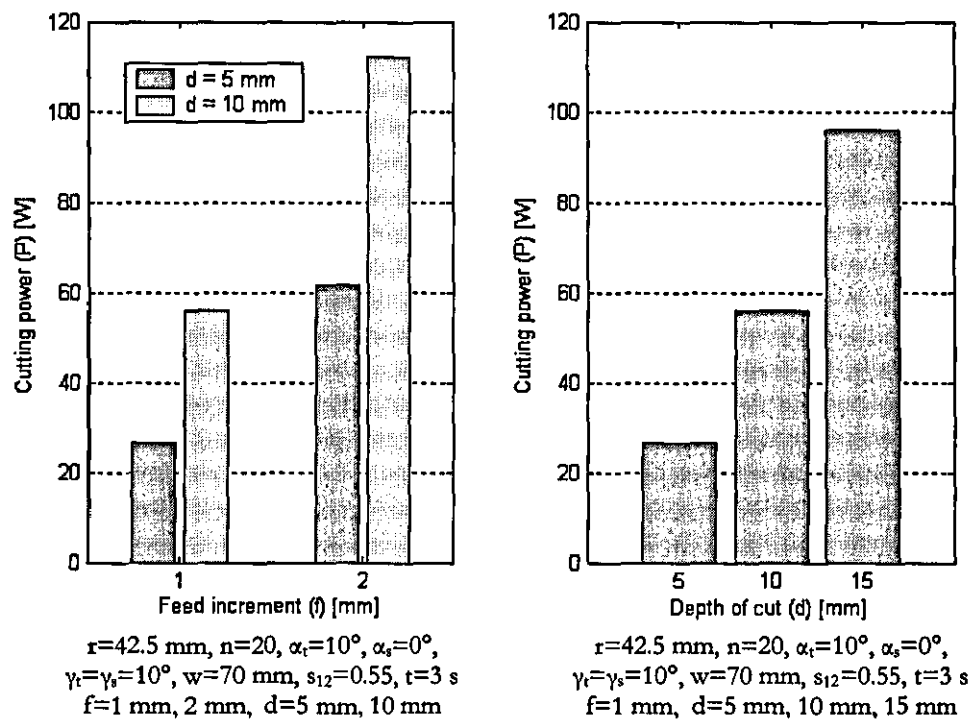


Figure 3.15 Measured power for Series #1 to #5

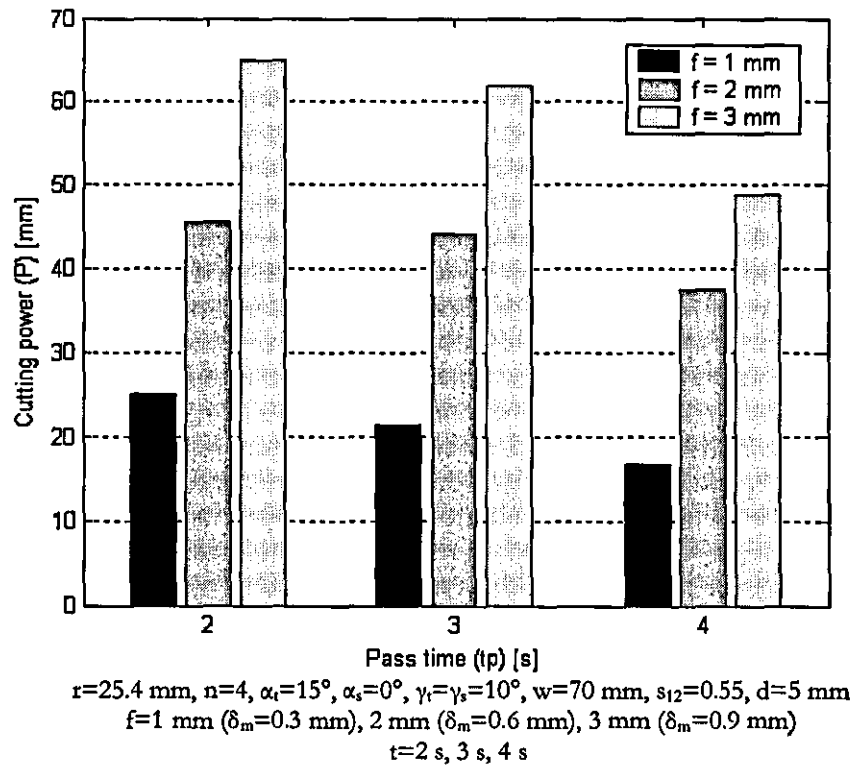


Figure 3.16 Measured power for Series #6 to #14

3.5 Summary

Chip severing phenomena, important parameters and cutting forces in rotary wood planing/moulding processes are presented. Factors which influence cutting forces are studied from the results of the previous work by Kivimaa and others. For the conventional processes, cutting speed has little or no effect on the cutting forces; whereas, the greatest influence on the magnitude of forces per cutting width is from cutter geometry parameters and chip thickness.

Influencing factors are theoretically adapted to the PIMM process. Cutting forces and power requirements are estimated for given theoretical machining conditions. It was discovered that the cutting speed, unlike in the conventional processes, has a great effect on the cutting forces in the PIMM due to the traverse movement of the cutter along the workpiece width.

Cutting power measurement rig is presented, experiment method is explained and results are discussed. Close correlation exists between the measured and estimated cutting power both in terms of magnitudes and tendencies.

Based on the measurement results, 100 W cutting power is sufficient for general PIMM operation. This requirement can be lowered by using cutters having larger rake angles. However, considering the small widths of the cutters, larger rake angles make the cutters more fragile and therefore more vulnerable to dulling; and this needs to be investigated by further experiments.

Chapter 4

System Modelling and Simulation

4.1 Introduction

This chapter is aimed at bringing the profile independent wood-moulding machine from an idea to the detailed design stage. Firstly, the overall system is divided into individual mechanical, electrical and software components and their requirements and constraints are clarified. Secondly, alternatives associated with each component are analysed and evaluated. Finally, the selected alternatives are combined in a simulation model and tested against overall machine requirements.

Figure 4.1 shows a schematic of the overall system. The process starts with a desired moulding profile input to the machine from a CAD file. The raw geometry data is then translated to a set of tasks and fed into the top-level reference generator. The reference generator sends individual tasks to the software mechanism which synchronizes the drives on the three axes with reference signals. These signals are amplified in the individual axes and the desired relative motion between the cutting tool and the workpiece is obtained via the motors and power transmission hardware.

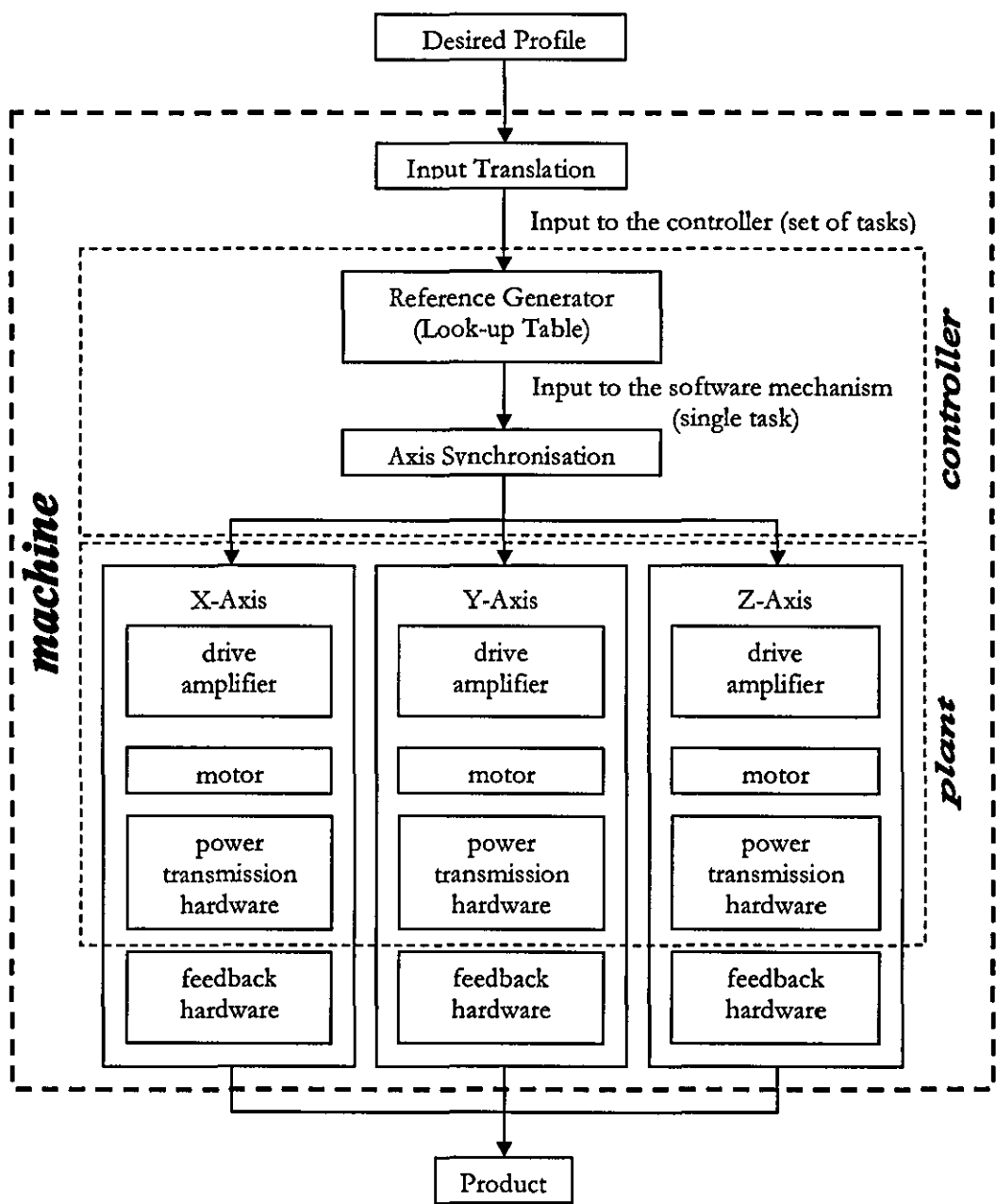


Figure 4.1 PIMM System

The system is divided in two main parts as the electro-mechanical hardware and the controller. The first part includes all of the hardware components in the X, Y and Z axes and is discussed in Section 4.2. The second part which is analysed in Section 4.3 contains everything from the profile input down to the reference signals to the axes. Section 4.4 presents the software simulation results of the overall system.

4.2 Electro-Mechanical Hardware

Due to the operation principle of the PIMM, two separate tasks are performed by using three drives. Drives on the X and Y axes move the cutter simultaneously and produce the desired geometry on the stationary workpiece. The drive on the Z-axis is responsible for feeding the workpiece in between two consecutive passes of the cutter along the width of the workpiece. Therefore, it is appropriate to study the X and Y axes together and Z-axis on its own.

4.2.1 Performance expectations from X and Y axis drives

Cutter positioning is the essential part of the PIMM concept. Dynamics of the X and Y axes drives determine the production speed and the geometric accuracy of the moulding. Therefore it is necessary to design fast, accurate and dynamically matched axes in order to achieve satisfactory production.

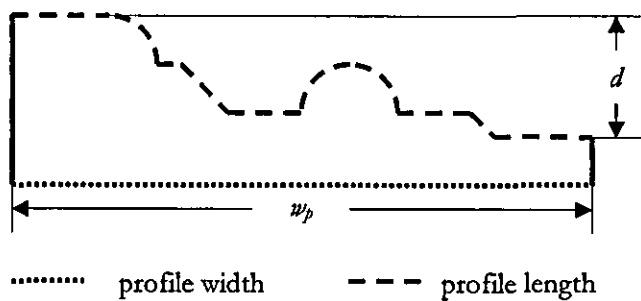


Figure 4.2 Moulding Dimensions

The first performance measure of the X and Y axes is the pass time t . This is the time taken for the cutter to travel from one side of the timber to the other along the width while cutting the desired geometry. By determining the desired pass time and the maximum workpiece width that can be machined by the PIMM, the speed requirement on the horizontal axis can be identified. However, on the vertical axis this is more complicated. As mentioned earlier, wood mouldings can be in various shapes and sizes. Some profiles can have long flat horizontal surfaces where the vertical drive does not move while machining. Some profiles, on the other hand,

can be highly demanding for the vertical drive. Examples of typical extremes are given in Appendix A. Therefore, rather than identifying the axis speed requirements individually, it is decided to determine the “path speed” (i.e. cutter travel speed on the profile).

A number of commercial moulding profiles with maximum profile width $w_p=100$ mm and maximum depth of cut $d=25$ mm were selected. The profile lengths were measured and compared to the profile widths (Figure 4.2). As a result, the profile lengths were found to be longer (18.90% to 22.3%) than the corresponding profile widths. Consequently, the mean path speed v_{mean} is formulated as in (4.1).

$$v_{mean} = \frac{w_p}{t} \cdot 120\% \quad (4.1)$$

where, w_p is the profile width and t is the time for one pass across the profile width. Figure 4.3 shows the plot of the mean path speed versus pass time for a 100 mm wide moulding.

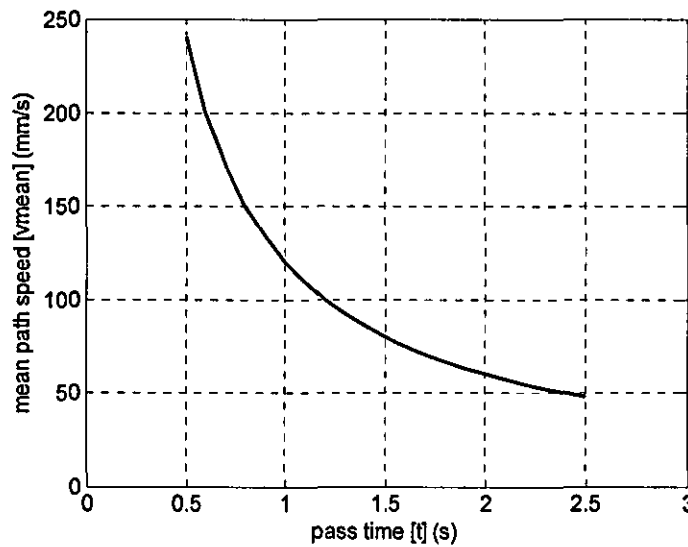


Figure 4.3 Mean path speed vs. pass time for a 100mm wide moulding

If assumed that in one cycle of the process, 90% of the time is elapsed during cutting and the rest 10% while timber feeding, then a fast machine with cycle time t_c less than 1 s and therefore pass time t less than 0.9 s can be achieved with a mean path speed of 135 mm/s or more. With this mean path speed, the PIMM produces acceptable quality mouldings (i.e. surface wave pitch $p=2.5$ mm) at a rate of 0.15 m/min. Production rate of the PIMM is discussed in more detail in Section 4.2.4.

Product quality in terms of geometric accuracy and waviness defects is the second performance measure of the X and Y axis drives. First of all, on every single pass the cutter must follow the desired geometry with sufficient accuracy. Although this procedure is managed by the software mechanism and the controller, it also needs accurate hardware. According to [1], tolerances for the geometric accuracy of the machined timber sections are between $\pm (0.1 - 0.5)$ mm depending of the end-usage of the product.

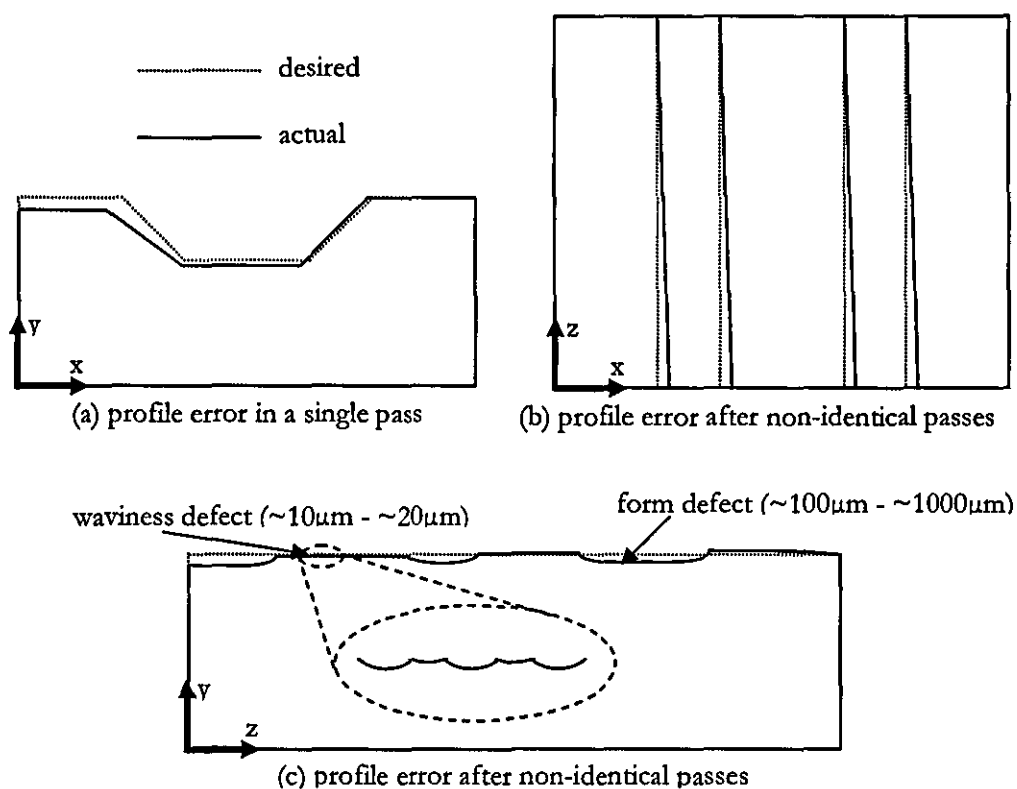


Figure 4.4 Geometric errors

The geometric accuracy within a single pass only affects the profile quality on the X-Y plane. It should be noted that in order to produce a single moulding, the PIMM must perform hundreds of passes. Relative position differences among the individual passes result in undesirable geometry on the X-Z and Y-Z planes.

Figure 4.4 illustrates profile errors on all three planes. Also on the Y-Z plane, those dissimilar passes generate surface waviness defects mentioned in Chapter 2. Hence it is critical to ensure that all the passes are identical and for that, the drives must be free from backlash and possess high repeatability.

4.2.2 Evaluation of hardware alternatives for X and Y axis drives

Various hardware alternatives exist for the design of the X and Y axis drives. Based on literature survey, four feasible options are listed as follows.

- ◆ Option 1: DC motor & timing belt
- ◆ Option 2: DC motor & leadscrew
- ◆ Option 3: DC motor & ballscrew
- ◆ Option 4: ThrustTube linear motor [72]

An evaluation matrix, as shown in Table 4.1, was used to compare the options against the drive requirements. The evaluation matrix provides a chart assessing and comparing alternative concepts in a systematic and objective way. In the evaluation matrix, three design objectives were considered for the drives. The first two, high product quality and high production rate, were discussed previously in this section. The third one is a collection of sub-objectives (i.e. cost, size, design simplicity), which apply to all design problems. Simplified weights were allocated to the objectives and, the weight of each objective was shared among its influencing factors with respect to their importance. For each influencing factor, the alternatives were valued relative to each other and weighted values were calculated.

Drive Evaluation Criteria for X and Y axes			DC Motor & Timing Belt		DC Motor & Leadscrew		DC Motor & BallScrew		ThrustTube Linear Motor	
Objectives	Influencing Factors	weight (w)	value (v)	weighted value (w * v)	value (v)	weighted value (w * v)	value (v)	weighted value (w * v)	value (v)	weighted value (w * v)
High product quality	high repeatability	0.20	4	0.80	8	1.60	8	1.60	9	1.80
	low backlash	0.15	4	0.60	8	1.20	8	1.20	9	1.35
	high accuracy	0.10	4	0.40	8	0.80	8	0.80	9	0.90
<i>Objective Total</i>		<i>0.45</i>		<i>1.80</i>		<i>3.60</i>		<i>3.60</i>		<i>4.05</i>
High production rate	high speed	0.10	8	0.80	6	0.60	7	0.70	10	1.00
	high agility	0.10	8	0.80	5	0.50	7	0.70	10	1.00
	low friction	0.05	8	0.40	5	0.25	7	0.35	10	0.50
	lightweight	0.05	9	0.45	7	0.35	5	0.25	1	0.05
<i>Objective Total</i>		<i>0.30</i>		<i>2.45</i>		<i>1.70</i>		<i>2.00</i>		<i>2.55</i>
Other objectives	low cost	0.15	9	1.35	8	1.20	4	0.60	1	0.15
	small size	0.05	6	0.30	8	0.40	6	0.30	1	0.05
	design simplicity	0.05	5	0.25	7	0.35	7	0.35	7	0.35
<i>Objective Total</i>		<i>0.25</i>		<i>1.90</i>		<i>1.95</i>		<i>1.25</i>		<i>0.55</i>
<i>Overall Total</i>		<i>1.00</i>		<i>6.15</i>		<i>7.25</i>		<i>6.85</i>		<i>7.15</i>

Table 4.1 Evaluation Matrix for the X and Y axes

For the *high product quality* objective, Option 1 was found to be greatly inferior to the other options with a weighted value of 1.80. While Option 2 and Option 3 have the same weighted value of 3.60, the Option 4 appeared to be the best choice with 4.05. However, the accuracy, repeatability and backlash values of the linear motors depend entirely on the linear position sensors (i.e. encoders) which are extremely high-priced compared to the rotary ones that can be used with the other drive options.

In terms of *high production rate* objective, again the Option 4 scored the best despite having the greatest moving mass among all options. Non-contact power transmission, therefore virtually zero friction and high efficiency of the ThrustTube linear motors resulted in the highest weighted values for three of the influencing factors. But again, this high performance can only be achieved by using expensive drive electronics that satisfy the high voltage requirements (160 – 320 VDC) of these motors.

For the set of *other objectives*, Option 2 gained the highest weighted value of 1.95, followed by Option 1 with a weighted value of 1.90. Twice as high cost of the ballscrews compared to the first two options result in Option 3 having a lower weighted value of 1.25. Option 4 scored far below the other three drive options because of high costs and large sizes of the linear drives.

Overall, Option 1 gained the lowest total weighted value of 6.15. Although it scored as the second best in the last two sets of objectives, its significantly low weighted value in the high product quality objective, which constitutes 45% of the overall weight, caused DC motor & timing belt drive to be the least suitable option. Option 3 scored average weighted values for all of the influencing factors and it came out the third with a total weighted value of 6.85. ThrustTube linear motor (Option 4), which gained an overall weighted value of 7.15, seems to be the best option in terms of the first two sets of objectives. However, as mentioned earlier, this superior performance can only be achieved by using expensive power amplifiers and feedback sensors; hence the total cost of the linear drives is

significantly higher than the other alternatives. Moreover, since there is no gearing exists for the linear motors, higher force can only be achieved by using a larger and heavier forcer (linear equivalent of the DC motor rotor). To the author's knowledge, only Copley Controls Corp. [72] manufactures this type of linear motors. Using the TB2506, which satisfy the PIMM's requirements, from the available product range results in a larger size system with greater moving mass and therefore higher power consumption. Although the ThrustTube linear motor technology is suitable for the PIMM concept, the available products are not found to be convenient for this application. Finally, despite being the last in the second objective due to relatively higher friction, Option 2 emerged as the best alternative with an overall weighted value of 7.25. To give an idea about the cost and performance of DC motor & leadscrew drives; for example, a maximum speed of 400 mm/s, and a continuous thrust over 120 N can be achieved at a cost of £500 per drive. This includes power amplifier, DC motor, anti-backlash leadscrew, linear ball guide and optical incremental encoder. Consequently, it was decided to go through to the software simulations with the DC motor & leadscrew drives for X and Y axes.

4.2.3 Mathematical modelling of X and Y axis drives

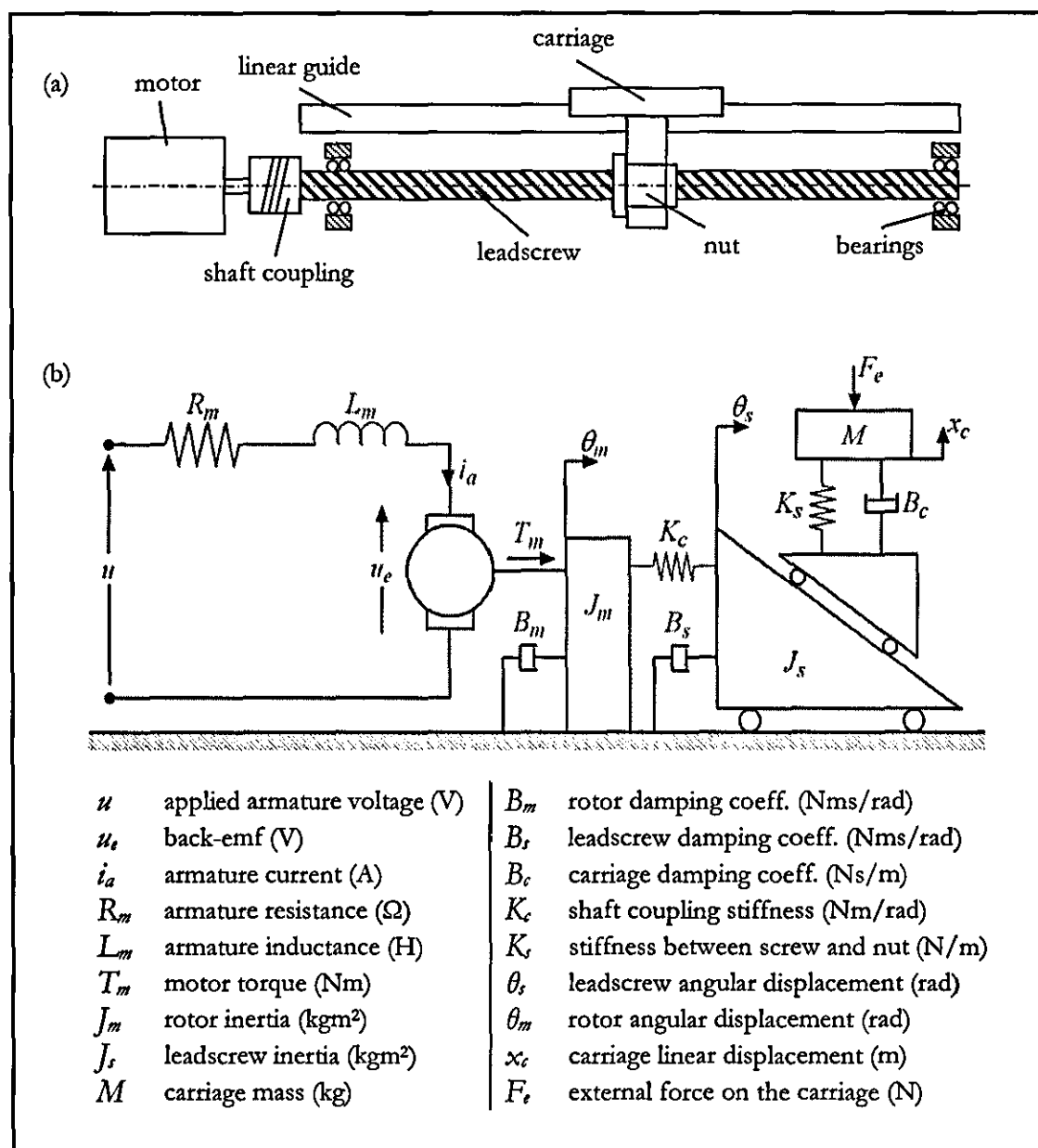


Figure 4.5 Drive mechanism (a) and dynamic model (b) of a single axis

Mathematical modeling serves as a foundation for comprehensive analytical investigation of the X and Y axis drives prior to detailed design. Figure 4.5 shows a typical [73][74][75][76] drive mechanism, dynamic model and associated parameters for a single axis. For each of the X and Y axis drives, a mathematical model was derived and implemented in Simulink as a block diagram. The rest of the section explains the mathematical modeling and implementation.

The motor is modeled [77][78] as a standard permanent magnet, armature controlled dc-motor. Figure 4.6 shows the block diagram in Simulink.

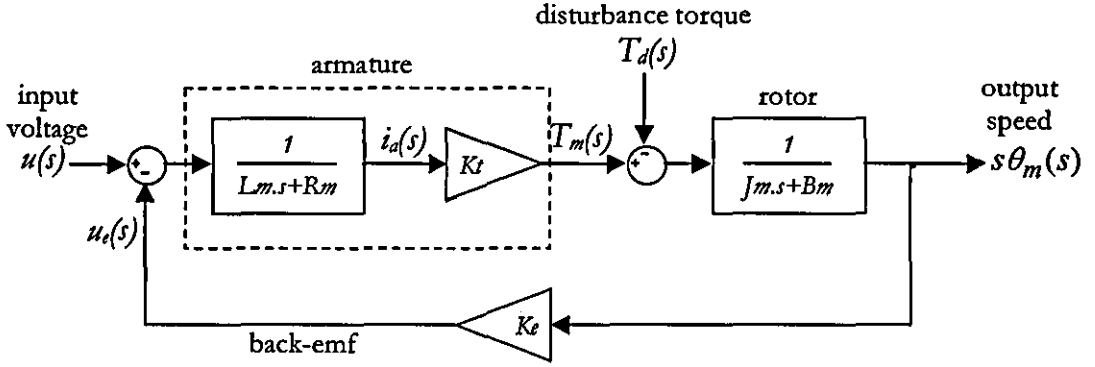


Figure 4.6 DC motor block diagram

The torque $T_m(s)$ developed by the motor is proportional to the armature current $i_a(s)$. In the *Laplace* domain, it is expressed as in (4.2), where K_t is the *torque constant* of the motor.

$$T_m(s) = K_t \cdot i_a(s) \quad (4.2)$$

The armature current $i_a(s)$ is related to the input voltage $u(s)$ applied to the armature as;

$$u(s) = (L_m \cdot s + R_m) \cdot i_a(s) + u_e(s) \quad (4.3)$$

where, $u_e(s)$ is the back-emf voltage proportional to the motor speed $s\theta_m(s)$, and it is given by (4.4) where K_e is the *back-emf constant*.

$$u_e(s) = K_e \cdot s\theta_m(s) \quad (4.4)$$

The mechanical equation of the motor is obtained by applying Newton's second law to the rotor (4.5). J_m and B_m are, respectively, moment of inertia and viscous damping coefficient of the rotor.

$$T_m(s) - T_d(s) = (J_m \cdot s + B_m) \cdot s \theta_m(s) \quad (4.5)$$

The disturbance torque $T_d(s)$ is due to various factors, such as; the inertia of the external load coupled to the motor shaft, friction, and cutting forces. If the coupling flexibility is neglected (i.e. infinitely stiff shaft coupling and leadscrew), the load inertia can be lumped with the rotor inertia after accounting for the possible existence of a speed reducer (i.e gear, belt, etc.) [79]. This approach is widely used in machine tools research, examples include [52], [80], and [81]. Consequently, for the drive models of the PIMM, considering the small inertia loads and cutting forces, the shaft coupling stiffness K_c and the stiffness between the leadscrew and nut K_r are neglected.

If two masses are linked through a stiff transmission with ratio r , then the input/output relations for position and velocity are as follows:

$$x_o = r \cdot x_i \quad \text{and} \quad \dot{x}_o = r \cdot \dot{x}_i \quad (4.6)$$

Since the kinetic energy remains invariable, the input mass appears on the output as:

$$M_i^o = r^{-2} \cdot M_i \quad (4.7)$$

Equation (4.7) holds whether M_i is a mass or inertia. It also holds for damping coefficients. If the motion is transformed from rotary to linear, as in the case of leadscrew, then r will be the leadscrew gain R_t (mm/rad) (4.8).

$$R_t = \frac{\text{lead}}{2\pi} \quad (4.8)$$

Therefore; for a directly driven leadscrew drive (Figure 4.5), the total equivalent inertia J and the total equivalent damping coefficient B , lumped at the rotor are calculated as follows:

$$J = J_m + J_s + M \cdot \left(\frac{1}{R_t} \right)^{-2} \quad (4.9)$$

$$B = B_m + B_s + B_c \cdot \left(\frac{1}{R_t} \right)^{-2} \quad (4.10)$$

At this point, although the inertias are lumped at the rotor, the disturbance torque $T_d(s)$ still exists and includes friction and cutting torques. Given the machining parameters, the latter can be estimated as explained in Chapter 3. On the other hand, a realistic friction model is not feasible at this stage of the investigation. Nevertheless, a fraction of the friction losses in the system can be included in the model by taking into account the leadscrew efficiency, which is obtained from the manufacturer's data. For a directly driven, infinitely stiff leadscrew drive, the efficiency e is expressed [79] as in (4.11), where $T_f(s)$ is the friction torque.

$$e = \frac{T_m(s) - T_f(s)}{T_m(s)} \quad \text{hence;} \quad e \cdot T_m(s) = T_m(s) - T_f(s) \quad (4.11)$$

Substituting equations (4.8) to (4.11) into equation (4.5) results in the mechanical equation of a single axis drive (4.12). For the horizontal drive, $F_e(s)$ is the cutting force, whereas, for the vertical drive it also includes the carriage weight (i.e. $M \cdot g$).

$$e \cdot T_m(s) - R_t \cdot F_e(s) = (J \cdot s + B) \cdot \frac{s x_c(s)}{R_t} \quad (4.12)$$

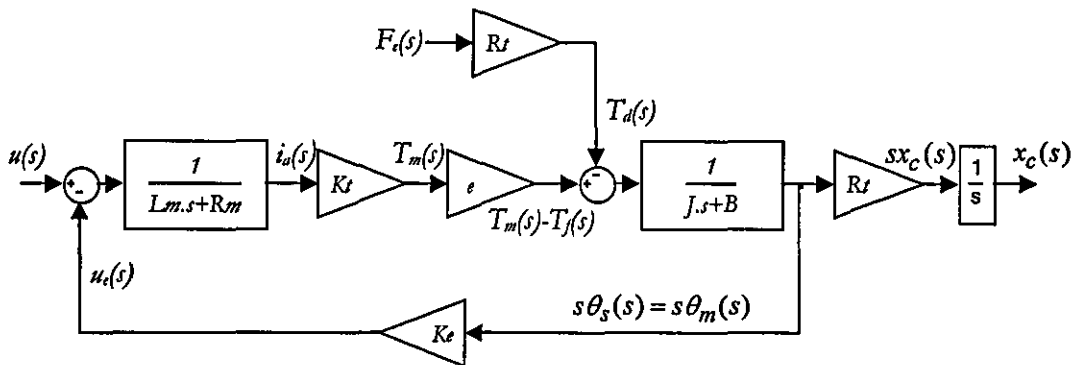


Figure 4.7 Block diagram from armature voltage to carriage position

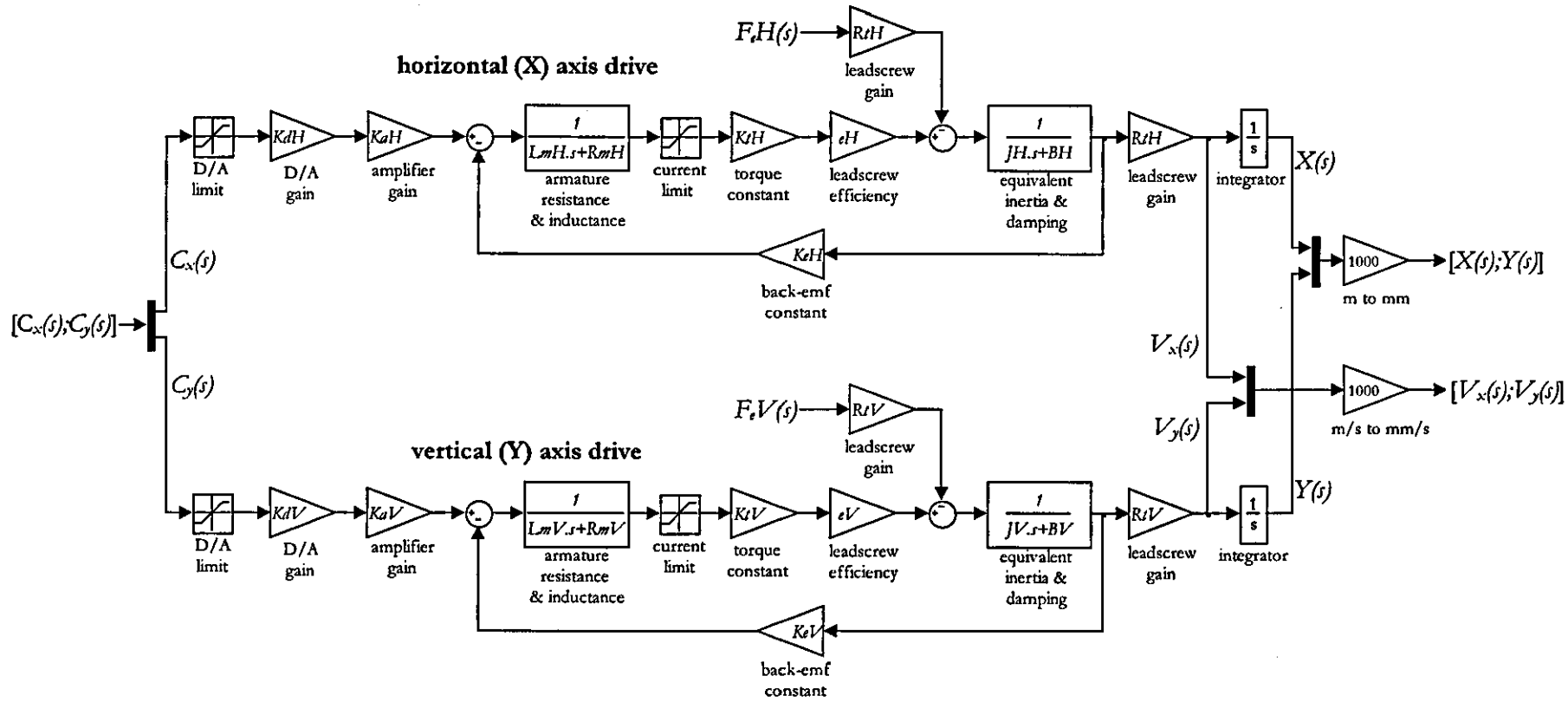


Figure 4.8 Complete block diagram of the X and Y axis drives

Figure 4.7 shows the Simulink block diagram of a single axis drive from the armature voltage input $u(s)$ to the carriage position $x_c(s)$. Using equations (4.2), (4.3), (4.4), and (4.12), or, alternatively, the block diagram (Figure 4.7), the transfer function is obtained (with $F_t(s)=0$) as follows:

$$G(s) = \frac{x_c(s)}{u(s)} = \frac{eK_t R_t}{s[(Js + B) \cdot (L_m s + R_m) + eK_t K_e]} \quad (4.13)$$

Prior to being applied as the armature voltage, the digital control signals are first converted to analog voltage signals in a digital-to-analog (i.e. D/A) converter and then amplified by a drive amplifier. The D/A converter and the drive amplifier are modeled as proportional gains K_d and K_a respectively (Figure 4.8). Equation (4.14) gives the transfer function from the digital control signal $C(s)$ to the carriage position $x_c(s)$.

$$G(s) = \frac{x_c(s)}{C(s)} = \frac{eK_t R_t K_d K_a}{s[(Js + B) \cdot (L_m s + R_m) + eK_t K_e]} \quad (4.14)$$

The complete block diagram of the horizontal (X) and vertical (Y) axis drives is shown in Figure 4.8, where the parameters for a particular drive are written with letters H for horizontal and V for vertical (i.e. $L_m H$, $K_t V$). In Figure 4.8, two saturation blocks are added to the model of each drive as presented in [82] and [83]. The first one defines the limit of the D/A converter and makes sure the control signal stays within these limits. The second block defines the limit of the current drawn by the motor. The maximum current value is obtained from the datasheet of the motor and, in the actual system, it is usually set in the drive amplifier.

The derived mathematical models of the X and Y axis drives are used in the software simulations presented later in this chapter. Also, their validity will be discussed in Chapter 6 through system identification procedures. The next section deals with the expected performance of the Z axis drive.

4.2.4 Expected performance and hardware of Z axis drive

Compared to the X and Y axis drives the Z-axis drive has less influence on the PIMM's performance. The two main requirements of the Z axis drive are feeding the part in between two passes of the cutter and holding the part rigidly in place during the pass.

The length of timber fed in between two consecutive passes not only determines the production rate but also it is equal to the surface waviness pitch p . This is due to the operation principle of the PIMM. A good quality surface is classified by a wave pitch of typically <1.5 mm, and a lower quality surface by a wave pitch of typically >2.5 mm [1][2]. Figure 4.9 shows a graph of production rate versus cycle time t_c for different waviness pitches.

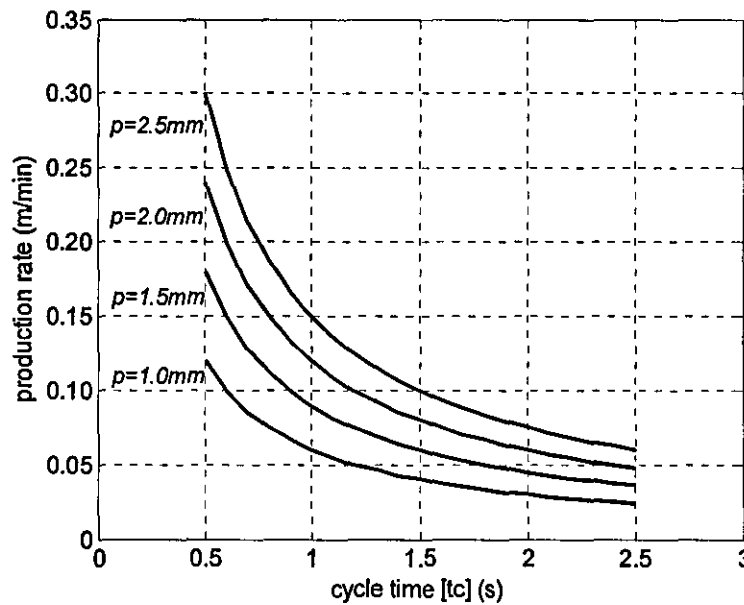


Figure 4.9 Production rate vs. cycle time for a 100 mm wide moulding

As mentioned earlier, it is assumed that in one cycle of the process 90% of the time is elapsed during cutting and the remaining 10% while timber feeding. For the target cycle time of 1 s for a 100 mm wide moulding, the feed should be performed in 0.1 s. Considering maximum feed of 2.5 mm for acceptable quality surface, then the Z-axis must be capable of 25 mm/s average speed.

With $t_c=1$ s and $p=2.5$ mm, the production rate corresponds to 0.15 m/min (Figure 4.9) for a 100 mm wide moulding. This rate is very slow even when it is compared to the production rate of a slower conventional moulding machine, which has a typical output of 6 m/min. However, it should be reminded that the PIMM is intended for much smaller volumes of production.

At this stage of the research, most emphasis was given on the contouring on X and Y axes and it was aimed to design a feed drive only to carry out experiments on small test specimens. Accordingly, it was decided to use a stepper motor and leadscrew arrangement for the Z-axis movement.

4.3 Control Structure and Algorithms

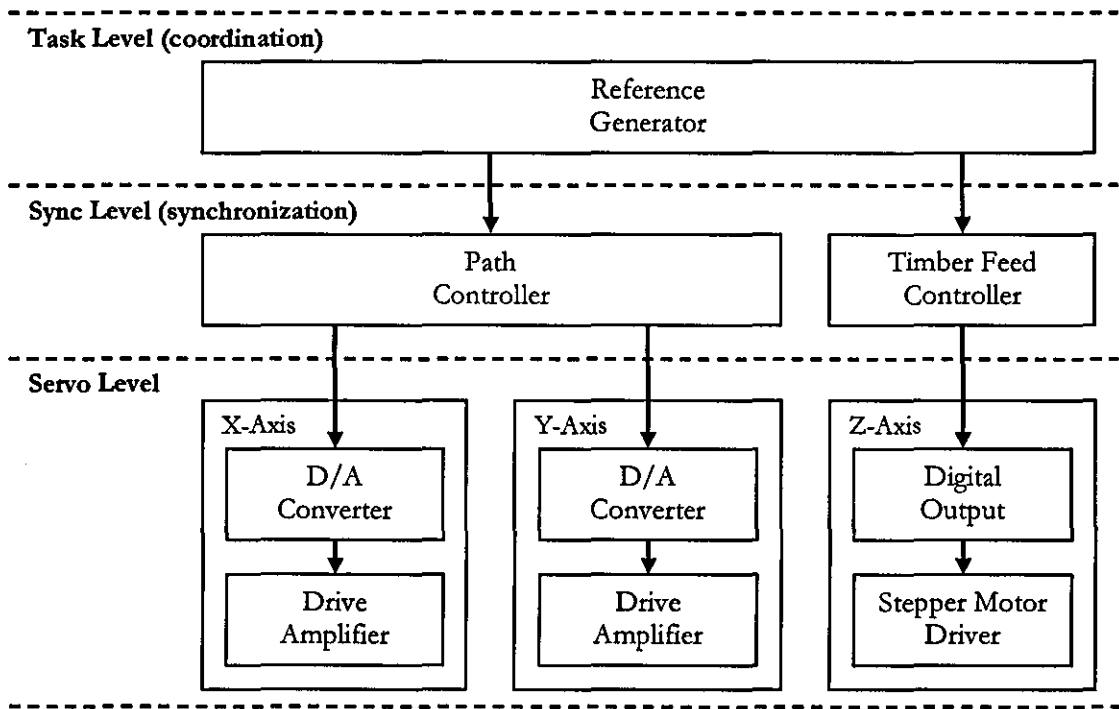


Figure 4.10 Control Structure

Figure 4.10 illustrates the overall controller structure of the PIMM. The levels of abstraction (i.e. task, sync, servo) are initially defined in [84]. Then; they are adapted to high speed, servo controlled manufacturing machinery in [18]. Here, they are applied specifically to the PIMM controller as follows:

Task Level: The *Reference Generator* contains the geometry of the target moulding profile (i.e. the path) and works in a closed-loop via receiving position feedback from the drive encoders. It generates reference commands (i.e. path segments) for the *Path Controller* and also triggers the *Timber Feed Controller* every time the path is completed.

Sync Level: The *Path Controller* synchronizes the X and Y axis drives to perform the tasks it receives from the *Reference Generator*. It acquires feedback from the drive encoders and works in a closed-loop.

The *Timber Feed Controller* works in an open-loop; and, when activated by the *Reference Generator*, it sends out the number of steps necessary to achieve the desired timber feed.

Servo Level: At this level, commands from the Sync Level are converted into voltages and in turn currents to drive the actuators. Servo Level components of the X and Y axis drives are already included in the mathematical models derived in Section 4.2.3, and therefore, will not be discussed in this section.

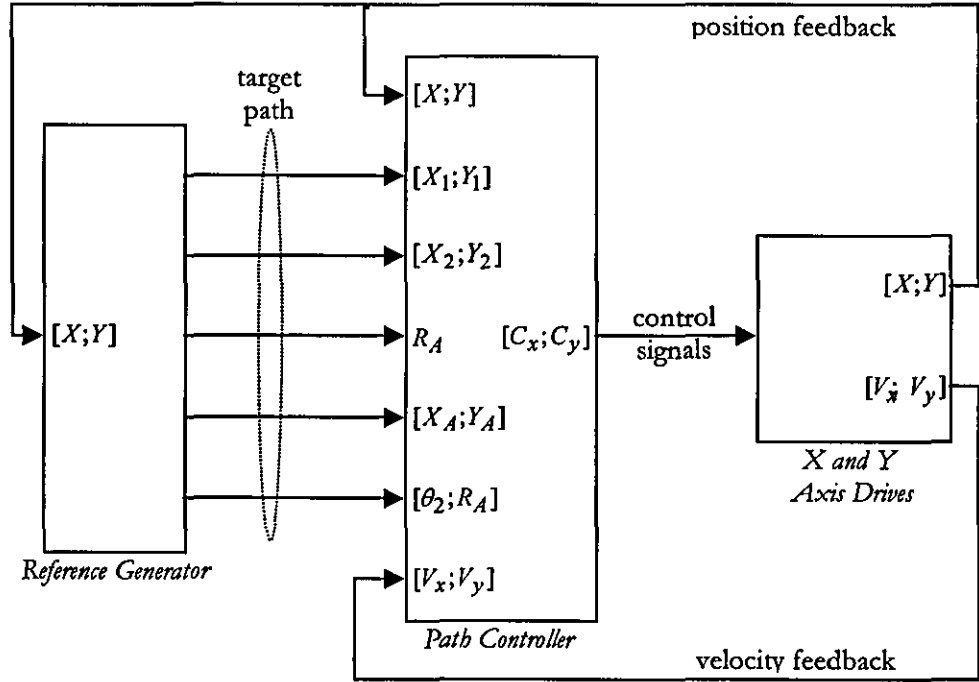


Figure 4.11 Generalized block diagram of the simulated system

Figure 4.11 shows a generalized block diagram of the PIMM in Simulink. Simulated system includes the X and Y axis drives (Figure 4.8) only, since they are the ones responsible for the accuracy and speed (i.e. 90%) of production. The *Reference Generator* is presented in Section 4.3.3, but before, Section 4.3.1 and 4.3.2 explain how the target moulding profile is input to the system. The *Path Controller* is explained in Section 4.3.4

4.3.1 Profile input

Desired profile geometry is input to the PIMM from a CAD drawing. Since the conventional moulders do not require any software input for the profiles they machine, there is no standard for geometry exchange. However, it was investigated whether there are CAD drawings of moulding profiles for design purposes or product catalogues.

A number of moulding manufacturers [85][86][87][88][89], especially in the US, are distributing electronic product catalogues containing profiles in “.dxf” and “.dwg” file formats. Some having more than thousand stock-range profiles accessible via the internet, they also accept custom designs from the customers. Both “.dxf” and “.dwg” are widely accepted drawing formats and they are supported by almost all of the CAD software packages. The only major difference between the two is that the “.dxf” is ASCII and “.dwg” is a binary format. For the PIMM, it was decided to use “.dxf” files because the necessary information is extracted much easier from ASCII text files than from the binary ones.

A “.dxf” file contains great deal of information about the drawing (i.e. line types, colors), but the only thing that needs to be extracted are the segment dimensions. Two-dimensional moulding profiles in “.dxf” files are made up of line and arc segments. An example of ASCII representations of a line and an arc in a “.dxf” file is given in Appendix B. To read the moulding profile from a target file, a function, *dxfread.m*, is implemented in Matlab. This function has two parts. The first part reads the dimensional information of all the segments in the file and stores them in an array. Figure 4.12 shows a flowchart of this part. The second part, which re-arranges and modifies the array in order to be used with the controller, is discussed in the next section.

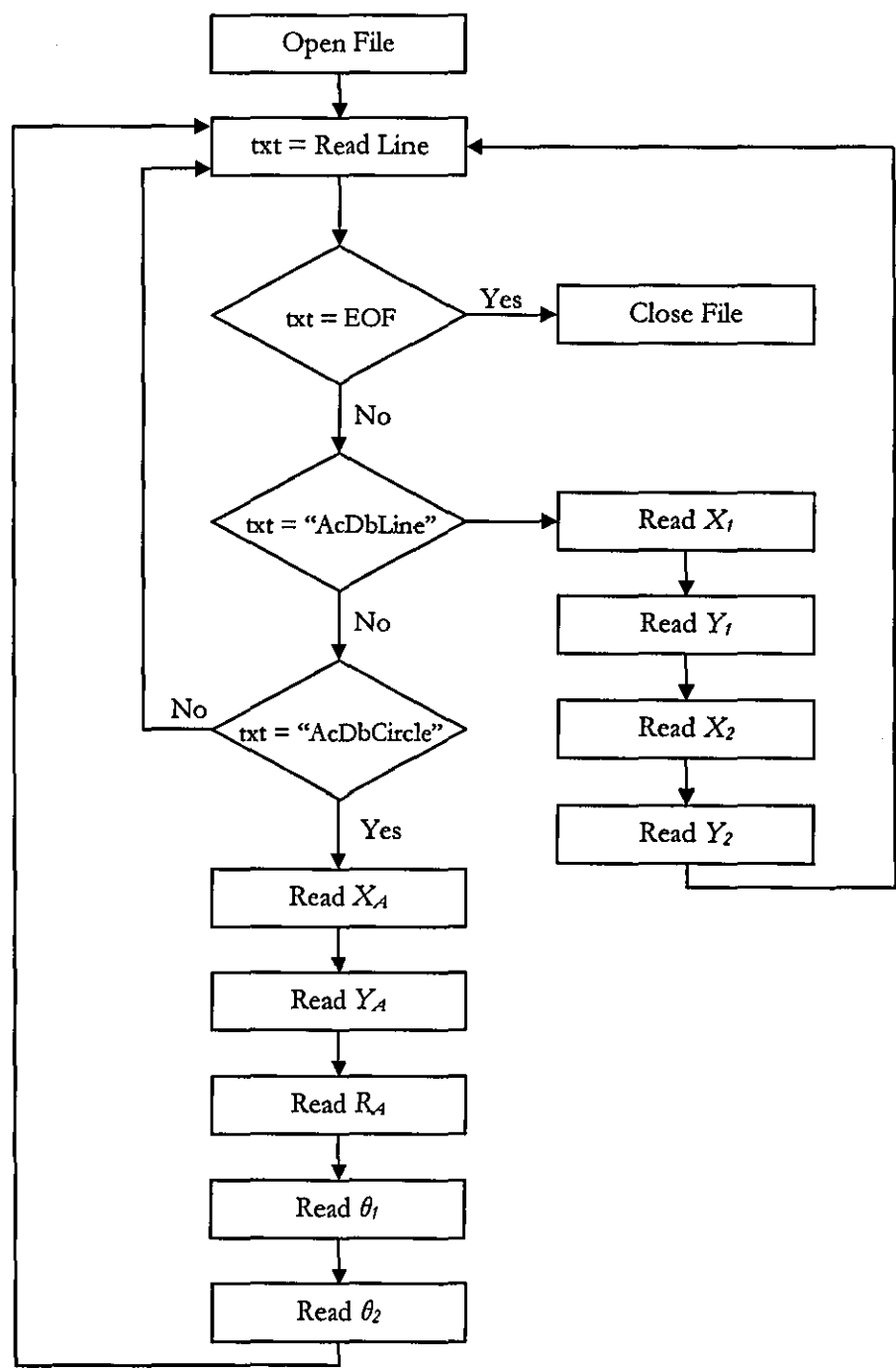


Figure 4.12 DXF input function “dxsfread.m” flowchart

4.3.2 Input Translation

The first part of the *dxsfread.m* reads all the segments from the target as they appear in the ASCII DXF file. However, since only one side of the timber is to be machined, the segments belonging to that side have to be picked out. Furthermore, the profile segments need to be sorted in the right order for the controller. This input translation, which is done by the second part of the function, is explained with a simple example. Full code listing of the *dxsfread.m* function is given in Appendix C.

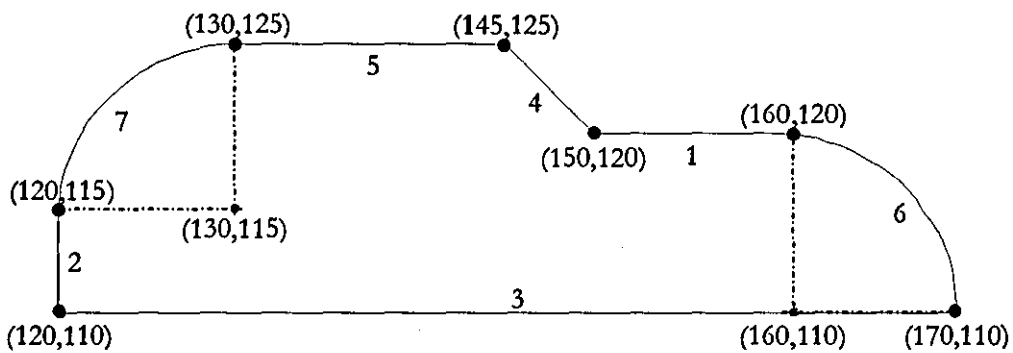


Figure 4.13 Raw DXF profile

	1	2	3	4	5	6	7
X_1	150	120	120	145	130	-	-
Y_1	120	115	110	125	125	-	-
X_2	160	120	170	150	145	-	-
Y_2	120	110	110	120	125	-	-
X_A	-	-	-	-	-	160	130
Y_A	-	-	-	-	-	110	115
θ_1	-	-	-	-	-	0	90
θ_2	-	-	-	-	-	90	180
R_A	-	-	-	-	-	10	10

Table 4.2 Raw segment array

Figure 4.13 shows a moulding profile composed of seven segments, five lines and two arcs. A number was assigned to each segment based on the order they appear in the ASCII file. When the file is read, the segments are stored in a $(9 \times i)$ array where i is the number of segments. For this profile, the raw segment array is given in Table 4.2.

First of all, the missing X-Y co-ordinates of the arc endpoints are calculated from the polar co-ordinates. Then the segments, which do not belong to the face to be machined, are eliminated. These are number 2 and 3. Consequently, the remaining segments are arranged from left-to-right and the segment array became as in Table 4.3. It should be noted that in DXF files arcs are always drawn anti-clockwise. When arranging from left-to-right, co-ordinates of the end points as well as the angles should be swapped if necessary, as in the case of entities 6 and 7.

	7	5	4	1	6
X_1	120	130	145	150	160
Y_1	115	125	125	120	120
X_2	130	145	150	160	170
Y_2	125	125	120	120	110
X_A	130	-	-	-	160
Y_A	115	-	-	-	110
θ_1	180	-	-	-	90
θ_2	90	-	-	-	0
R_A	10	-	-	-	10

Table 4.3 Processed segment array

Finally, the left end of the profile is assigned to (0, 0) and all the other points are modified accordingly. Figure 4.14 illustrates the graphical representation of the final profile and Table 4.4 shows the array which is going to be the input to the controller. For this array, the term “profile array” will be used in the following sections of this text.

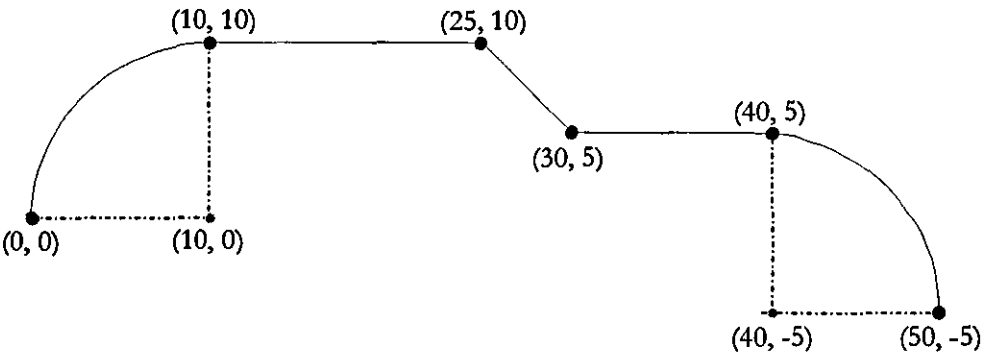


Figure 4.14 Final profile

X_1	0	10	25	30	40
Y_1	0	10	10	5	5
X_2	10	25	30	40	50
Y_2	10	10	5	5	-5
X_A	10	-	-	-	40
Y_A	0	-	-	-	-5
θ_1	180	-	-	-	90
θ_2	90	-	-	-	0
R_A	10	-	-	-	10

Table 4.4 Profile array

The *dxgread.m* function needs to be executed (i.e. `dxgread('Filename.dxf')`) in the Matlab workspace prior to the simulations in Simulink. The output of the function (i.e. the profile array) is assigned to a variable *P*, which is accessed by the *Reference Generator* presented in the next section.

4.3.3 Reference Generator

The *Reference Generator* stores the profile array P in a two dimensional look-up table and supplies the profile segments to the path controller when necessary. When the process starts, the *Reference Generator* supplies the first segment (i.e. first column of the look-up table) to the path controller and checks the distance to the end point of this segment every time the system is sampled. If the distance ($dist$) is smaller than the allowed tolerance value ($tolerance$) then the next segment is supplied.

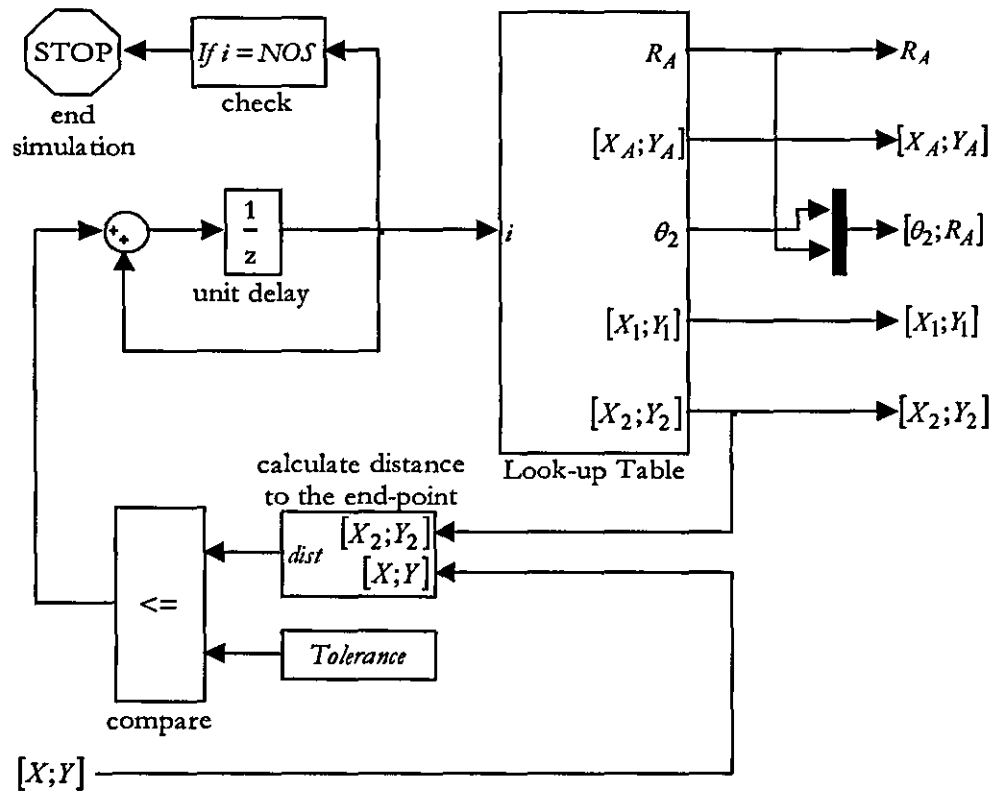


Figure 4.15 Block diagram of the *Reference Generator*

The Simulink block diagram of the *Reference Generator* is shown in Figure 4.15. The two variables i and NOS represent the look-up table column index and the number of segments in the profile respectively. Figure 4.16 shows the flowchart of the reference generator operation at each sample.

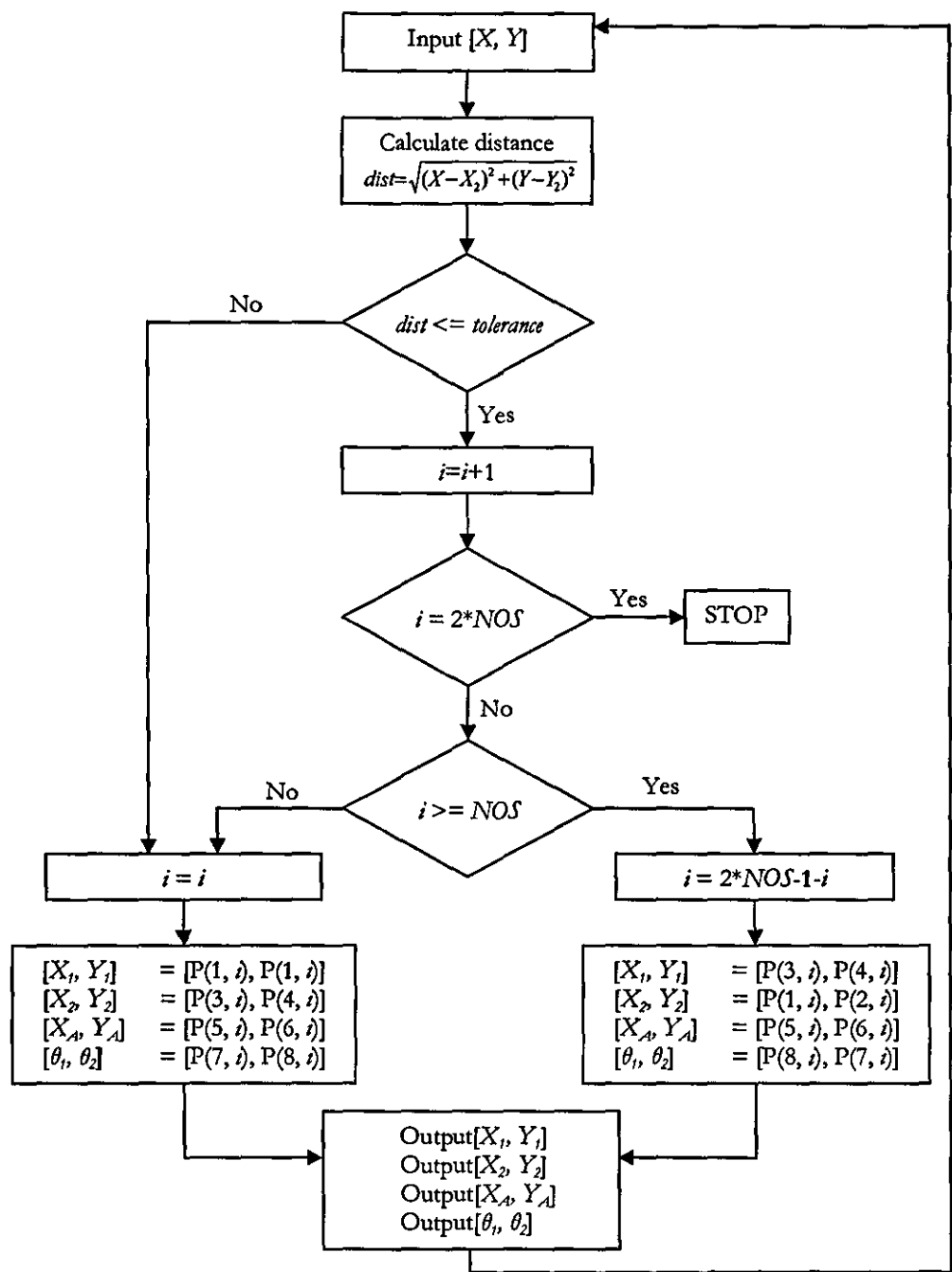


Figure 4.16 Reference generator flowchart

It should be noted that, in a Simulink look-up table, the index of the first column is zero. Therefore, the first segment is supplied when $i=0$ and, a single left-to-right pass ends when $i=NOS$. While $NOS \leq i < 2*NOS$, the motion is from right-to-left, and therefore the start and end values (i.e. $X_1, Y_1, X_2, Y_2, \theta_1, \theta_2$) of the segments are swapped.

4.3.4 Path Controller

Before presenting the details of the designed *Path Controller*, it is useful to outline the motives for this particular design.

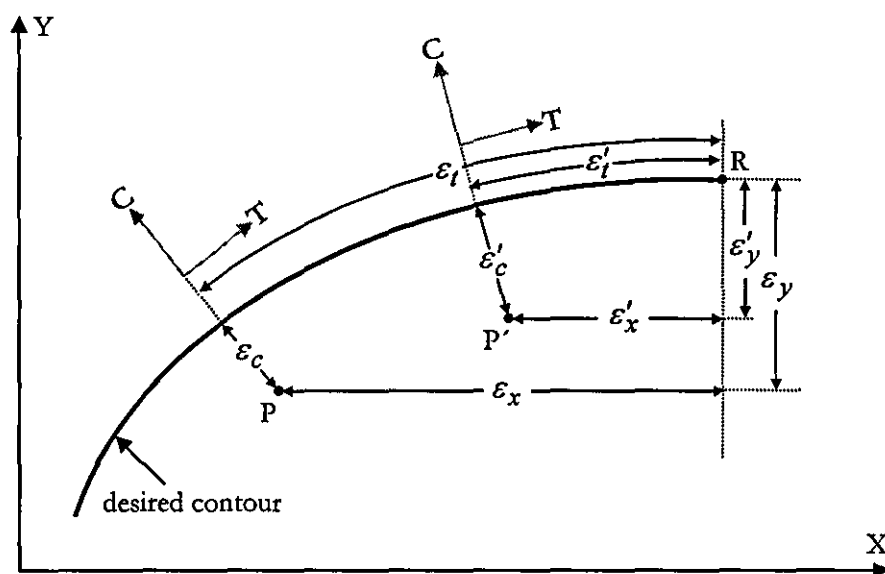


Figure 4.17 Error components for different cutter locations

Figure 4.17 illustrates a typical bi-axial (X-Y) contour tracking application. The major concerns in these applications are the tangential error ϵ_t and the contour error ϵ_c . Conventional motion controllers, discussed in Section 2.5.2 and 2.5.3, focus on the elimination of axial errors ϵ_x and ϵ_y , hence expect a reduction in ϵ_t and ϵ_c . However, this is not always the case [20]. For example, from Figure 4.17, when the actual position moves from P to P' to reach the reference position R , the axial errors as well as the tangential error reduces (i.e. $\epsilon'_x < \epsilon_x$, $\epsilon'_y < \epsilon_y$, $\epsilon'_t < \epsilon_t$) but the contour error becomes greater ($\epsilon'_c > \epsilon_c$).

The cross-coupled-controllers (CCC), presented in Section 2.5.4, employ an additional controller which compensates the axial controllers in order to eliminate the contour error ϵ_c . However, in practice, the coupled effect between the axial controllers and the CCC may cause degradation in the tracking performance, and consequently bring a difficulty in the designs of these controllers [54].

Finally, the controllers with coordinate transformation (Section 2.5.5) decouple the error dynamics into tangential and normal directions, and enable the design of the respective controllers independently of each other [54][55][56][57]. This is done through transformation between the machine frame X-Y and the trajectory frame T-C. As shown in Figure 4.17, T and C axes are, respectively, tangent and normal to the contour, so that ε_t and ε_c are the axial error components of this frame.

The designed *Path Controller* also features coordinate transformation. The trajectory coordinate frame T-C rotates around its origin to align the T-axis tangential to the target path; hence, the C-axis is always normal to the contour. The control action is directly applied on the tangential error ε_t and the contour error ε_c , which are effectively the axial error components on the T-C frame. Generally, the control action on the T-axis controls the speed along the path while the one on the C-axis controls the contour error. Unlike the other controllers of the same type, the *Path Controller* is not designed to work with time-based reference input commands. Instead, it receives the complete geometry of the target (i.e. profile segment) from the *Reference Generator*. In that respect, it is similar to the Scalar-Field Control Technique [42] described in Section 2.5.6.

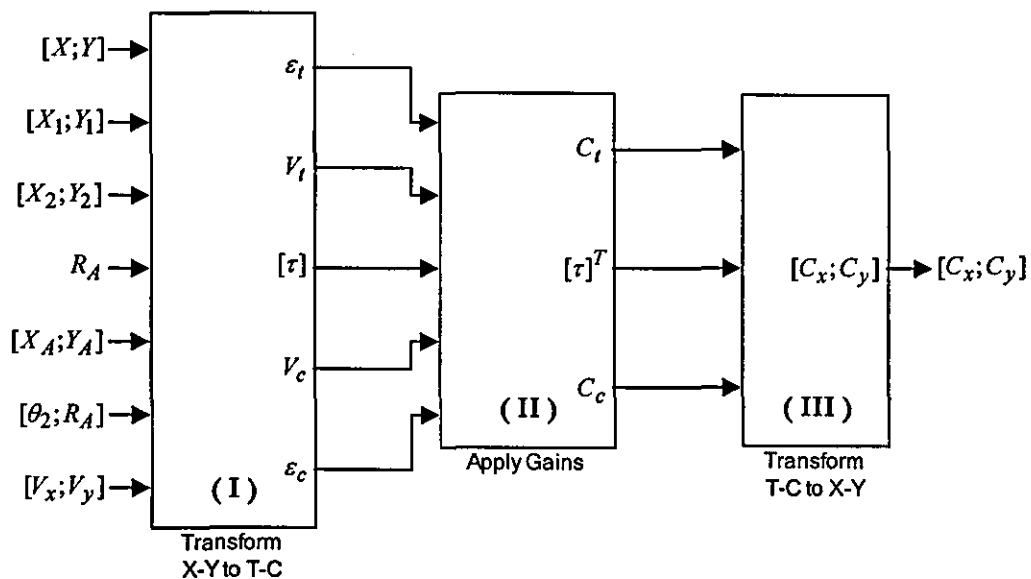


Figure 4.18 Generalized block diagram of the *Path Controller*

Figure 4.18 shows the generalized block diagram of the *Path Controller* in Simulink. Its operation principle is explained in three parts as follows:

Part I – Coordinate transformation from X-Y to T-C: Transformation from the machine coordinate frame X-Y to the trajectory coordinate frame T-C is performed by defining a transformation matrix $[\tau]$.

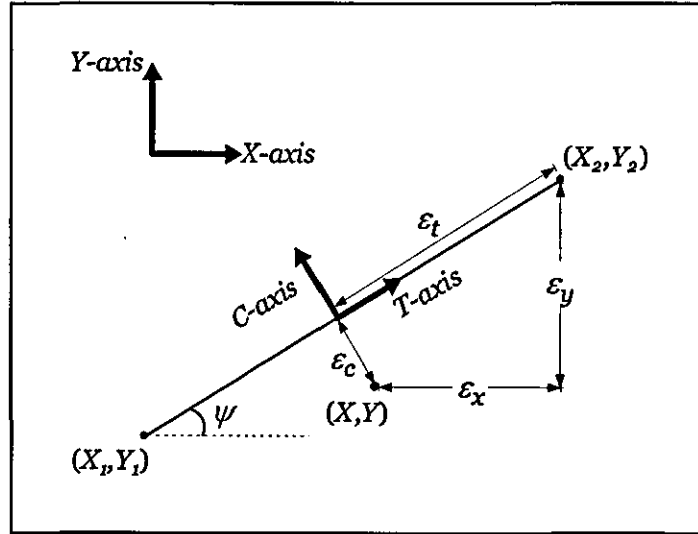


Figure 4.19 Coordinate transformation for line segments

For a line segment (Figure 4.19), the T-C frame remains fixed from the start point of the segment (X_1, Y_1) to the end point (X_2, Y_2) . Let ψ be the inclination angle between the X-Y and the T-C frames, then the transformation matrix can be defined as:

$$[\tau] = \begin{bmatrix} \cos(\psi) & \sin(\psi) \\ -\sin(\psi) & \cos(\psi) \end{bmatrix} \quad (4.15)$$

such that,

$$\begin{bmatrix} \varepsilon_t \\ \varepsilon_c \end{bmatrix} = [\tau] \cdot \begin{bmatrix} \varepsilon_x \\ \varepsilon_y \end{bmatrix} \quad (4.16)$$

If (X, Y) is the actual position at any instant, then the equations (4.15) and (4.16) can be written as:

$$[\tau] = \begin{bmatrix} \frac{X_2 - X_1}{\sqrt{(X_2 - X_1)^2 + (Y_2 - Y_1)^2}} & \frac{Y_2 - Y_1}{\sqrt{(X_2 - X_1)^2 + (Y_2 - Y_1)^2}} \\ \frac{Y_1 - Y_2}{\sqrt{(X_2 - X_1)^2 + (Y_2 - Y_1)^2}} & \frac{X_2 - X_1}{\sqrt{(X_2 - X_1)^2 + (Y_2 - Y_1)^2}} \end{bmatrix} \quad (4.17)$$

$$\begin{bmatrix} \varepsilon_t \\ \varepsilon_c \end{bmatrix} = [\tau] \cdot \begin{bmatrix} X_2 - X \\ Y_2 - Y \end{bmatrix} \quad (4.18)$$

Also, the velocities on the X-Y frame are transformed to the T-C frame by the equation (4.19). The velocity on the T-axis V_t represents the path speed, and the one on the C-axis V_c shows the rate of change of the contour error.

$$\begin{bmatrix} V_t \\ V_c \end{bmatrix} = [\tau] \cdot \begin{bmatrix} V_x \\ V_y \end{bmatrix} \quad (4.19)$$

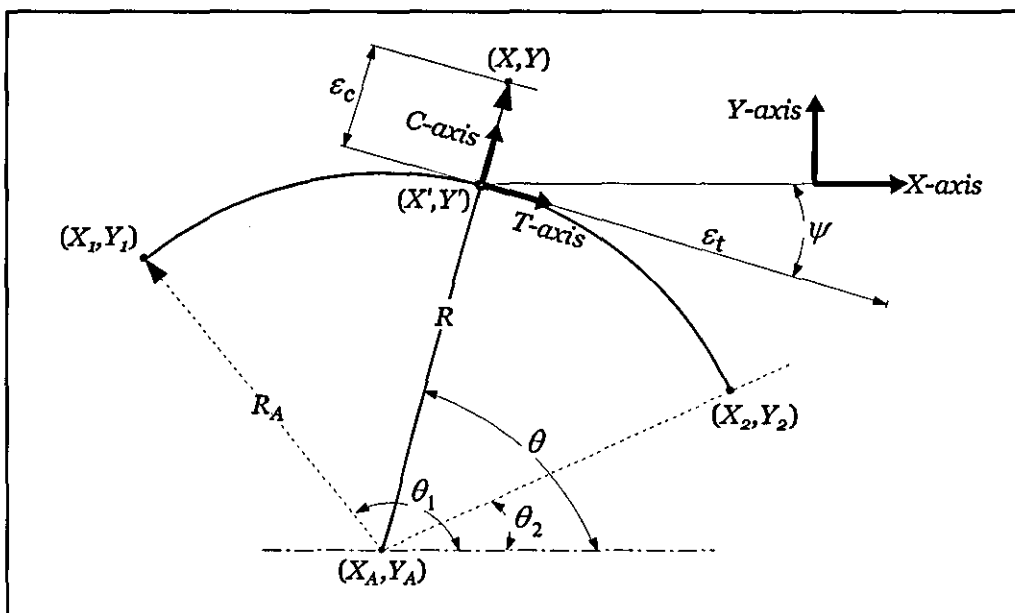


Figure 4.20 Coordinate transformation for arc segments

For an arc segment (Figure 4.20), the error components ε_t and ε_c are calculated by using the polar coordinates R and θ . However, $[\tau]$ is still defined for velocity transformation.

If (X_A, Y_A) is the centre point of the arc and (X, Y) is the actual position at any instant, then the polar coordinates R and θ are calculated by the following equations.

$$R = \sqrt{(X - X_A)^2 + (Y - Y_A)^2} \quad (4.20)$$

$$\theta = \arctan\left(\frac{Y - Y_A}{X - X_A}\right) \quad (4.21)$$

Consequently, the contour error ε_c is found from the difference between the radius of the reference arc R_A and the instantaneous radius R , and the tangential error ε_t becomes equal to the length of the arc between the points (X', Y) and (X_2, Y_2) (Figure 4.20). Equations (4.22) and (4.23) show the calculations.

$$\varepsilon_c = R_A - R \quad (4.22)$$

$$\varepsilon_t = 2 \cdot \pi \cdot R_A \cdot \frac{\theta - \theta_2}{360} \quad (4.23)$$

While tracking an arc segment, the T-C frame is not fixed as in the case of a line segment. It continuously rotates due to the changing tangent. Therefore, $[\tau]$ has to be re-defined at every sample. The formulation for $[\tau]$ is the same as in the equation (4.15), but the inclination angle ψ is determined as follows:

$$\psi = \theta - 90^\circ \quad (4.24)$$

where, θ is the polar coordinate of the actual position (X, Y) at any instant. Once $[\tau]$ is defined, the velocity transformation is also the same as in the case of line segments (4.19).

Part II – Application of the controller gains: After the coordinate transformation, the *Path Controller* turns into a simple proportional position controller, in which the position error components ε_t and ε_c are multiplied by the gains $K_p T$ and $K_p C$ respectively. This is shown in the following equation (4.25), where C_t and C_c are the controller outputs on the T-C frame.

$$\begin{bmatrix} C_t \\ C_c \end{bmatrix} = \begin{bmatrix} KpT & 0 \\ 0 & KpC \end{bmatrix} \times \begin{bmatrix} \varepsilon_t \\ \varepsilon_c \end{bmatrix} \quad (4.25)$$

Alternatively, the position loop can be extended to be a cascaded position-velocity loop by using also the transformed velocities V_i and V_o . The equation of the cascaded design is as follows:

$$\begin{bmatrix} C_t \\ C_c \end{bmatrix} = \begin{bmatrix} KvT & 0 \\ 0 & KvC \end{bmatrix} \times \left(\left(\begin{bmatrix} KpT & 0 \\ 0 & KpC \end{bmatrix} \times \begin{bmatrix} \varepsilon_t \\ \varepsilon_c \end{bmatrix} \right) - \begin{bmatrix} V_t \\ V_c \end{bmatrix} \right) \quad (4.26)$$

where, $K_v T$ and $K_v C$ are proportional velocity gains. Figure 4.21 shows the Simulink block diagram that can be used with both control methods. The preferred method is selected manually via the Switch blocks.

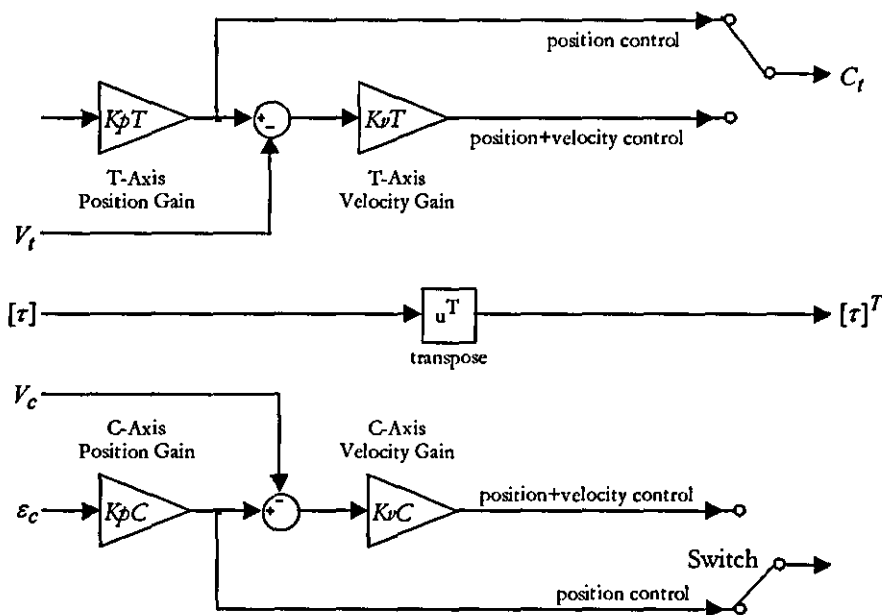


Figure 4.21 Block diagram for the application of the controller gains

Part III – Coordinate transformation from T-C to X-Y: This is the final part of the *Path Controller*. The controller output on the T-C frame is transformed back to the X-Y frame and sent to the drives. Equation (4.27) shows the transformation.

$$\begin{bmatrix} C_x \\ C_y \end{bmatrix} = [\tau]^T \cdot \begin{bmatrix} C_t \\ C_c \end{bmatrix} \quad (4.27)$$

The next section discusses the software simulations performed in Matlab/Simulink.

4.4 Simulations

This section presents the Matlab/Simulinks simulations.

4.4.1 Actuator selection for the simulated system

In order to select the DC motors and the leadscrews of the X and Y axis drives, the market is researched for the available options. Within the complete range of products, the sizes of the considered ones are categorized as miniature. For the miniature DC servo-motors, there are plenty of manufacturers; whereas for the leadscrews this is not the case. Therefore, the leadscrews are selected first and the motors are sized accordingly.

Diameter (mm)	Lead (mm)	Efficiency (%)
6.35	1	40
	1.5	52
	2	59
	3	68
	10	78

Table 4.5 Miniature anti-backlash leadscrews from Reliance Ltd. [90]

Reliance Ltd. [90] offers a range of miniature anti-backlash leadscrews. The available leads and the corresponding efficiencies are given in Table 4.5. At smaller leads, the efficiency is lower due to increased friction, whereas higher leads produce less thrust force for a given input torque. Also, very high leads (i.e. 10mm) introduce back-driving effect; which is not desirable for the vertical drive, since the drive's weight could back-drive the leadscrew. As a result, leadscrews with 3 mm leads are chosen for the horizontal and vertical drives.

In Section 4.2.1, the path mean speed is targeted to be 135 mm/s. Accordingly, DC servo-motors, which can achieve a maximum speed of 400 mm/s with the selected leadscrews, are shortlisted (Table 4.6) from Portescap [91] and Maxon [92].

		Escap 25GST2R82 – 216P	Escap 25GT2R82 – 219P	Maxon RE30 268214	Escap 30GT2R82 – 234P
Rated power	W	27	40	60	83
Nominal voltage	V	12	12	24	18
No load speed	rpm	11300	9500	8810	8500
Stall torque	Nm	0.150	0.246	1.020	0.758
Max. cont. torque	Nm	0.027	0.043	0.087	0.087
Weight	g	111	145	238	310

Table 4.6 Shortlisted DC motors

Since all of the shortlisted motors satisfy the speed requirement, the selection is based on the torque characteristics and weight. The motor weight is important because one of the drives is carried by the other. As can be seen in Table 4.6, the weight is almost directly proportional to the rated power. The Maxon RE30 stands out with superior torque characteristics. Compared to the Escap 30GT2R82 it delivers 25% more stall torque and weighs 22% less. Also compared to the Escap 30GT2R82, despite being 65% heavier, it delivers four times greater stall torque, and two times more continuous torque. Consequently, the Maxon RE30 is selected for the horizontal and vertical drives.

4.4.2 Simulation parameters and inputs

parameter			horizontal drive value	vertical drive value
D/A limit			± 8192	± 8192
D/A gain	(V)	K_d	10/8192	10/8192
amplifier gain	(V/V)	K_a	2.4	2.4
current limit	(A)	I_{lim}	± 4	± 4
armature inductance	(H)	L_m	0.00012	0.00012
armature resistance	(Ohm)	R_m	0.582	0.582
motor torque constant	(Nm/A)	K_t	0.026	0.026
motor back-emf constant	(Vs/rad)	K_e	0.026	0.026
leadscrew efficiency		e	0.68	0.68
leadscrew gain	(m/rad)	R_s	0.000477	0.000477
equivalent inertia	(kgm ²)	J	3.62×10^{-6}	3.65×10^{-6}
equivalent damping coeff.	(Nms/rad)	B	1.25×10^{-5}	1.25×10^{-5}
carriage mass	(kg)	M	0.3	1
cutting force	(N)	F_c	5	5

Table 4.7 Simulation parameters

Simulations are performed with the parameters listed in Table 4.7. The motor and leadscrew values are taken from manufacturer's data. The equivalent damping coefficients and the carriage masses estimated. The cutting force acting on the horizontal drive is approximated as a constant force opposing the direction of motion (4.28). For the vertical drive, it is assumed that the cutting force is acting only when the drive is moving downwards (i.e. $-Y$ direction). The external force on the vertical drive also includes the weight of the vertical carriage (4.29).

$$F_{eH} = \begin{cases} -F_c \cdot \text{sgn} \dot{x} & , \dot{x} \neq 0 \\ 0 & , \dot{x} = 0 \end{cases} \quad (4.28)$$

$$F_{eV} = \begin{cases} -M_c V \cdot g & , \dot{y} \geq 0 \\ F_c - M_c V \cdot g & , \dot{y} < 0 \end{cases} \quad (4.29)$$

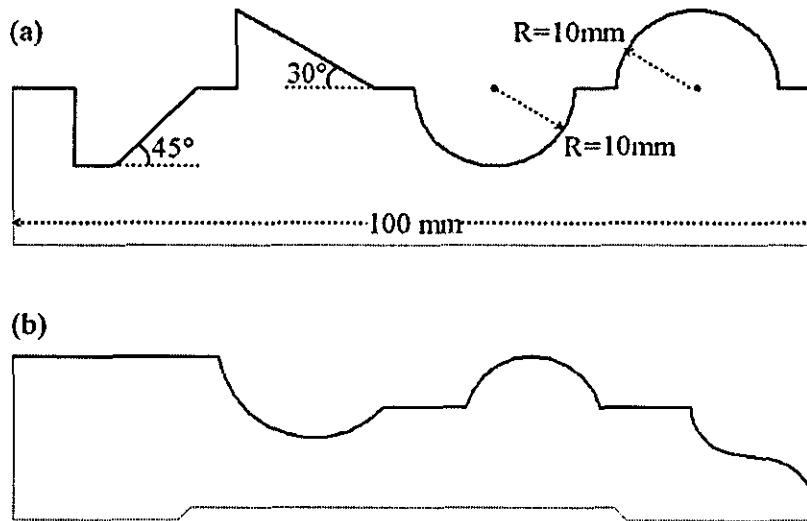


Figure 4.22 Simulation inputs (a) test profile (b) real moulding profile

Two input profiles are used in the simulations. The first one, shown in Figure 4.22(a), is a purpose generated test profile, and it is designed to assess the system performance on profile segments with different geometries such as:

- ◆ horizontal lines
- ◆ vertical lines
- ◆ sloped lines
- ◆ concave arcs
- ◆ convex arcs

The *Path Controller* is tuned through the simulations on the test profile. The final settings are tested on a real moulding profile (Figure 4.22(b)) for verification. The next section presents and discusses the simulation results.

4.4.3 Simulation Results

A single left-to-right pass, along the profile width, is simulated in Simulink. The controllers are tuned in order to achieve the following targets:

- ♦ Primary target: Accuracy ($\varepsilon_c \leq 0.1$ mm)
- ♦ Secondary target: Speed ($v_{mean} \geq 135$ mm/s)

Initially, the *Path Controller* is switched to proportional position controller mode as in (4.25), and the gains $K_p T$ and $K_p C$ are tuned by guided trial-and-error. Figure 4.23(a) shows the resultant profile, where the end-points of the profile segments are indicated with “▲” and “▼” for clarity.

In Figure 4.23(b), the contour error ε_c is plotted against the horizontal position X . The maximum contour error (i.e. ε_{max}) is 0.1 mm, therefore the accuracy target is met. The error spikes are expected due to the *tolerance* value in Table 4.7. They represent the segment end-points, where the *Reference Generator* supplies the next segment to the *Path Controller*.

The path speed V_t is plotted in Figure 4.23(c) against the horizontal position X . This allows better observation of the velocity behavior on most of the profile segments. On the other hand, the velocity on the two vertical segments appears as spikes. Since the velocity is not controlled in this simulation, the system is accelerated to greater speeds on longer segments. The maximum speed is recorded as 306 mm/s, however, the mean path speed v_{mean} stayed at 22.27 mm/s, which is six times slower than the targeted value.

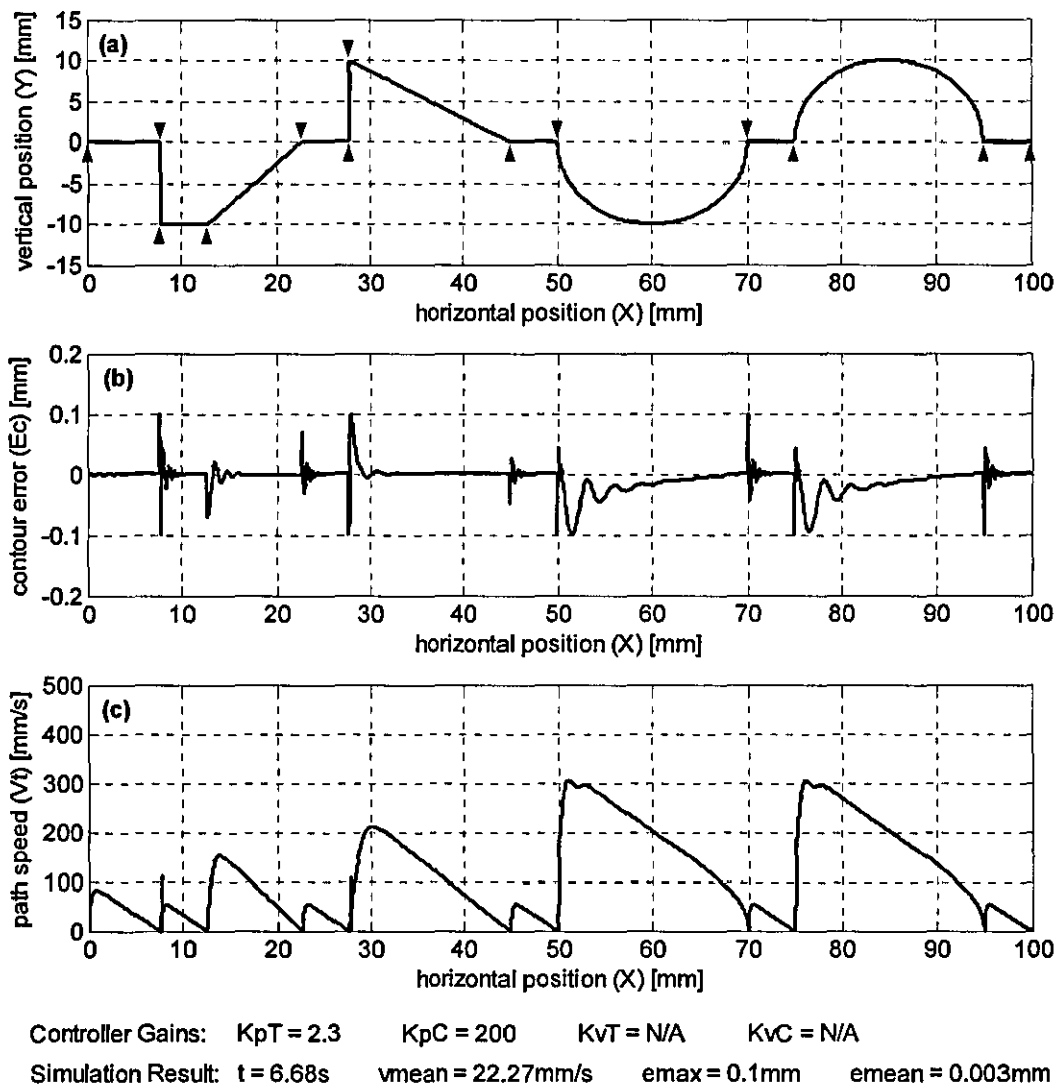


Figure 4.23 Simulation results: Initial performance (a) test profile (b) contour error vs. horizontal position (c) path speed vs. horizontal position

For the second simulation, the *Path Controller* is switched to cascaded position-velocity mode. Also, the path speed V_t is limited to 175 mm/s. The result is shown in Figure 4.24.

Contour error plot in Figure 4.24(b) indicates a very smooth tracking performance. The maximum contour error is recorded as 0.09 mm, hence, the accuracy target is met. As can be seen in Figure 4.24(c); limiting the maximum speed allowed the drives to decelerate later, therefore, the mean path speed v_{mean} is increased to 138.51 mm/s, and the speed target is also achieved.

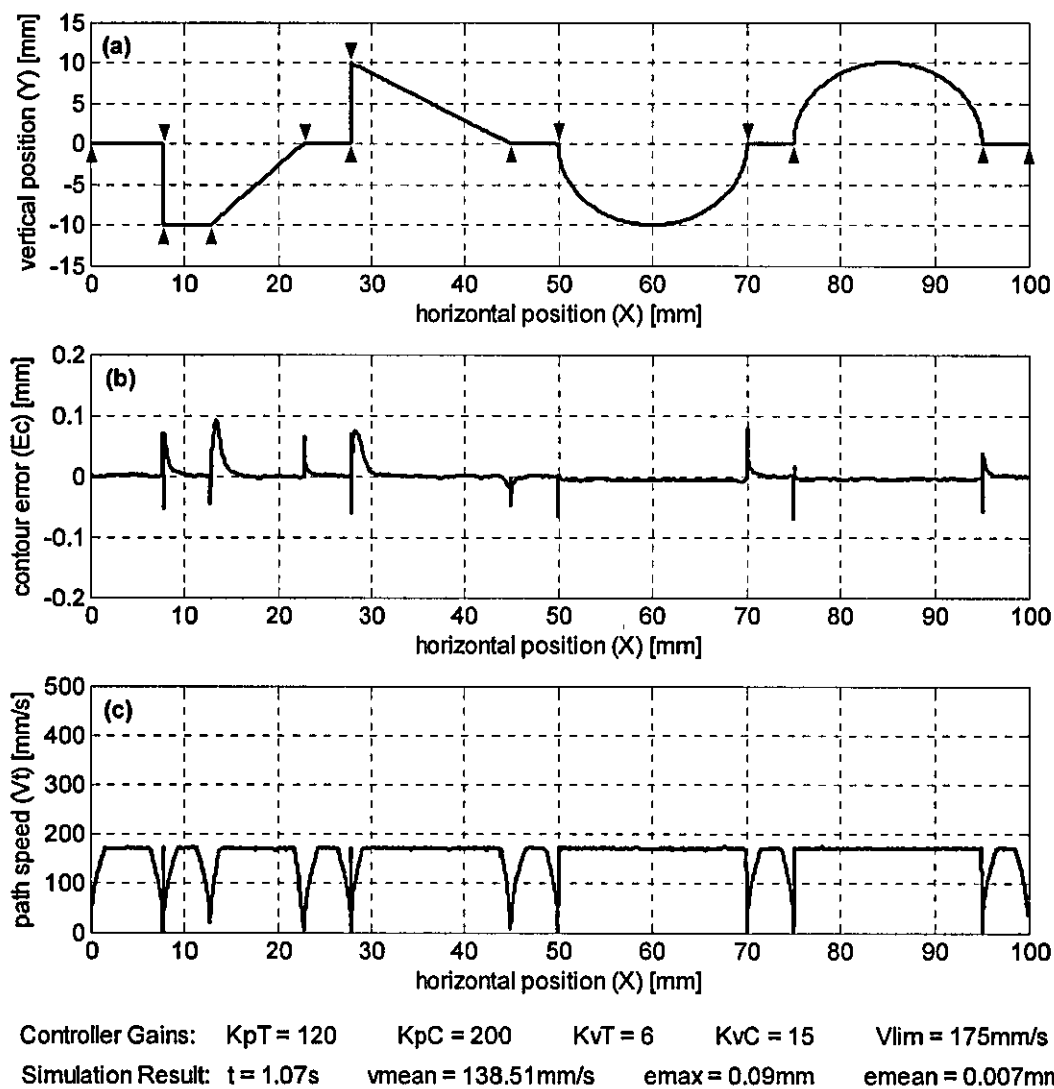


Figure 4.24 Simulation results: Cascaded controller and velocity limit (a) test profile (b) contour error vs. horizontal position (c) path speed vs. horizontal position

As mentioned previously, some of the friction losses in the system are taken into account in the Simulink model by including the leadscrew efficiency e . This, however, only represents the dynamic (i.e. Coulomb) friction. In the actual system, static friction (i.e. Stiction) also exists and may cause tracking errors when one of the drives encounters zero velocity crossings. For example; while tracking the semi-circles in Figure 4.24(a), the vertical drive crosses zero velocity at $X=60 \text{ mm}$ and $X=85 \text{ mm}$, whereas the horizontal drive does not. If static friction was present in the simulation, it might have caused relatively large contour errors referred to as “quadrant glitches” [93]. In the actual system, this is prevented

either by friction compensation, which requires friction model and identification; or by splitting the semi-circles into two segments so that both drives stop when one of them changes direction. The latter option is simulated and the result is given in Figure 4.25.

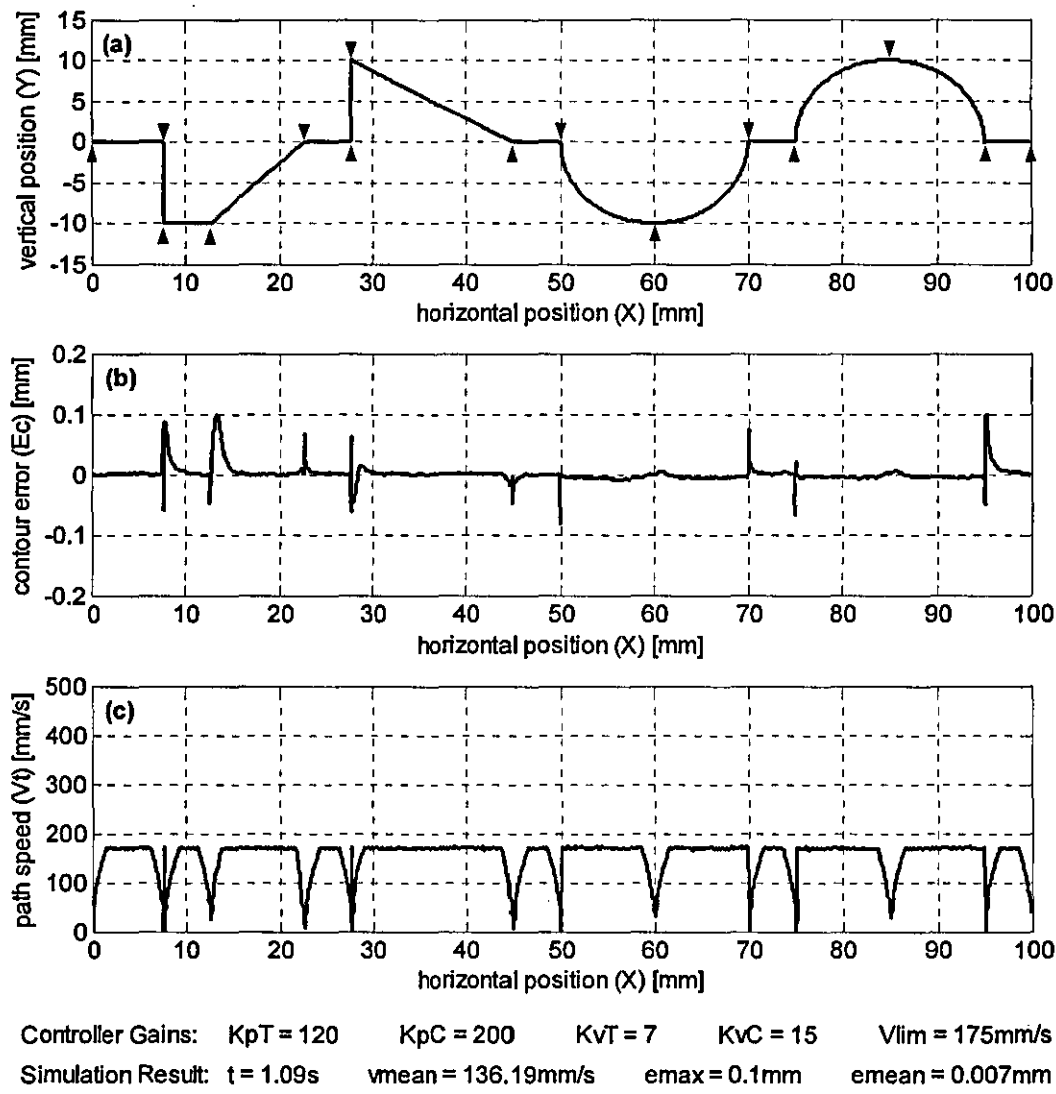


Figure 4.25 Simulation results: Cascaded controller, velocity limit, and split arcs (a) test profile (b) contour error vs. horizontal position (c) path speed vs. horizontal position

Splitting the two semi-circles resulted in two more points to stop (i.e. $X=60$ and $X=85$ in Figure 4.25(a)); consequently, the mean path speed is reduced. However, this reduction is kept at minimum by increasing the tangential velocity gain K_{vT} .

As a result, speed and accuracy targets are still achieved on the profile with split arcs.

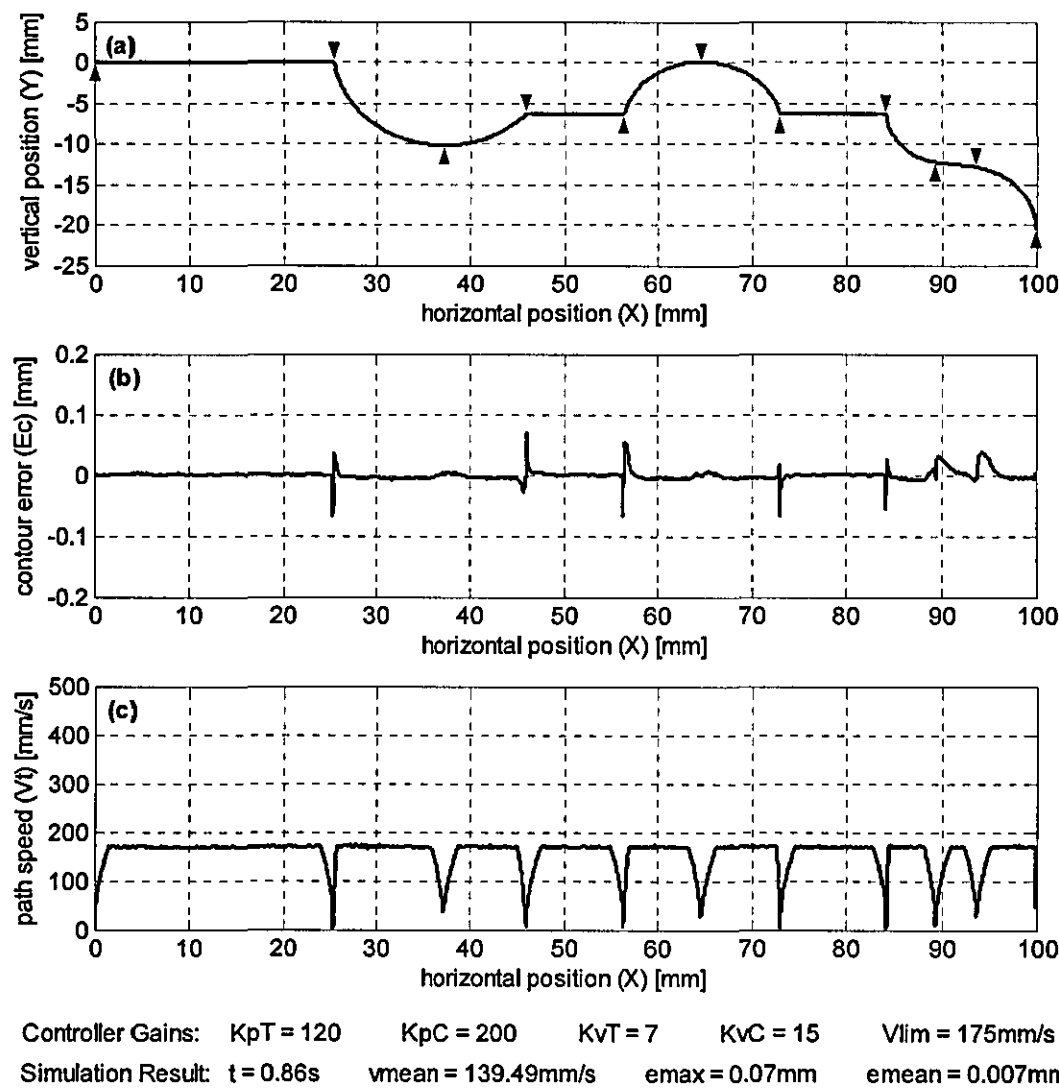


Figure 4.26 Simulation results for the real moulding profile (a) moulding profile (b) contour error vs. horizontal position (c) path speed vs. horizontal position

Finally, the input is changed to the real moulding profile in Figure 4.22(b), and the system is simulated with the same controller parameters as in the previous simulation. The result in Figure 4.26 shows a very smooth tracking performance and the simulation meets both targets with a maximum contour error of 0.07 mm and a mean path speed of 139.49 mm/s.

Overall, the simulation results confirm the feasibility of the PIMM concept and show that the target path speed of 135 mm/s, which corresponds to a production rate of 0.15 m/min, can be achieved with contour errors less than 0.1 mm.

4.5 Summary

This chapter is aimed at bringing the profile independent wood-moulding machine from an idea to the detailed design stage. The system is studied in two main parts.

The first part is the electro-mechanical hardware and it includes X, Y and Z axis drives. The X and Y axis drives are responsible for cutter positioning, which is the essential part of the PIMM concept. Dynamics of the X and Y axis drives determine the production speed and the geometric accuracy of the moulding. Firstly, the expected performance in terms of speed and accuracy is identified. Production rate for a 100 mm wide moulding with acceptable quality (i.e. surface wave pitch $p=2.5$ mm) is targeted as 0.15 m/min. For this target, the mean tracking speed along the path corresponds to 135 mm/s. Also, the measure for the geometric accuracy is chosen to be the contour error, and the maximum value is targeted as 0.1 mm. Secondly, actuator alternatives are evaluated for the X and Y axis drives. DC motor-leadscREW drives emerged as the best option. Consequently, mathematical models are derived and implemented in Simulink.

The second part of the system includes the control structure and algorithms. In this part, firstly it is decided to input desired profile geometry from CAD files in DXF format. Also, algorithms are presented for extracting profile data from DXF files. The extracted profile data is stored in the *Reference Generator* which governs the top-level coordination of the machine drives. The designed *Path Controller* synchronizes the X and Y axis drives to produce the desired profile.

Finally, the system is simulated and the results confirmed the feasibility of the PIMM concept. Moreover, it was shown that the targeted performance can be achieved.

Chapter 5

PIMM Test Rig

5.1 Introduction

This chapter deals with some design aspects of the PIMM test rig that has been designed and built in order to investigate feasibility and effectiveness of the new concept.

Firstly, in Section 5.2, some mechanical design aspects are covered. Then in Section 5.3, the employed control hardware is explained. Two different software applications were designed for the PIMM test rig. The first one, covered in Section 5.4, is based on Simulink Real-Time Windows Target prototyping environment and it is mainly for mathematical model validation and system identification purposes. The second one is currently the main application for the test rig and it is designed in Visual Basic 6, and presented in Section 5.5. Finally in Section 5.6; future plans on the PIMM test rig, which will be applied during an innovation fellowship following this research work, are summarized.

5.2 Mechanical Design

In designing the test rig, a modular approach has been followed. The test rig is divided to four sub-systems as cutter assembly, horizontal drive, vertical drive, and timber feed drive which also acts as the frame of the machine. This modular design approach allowed different designs of one or more subsystems to be experimented while the rest of the test-rig remain unchanged.

Prior to the design of the individual sub-systems, a thorough investigation on the commercially available hardware components (i.e. power transmission, linear motion products) had been performed. Feasible alternatives were evaluated with the criteria being various properties such as size, weight, accuracy, and cost.

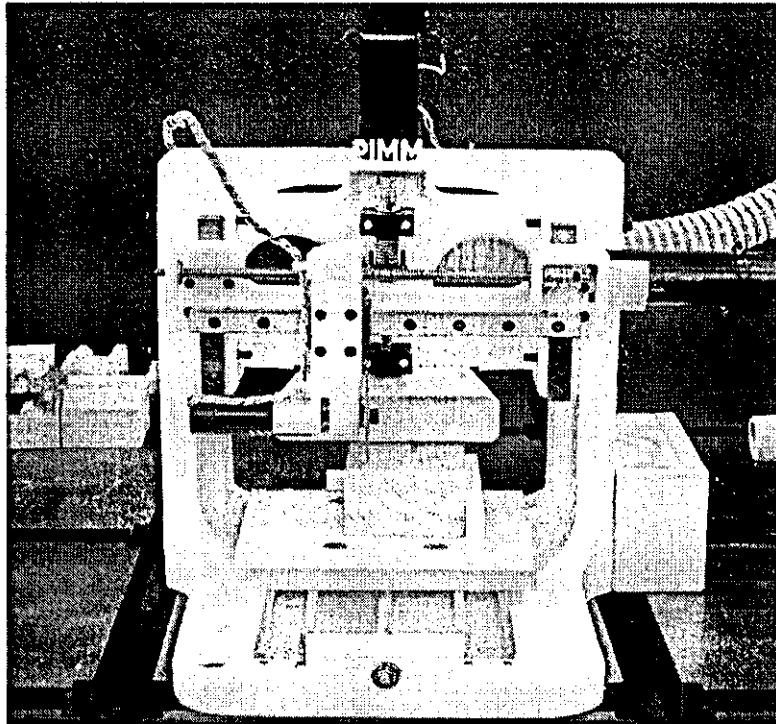


Figure 5.1 PIMM test-rig

Small magnitudes of the forces generated in the process allowed the use of rapid prototyping plastics for various parts of the test-rig. With the help of rapid prototyping, the initial build time of the test-rig and also the modification times were considerably shortened.

The test rig is designed only to accommodate small test specimens. Longer workpiece lengths are not considered. Also, suitable off-the-shelf cutters are used and dedicated cutter design has not been performed.

Figure 5.1 shows a picture of the most recent test-rig. Some previous designs are given in Appendix D. The remainder of this section deals with the test-rig sub-systems.

5.2.1 Cutter assembly (θ -Axis)

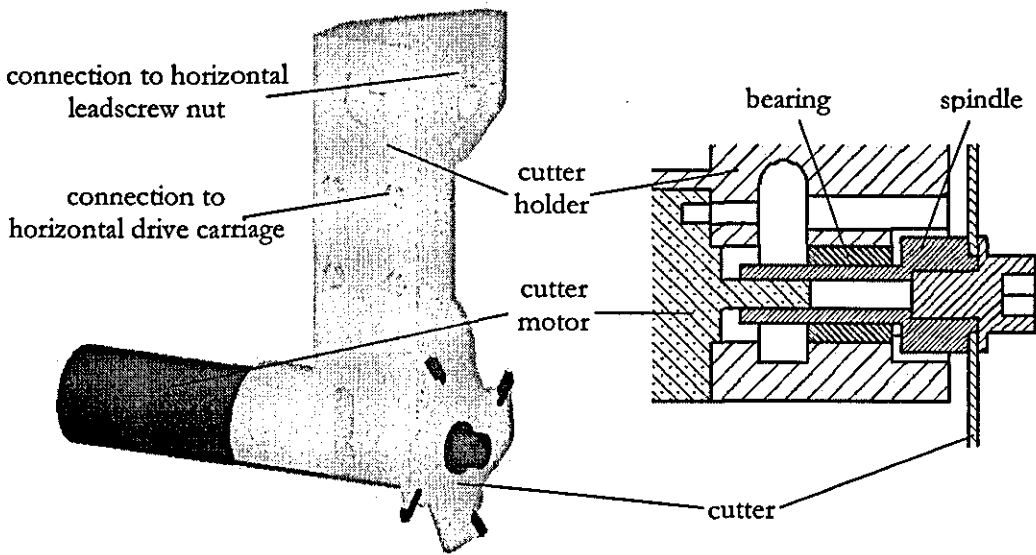


Figure 5.2 Cutter assembly

An overhung spindle arrangement was employed for the cutter assembly as depicted in Figure 5.2. This arrangement was chosen mainly for its simplicity. A 4-tooth slotting saw having 50.8 mm diameter and 1.6mm kerf is located on the overhung end of the spindle which is connected directly to the motor shaft. The Maxon EC22 brushless DC motor rotates at up to 22000 rpm at 32 VDC and delivers a power of 50 W. Full specifications of the cutter motor is given in Appendix E. It was aimed to minimize the moving mass in the system and therefore, considering the small cutting forces, the cutter holder is made from rapid prototyped (SLS) nylon.

In this arrangement, the maximum depth of cut is equal to the difference between motor radius and cutter radius, and in this case 14.4 mm. Deeper cuts can be produced by using a larger diameter cutter. Alternatively, the motor can be located away from the cutter, i.e. on top of the cutter holder, and transmission such as belt/pulley can be employed between the motor and the cutter.

The cutter assembly connects to the horizontal axis drive carriage and the horizontal leadscrew nut as shown in Figure 5.2 and Figure 5.3.

5.2.2 Horizontal drive (X-Axis)

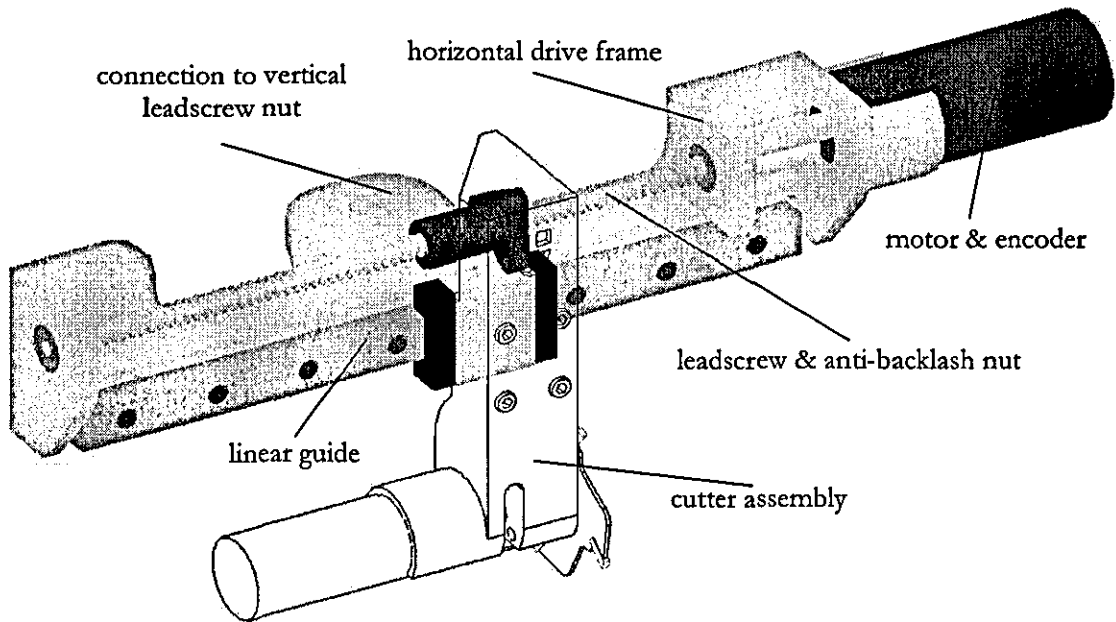


Figure 5.3 Horizontal drive

The horizontal drive consists of a motor, leadscrew, linear guideway and a frame (Figure 5.3). The Maxon RE30 permanent magnet DC motor is rated 60W, and the maximum speed and torque values are, respectively, 8800 rpm and 1 Nm at 24 VDC. A flexible shaft coupling connects the motor to a leadscrew with 3 mm lead which is coupled with an anti-backlash nut. The precision linear guide carriage, together with the leadscrew nut, attaches to the cutter assembly and carries it along the horizontal axis. All the components connect to the drive frame which is

made of rapid prototyped (i.e. SLS) nylon. Full specifications of the drive hardware can be found in Appendix F.

The maximum travel of the cutter assembly along the horizontal axis is 120 mm and its position is controlled closed-loop. Position feedback is obtained from an incremental encoder which is attached to the motor shaft. The HEDS 5540 encoder is capable of 2000 quadrature counts per revolution.

Table 5.1 lists some important parameters of the horizontal drive. Detailed calculations of these parameters are provided in Appendix G.

Parameter	Value
Maximum travel (mm)	120
Maximum linear speed (mm/s)	440
Maximum continuous thrust (N)	123
Translating mass (kg)	0.25
Rotating inertia (kgm^2)	3.61e^{-6}

Table 5.1 Horizontal drive parameters

The horizontal drive is carried by the vertical axis drive, which is presented in the next section.

5.2.3 Vertical drive (Y-Axis)

The vertical drive shown in Figure 5.4 contains the same hardware components (i.e motor, encoder, leadscrew, linear guide) as the horizontal drive (see Appendix F). The operation principle is also the same except the leadscrew runs in the centre of two linear guides. Additionally, the drive features a dust extraction nozzle which connects to a suction pipe behind the drive frame. Even a vacuum cleaner can be used as the dust extractor. Some important parameters of the vertical drive are shown in Table 5.2, and detailed calculations are given in Appendix G.

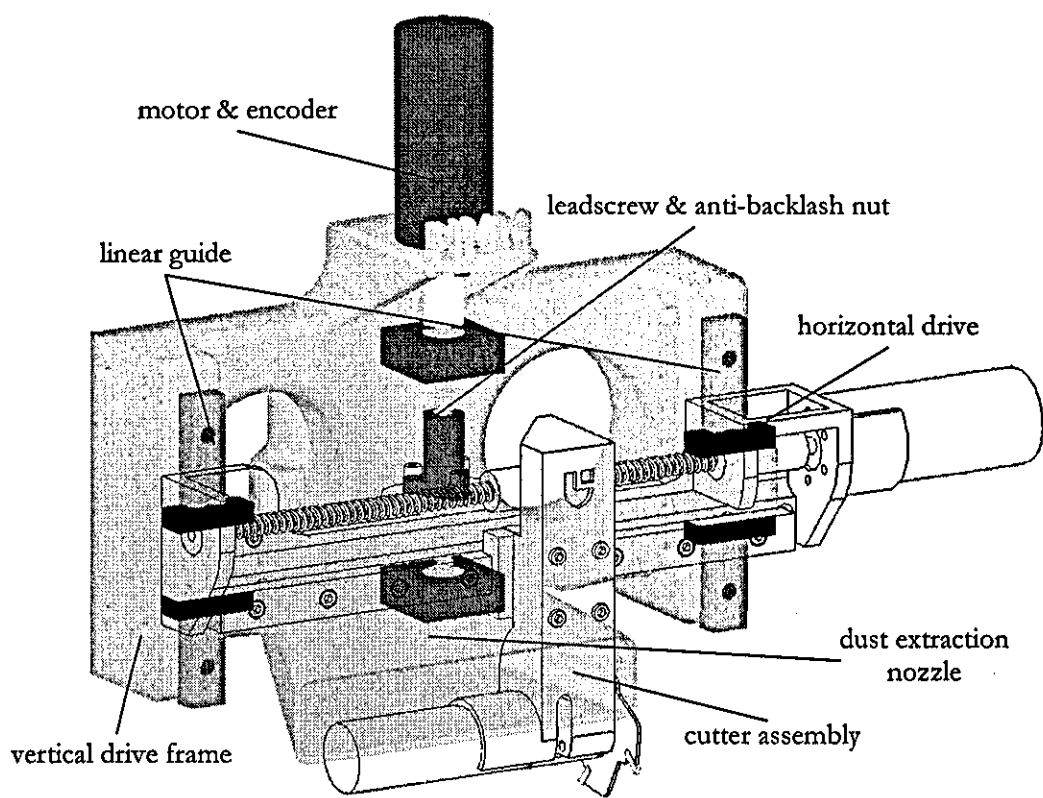


Figure 5.4 Vertical drive

Parameter	Value
Maximum travel (mm)	30
Maximum linear speed (mm/s)	440
Maximum continuous thrust (N)	123
Translating mass (kg)	0.9
Rotating inertia (kgm ²)	3.63e ⁻⁶

Table 5.2 Vertical drive parameters

5.2.4 Timber feed drive (Z-Axis) and machine frame

Timber feed drive in Figure 5.5 is designed as a temporary solution in order to develop the PIMM concept. It accommodates small timber specimens, up to 100 mm long, which are screwed onto the mounting plate. The mounting plate bolts to the feed table, and they are driven by a stepper motor and leadscrew arrangement. The maximum feed speed achieved by the drive is 5 mm/s. Although this value is lower than the target speed of 25 mm/s (see Section 4.2.5), it is sufficient for the proof-of-concept investigations. Full specifications of the drive hardware can be found in Appendix H.

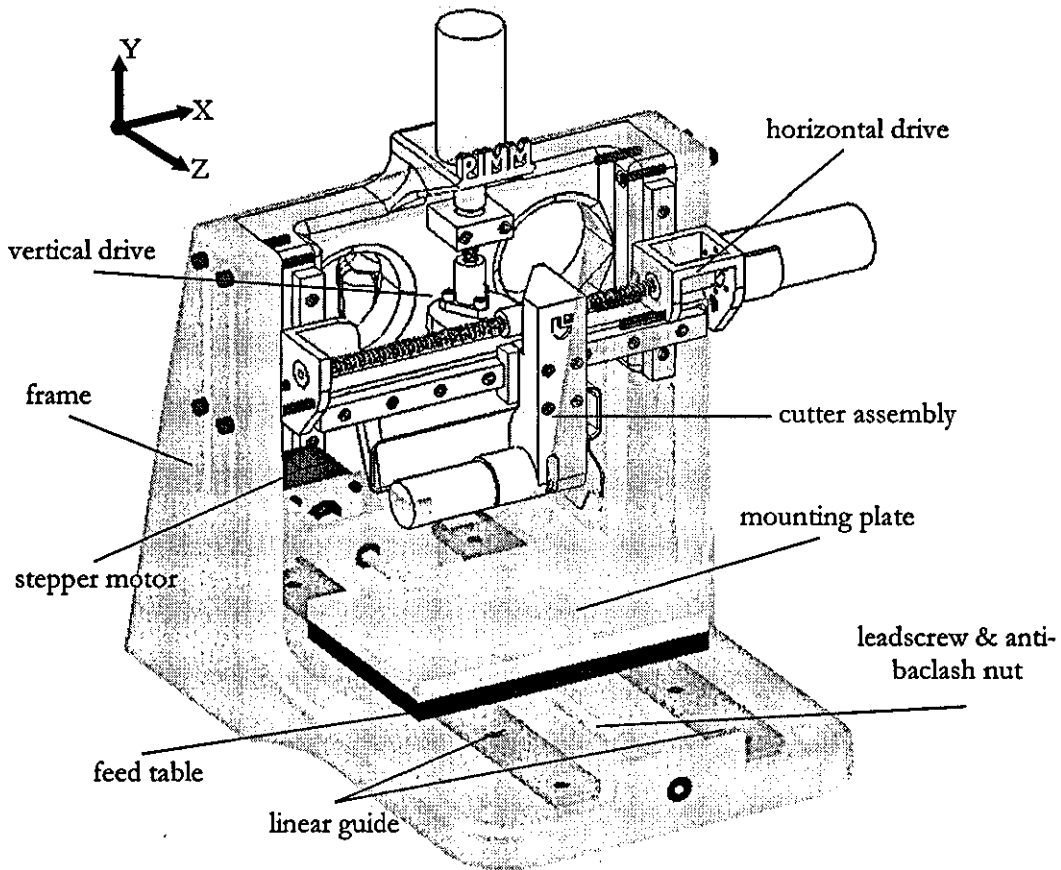


Figure 5.5 Timber feed drive and machine frame

The frame is constructed in single piece from rapid prototyped (SLS) nylon and acts as the main machine frame. The vertical drive is placed in between the side walls as shown in Figure 5.5, and it can be moved up and down in order to adjust for different workpiece heights up to 50 mm. After the adjustment, it is fixed in place by tightening the four bolts on either side of the main frame.

The maximum dimensions of the fully assembled test rig are 300 mm, 350mm and 360 mm on X, Y and Z directions respectively. The test rig can be defined as a miniature moulding machine. In its current state, timber specimens having up to 100 mm width, 100 mm length and 50 mm height can be machined with a maximum depth of cut of 14.4 mm. Some photographs, animations and videos of the test rig are provided in the accompanying CD (Appendix M). The following sections of this chapter deal with the control hardware and software of the system.

5.3 Control Hardware

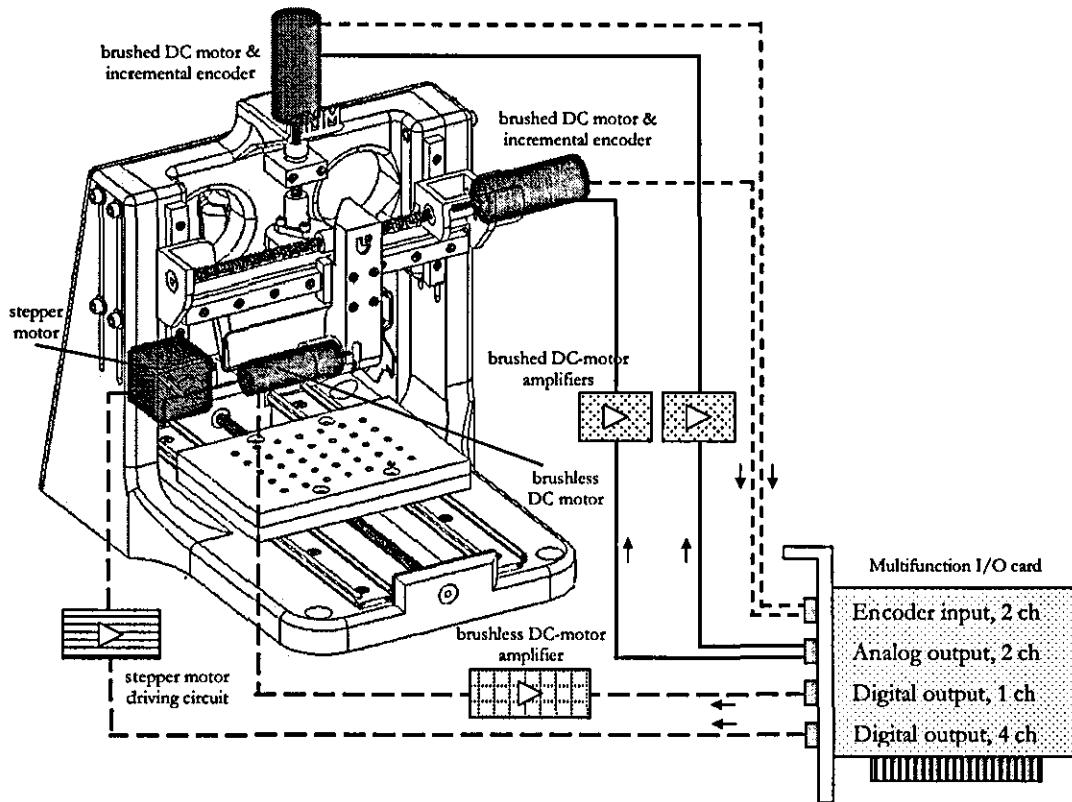


Figure 5.6 System diagram

The system diagram of the test rig shown in Figure 5.6 illustrates all key components of the instrumentation along with the signal flow between the test rig and the control computer which is represented by the multifunction I/O card. Control hardware is divided into two groups. The first group covers the control computer and the multifunction I/O card, and the second group includes driving amplifiers for the motors.

5.3.1 Control computer and multifunction I/O card

Control computer is used to acquire readings from the incremental encoders and to send out signals to the motor driving amplifiers. Horizontal (X-axis) and vertical (Y-axis) drives operate in closed loop; a control algorithm adjusts the input voltage to the motor driving amplifiers according to the encoder readings in real time. The control computer also allows logging encoder readings during

operation, in order to display and evaluate system performance. Timber feed drive (Z-axis) stepper motor is controlled open loop, where the control computer sends out the number of steps necessary to achieve the required timber feed. However, the operation of the timber feed drive is synchronized to the horizontal and vertical drives. Timber feed only takes place when the X and Y axis drives stop after each pass along the width of the workpiece. Finally, an on/off control is employed for the cutter drive. When started, the cutter motor runs at the speed that is set in the drive amplifier hardware.

The control computer is a standard PC with Pentium III 800 MHz processor and 256 MB memory, running Windows 2000 operating system. The biggest advantage of using a standard PC as the controller is the ease of implementation, modification and testing of the desired control logic. Moreover, appealing graphical user interfaces (GUI) can be designed together with powerful algorithms by using various software tools. Also, as a result of rapid advancements in computer technology; a PC like the one being used, which is sufficient for the purposes of this system, is inexpensive.

The communication between the control computer and the drives is done via interface hardware providing analog and digital I/O. In choosing the interface hardware, it was decided to use a multifunction PC card which is flexible in terms of both the hardware capabilities (I/O) and software compatibility. A Sensoray Model 626 PCI multifunction I/O card is selected and installed in the control computer. The following lists the reasons for choosing this particular card.

- ◆ Compatibility with Windows, Linux, QNX.
- ◆ Compatibility with Visual Basic, C, Simulink Real-Time Windows Target and Simulink xPC Target.
- ◆ All in one card; satisfies all the requirements of the current system.
- ◆ Extra resources (i.e. digital and analog I/O) available for future development of the system

- ♦ Reasonable cost; under £400.

Interface	Parameter	Description
Bus	Type	PCI, 32-bit, 33 MHz
Digital I/O	Number of channels	48 (each channel can be either input or output)
Encoder	Input characteristics	Differential pair/TTL/CMOS compatible
	Counter size	24 bits
	Number of channels	6
D/A	Resolution	14 bits including sign
	Output range	± 10 V
	Number of channels	4
	Conversion time	Approximately 200 μ s/channel

Table 5.3 I/O card specification [94]

Interface	Port Number	Allocation
D/A	0	Vertical drive motor (Y-Axis)
	3	Horizontal drive motor (X-Axis)
Encoder	0	Horizontal drive encoder (X-Axis)
	1	Vertical drive encoder (Y-Axis)
Digital I/O	0	Cutter motor
	20, 21, 22, 23	Timber feed drive stepper motor (Z-Axis)

Table 5.4 Allocation of the I/O ports

Table 5.3 lists the details of Sensoray 626 interfaces that are used by the system (see Figure 5.6). Allocation of the individual I/O ports to the test-rig hardware is given in Table 5.4. Full specification of Sensoray 626 can be found in Appendix I.

5.3.2 Driving amplifiers

Power amplifiers drive the axis motors according to the signals they receive from the control computer. For the permanent magnet DC motors of the X and Y axis drives, Maxon ADS 50/5 4-Q-DC pulse width modulated (PWM) servoamplifiers are used. Required motor speed is determined by set-values sent from the control computer via the analogue output ports of the interface card. The speed would drop with increasing motor load. To maintain the speed at the desired value; the amplifiers are adjusted to run in IxR compensation mode, in which the output to the motor is increased with increasing motor current. The advantage of this method is that the amplifier does not require encoder or tacho feedback from the

motor. Some selected properties of these amplifiers are stated in Table 5.5, a detailed description can be found in Appendix J.

Property	Value
Supply voltage (Vcc)	12 -50 VDC
Max. output voltage	0.9*Vcc
Max. output current	10 A
Continuous output current	5 A
Switching frequency	50 kHz
Efficiency	95%
Set value	-10...+10 VDC

Table 5.5 Driving amplifier properties for X and Y axis motors

The cutter motor is driven by a Maxon AECS 35/3 1-Q-EC sensorless amplifier. This amplifier drives electronically commutated (brushless) DC motors. With the aid of opposing EMF, the current rotor position is evaluated and the partial coils are controlled [95]. Although the motor speed could be set by analogue set values from the computer, the on-board potentiometer is used for simplicity. Computer only sends activate/deactivate signals to the brake input of the amplifier via a digital output port of the interface card. Some selected properties of this amplifier are given in Table 5.6, a detailed description can be found in Appendix K.

Property	Value
Supply voltage (Vcc)	8 - 35 VDC
Max. output current	5 A
Continuous output current	3 A
Speed range (typical)	1000 – 90000 rpm

Table 5.6 Driving amplifier properties for cutter motor

Finally, the stepper motor of the timber feed drive is driven by a purpose built power switching circuit with eight field effect transistors (FETs). It enables half-step and full-step operation of the stepper motor. Steps are initiated one-by-one from the control computer through four digital output ports of the interface card.

5.4 Software Implementation in Simulink

Real-Time Windows Target (RTWT) enables the user to run Simulink models in real-time on PCs for rapid prototyping or hardware-in-the-loop simulation of control system and signal processing algorithms. Real-time executions can be created and controlled entirely through Simulink. The highly optimized RTWT kernel runs at the highest priority (i.e. Ring 0) in the Windows environment. Other Windows applications continue to run during operation and can use all CPU cycles not needed by the real-time task [96]. Most RTWT models can achieve up to 10kHz sampling rate, which is also sufficient for the PIMM.

A typical process of developing a real-time application in the Real-Time Windows Target environment involves the following steps.

- ◆ The real time application is designed in Simulink. The RTWT environment allows adding blocks into Simulink diagram for interfacing the I/O card.
- ◆ The Real-Time Workshop (RTW), then compiles the Simulink diagram, which represents the real-time application. The result of this compilation is a C code.
- ◆ The C code is then compiled by a C compiler to obtain an executable binary file.
- ◆ By selecting Simulink external mode, the Real-Time Windows Target kernel loads the binary application file into the memory and establishes a connection between the hardware and Simulink.

The real time execution is started from the computer. Upon execution, the real-time signals can be displayed live with the standard Simulink Scope blocks. Also, the run-time data can be captured and stored in MAT-files for additional off-line analysis and visualization in MATLAB. Detailed information on Real-Time Windows Target can be found in [96].

Implementation of the PIMM system in Simulink RTWT is done by replacing the mathematical model of the motion system (i.e. X and Y axis drives), described in Section 4.2.4, with the model shown in Figure 5.7. This model does not contain any information on the drive hardware parameters. It only specifies how, where and when the data should be sent to and received from the hardware. The rest of the PIMM model, namely, reference generator, control algorithm and output visualizations remain unchanged. This enables direct comparison between the mathematical model and the real hardware.

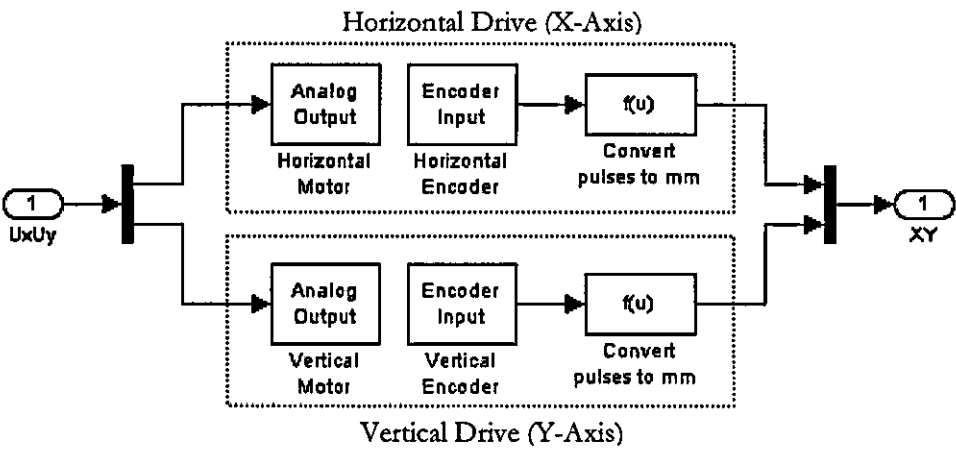


Figure 5.7 PIMM model for Real-Time Windows Target

The RTWT implementation is done for mathematical model validation and system identification purposes only. The Simulink model is designed to perform a single pass along the width of the workpiece at each execution. Also, it is decided to keep the model as simple as possible. Consequently, timber feed and cutter drives are not implemented in Simulink and operated manually.

5.5 Software Implementation in Visual Basic 6

Visual Basic is the first and the most widely used object oriented, visual programming environment used for developing Windows applications. “Visual Programming” is the method of creating graphical user interfaces (GUI) by placing objects on the screen at design time, rather than writing numerous lines of

code to describe the appearance and orientation of the interface elements. Visual Basic (VB) is based on BASIC (Beginners All-Purpose Symbolic Instruction Code) programming language. However, VB is evolved from the original BASIC language and now contains several hundred statements, functions and keywords many of which refer directly to Windows GUI. Visual Basic also includes numerous tools, visual components, application templates and wizards that are very useful from the start of the programming to the end of compiling and debugging. Although Visual Basic 6 (VB6) is an older version in its product family, the capabilities of this version is sufficient for the needs of the PIMM software. More information on VB6 can be found in [97].

Unlike the Simulink one, Visual Basic 6 implementation is aimed to be the main, fully functional software for the PIMM. Compiled version of the software can be installed together with the Sensoray 626 interface card to any Windows PC without the need for any other software.

The main functionality of the software is to load CAD drawings of moulding profiles and to control machine axes. Other than the basic functionality, the present software includes some advanced features such as controller tuning and error monitoring. These features are implemented for optimization purposes and they might not be needed by the end-users of the system.

This section presents overall structure, data structure, functionality and graphical user interface of the software implemented in Visual Basic 6. The source code can be found in the accompanying CD (Appendix M).

5.5.1 Program structure

At design time, a Visual Basic application is represented by a *project*. The PIMM software consists of one *project* file (‘.vbp’), five *form* files (‘.frm’) and six *module* files (‘.bas’). The *form* files contain visual components together with source code, whereas, *module* files can only contain source code. Table 5.7 lists the files that

constitute the PIMM project. These files, except 'Win626.bas', will be referred throughout the following sections; therefore, detailed descriptions are not presented here.

File Name	Type	Description
PIMM.vbp	<i>project</i>	main file that links all files in the project
Main.frm	<i>form</i>	main window containing menus, toolbars and all other forms
Graph.frm	<i>form</i>	displays the moulding profile to be machined
Analysis.frm	<i>form</i>	displays some machining results after each pass
List.frm	<i>form</i>	displays the profile array (refer to Section 4.3.2)
Settings.frm	<i>form</i>	displays accuracy, sampling rate and controller gain settings
Common.bas	<i>module</i>	contains various functions
Control.bas	<i>module</i>	control algorithm for X and Y axis drives (refer to Section 4.3.4)
Drawing.bas	<i>module</i>	procedures required for Graph.frm and Error.frm
ImpExp.bas	<i>module</i>	procedures for loading and saving moulding profiles
APITimer.bas	<i>module</i>	high resolution API timer
Win626.bas	<i>module</i>	provides link to 'S626.dll'

Table 5.7 Visual Basic files in the PIMM project

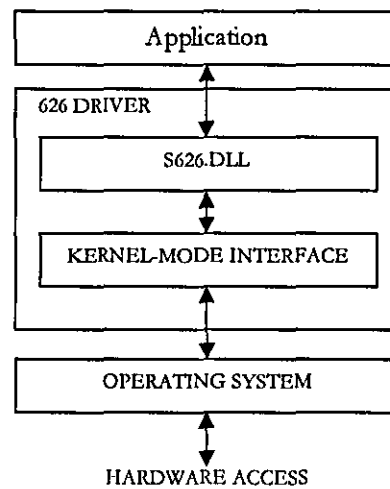


Figure 5.8 Block diagram of the software hierarchy [98]

The *module* file 'Win626.bas' is required for the Sensoray 626 interface card and it provides a link between the project and the 'S626.dll' dynamic link library. The interface card is configured and accessed with the help of specific functions and instructions contained in the file. Figure 5.8 illustrates the hierarchy from software application to hardware access.

5.5.2 Data structure

File formats

There are three ASCII formats recognized by this application; ‘.dxf’, ‘.pim’, and ‘.dat’. Import-export procedures for these formats are implemented in ‘ImpExp.bas’ module file.

◆ ‘.dxf’

Moulding profiles in two-dimensional ASCII DXF files can only be imported to the application. Profiles created or modified in the application can not be saved in DXF format. For DXF reading and translating methods refer to Section 4.3.1 and Section 4.3.2 respectively.

◆ ‘.pim’

Files with ‘.pim’ extension consist of a single column of numbers, of which, every nine rows define a segment of a profile. It can be thought as if the columns of the ‘profile array’, described in Section 4.3.2, are written in a single column one after the other, starting from the first. The ‘.pim.’ files can be opened and saved by the application.

◆ ‘.dat’

This file type is used for recording machining results during the development of the test-rig. These files comprise comma-separated ASCII data and they can be imported to MATLAB or any spreadsheet software for analysis purposes. First two lines of the file contain completion time and maximum contour error of a single pass. The next two lines accommodate the gains used in the path controller. The rest of the file records the *Samples* array explained below.

Data handling

The application uses many variables and arrays for storing reference and sampled data. The most important ones are summarized below.

◆ *Target*

Target contains geometric data of the moulding profile to be machined. Essentially it is the same as the 'profile array' explained in Section 4.3.2. The only difference is; in the 'profile array' each column represents a profile segment, but in *Target*, segments are placed in rows. The maximum number of segments is limited to 100.

◆ Active segment variables (*ind*, *X1*, *Y1*, *X2*, *Y2*, *XA*, *YA*, *Tb1*, *Tb2*, *RA*)

For the sake of programming simplicity, parameters of the profile segment, which is being processed, are extracted from the *Target* array and assigned to individual variables. Assignment is performed by the *AssignSegment* sub-routine in *Common.bas*. Table 5.8 lists the definitions of the active segment variables.

Variable	Definition
<i>ind</i>	position (row number) of the segment in the <i>Target</i> array
<i>X1</i>	start point x coordinate
<i>Y1</i>	start point y coordinate
<i>X2</i>	end point x coordinate
<i>Y2</i>	end point y coordinate
<i>XA</i>	arc centre x coordinate (0 if segment is a line)
<i>YA</i>	arc centre y coordinate (0 if segment is a line)
<i>Tb1</i>	start point arc angle (0 if segment is a line)
<i>Tb2</i>	end point arc angle (0 if segment is a line)
<i>RA</i>	arc radius (0 if segment is a line)

Table 5.8 Active segment variables

◆ *Samples*

This is a two-dimensional array that stores sampled data points, and it consists of 3 columns and 100000 rows. First, second and third columns contain horizontal position (*X*), vertical position (*Y*) and contour error (ϵ_c) in millimeters respectively; where contour error (ϵ_c) is the distance from the sampled point to the nearest point on the target path. Each row represents a single point and every time the system is sampled, a new row is added to the array. The data points in the *Samples* array are only from a single pass over the workpiece. After each pass, the array is emptied and the next pass is started with a blank array.

5.5.3 Data capture and manipulation functions

In this section, major functions of the application are explained and their implementations are illustrated by flowcharts.

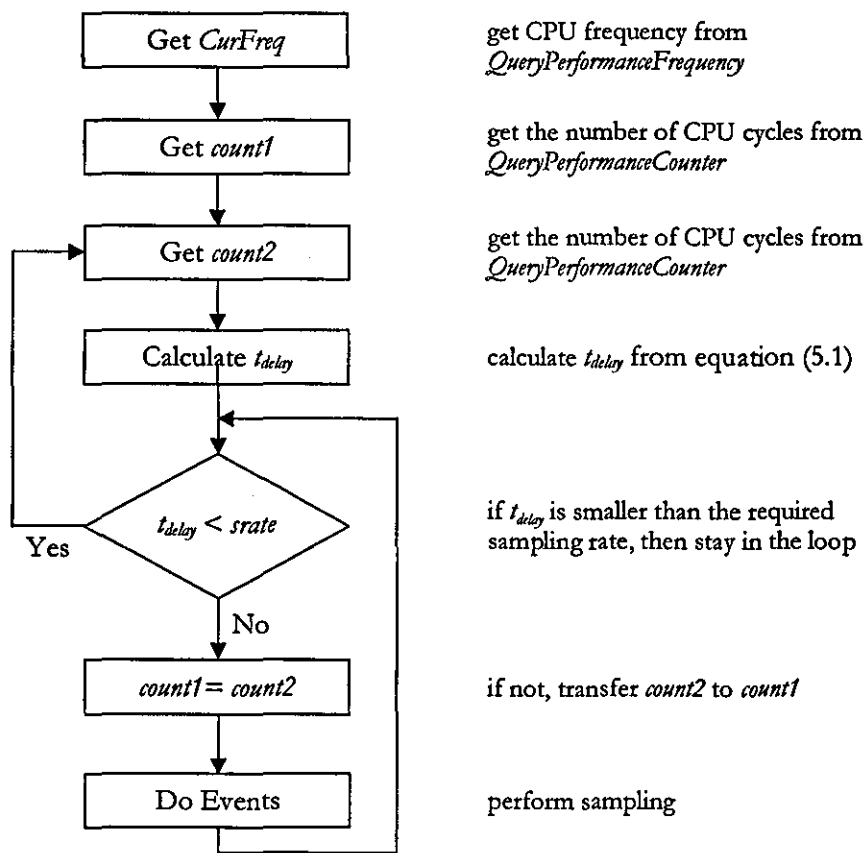


Figure 5.9 Flowchart – API timer

High resolution API timer

In Visual Basic, periodic events are controlled by VB Timer objects. However, Timer objects can only go up to 100 Hz sampling frequency; and that makes them unsuitable for this application. The implemented API timer is one of the alternatives to the conventional VB Timer, and it works like a typical delay loop. Although its application is not as straightforward as its counterpart, the API timer easily provides 2 kHz frequency.

The flowchart in Figure 5.9 illustrates the principle of the implemented API timer, where *srate* is the desired sampling rate. The API timer uses two functions,

QueryPerformanceFrequency and *QueryPerformanceCounter*, in *APITimer.bas* file to access the Windows kernel. The first one gets the CPU frequency of the system and the second one gets the current number of CPU cycles the system has been on. If the number of CPU cycles is read twice over a certain interval t_{delay} and stored in two different variables *count1* and *count2*, and if *CurFreq* is the variable where the CPU frequency is stored; then the following equation (5.1) gives t_{delay} in seconds.

$$t_{delay} = \frac{count2 - count1}{CurFreq} \quad (5.1)$$

Outer loop for path control

The outer loop (Figure 5.10) is coded in the *Main.frm* file and it is initiated by clicking the *GO* button on the *Machine Profile* toolbar (refer to Section 5.5.4). Upon initiation, the program calls the *ControlTimer* sub-routine which later triggers the inner control loop. After exiting the *ControlTimer* sub-routine, state of the *ORRepeat* variable is checked. If the state is *True*, the sub-routine is re-entered; if *False*, then all the drive motors are stopped.

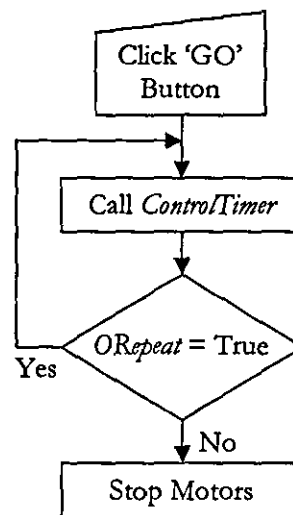


Figure 5.10 Flowchart - Outer control loop

The variable *ORRepeat* is set by two buttons on the GUI (refer to Section 5.5.4) and it determines whether single-pass or continuous operation is required. By default, *ORRepeat* is set to *False* (i.e. single-pass).

Inner loop for path control

The inner control loop is implemented in the *ControlTimer* sub-routine which is called from the outer loop. This sub-routine is built around the above explained API Timer and resides in the *Common.bas* file. Besides hosting the inner loop and linking to the outer loop, it also controls timber feeding and display procedures. Figure 5.11 shows the flowchart of *ControlTimer* sub-routine. The elements of the flowchart are numbered and their brief explanations are given in Table 5.9.

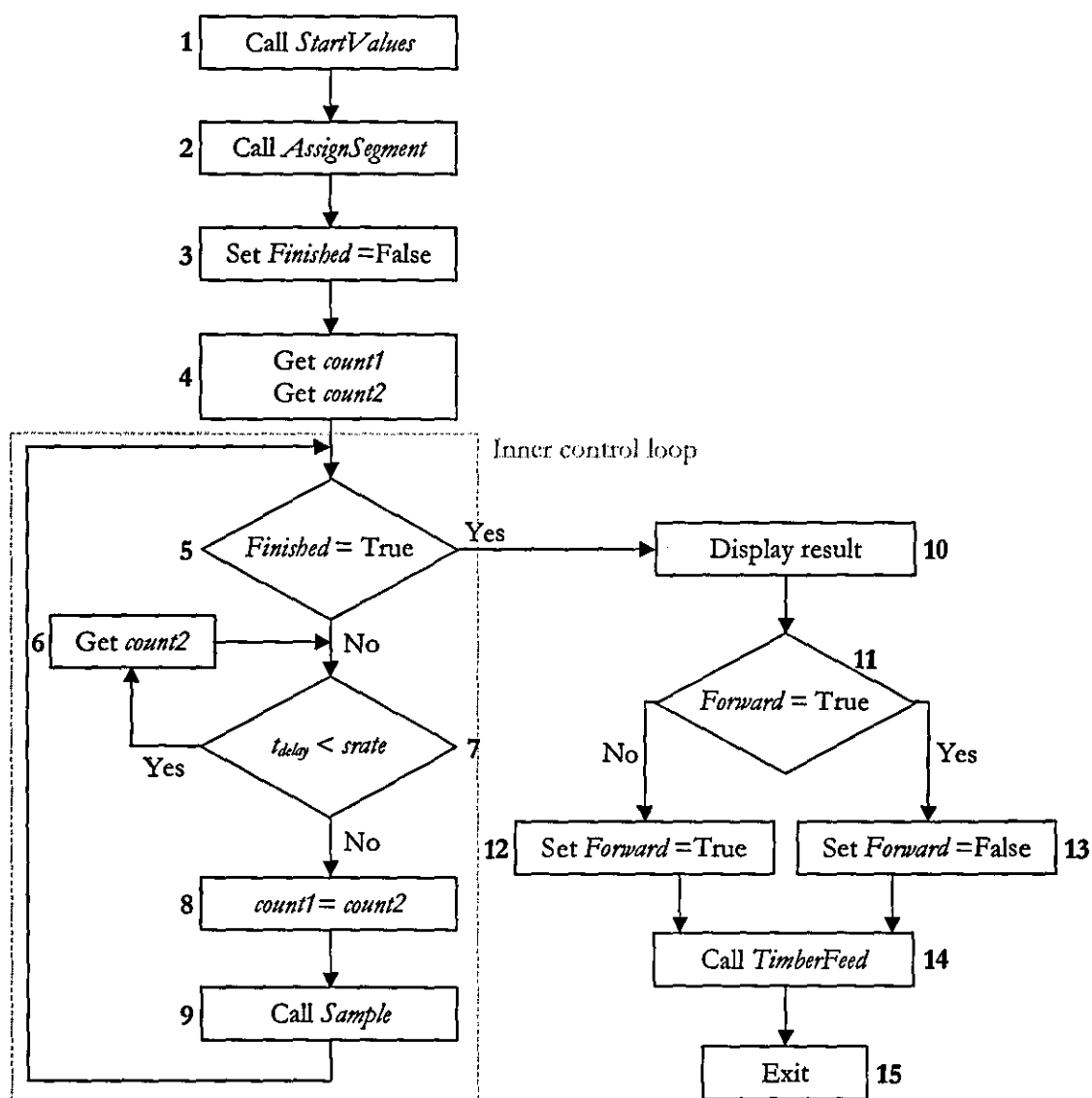


Figure 5.11 Flowchart – *ControlTimer*

1	Call <i>StartValues</i>	Call <i>StartValues</i> sub-routine from <i>Common.bas</i> . This sub-routine initializes the variables and screen display.
2	Call <i>AssignSegment</i>	Call <i>AssignSegment</i> sub-routine from <i>Common.bas</i> . This sub-routine identifies the profile segment to be machined.
3	Set <i>Finished</i> = False	Set the state of the boolean variable <i>Finished</i> to False. This variable's state turns to True when all the segments of the profile are completed.
4	Get <i>count1</i> , Get <i>count2</i>	Get <i>count1</i> and <i>count2</i> from <i>APITimer.bas</i> .
5	<i>Finished</i> = True	Check the state of <i>Finished</i> .
6	Get <i>count2</i>	Get <i>count2</i> from <i>APITimer.bas</i> .
7	<i>t_{delay}</i> < <i>srate</i>	Check if <i>t_{delay}</i> (5.1) is smaller than the desired sampling rate <i>srate</i> .
8	<i>count1</i> = <i>count2</i>	Transfer <i>count2</i> value to <i>count1</i> .
9	Call <i>Sample</i>	Call <i>Sample</i> sub-routine (Figure 5.12).
10	Display result	Display result on the screen.
11	<i>Forward</i> = True	Check the state of the boolean variable <i>Forward</i> . <i>Forward</i> 's value is True when the profile is followed from left to right and vice versa.
12	Set <i>Forward</i> = True	Set <i>Forward</i> to True.
13	Set <i>Forward</i> = False	Set <i>Forward</i> to False.
14	Call <i>TimberFeed</i>	Call <i>TimberFeed</i> sub-routine.
15	Exit	Exit <i>ControlTimer</i> sub-routine and return to outer loop.

Table 5.9 Flowchart details - *ControlTimer*

Sampling and path control algorithms are handled in the inner loop by the *Sample* sub-routine of *Common.bas*. *Sample* can be described as a gateway to many other sub-routines and functions. On its own, it only performs some logical operations but the functions it calls connect to the hardware and apply the path control algorithms described in Section 4.3.4. Figure 5.12 shows the flowchart of *Sample* sub-routine. The elements of the flowchart are numbered and their brief explanations are given in Table 5.10.

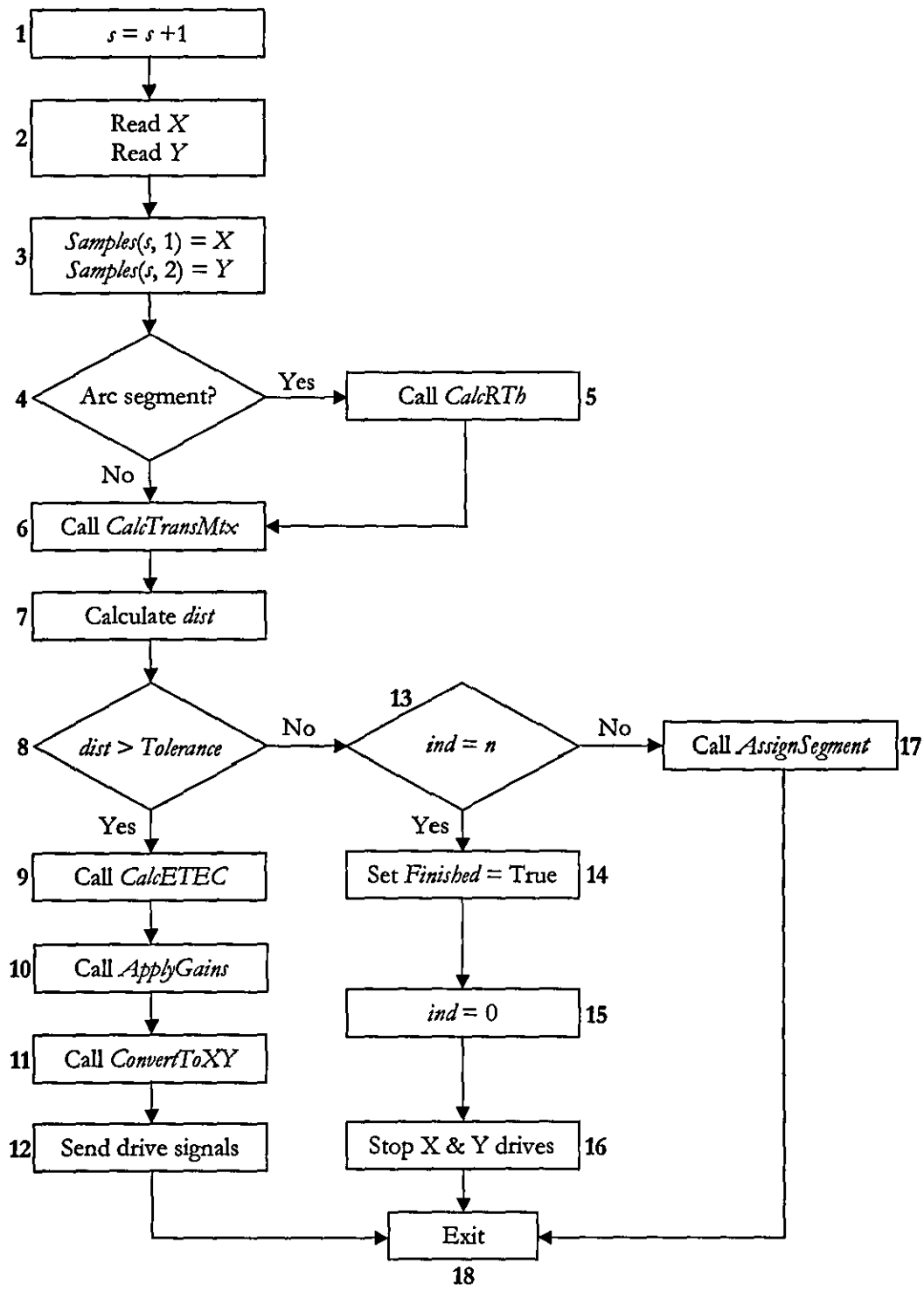


Figure 5.12 Flowchart – *Sample*

1	$s = s + 1$	Increment the number of samples s .
2	Read X Read Y	Read horizontal and vertical drive encoders and convert to millimetres.
3	$Samples(s, 1) = X$ $Samples(s, 2) = Y$	Add X and Y to $Samples$ array.
4	Arc Segment?	Check if the machined segment is an arc.
5	Call <i>CalcRTh</i>	Call <i>CalcRTh</i> sub-routine, which calculates the polar coordinates R and θ (refer to Section 4.3.4), from <i>Control.bas</i> .
6	Call <i>CalcTransMtx</i>	Call <i>CalcTransMtx</i> sub-routine from <i>Control.bas</i> . This sub-routine calculates the transformation matrix $[T]$ (refer to Section 4.3.4).
7	Calculate $dist$	$dist$ is the direct distance between the current position and the end-point of the profile segment that is being machined (refer to Section 4.3.3).
8	$dist > Tolerance$	Check $dist$ against the allowed <i>Tolerance</i> . If $dist$ is greater than the <i>Tolerance</i> , then the machine carries on machining the current segment. Else, the next segment is started.
9	Call <i>CalcETEC</i>	Call <i>CalcETEC</i> sub-routine from <i>Control.bas</i> . <i>CalcETEC</i> calculates the errors ϵ_r and ϵ_c (refer to Section 4.3.4).
10	Call <i>ApplyGains</i>	Call <i>ApplyGains</i> sub-routine, which applies controller gains, from <i>Control.bas</i> (refer to Section 4.3.4).
11	Call <i>ConvertToXY</i>	Call <i>ConvertToXY</i> sub-routine from <i>Control.bas</i> . This sub-routine converts the control signals back to X-Y coordinates (refer to Section 4.3.4).
12	Send drive signals	Send control signals to the horizontal and vertical drives.
13	$ind = n$	Check if the index ind of the current segment in the <i>Target</i> array is equal to the total number of profile segments n (refer to Section 5.5.2).
14	Set $Finished = True$	Set <i>Finished</i> to True.
15	$ind = 0$	reset segment index (refer to Section 5.5.2).
16	Stop X & Y drives	Stop horizontal and vertical axis drives.
17	Call <i>AssignSegment</i>	Call <i>AssignSegment</i> sub-routine from <i>Common.bas</i> . This sub-routine identifies the profile segment to be machined.
18	Exit	Exit <i>Sample</i> sub-routine.

Table 5.10 Flowchart details - *Sample*

5.5.4 Graphical User Interface

This section presents graphical user interface (GUI) of the software designed in Visual Basic 6. Main controls are marked with numbers and their functionality is explained.

Main window (*Main.frm*)

This is the master window of the software and it carries all the other windows and toolbars. Closing the main window terminates the application. The major controls on this window are explained below with reference to the numbers in Figure 5.13. In the explanations, the term ‘active profile’ is used to describe the target moulding profile to be machined.

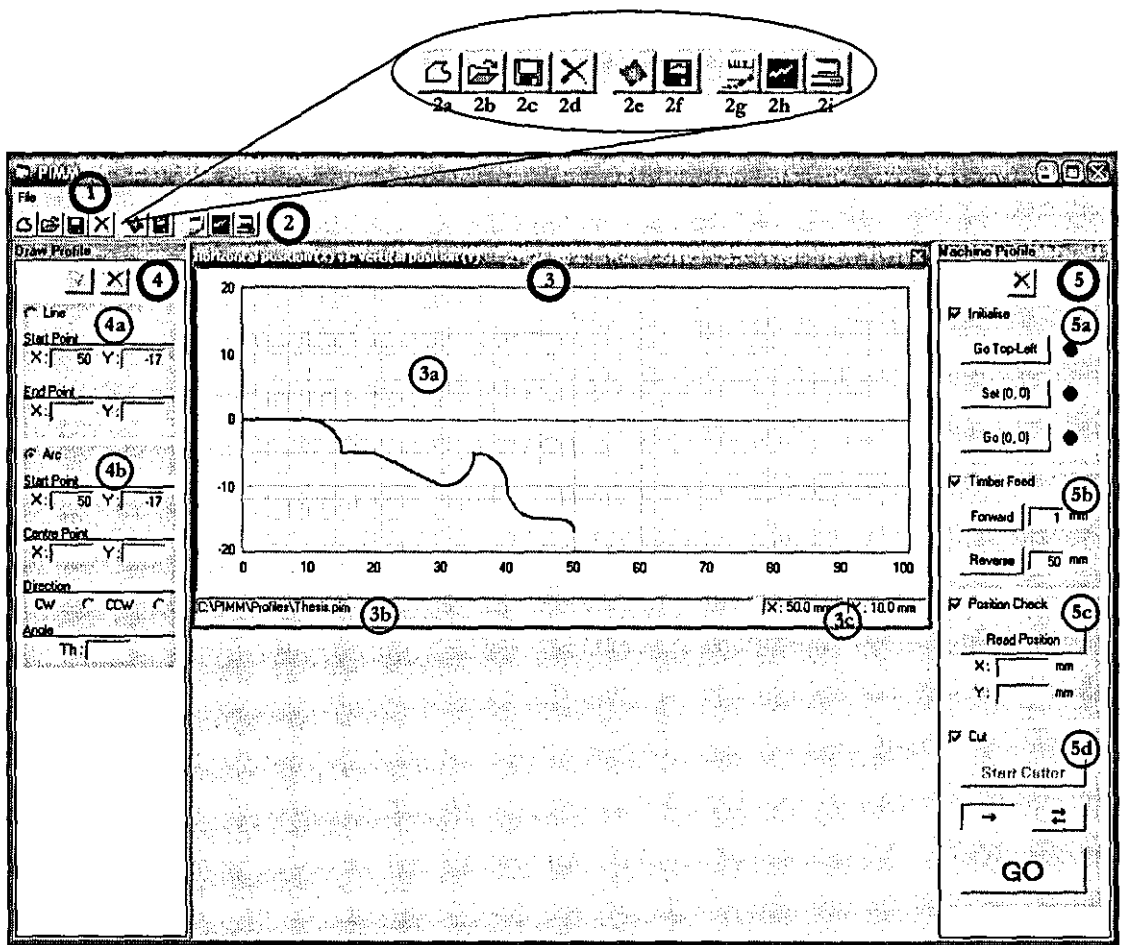


Figure 5.13 Main window

-
- 1 *Menu Bar* includes dropdown menus which have the same functionality as the *Main Toolbar* (#2).
 - 2 *Main Toolbar* consists of nine buttons to provide quick access to certain functions.
 - 2a – displays *DrawProfile* toolbar.
 - 2b – opens a standard *Open Dialog* to load a moulding profile.
 - 2c – opens a standard *Save Dialog* to save the ‘active profile’.
 - 2d – closes the ‘active profile’.
 - 2e – displays *Machine Profile* toolbar.
 - 2f – opens a standard *Save Dialog* to save machining result in ‘.dat’ format.
 - 2g – displays/hides *Segment List* window.
 - 2h – displays/hides *Analysis* window.
 - 2i – displays/hides *Settings* window.
 - 3 *Graph Window* displays the ‘active profile’ and also the machining result after every pass.
(*Graph.frm*)
 - 3a – plot of horizontal position (X) vs. vertical position (Y) in mm.
 - 3b – full file path of the loaded profile.
 - 3c – co-ordinates of the mouse-cursor when it is on the X vs. Y plot (#3a).
 - 4 *Draw Profile* includes drawing tools to create an ‘active profile’ from scratch. Also, segments can be added to a previously created/loaded profile.
Toolbar
 - 4a – a line is drawn from the *Start Point* to the *End Point* on the *Graph Window* (#3). *End Point* co-ordinates are entered by the user. If starting from scratch, the *Start Point* co-ordinates are (0, 0). If not, then they are automatically assigned the *End Point* co-ordinates of the last segment in the profile.
-

4b – a circular arc is drawn from the *Start Point* by entering *Centre Point* co-ordinates, *Direction* and *Arc Angle*. Assignment of the *Start Point* co-ordinates is the same as in the line drawing tool (#4a). *Direction* can be either clockwise *CW* or anti-clockwise *CCW*. *Arc Angle* is entered in degrees.

- 5 *Machine Profile* contains controls for hardware initialization and machining.
- Toolbar*
- 5a – *Go Top-Left* button moves the cutter to the top-left extreme. *Set (0, 0)* button sets the co-ordinates of the current position of the cutter to (0, 0). *Go (0, 0)* button moves the cutter to a pre-defined (0, 0) position. The colours of the round indicators next to the buttons are initially red. After a button is pressed and the corresponding function is completed, its indicator turns to green.
- 5b – timber feed is activated by *Forward* and *Reverse* buttons. The amount of feed (in millimetres) in either direction is entered by the user into the corresponding textboxes. The forward feed value also determines the amount of timber fed in between the passes during continuous machining.
- 5c – *Read Position* button reads the horizontal (X) and vertical (Y) drive encoders, converts counts to millimetres, and displays the cutter position co-ordinates in the provided textboxes.
- 5d – *Start Cutter* button activates the cutter motor. Upon activation the button displays *Stop Cutter* and pressing it again turns the cutter motor off. The buttons with single arrow and double arrow set the machine to single pass and continuous operation respectively. *GO* button starts machining. During machining the button displays *STOP* and pressing it cause all the drives to stop.

Segment List window (List.frm)

This window, shown in Figure 5.14, displays the *Target* array (refer to Section 5.5.2). In other words, it lists the geometric parameters of the segments in the ‘active profile’. Each row represents an individual segment and when a row is clicked, the corresponding segment in the *Graph* window is highlighted with blue colour. The segments can only be deleted from the list from bottom to top by double-clicking the last row. When a new segment is added to the profile by the *Draw Profile* toolbar, its parameters also appear in the *Segment List* window.

Segment List								
X1	Y1	X2	Y2	XC	YC	Th1	Th2	RA
00.00	00.00	10.00	00.00	00.00	00.00	00.00	00.00	00.00
10.00	00.00	15.00	-5.00	10.00	-5.00	90.00	00.00	5.00
15.00	-5.00	20.00	-5.00	00.00	00.00	00.00	00.00	00.00
20.00	-5.00	30.00	-10.00	00.00	00.00	00.00	00.00	00.00
30.00	-10.00	35.00	-5.00	30.00	-5.00	270.00	360.00	5.00
35.00	-5.00	40.00	-10.00	35.00	-10.00	90.00	00.00	5.00
40.00	-10.00	45.00	-15.00	45.00	-10.00	180.00	270.00	5.00
45.00	-15.00	48.00	-15.00	00.00	00.00	00.00	00.00	00.00
48.00	-15.00	50.00	-17.00	48.00	-17.00	90.00	00.00	2.00

Double-Click the last segment to delete.

Figure 5.14 Segment List window

Analysis window (Analysis.frm)

The *Analysis* window displays some machining results and it is updated after every pass. Features of this window are explained below with reference to the numbers in Figure 5.15.

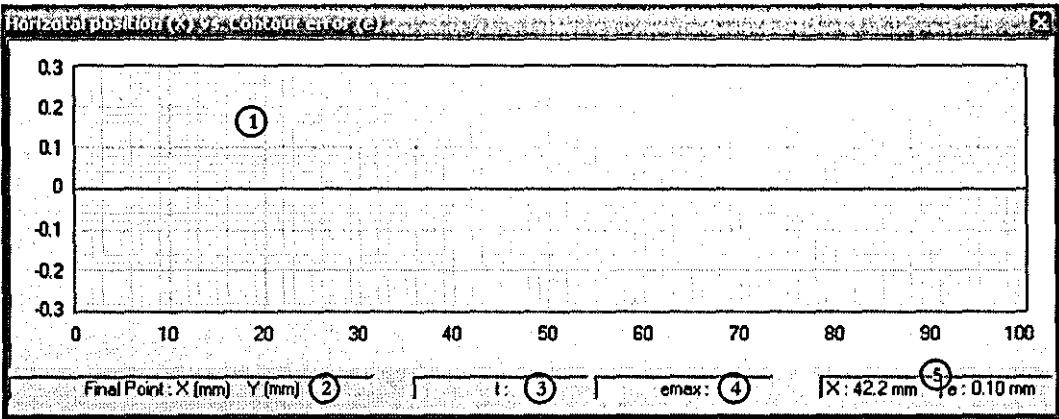


Figure 5.15 Analysis window

- | | | |
|---|----------------------------|---|
| 1 | <i>Error Plot</i> | displays a plot of horizontal position (X) vs. contour error (ϵ_c) in mm. |
| 2 | <i>Final Point</i> | displays the co-ordinates of the point where the cutter stops after each pass. |
| 3 | <i>Pass time</i> | displays the time taken for the pass in seconds. |
| 4 | <i>Max. Contour Error</i> | displays the maximum contour error in a pass. |
| 5 | <i>Cursor co-ordinates</i> | displays co-ordinates of the mouse-cursor when it is on the X vs. ϵ_c plot (#1). |

Settings window (*Settings.frm*)

This window allows modification of accuracy and path controller settings. Its controls are explained below with reference to the numbers in Figure 5.16.

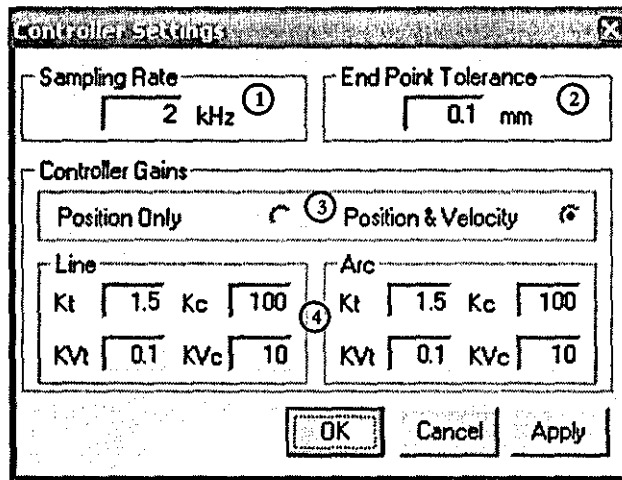


Figure 5.16 Settings window

- | | | |
|---|----------------------------|---|
| 1 | <i>Sampling Rate</i> | desired sampling rate is entered in kHz (refer to Section 5.5.3). |
| 2 | <i>End Point Tolerance</i> | required segment end point tolerance is entered in mm (refer to Section 5.5.3). |
| 3 | <i>Controller Type</i> | controller type is selected by clicking the option buttons. |
| 4 | <i>Controller Gains</i> | controller gains for line and arc segments are entered by the user. If <i>Position Only</i> is selected as controller type (#3), then gains on the second row (i.e. KV_t , KV_c) are disabled. |

5.6 Future Plans

The PIMM project has been granted innovation funding from the Loughborough University Intellectual Property Office. The following list summarizes the future development plans of the PIMM test-rig.

Cutter assembly

- ◆ Design of a dedicated, optimized cutting tool.
- ◆ Design and production of a new cutter assembly, in which a larger, more powerful motor is located away from the cutter, to produce deeper cuts.

Timber feed drive

- ◆ Design and production of a new timber feed drive capable of feeding longer (i.e. 2 m) workpieces.

I/O hardware

- ◆ Implementation of USB (Universal Serial Bus) interface hardware instead of the currently used PCI card. This enables the PIMM to be portable and Plug-and-Play.

Visual Basic software

- ◆ Optimization and de-bugging to achieve stable and fail-safe software with simple, user-friendly interface.

5.7 Summary

The designed proof-of-concept PIMM test-rig, which can be described as a miniature wood-moulding machine, is presented. Mechanical design is divided into four subsystems as cutter assembly, horizontal axis drive, vertical axis drive and timber feed drive. Hardware components of the individual subsystems are detailed and their important parameters are identified. The current timber feed drive is employed temporarily and it only accommodates small timber specimens. However, this is sufficient for the experimental investigation of the new concept.

Due to simplicity, flexibility and reasonable cost of PC-based systems, a standard PC equipped with a multifunction I/O card is used as the controller. Structure of the test-rig instrumentation is presented together with specifications of the used control electronics.

Two different control softwares are implemented in Simulink and Visual Basic 6. The former one is less detailed and it is only intended for system identification and model verification purposes. The latter one acts as the main software for the test-rig. Currently it is experimental and contains some extra features, which might not be needed by the end-users of the system. Detailed description of the implementation in terms of program structure, algorithms, and GUI is provided.

Finally, the future plans on development of the PIMM test-rig are listed. These are intended to be carried out during an innovation fellowship following this research work.

Chapter 6

System Identification and Model Validation

6.1 Introduction

This chapter is aimed at identification of system parameters for mathematical model refinement and validation. Initially, the models only contain parameters from manufacturer's datasheets and they do not include disturbances which surely exist in the PIMM test-rig. One can not expect these models to represent the real system accurately. System identification procedures are employed in order to verify the known parameters as well as to discover the unknown disturbances.

In Section 6.2, the reliability of the previously presented Simulink RTWT model, which is used to communicate with the real system, is verified. Then in Section 6.3, the electrical part of the drives, namely, amplifier and DC motor, is identified. Section 6.4 deals with friction identification, modeling, and simulation. Also, the carriage weight in the vertical (Y) axis drive model is validated. Finally in Section 6.5, a brief summary of the chapter is presented and the final model parameters are listed.

6.2 Validation of the Simulink RTWT Model

Firstly, in order to verify the validity of the Simulink RTWT model (Figure 5.7), two simple experiments are performed. In the first experiment, voltage at the analog output ports of the I/O card is measured with a voltmeter while structured control signals are being sent from the RTWT model. The voltmeter readings are found to be in agreement with the sent values.

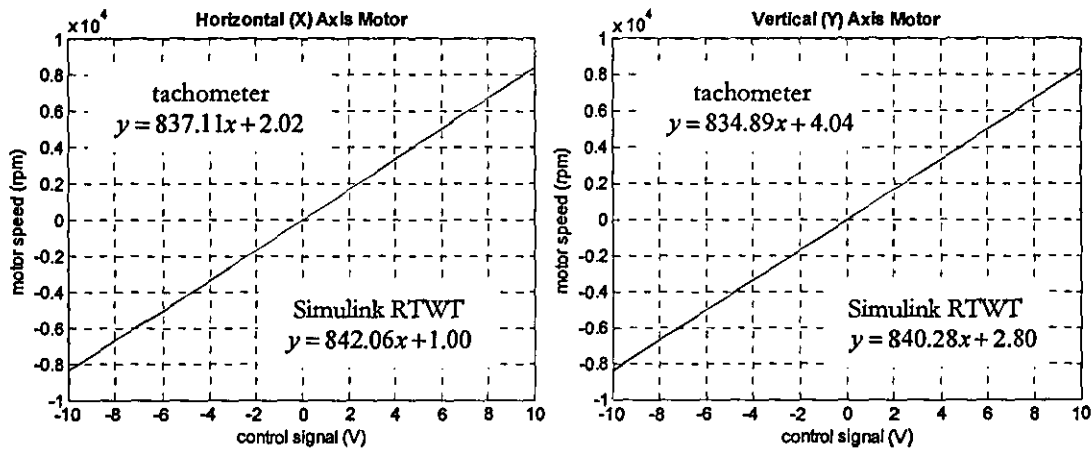


Figure 6.1 Steady-state curves of the drive motors

In the second experiment, the leadscrews are disconnected from the motors and control signal to amplifiers is increased from 0V to 10V in 1V increments in both directions. Steady-state velocity at each interval is measured from the motor shaft by an optical tachometer. At the same time, the velocity is also estimated in RTWT model by differentiating the encoder signals with respect to time. Steady-state equations are derived from both sets of data and shown in Figure 6.1. The maximum difference between the results is found to be less than 0.6%, therefore, validity of the Simulink RTWT model is verified.

In the following sections of this chapter, the term “measured data” will be used for the data obtained via the Simulink RTWT model.

6.3 Identification of Amplifier and DC Motor Parameters

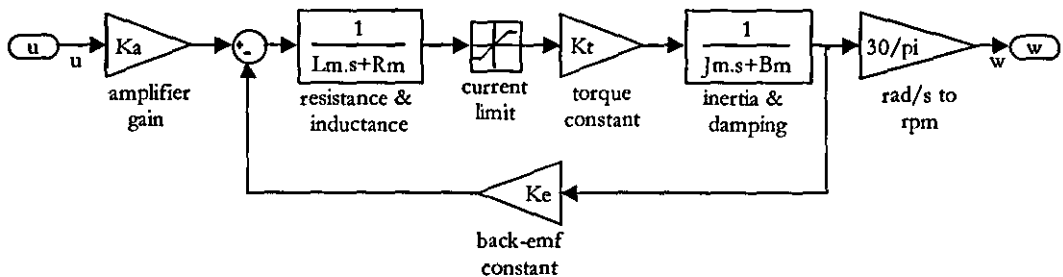


Figure 6.2 Amplifier and DC motor model

Figure 6.2 shows a mathematical Simulink model of an amplifier and a DC motor, output of which is compared to the measured data in the identification process. In this model, the amplifier is represented by a gain block and a current limiter. Initially, the amplifier and motor parameters are obtained from manufacturer's datasheets and given in Table 6.1. A value for the rotary viscous damping coefficient B_m , which generally exists in the motor bearings, was not available; hence, for now, it is assumed to be zero.

Parameter		Horizontal (X) Axis	Vertical (Y) Axis
amplifier gain (V/V)	K_a	2.4	2.4
amplifier current limit (A)	I_{lim}	-4/+4	-4/+4
armature inductance (H)	L_m	0.00012	0.00012
armature resistance (Ohm)	R_m	0.582	0.582
motor torque constant (Nm/A)	K_t	0.026	0.026
motor back-emf constant (Vs/rad)	K_e	0.026	0.026
rotor inertia (kg.m ²)	J_m	$3.3 \cdot 10^{-6}$	$3.3 \cdot 10^{-6}$
rotary damping coeff. (Nms/rad)	B_m	0	0

Table 6.1 Amplifier and motor parameters before identification

To see how close the model represents the actual system (i.e. amplifier and motor) with the initial parameters, the same input is applied to the system (via RTWT) and the model. The control voltage to both amplifiers is increased 1V at every 0.1s from 0V to 10V in positive and negative directions. Figure 6.3 shows the simulation results against the measured data.

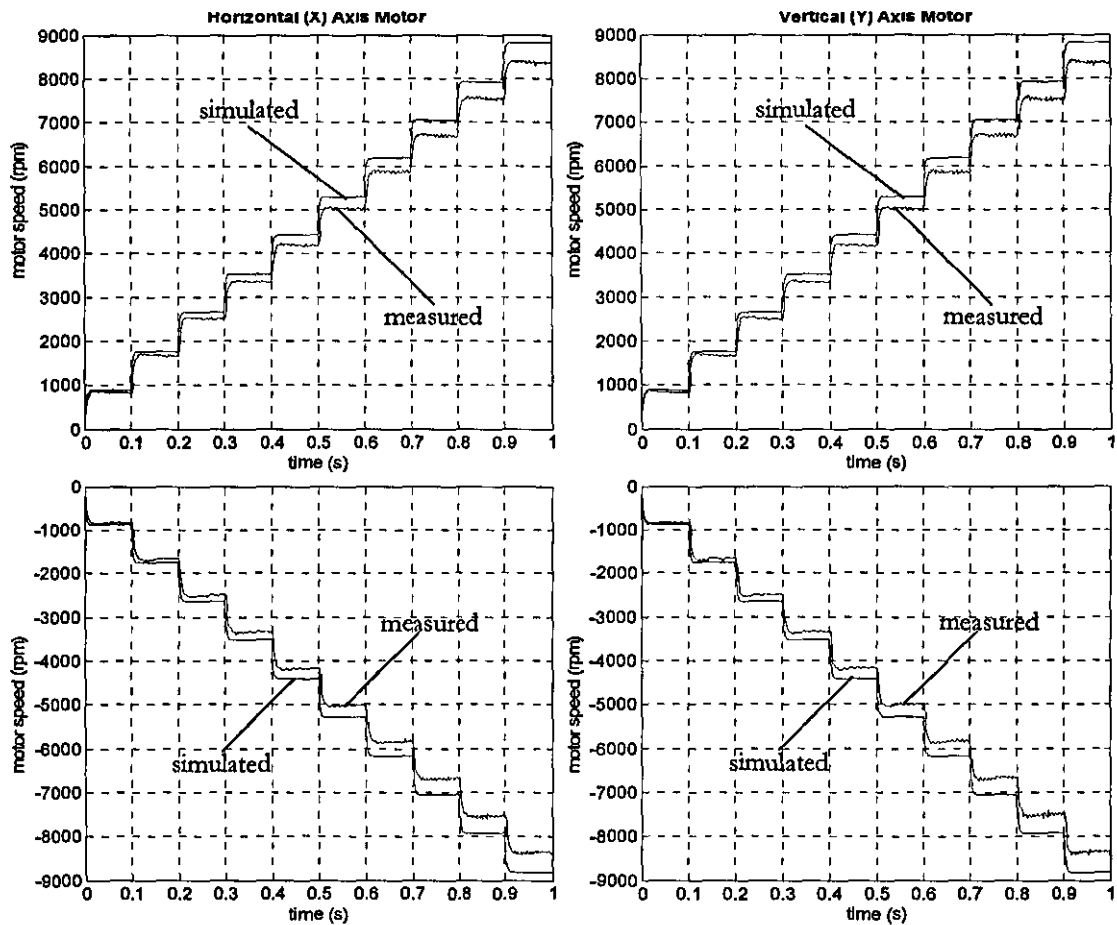


Figure 6.3 Amplifiers and motors before identification

As can be seen in Figure 6.3, the actual system is running slower than the simulation. For this variance, three causes are identified and listed in Table 6.2 together with the model parameters that need to be tuned in order to remedy the effects. Tuning is done by structured tests; whenever a parameter is changed, the simulation is re-run and the results are compared to the measured data. The performance criteria that are used are the IAE, which is the integral of the absolute value of error, and the ITAE, which is the integral of the time multiplied by the absolute value of error. They are defined by the equations (6.1) and (6.2), where ε_i is the velocity error at the i^{th} sampling time. Also, for easier comparison, the performance factors P_{IAE} and P_{ITAE} are defined (6.3), which show the performance of a simulation relative to the initial simulation before the identification. The employed performance criteria are commonly used in the field of machine control [52][99], and the rationale is explained by some typical examples in Appendix L.

Cause	Description	Parameter
Gain difference	At steady-state, simulated speed is always higher than the measured one. This is due to the model having higher gain than the actual system.	amplifier gain (K_a)
Damping difference	Difference between the measured and simulated data increase proportional to the speed. Therefore, the actual system can be said to have higher damping than the simulated one.	rotary damping coeff. (B_m)
Time constant difference	When the input is changed, the simulated speed changes more abruptly than the measured speed. This shows that the model has a smaller time constant than the actual system.	motor torque constant (K_t)

Table 6.2 Causes of model variance

$$IAE = \sum_i |\varepsilon_i| \quad (6.1)$$

$$ITAE = \sum_i t_i |\varepsilon_i| \quad (6.2)$$

$$P_{IAE} = \frac{IAE}{IAE_{init}} \quad P_{ITAE} = \frac{ITAE}{ITAE_{init}} \quad (6.3)$$

Table 6.3 lists the final amplifier and motor parameters. The ones written in **bold** are the tuned values which achieved the lowest P_{IAE} and P_{ITAE} . Results of the final simulation is plotted against the measured data and shown in Figure 6.4 with the corresponding P_{IAE} and P_{ITAE} . On average, the simulation with the identified parameters is 88% closer to the actual system, than the initial simulation in Figure 6.3, according to the P_{IAE} , and 90% according to the P_{ITAE} .

Parameter		Horizontal (X) Axis	Vertical (Y) Axis
amplifier gain (V/V)	K_a	2.31	2.30
amplifier current limit (A)	I_{lim}	-4/+4	-4/+4
armature inductance (H)	L_m	0.00012	0.00012
armature resistance (Ohm)	R_m	0.582	0.582
motor torque constant (Nm/A)	K_t	0.0195	0.0195
motor back-emf constant (Vs/rad)	K_e	0.026	0.026
rotor inertia (kg.m ²)	J_m	3.3*10 ⁻⁶	3.3*10 ⁻⁶
rotary damping coeff. (Nms/rad)	B_m	0.8*10⁻⁵	0.8*10⁻⁵

Table 6.3 Amplifier and motor parameters after identification

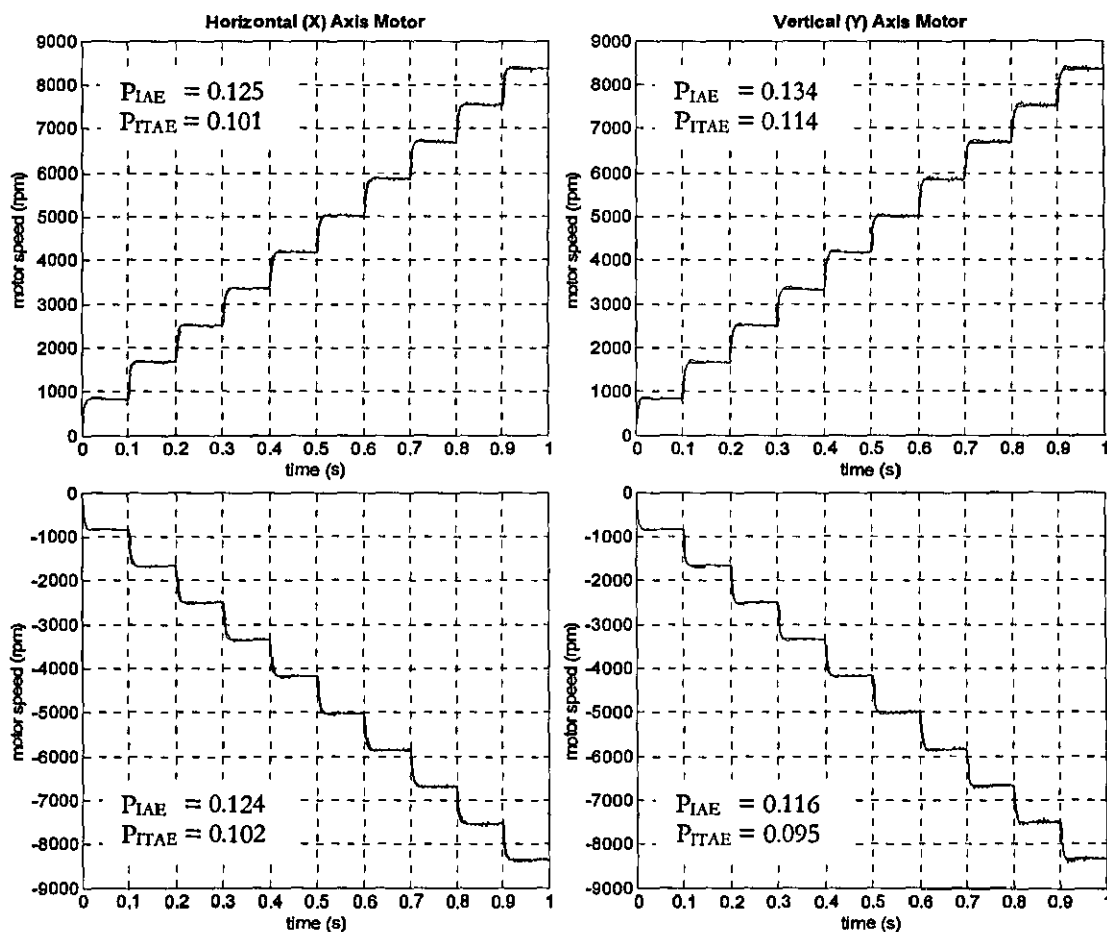


Figure 6.4 Amplifiers and motors after identification

As a result, this section brings the mathematical models of the amplifiers and DC motors to sufficient proximity to the actual hardware. When the whole electro-mechanical drive is considered, the electrical part of the drive is identified. The following sections work on fully assembled horizontal and vertical axis drives, and identify mechanical parameters such as friction and weight.

6.4 Identification of Disturbances on X and Y Axis Drives

This section mainly deals with friction identification, modeling, and simulation.

6.4.1 Ideal drive model and performance

Figure 6.5 shows the Simulink model of an ideal drive which is used for both horizontal and vertical axes. The model is essentially the same as the one in previous section (Figure 6.2). Only the rotor inertia J_m and the damping coefficient B_m are replaced with the total equivalent inertia J and the total equivalent damping coefficient B . These parameters are lumped at the rotor of the motor and their calculations were explained previously in Section 4.2.3. Both drives are assumed frictionless, and the effect of gravity on the vertical drive is ignored. Since the feedback in the actual drives is supplied from a rotary encoder on the motor shaft, output of the model is not converted to linear units.

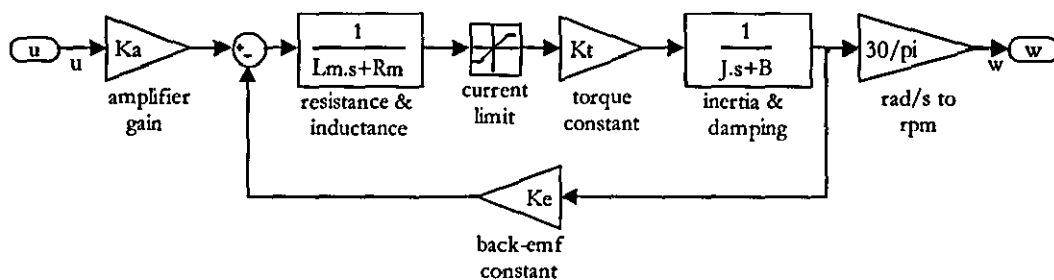


Figure 6.5 Ideal single-axis drive model

For the simulations, the already identified amplifier and motor parameters (Table 6.3) are used with ones in Table 6.4. When calculating the equivalent inertias, the carriages are weighed and the leadscrews are assumed to be cylinders. Carriage damping (viscous friction) B_c is neglected, and hence the equivalent coefficients B became equal to B_m .

In the actual system, the vertical drive frame is disconnected from the machine frame and laid on its back. Consequently, both drives are made to operate on the horizontal plane and the effect of gravity on the vertical (Y-axis) drive is cancelled.

Parameter		Horizontal (X) Axis	Vertical (Y) Axis
equivalent inertia (kg.m^2)	J	$3.61 \cdot 10^{-6}$	$3.63 \cdot 10^{-6}$
leadscrew inertia (kg.m^2)	J_s	$2.52 \cdot 10^{-7}$	$1.27 \cdot 10^{-7}$
carriage mass (kg)	M	0.25	0.90
equivalent damping coeff. (Nms/rad)	B	$0.8 \cdot 10^{-5}$	$0.8 \cdot 10^{-5}$
carriage damping coeff. (Ns/m)	B_c	0	0

Table 6.4 Drive parameters

The following inputs (Figure 6.6) are applied to the drives and the model. Due to leadscrew length limitations, the full motor speed operating range could not be applied. For trapezoid input, X and Y axis drives are given maximum control voltages of 5V and 4V respectively. The amplitude of the sinus input is 5V for both of the drives but the period is halved for the Y axis due to very short length (i.e. 30mm) of the drive.

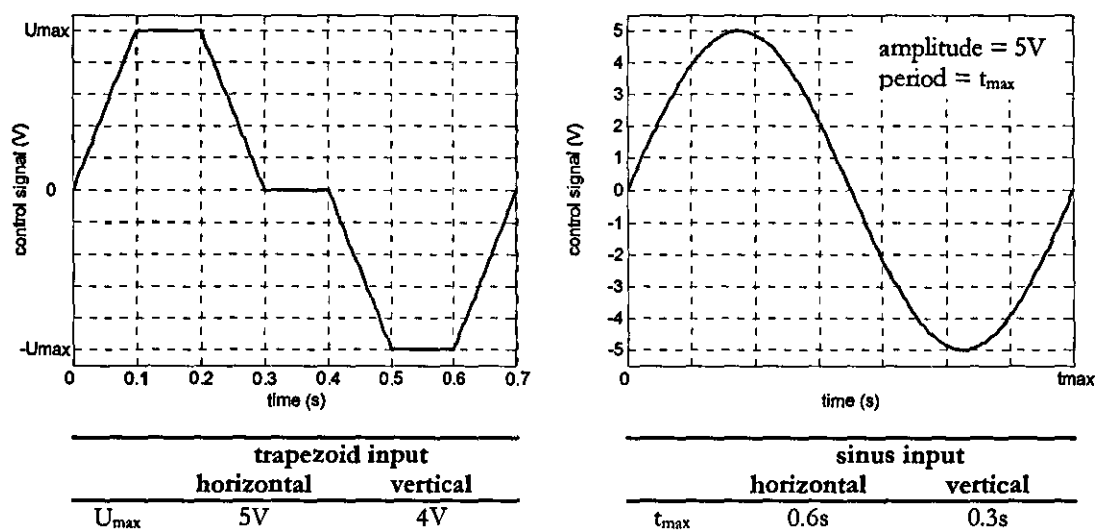


Figure 6.6 Drive inputs for disturbance identification

The responses of the ideal models and the actual drives are shown in Figure 6.7. As expected, the actual drives lag behind the ideal models. This is more evident on the vertical (Y) axis. In the previous section, the identified amplifier and motor parameters (Table 6.3) are shown to be accurate. If it is also assumed that, the calculated equivalent inertias are reasonably close to reality; then friction can be accounted for the deviation from the ideal responses.

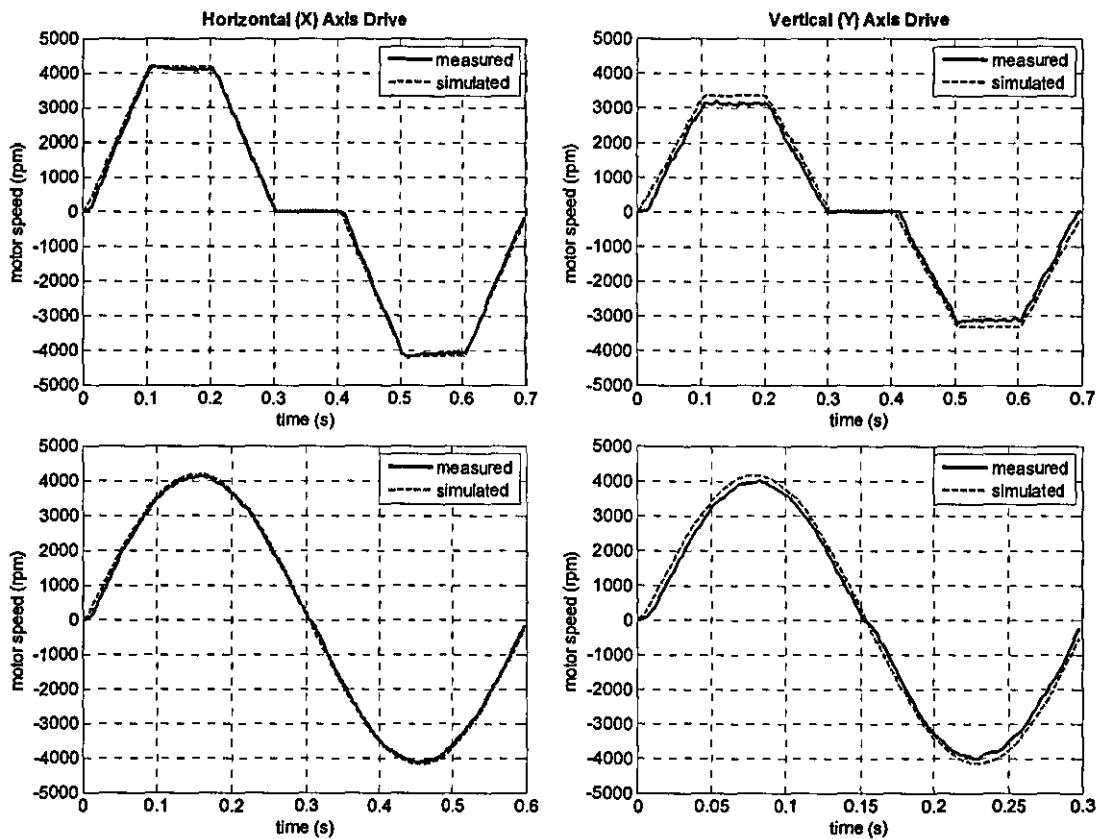


Figure 6.7 Ideal vs. actual drives

In the next section, sources and effects of friction are explained and its modeling, identification and simulation are presented.

6.4.2 Friction identification, modeling and simulation

Friction is always present in any physical system. In electro-mechanical drive systems, the source of friction [93] includes the motor and leadscrew bearings, the interface between the screw and nut, and the linear guide. Friction is difficult to measure and model, but is important to consider, because it can deteriorate the system performance. Friction models have been discussed extensively in the literature; for example [100], [101], [102], and [103]. It is well established that the friction force varies as a function of velocity, but there is not general agreement on the character of the friction force. Figure 6.8 illustrates a classical friction model, which combines the following four components of friction.

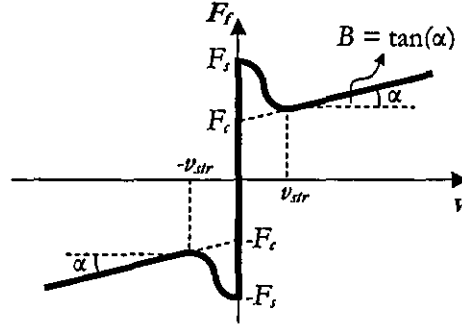


Figure 6.8 Classical friction model [98]

- ◆ **Static friction (Stiction):** It describes the friction force at rest. Static friction F_s counteracts external forces below a certain level and thus prevents an object from moving. The friction force F_f for zero velocity is a function of the external force F_e and not the velocity v . This can be modeled by equation (4.1), where F_s is the break-away force.

$$F_f = \begin{cases} F_e & , \quad v=0, |F_e| < F_s \\ F_s \cdot \text{sgn} F_e & , \quad v=0, |F_e| \geq F_s \end{cases} \quad (6.4)$$

- ◆ **Coulomb (dynamic) friction:** Coulomb friction F_c opposes motion and its magnitude is independent of velocity. It can therefore be described as;

$$F_f = F_c \cdot \text{sgn} v \quad (6.5)$$

- ◆ **Viscous friction (damping):** A friction component that is proportional to the velocity and, in particular, goes to zero at zero velocity. It is normally described as in equation (6.6), where B is the viscous damping coefficient.

$$F_f = B \cdot v \quad (6.6)$$

- ◆ **Stribeck friction (Stribeck effect):** More accurate modeling at very low velocities has shown that the friction force which falls from the break-away level F_s , to the Coulomb level F_c , is not discontinuous, but is a function of

velocity [100]. This continuous dependence of friction on velocity is called the *Stribeck curve*, and is described by;

$$F_f(v) = F_c + (F_s - F_c) \cdot e^{-|v/v_{str}|^k} \quad (6.7)$$

where v_{str} is called the *Stribeck velocity* and k is an empirical parameter.

Combining the individual models from (4.1) to (6.7) defines the classical friction model (Figure 6.8) in (6.8) and (6.9).

$$F_f = \begin{cases} F_f(v) & , v \neq 0 \\ F_e & , v = 0, |F_e| < F_s \\ F_s \cdot \text{sgn} F_e, v = 0, |F_e| \geq F_s \end{cases} \quad (6.8)$$

$$F_f(v) = \left[F_c + (F_s - F_c) \cdot e^{-|v/v_{str}|^k} \right] \cdot \text{sgn} v + B \cdot v \quad (6.9)$$

For Simulink implementation, some modifications are performed on the classical friction model. Firstly, the frictional force is modeled [52] simply as a disturbance voltage U_f to the single-axis drive (Figure 6.9) and, instead of the linear velocity v the angular velocity ω is used.

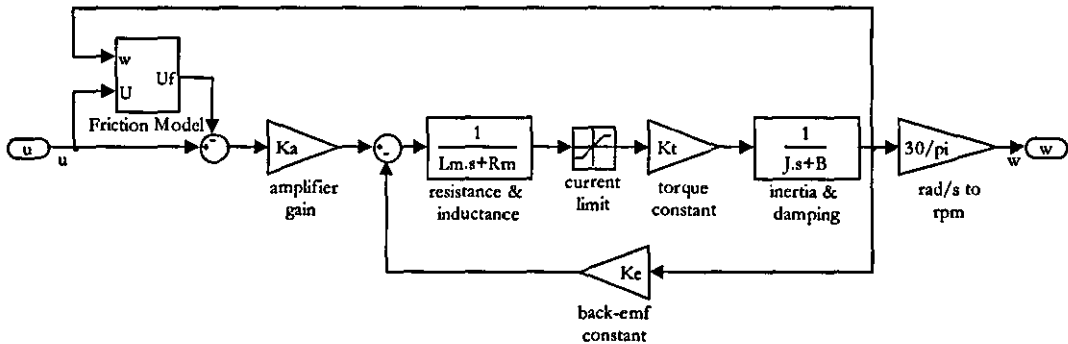


Figure 6.9 Single-axis drive model with friction

Secondly, since the viscous friction (damping) B is already included in the drive model, it is removed from the friction model.

Finally, the zero velocity is re-defined to be between $-\Delta$ and $+\Delta$ as presented in [104]. The reason for this is; because the model is used in a numerical simulation, there will be a ripple in velocity around zero. For example, when F_e is zero and v is positive, v will decrease to zero due to the frictional force F_f . When v goes to zero, there should be no friction acting on the drive and the drive should stop. However, it is difficult to integrate a function numerically and get exactly zero velocity. Thus, the Simulink integration routine will overshoot zero velocity and a negative velocity will result. This negative velocity will cause a positive friction force to be applied to resist the movement of the drive, which may again cause an overshoot, and as a result, the velocity v will oscillate around zero.

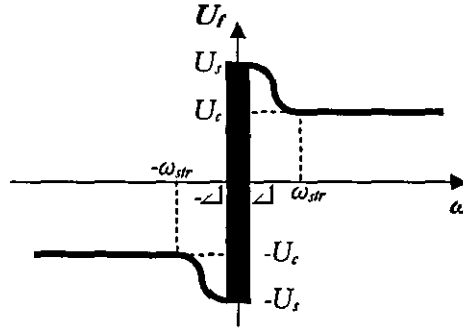


Figure 6.10 Modified friction model

Figure 6.10 depicts the modified friction model defined by the equations (6.10) and (6.11).

$$U_f = \begin{cases} U_f(\omega) & , \quad |\omega| > \Delta \\ U_e & , \quad |\omega| \leq \Delta, |U_e| < U_s \\ U_s \operatorname{sgn} U_e & , \quad |\omega| \leq \Delta, |U_e| \geq U_s \end{cases} \quad (6.10)$$

$$U_f(\omega) = \left[U_c + (U_s - U_c) \cdot e^{-[(|\omega| - \Delta) / (\omega_{str} - \Delta)]^k} \right] \cdot \operatorname{sgn} \omega \quad (6.11)$$

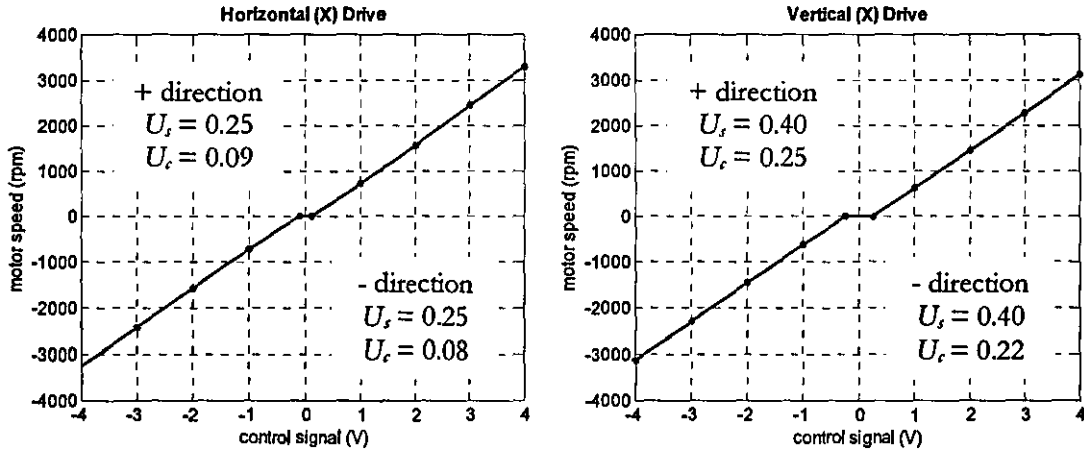


Figure 6.11 Steady-state curves of the horizontal (X) and vertical (Y) drives

Stiction U_s and Coulomb friction U_c values of the X and Y axis drives are determined by running several experiments; as presented in [52], [100], and [105]. The following experimental procedure is applied to positive and negative directions of motion.

1. Set the drive at rest.
2. Increase the control input until the drive starts to move.
3. Record this value of the control input as U_s .
4. Choose several equally spaced control inputs which are greater than U_s .
5. Apply these control inputs to the drive and record the steady state velocity.
6. Use a first order equation to fit these data points.
7. U_c is equal to the control input which corresponds to zero velocity.

The results of these experiments and the corresponding friction values are shown in Figure 6.11. Data points marked by '•' are the steady-state angular velocities of the step responses.

The zero velocity limit Δ is obtained by structured trial-and-error, where different values of δ near zero were tried until no ripple in the velocity was present [52].

The identification of Stribeck friction parameters k and v_{str} requires thorough investigation at extremely low speeds by using very accurate sensors [105]. This

investigation is beyond the scope of this research, and therefore, the empirical parameter k is taken from [105] as 2, and v_{str} is decided to be evaluated by structured trial-and-error. Likewise, the carriage damping coefficient B_c is also obtained by structured trial-and-error. In determining these parameters, numerous simulations are run with the inputs in Figure 6.6, and the results are compared to the measured data. The performance criteria are the previously explained IAE and ITAE.

The following table (Table 6.5) lists the values that achieved the lowest IAE and ITAE. For simplicity, the friction model is made symmetrical and the same values are used for both positive and negative directions of motion.

Parameter		Horizontal (X) Axis	Vertical (Y) Axis
Stiction break-away voltage (V)	U_s	0.25	0.4
Coulomb friction (V)	U_c	0.085	0.24
Re-defined zero velocity limit (rad/s)	Δ	0.1	0.1
Stribeck velocity (rad/s)	ω_{str}	140	120
Stribeck empirical parameter	k	2	2
Carriage viscous friction (damping) (Ns/m)	B_c	14	20
Equivalent damping coeff. (Nms/rad)	B	1.12×10^{-5}	1.26×10^{-5}

Table 6.5 Identified friction parameters

Figure 6.12 shows the results of the simulations including the modified friction model with the parameters in Table 6.5.

	horizontal (X) axis drive		vertical (Y) axis drive	
	trapezoid input	sinus input	trapezoid input	sinus input
acceleration zones (s)	(0 - 0.1) & (0.4 - 0.5)	(0 - 0.15) & (0.3 - 0.45)	(0 - 0.1) & (0.4 - 0.5)	(0 - 0.075) & (0.15 - 0.225)
deceleration zones (s)	(0.2 - 0.3) & (0.6 - 0.7)	(0.15 - 0.3) & (0.45 - 0.6)	(0.2 - 0.3) & (0.6 - 0.7)	(0.075 - 0.15) & (0.225 - 0.3)
OVERALL (s)	(0 - 0.7)	(0 - 0.6)	(0 - 0.7)	(0 - 0.3)

Table 6.6 Acceleration and deceleration zones

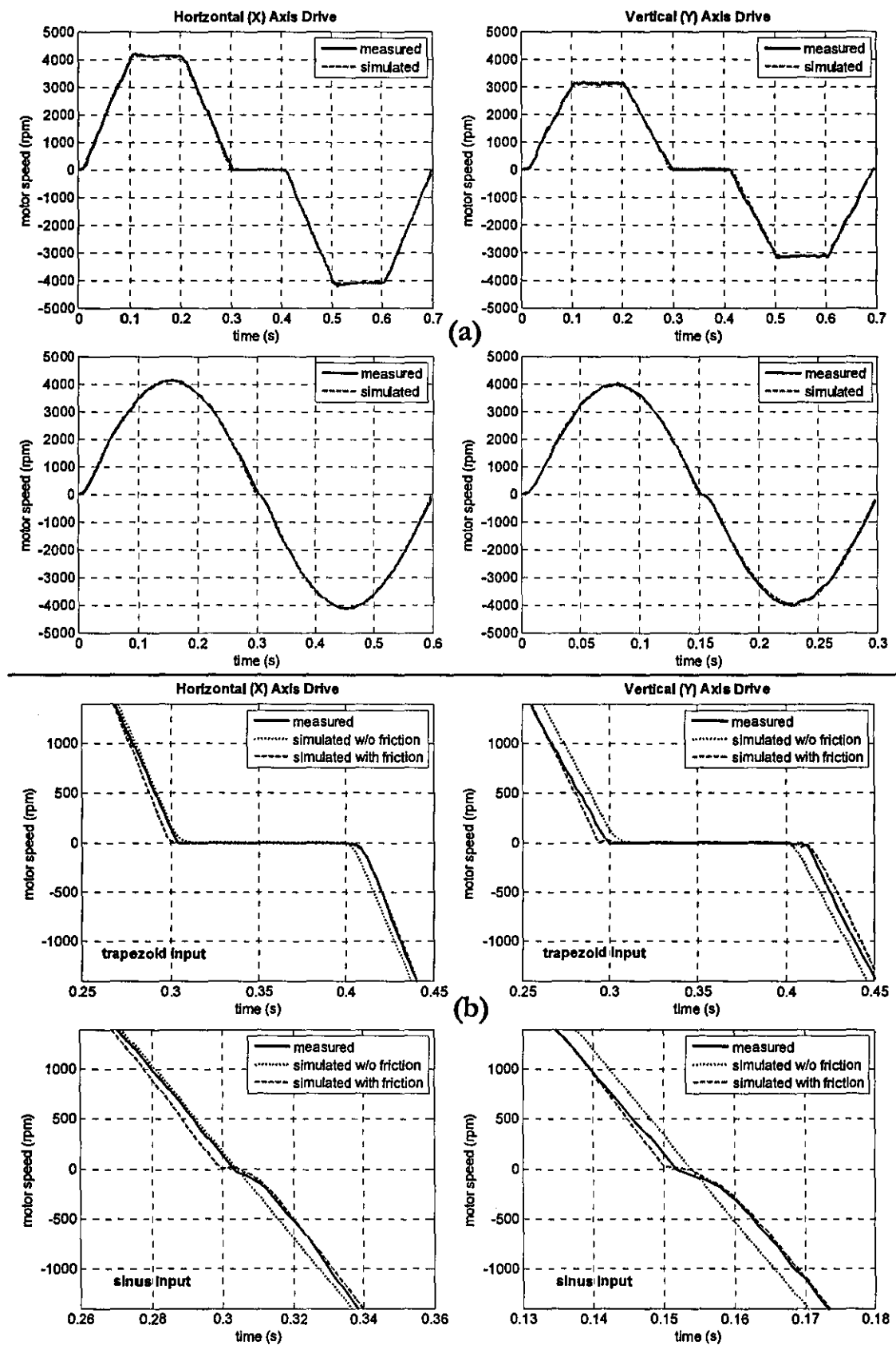


Figure 6.12 Simulation results with the modified friction model; (a) general performance, (b) acceleration & deceleration performance

	horizontal (X) axis drive				vertical (Y) axis drive			
	trapezoid input		sinus input		trapezoid input		sinus input	
	P_{IAE}	P_{ITAE}	P_{IAE}	P_{ITAE}	P_{IAE}	P_{ITAE}	P_{IAE}	P_{ITAE}
acceleration	0.228	0.162	0.234	0.269	0.300	0.409	0.224	0.302
deceleration	0.748	0.570	0.431	0.404	0.175	0.199	0.165	0.173
OVERALL	0.429	0.433	0.326	0.362	0.205	0.222	0.197	0.219

Table 6.7 Simulation performance with the modified friction model

Table 6.7 lists the performance factors P_{IAE} and P_{ITAE} relative to the ideal drive performance in Figure 6.7. The values for acceleration and deceleration are calculated for the corresponding zones in Table 6.6, and the overall values include the steady-state zones of the trapezoid responses.

As can be seen from Figure 6.12(a) and Table 6.7, inclusion of friction brought the drive models, especially the vertical drive, much closer to the actual drives compared to the frictionless ideal models in Figure 6.7. On average, the modeling error is reduced by 60% for the horizontal drive and 78% for the vertical drive.

In order to assess the performance of the friction model in more detail, zoomed views of acceleration and deceleration zones within the *Stribeck* regime are examined (Figure 6.12(b)). It was observed that; although the simulated accelerations are reasonably close to the actual drive performance, the decelerations lag behind the measured curve as the velocity decreases. A similar friction-velocity relation is observed in [106], where the friction force is found to be lower for decreasing velocities than for increasing velocities. This phenomenon is illustrated in Figure 6.13. The hysteresis loop becomes wider as the velocity variations become faster.

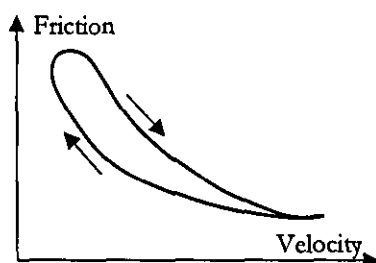


Figure 6.13 The friction-velocity relation observed in [104]

To remedy the deceleration lag, the friction model is further modified to bypass *Stribeck* regime during deceleration. The bypass decision is made by comparison of velocity ω and acceleration $\dot{\omega}$ directions. The acceleration is estimated by differentiating velocity with respect to time. The resulting friction model is illustrated in Figure 6.14, and is defined by (6.12) and (6.13).

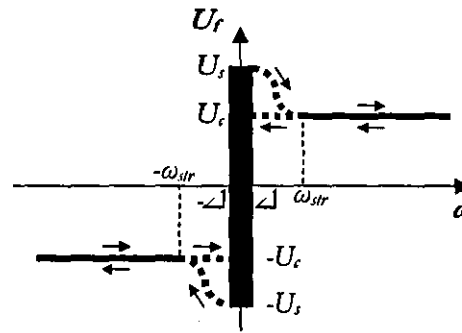


Figure 6.14 Final friction model

$$U_f = \begin{cases} U_f(\omega) & , |\omega| > \Delta, \text{sgn } \omega = \text{sgn } \dot{\omega} \\ U_e & , |\omega| \leq \Delta, |U_e| < U_s \\ U_s \text{sgn } U_e & , |\omega| \leq \Delta, |U_e| \geq U_s \\ U_c \cdot \text{sgn } \omega & , \text{otherwise} \end{cases} \quad (6.12)$$

$$U_f(\omega) = \left[U_c + (U_s - U_c) \cdot e^{-[(|\omega| - \Delta) / (\omega_{str} - \Delta)]^k} \right] \cdot \text{sgn } \omega \quad (6.13)$$

Simulations are repeated using the same parameters in Table 6.5 but with the final friction model. The results and the relative performance of simulations are given in Figure 6.15 and Table 6.8 respectively.

	horizontal (X) axis drive				vertical (Y) axis drive			
	trapezoid input		sinus input		trapezoid input		sinus input	
	P_{IAE}	P_{ITAE}	P_{IAE}	P_{ITAE}	P_{IAE}	P_{ITAE}	P_{IAE}	P_{ITAE}
acceleration	0.228	0.162	0.234	0.269	0.300	0.409	0.224	0.302
deceleration	0.507	0.442	0.261	0.256	0.158	0.149	0.154	0.164
OVERALL	0.358	0.364	0.246	0.261	0.201	0.213	0.188	0.208

Table 6.8 Simulation performance with the final friction model

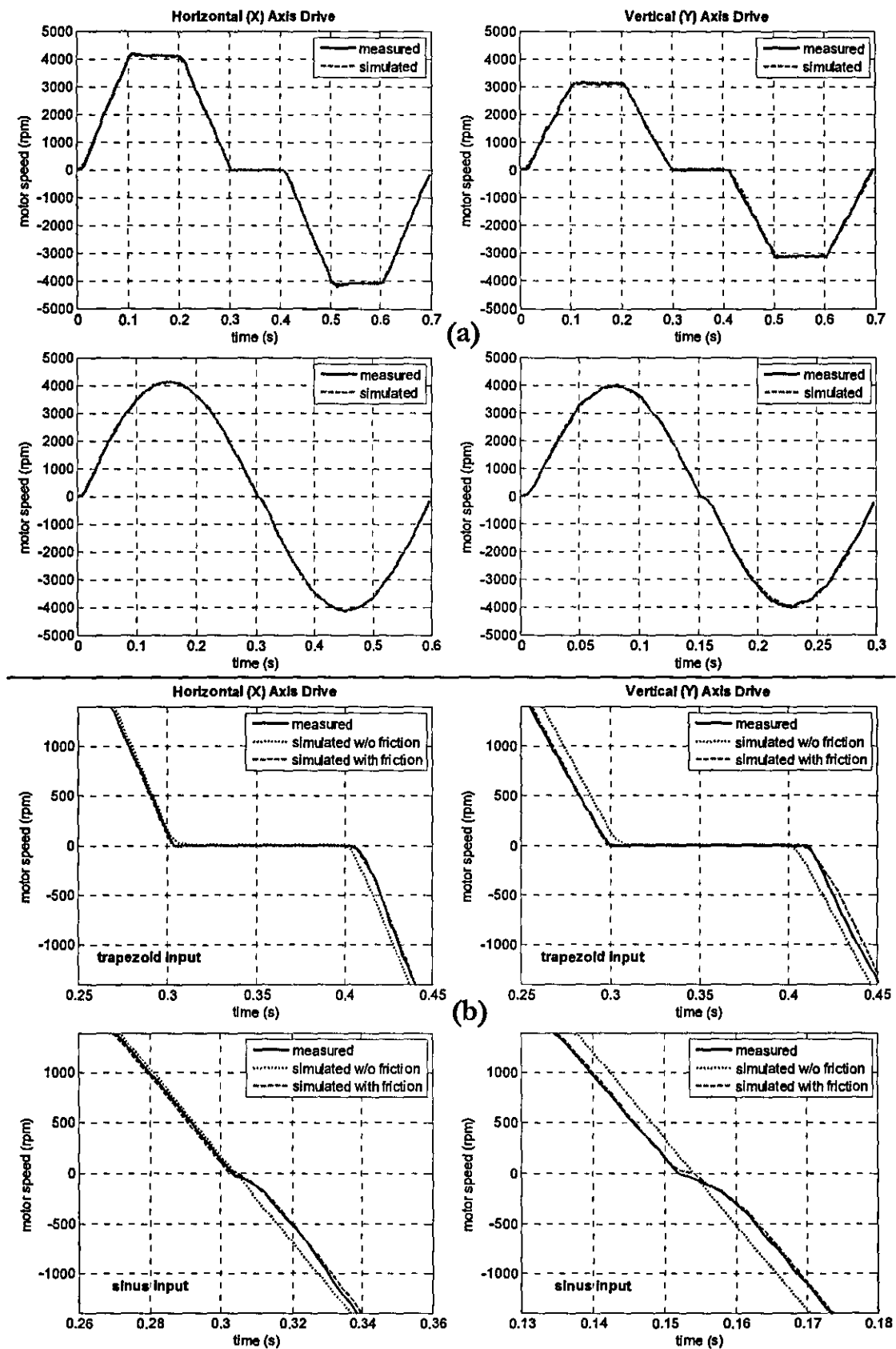


Figure 6.15 Simulation results with the final friction model; (a) general performance, (b) acceleration & deceleration performance

The final friction model remedied the deceleration lag, and the simulations performed equally well on both acceleration and deceleration zones (Figure 6.15(b)). Consequently, on average, the overall performance is further increased by 10% for the horizontal drive and 2% for the vertical drive (Table 6.8).

It should be noted that, even if friction identification aims at an accurate estimation of structural and parametric friction, there will always be some mismatch between estimated and actual friction [105]. However, using the identified values in friction compensation is proved [52][93][103] to increase drive performance and dynamics.

6.4.3 Validation of carriage weight in the Y-axis drive model

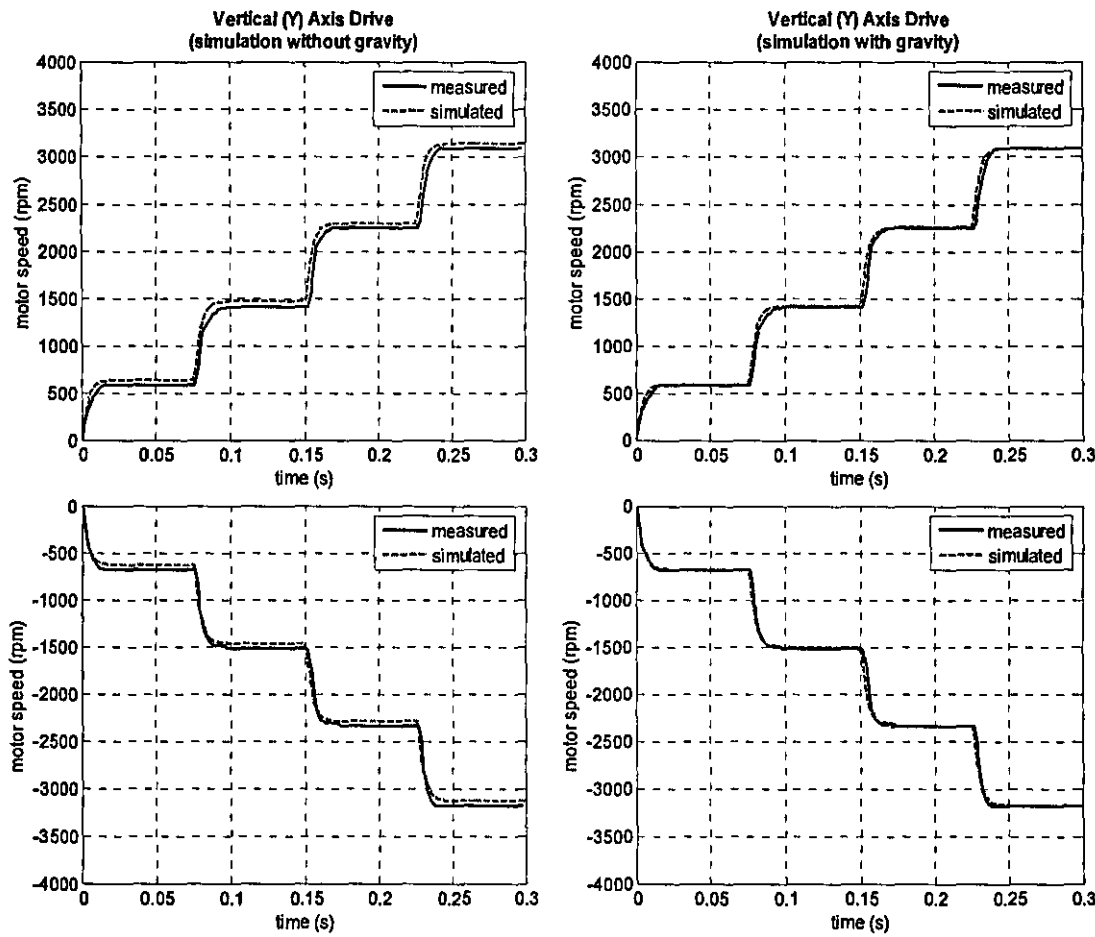


Figure 6.16 Effect of gravity on the vertical drive

The experiments reported in the previous sections of this chapter had been carried out while both of the drives operate on the horizontal plane. However, during the normal PIMM operation, the Y-axis drive works in the vertical plane and is affected by gravitational acceleration.

At this point; since the rest of the Simulink model is reasonably close to the actual system, the weight of the vertical carriage is added to the model. A set of simulations are run and compared to experiments, which are performed on the vertical plane, for verification. As the input, the control voltage is increased 1V at every 0.075s from 0V to 4V in positive and negative directions.

Figure 6.16 shows the simulation results against the measured data. As expected, in the absence of drive weight, the simulation is quicker on the positive Y (upwards) direction and slower on the negative (downwards) direction. Inclusion of the drive weight brings the simulation reasonably close to the measured data, and hence, verifies the Simulink model.

6.5 Summary

Initially, the mathematical models only contain parameters from manufacturer's datasheets and they do not include disturbances which surely exist in the PIMM test-rig. System identification procedures are employed in order to verify the known parameters as well as to discover the unknown disturbances.

In this chapter, the actual system parameters were identified by comparison of the simulated responses with the actual system response, which is captured via the previously explained Simulink RTWT model. Firstly, the accuracy of the RTWT model, in communicating with the actual system, was confirmed. Secondly, some parameters in the electrical part of the drives, namely the amplifiers and motors, were identified. Then, mathematical models were derived to represent drive friction, and the actual friction values were estimated. Finally, the carriage weight in the vertical (Y) axis drive model was validated. Table 6.9 shows the complete list of drive and friction parameters on the horizontal and vertical axes.

parameter			horizontal drive value	vertical drive value	
drive	amplifier gain	(V/V)	K_a	2.31	2.3
	amplifier current limit	(A)	I_{lim}	± 4	± 4
	armature inductance	(H)	L_m	0.00012	0.00012
	armature resistance	(Ohm)	R_m	0.582	0.582
	motor torque constant	(Nm/A)	K_t	0.0195	0.0195
	motor back-emf constant	(Vs/rad)	K_e	0.026	0.026
	leadscrew gain	(m/rad)	R_t	0.000477	0.000477
	equivalent inertia	(kgm ²)	J	3.61×10^{-6}	3.63×10^{-6}
	equivalent damping coeff.	(Nms/rad)	B	1.12×10^{-5}	1.26×10^{-5}
	carriage mass	(kg)	M	0.25	0.90
friction	stiction break-away voltage(V)		U_s	0.25	0.4
	Coulomb friction	(V)	U_c	0.085	0.24
	re-defined zero velocity limit (rad/s)		Δ	0.1	0.1
	Stribeck velocity	(rad/s)	ω_{str}	140	120
	Stribeck empirical parameter		k	2	2

Table 6.9 Final model parameters

It should be noted that, some mismatch always exist between a model and an actual system. However, the explained system identification procedures resulted in a more accurate representation of the PIMM test-rig by the mathematical models. This accuracy improvement was shown to be up to 80%. Furthermore, the identified friction can also be used for compensation purposes in order to increase the drive performance. The applied friction compensation technique will be presented in the next chapter, which discusses the machining experiments.

Chapter 7

Machining Investigations

7.1 Introduction

This chapter presents a discussion through machining experiments performed in the PIMM test-rig. The limitations and performance of the PIMM concept, in terms of speed and accuracy, are investigated. Weak points of the current implementation are identified and potential improvements suggested.

7.2 Machining Investigations

This section discusses the machining experiments.

7.2.1 Influence of the cutter thickness on the resultant profile

Despite being small (i.e. 1-2 mm), the cutter has a thickness on the plane of the profile (i.e. x-y plane). If not considered, the cutter thickness causes variance between the target and the resultant profile. A typical example of this is depicted in Figure 7.1.

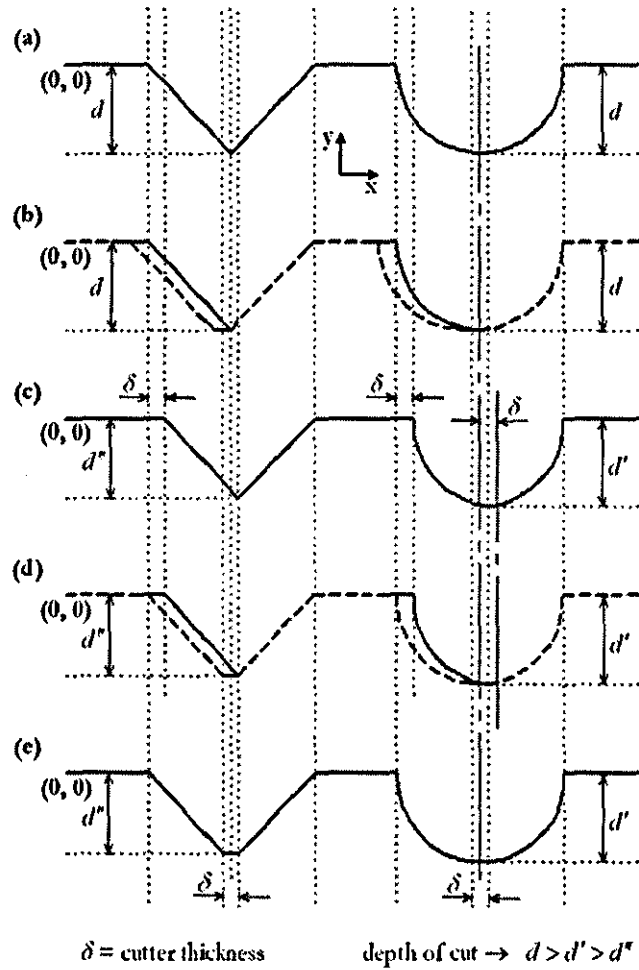


Figure 7.2 Effect of cutter thickness on concave features (a) target profile, (b) target and result without compensation, (c) compensated profile, (d) target and result with compensation, (e) result with compensation

In the previous example, the inaccuracy due to the cutter thickness is eliminated, but the target profile includes only convex features. On the other hand, concave detail is limited by the cutter thickness. An extreme case would be that of a slit, which is thinner than the cutter. The next example (Figure 7.2) describes the effect of the cutter thickness on concave features.

Figure 7.2(b) shows the resultant profile (dashed-lines) after the target in Figure 7.2(a) is machined without compensation. When the target is modified (Figure 7.2(c)) with the above described technique, the resultant profile matches the form of the original target (Figure 7.2(d)). However, the compensation in effect bypasses the parts of the features which are thinner than the cutter, and leaves flat

surfaces at the bottom (Figure 7.2(e)). Consequently, the depths of the resultant features are smaller (i.e. $d' < d$ and $d'' < d$). The amount of depth reduction depends on the cutter thickness δ as well as the profile geometry.

As a result, cutter thickness compensation eliminates the form variance between the target and resultant profiles. However, the concave detail will always be limited by the cutter thickness; hence it can be improved by using thinner cutters.

7.2.2 Path speed limitation due to the available cutting power

In the PIMM test-rig, described in Chapter 5, the path speed is primarily limited by the power of the cutter motor. As explained in Chapter 3; if the depth of cut and the cutter angular speed is kept constant, increasing the path speed results in larger chips to be severed, and therefore increases the cutting power.

To determine the maximum path speed for reliable operation of the cutter, a set of experiments are performed on a 70 mm wide redwood test specimen. The cutter speed, the depth of cut and the feed increment are set at 17000 rpm, 10 mm, and 1 mm respectively. Starting from 90 mm/s, the maximum path speed is increased by 10 mm/s after each pass, and the cutter speed is measured.

A significant reduction (i.e. 30%) in cutter speed is observed when the path speed is 140 mm/s, and on the following pass, when the path speed is 150 mm/s, the cutter is stalled. Consequently, the maximum path speed is limited to 130 mm/s.

7.2.3 Experiment setup

The experiments are performed on a 67.1 mm wide redwood specimen. As the reference input, the profile in Figure 7.3(a) is generated. A 1.6 mm thick, 4-tooth slotting saw is used as the cutter, and the reference profile is modified (Figure 7.3(b)) to compensate the cutter thickness.

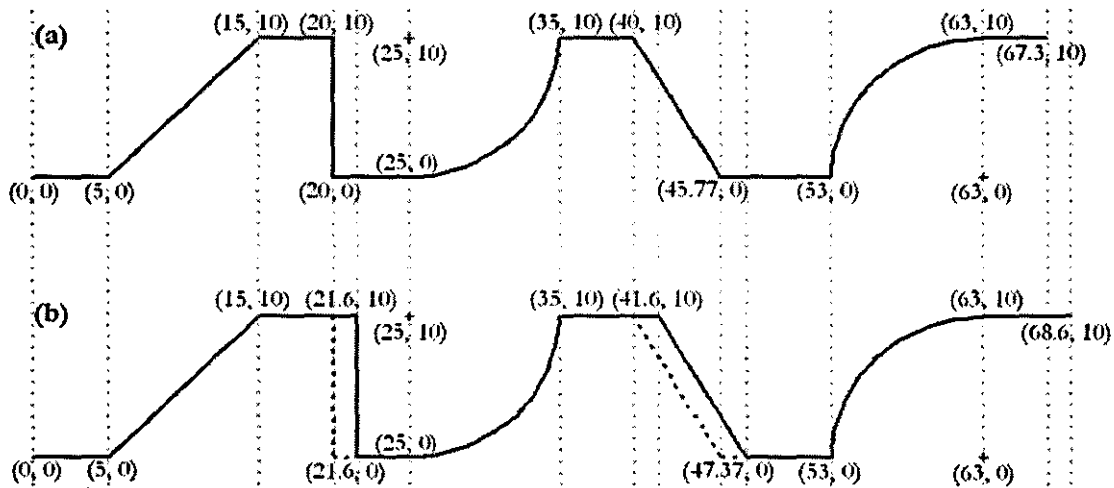


Figure 7.3 Reference input for the experiments (a) target profile (b) compensated profile

parameter		value	
cutter speed	(rpm)	ω	17000
feed increment	(mm)	f	1

Table 7.1 Machining parameters for the experiments

Path Controller			Reference Generator
tangential (T) axis		normal (C) axis	
end-point tolerance (mm)	N/A		0.1
loop type	position-velocity		N/A
position gain	K_p	80	200
velocity limit (mm/s)	V_{lim}	130	N/A
velocity gain	K_v	1.2	N/A
sampling frequency (kHz)			2

Table 7.2 Controller parameters for the experiments

Table 7.1 and Table 7.2, respectively, list the machining and controller parameters. The next section explains the friction compensation applied on the drives and the following sections discuss the results of the experiments.

7.2.4 Friction compensation

Based on the findings of Section 6.4.2, friction losses in the X and Y axis drives are compensated. The digital control signals C_x and C_y are enhanced with the compensation signals C_{fx} and C_{fy} such that:

$$C_x = C_x + Cf_x \quad (7.1)$$

$$C_y = C_y + Cf_y \quad (7.2)$$

Cf_x and Cf_y are calculated at every sample, based on the friction model defined by equations (6.14) and (6.15), but the *Stribeck* friction regime is ignored due to difficulties in estimating the acceleration from the encoder feedback. Equations (7.3) and (7.4) define the compensation signals, and the related parameters are listed in Table 7.3.

$$Cf_x = \begin{cases} Cs_x \cdot \text{sgn } C_x & , \quad |\dot{x}| \leq \Delta\dot{x} \\ Cc_x \cdot \text{sgn } \dot{x} & , \quad |\dot{x}| > \Delta\dot{x} \end{cases} \quad (7.3)$$

$$Cf_y = \begin{cases} Cs_y \cdot \text{sgn } C_y & , \quad |\dot{y}| \leq \Delta\dot{y} \\ Cc_y \cdot \text{sgn } \dot{y} & , \quad |\dot{y}| > \Delta\dot{y} \end{cases} \quad (7.4)$$

parameter		horizontal axis	vertical axis
Stiction break-away signal	C_s	200	250
Coulomb friction signal	C_c	80	200
Re-defined zero velocity limit (mm/s)	Δ	0.2	0.2

Table 7.3 Friction compensation parameters

7.2.5 Effects of cutting forces on the performance

In order to investigate the effects of cutting forces on the performance, in terms of accuracy and speed, two sets of experiments were carried out. Each set is composed of three left-to-right passes along the compensated test profile. The first set was performed without a workpiece (i.e. air cutting) and represents zero cutting force conditions. In the second set of experiments, a redwood specimen was machined.

Figure 7.4 shows the contour error plots from the experiments. For clarity, pass1 and pass3 data are shifted on the contour error axis by +0.2 mm and -0.2 mm respectively.

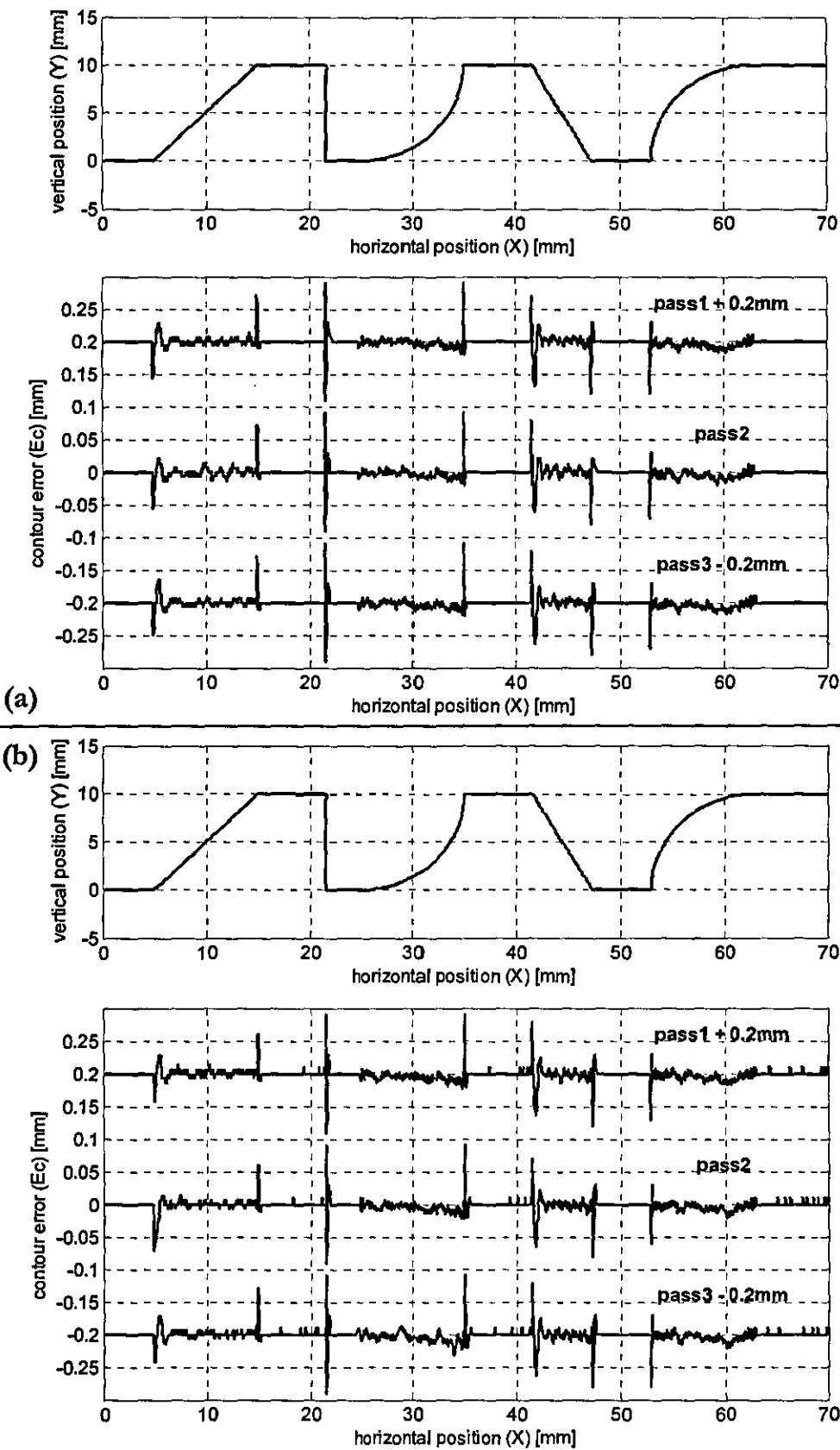


Figure 7.4 Contour error plots for (a) air cutting (b) wood cutting

The error spikes represent the segment end-points, where the next profile segment is supplied by the *Reference Generator*. In general, characteristic of the plots appear to be almost identical regardless of the cutting conditions. For further analysis, specific results are given in Table 7.4.

	air cutting			wood cutting		
	pass 1	pass 2	pass 3	pass 1	pass 2	pass 3
pass time (s)	1.274	1.285	1.273	1.259	1.261	1.240
max. contour error (mm)	-0.09	-0.09	-0.09	-0.09	-0.09	-0.09
mean contour error (mm)	0.005	0.005	0.005	0.005	0.005	0.005
IAE	10.30	10.82	10.36	10.72	11.01	11.01
ITAE	6.27	6.12	6.23	5.67	5.72	5.80

Table 7.4 Air cutting and wood cutting experiment results

Unexpectedly, the wood cutting passes are slightly faster (i.e. 1% to 3.6%) than the air cutting ones. This can be explained by the resistance of the workpiece against the cutter. The resistance causes the cutter to oscillate less after the error spikes; hence, the tangential effort component becomes slightly more dominant than the normal component. The reduced oscillation also explains the lower ITAE values of the wood cutting experiments. On the other hand, increased vibration due to the cutter-workpiece interaction can be accounted for the higher IAE values. The maximum value of the contour error is the same for all the passes to the hundredth of a millimeter. This value (i.e. 0.09 mm) also meets the accuracy target.

Based on the results above, it can be concluded that the effects of the cutting forces on the system performance is negligible for the experimented machining conditions. However, it should be reminded that the machining parameters and the velocity limit used in the experiments already consider the cutting power limitations (refer to Section 7.2.2). The mean path speed of the wood cutting experiments was recorded to be 80 mm/s, which is 40% less than the targeted 135 mm/s. Therefore it is better to say that, the effect of the cutting forces on the operation of the X-Y axis drives is negligible, provided that the cutting power is available for the desired task.

7.2.6 Comparison of the passes on different directions

The PIMM operates bi-directional on the X-axis; therefore it needs to perform similarly on left-to-right and right-to-left passes, in order to achieve the desired product quality. The wood cutting results of the previous section show the similarity of the individual passes when the profile is followed from left-to-right. In this section, those results are compared to another set of results obtained by machining the same profile on the same specimen, but from right-to-left.

Figure 7.5 shows the contour error plots from the experiments, and Table 7.5 lists the detailed results.

result	left-to-right			right-to-left		
	pass 1	pass 2	pass 3	pass 1	pass 2	pass 3
pass time (s)	1.259	1.261	1.240	1.253	1.242	1.250
max. contour error (mm)	-0.09	-0.09	-0.09	-0.09	-0.09	-0.09
mean contour error (mm)	0.005	0.005	0.005	0.005	0.006	0.005
IAE	10.72	11.01	11.01	11.06	11.88	11.17
ITAE	5.67	5.72	5.80	5.17	5.65	5.40

Table 7.5 Pass direction experiment results

The results in Table 7.5 do not indicate a significant dependence on pass direction in terms of pass times and accuracy. It means that the drives respond equally well to the control signals in both directions. However, due to the employed control logic, characteristic of the contour error plots shows differences depending on the pass direction (Figure 7.5). This is best observed at the error spikes representing reference switch from one segment to another. The *Reference Generator* supplies the next segment to the *Path Controller* when the distance to the end-point of the actively followed segment is less than the pre-defined tolerance. Also, the segment end-points are approached from different directions for left-to-right and right-to-left passes. Therefore, positions and magnitudes of the error spikes depend on the pass direction.

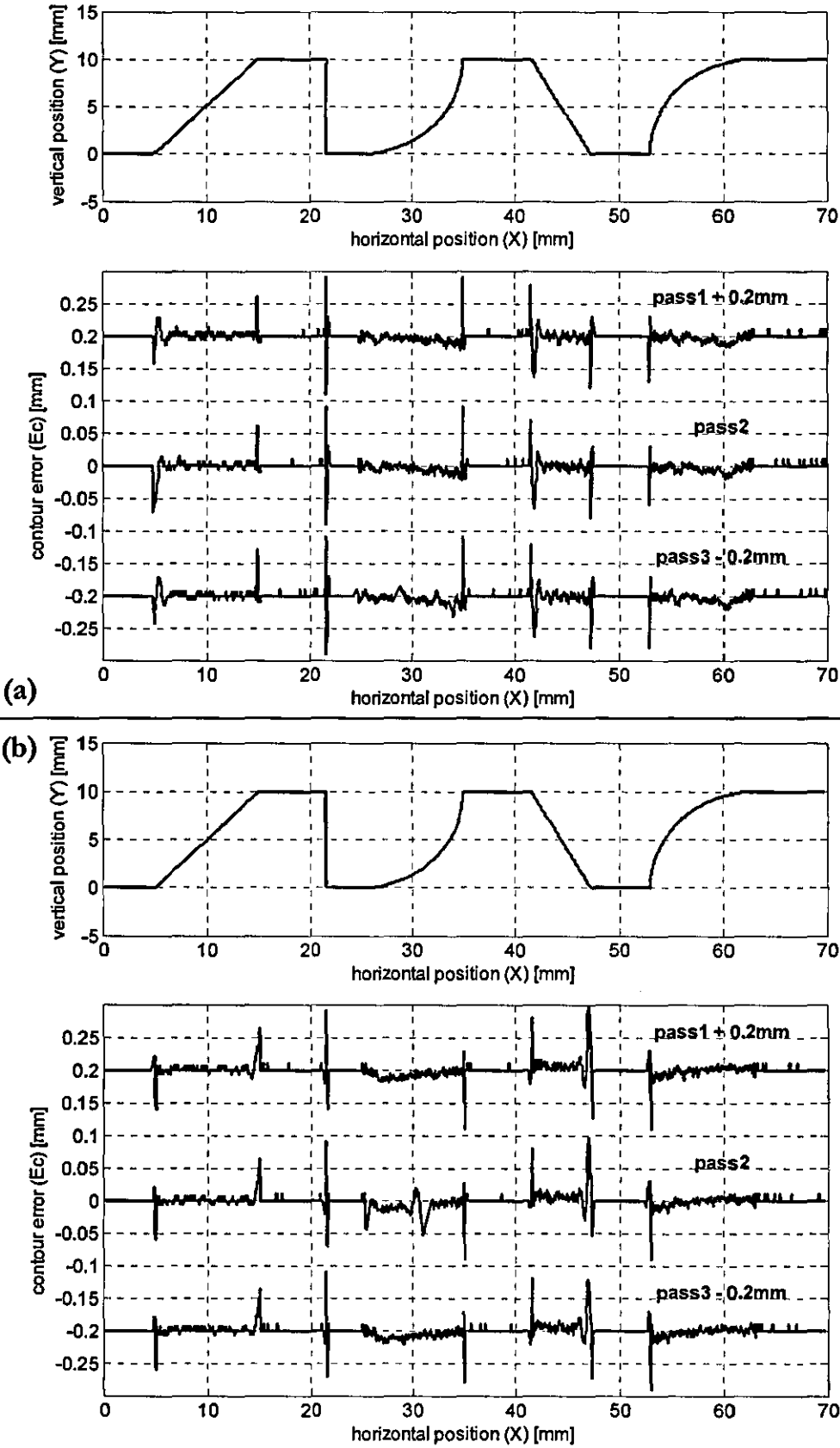


Figure 7.5 Contour error plots for (a) left-to-right passes (b) right-to-left passes

Table 7.6 lists the point coordinates (X, Y), where the reference is switched during the experiments. For example, on the left-to-right passes, the reference switches from the second segment to the third segment at (14.99, 9.94). At this point, the calculated contour error is referenced to the third segment (Figure 7.5(a)). Whereas on the right-to-left passes, the reference switches from the third segment to the second segment at (15.09, 10.00), and the error spike at this point represents the contour error value referenced to the second segment (Figure 7.5(b)).

compensated reference	left-to-right			right-to-left		
	pass 1	pass 2	pass 3	pass 1	pass 2	pass 3
5.00, 0.00	4.95, 0.01	4.92, 0.01	4.95, 0.01	5.07, 0.06	5.06, 0.06	5.07, 0.06
15.00, 10.00	14.94, 9.94	14.94, 9.94	14.94, 9.94	15.09, 10.00	15.09, 10.00	15.09, 10.00
21.60, 10.00	21.51, 10.00	21.51, 10.00	21.51, 10.00	21.60, 9.91	21.60, 9.91	21.60, 9.91
21.60, 0.00	21.60, 0.09	21.60, 0.09	21.60, 0.09	21.66, 0.00	21.67, 0.00	21.67, 0.00
25.00, 0.00	24.92, 0.00	24.92, 0.00	24.92, 0.00	25.09, 0.00	25.09, 0.00	25.06, 0.00
35.00, 10.00	34.99, 9.91	35.00, 9.91	35.00, 9.91	35.09, 10.00	35.09, 10.00	35.08, 10.00
41.60, 10.00	41.51, 10.00	41.52, 10.00	41.51, 10.00	41.64, 9.92	41.64, 9.92	41.64, 9.92
47.37, 0.00	47.33, 0.08	47.33, 0.08	47.33, 0.08	47.46, -0.01	47.43, 0.00	47.46, -0.01
53.00, 0.00	52.93, 0.00	52.94, 0.00	52.92, 0.00	53.00, 0.09	53.01, 0.09	53.01, 0.09
63.00, 10.00	62.91, 9.99	62.91, 9.99	63.00, 10.00	63.09, 10.00	63.09, 10.00	63.09, 9.99

Table 7.6 Reference switch points for passes on different directions

As mentioned previously, the position feedback is obtained from the encoders on the motor shafts. Hence, the presented error data do not provide information about the possible inaccuracy due to structural deformations in the system. The overall accuracy is investigated in the following two sections via measurements on the machined specimen.

7.2.7 Accuracy measurements on a Coordinate Measuring Machine

The specimen, which is used in the experiments of the previous sections, is measured in a Coordinate Measuring Machine (CMM). Three sets of measurements are performed on different locations along the Z-axis (i.e. along the length of the timber). The locations are 5 mm, 30 mm and 55 mm from the front face (Figure 7.6).

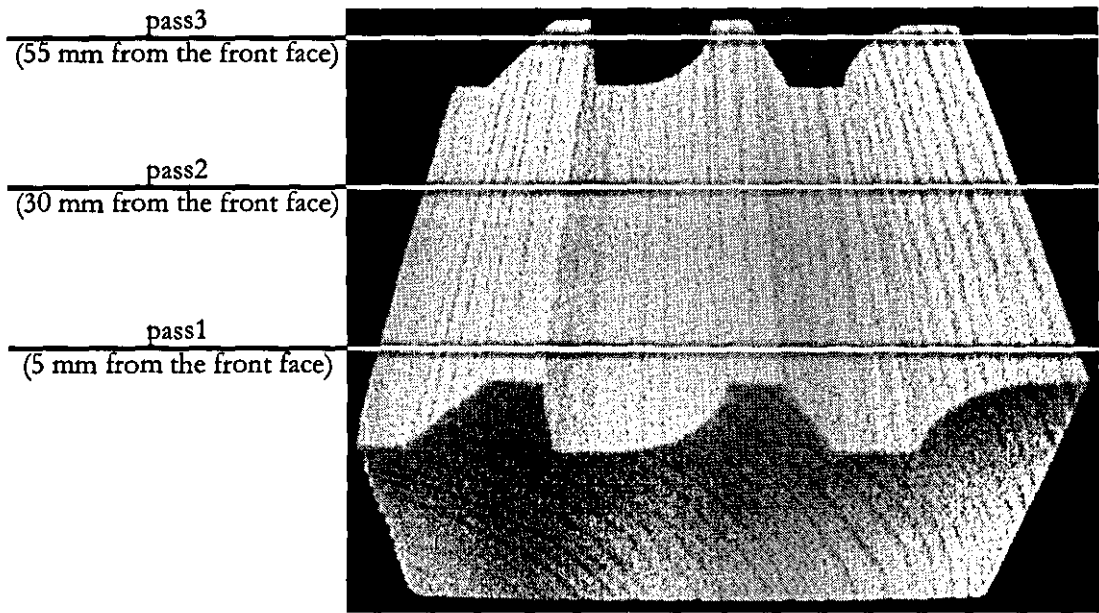


Figure 7.6 Measured specimen

In each measurement, the CMM probe is touched two arbitrary points per line segment and three points per arc segment. From the points, the equation of each segment is derived and the intersection points (X, Y) of the neighboring segments are calculated. Table 7.7 lists the intersection points, where the points joining a line and an arc segment are written in **bold**.

reference	pass1	pass2	pass3
5.00, 0.00	5.23, 0.00	5.16, 0.00	5.17, 0.00
15.00, 10.00	15.17, 10.01	15.16, 10.03	15.23, 10.02
20.00, 10.00	19.89, 9.96	19.85, 10.01	19.96, 10.00
20.00, 0.00	20.01, 0.06	20.07, 0.02	20.01, -0.05
25.00, 0.00	24.46, -0.03	24.88, 0.04	26.30, 0.43
35.00, 10.00	35.56, 9.98	35.70, 10.01	35.17, 10.00
40.00, 10.00	40.09, 9.98	40.13, 10.00	40.19, 10.03
45.77, 0.00	46.00, 0.04	46.07, 0.08	45.90, 0.14
53.00, 0.00	53.44, 0.05	53.49, 0.05	53.44, 0.00
63.00, 10.00	63.20, 10.01	63.18, 9.99	63.30, 10.05
IAE	2.58, 0.27	2.46, 0.26	3.18, 0.72
average error	0.26, 0.03	0.25, 0.03	0.32, 0.07

Table 7.7 CMM Results: Intersection point coordinates (X, Y) in millimeters

The IAE values in Table 7.7 are calculated by integrating the X and Y axis errors between the reference points and the calculated points of the passes. The average errors are calculated by dividing the IAEs to the number of intersection points. They show that the absolute error is up to nine-times greater on the X-axis than on the Y-axis.

	reference	reference - pass1	reference - pass2	reference - pass3	pass2 - pass1	pass3 - pass1	pass3 - pass2
	5.00, 0.00	0.23	0.16	0.17	0.07	0.06	0.01
	15.00, 10.00	0.17	0.16	0.23	0.02	0.06	0.07
	20.00, 10.00	0.12	0.15	0.04	0.06	0.08	0.11
	20.00, 0.00	0.06	0.07	0.05	0.07	0.11	0.09
	25.00, 0.00	0.55	0.13	1.37	0.43	1.90	1.47
	35.00, 10.00	0.56	0.70	0.17	0.14	0.39	0.53
	40.00, 10.00	0.09	0.13	0.19	0.04	0.11	0.07
	45.77, 0.00	0.23	0.31	0.19	0.08	0.14	0.18
	53.00, 0.00	0.44	0.49	0.44	0.05	0.05	0.07
	63.00, 10.00	0.20	0.18	0.30	0.03	0.11	0.14
total	IAE 1	2.65	2.48	3.16	1.01	3.02	2.74
	average error 1	0.26	0.25	0.32	0.10	0.30	0.27
w/o arcs	IAE 2	0.90	0.99	0.88	0.35	0.56	0.53
	average error 2	0.15	0.16	0.15	0.06	0.09	0.09

Table 7.8 CMM results: Calculated distances (mm) between the intersection points

Table 7.8 lists the calculated distances between the reference points and the points measured in CMM, as well as the distances between the points measured on different passes. Two different IAEs and average errors are calculated. The first ones (i.e. IAE 1, average error 1) include all the intersection points, whereas the second ones (i.e. IAE 2, average error 2), only include the points joining two line segments (i.e. excludes the values written in **bold**). Their respective comparison indicates that more than 65% of the total error (i.e. IAE) between the reference and the measurements is caused by the excluded points. Among different measurements, this goes up to 81% as in the case of pass3-pass1.

Excluding the aforementioned points, the measured intersection points deviate from the reference 0.16 mm on average with a maximum of 0.31 mm occurring in

the pass2. Within measurements the average deviation is 0.09 mm with a maximum 0.18 mm between pass3 and pass2.

	reference	pass1	pass2	pass3
Centre Point	25.00, 10.00	21.64, 10.95	24.86, 10.92	25.95, 9.37
Diameter (mm)	20	22.12	21.75	18.44
Centre Point	63.00, 0.00	62.99, 0.60	62.87, 0.67	36.37, 0.14
Diameter (mm)	20	18.94	18.81	19.87

Table 7.9 CMM results: Arc centre points and diameters

The greater errors occurring at arc intersections are primarily caused by the measurement method. As mentioned previously, three arbitrary points are taken from the arc segments. This allows the CMM to fit circles (Table 7.9) passing through the taken points assuming that the measured geometry is a perfect circular arc. In reality, however, this is not the case, and three points are not sufficient to provide information about the form of the arc. Moreover, the measured points are also affected by the surface texture of the timber. As a result, the fitted arcs and their intersection points with the other segments do not reflect the real geometry.

Overall, detailed results on the absolute accuracy could not be obtained from the CMM. On the other hand, the proximity of the three measurements along the Z-axis confirms the repeatability of the system. The next section presents an alternative measurement method by processing a scanned profile image.

7.2.8 Accuracy measurements of a scanned profile image

This section presents the measurements performed on a scanned profile image via image processing. In addition to coordinate and distance measurements, this method also allows visual comparison between the reference and the resultant profile by superimposing one over the other; hence provides insight about the form variations in the resultant profile.

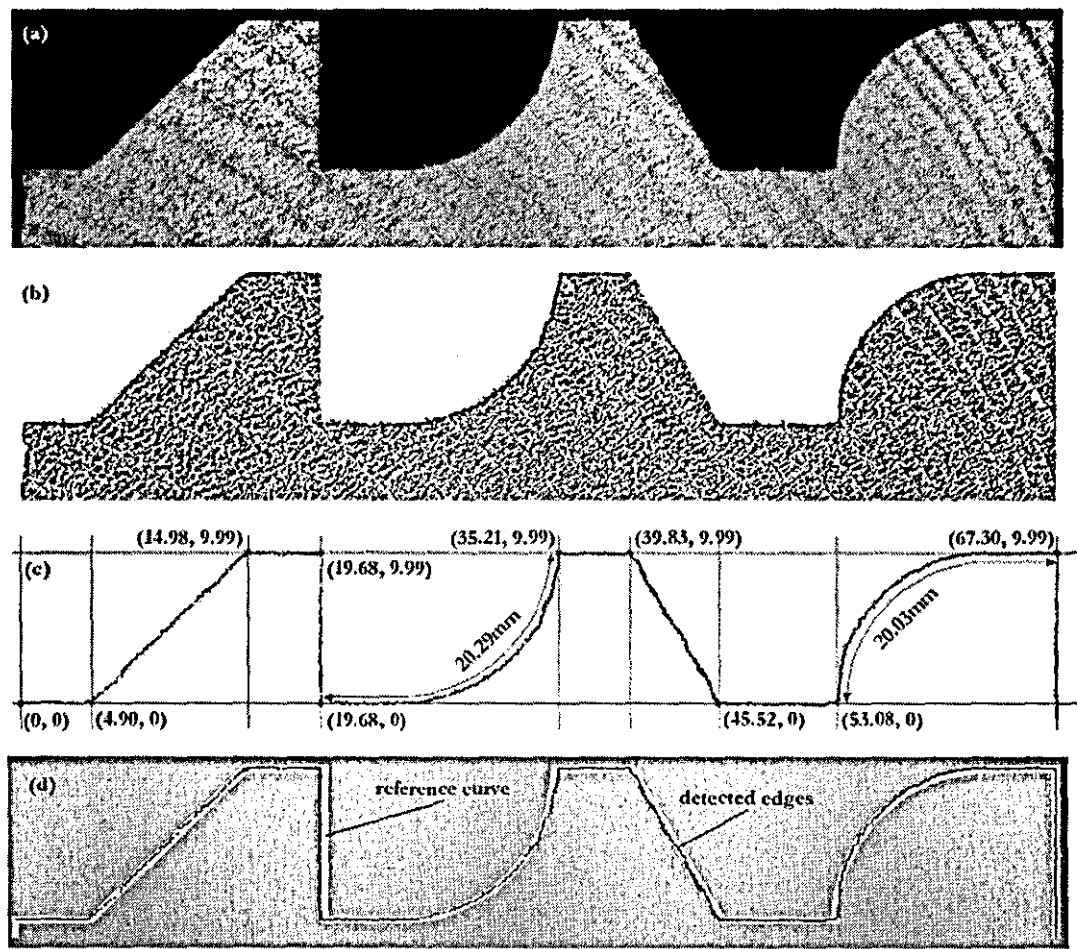


Figure 7.7 Measurements of a scanned profile image (a) scanned image (b) processed image (c) measurements on the detected edges (d) reference curve vs. detected edges

Firstly, the front face of the machined specimen is scanned with 600 dpi resolution (Figure 7.7(a)) on standard flatbed scanner. With this resolution, each pixel of an image corresponds to 0.042 mm. Secondly, the scanned image is processed (Figure 7.7(b)) in order to detect the edges of the profile. Then, the detected edges are extracted from the rest of the image and the intersection points are approximately marked (Figure 7.7(c)). Finally, the coordinates of the intersection points are measured in pixels relative to the left-hand-side edge of the profile.

The pixel coordinates are converted to millimeters and listed in Table 7.10. The highest errors (i.e written in *italic* in Table 7.10) appeared on the end-points of the segments that are compensated for the cutter thickness. This can also be observed

in Figure 7.7(d), where the detected edges are superimposed on the reference profile. To investigate the sources of these errors, the thickness of each cutter tooth is measured with a *Vernier* caliper. Three out of four is found to be 1.6 mm thick, but the other one is measured as 1.86 mm. This explains the occurrence of large errors on the compensated segments, and shows that the profiles should be compensated for the thickest tooth. If the difference between the tooth thicknesses is subtracted from the relevant calculated distances in Table 7.10, the total (i.e. IAE) and the average error values become 0.63 mm and 0.08 mm respectively. These values include two of the four arc end points. The other two could not be detected from the image due to smooth transitions between segments.

intersection points		distance
reference	image	refer.-image
5.00, 0.00	4.90, 0.00	0.10
15.00, 10.00	14.98, 9.99	0.02
20.00, 10.00	19.68, 9.99	0.32
20.00, 0.00	19.68, 0.00	0.32
25.00, 0.00	-	-
35.00, 10.00	35.21, 9.99	0.21
40.00, 10.00	39.83, 9.99	0.17
45.77, 0.00	45.52, 0.00	0.25
53.00, 0.00	53.08, 0.00	0.08
63.00, 10.00	-	-
IAE	1.47, 0.04	1.47
average error	0.18, 0.01	0.18

Table 7.10 Image processing results: Intersection point coordinates (X, Y) and their calculated distances to the reference points

In Figure 7.7(d), the reference profile virtually passes through the centre of the white line, which is 0.42 mm (i.e. 10 pixels) thick. Thus, any point on the white line is within 0.21 mm proximity to the reference profile. The black line is the extracted edge of the scanned profile and its average thickness is measured to be 0.17 mm (i.e. 4 pixels). If it is assumed that the real edge passes through the centre of the black line; then the maximum error becomes 0.125 mm (i.e. $(0.42-0.17)/2$) while the white line covers the black line. This condition occurs at the majority of

points along the profile. Therefore, based on this measurement method, it can be concluded that the accuracy of the system is within ± 0.125 mm.

The image processing method is believed to provide more accurate results if applied on the images of plastic specimens. Machining of plastics in the PIMM is potentially possible but has not been investigated in detail. However, it is recommended for future work.

7.3 Investigation of Design Improvements via Simulation

The machining investigations confirmed that the targeted accuracy can be achieved. On the other hand, it is shown that the designed test-rig can not meet the production rate target due to reduced path speed caused by the limited cutting power. The cutting power, and consequently the path speed, can be increased by replacing the cutter motor with a more powerful one. This possibly results in a re-design of the cutter assembly and may require additional power transmission hardware. In any case, using a more powerful motor increases the weight of the cutter assembly.

The aim of this section is to determine the effects of increased drive weight on the performance due to possible replacement of the cutter assembly. This is explored through software simulations and presented in Section 7.3.2. Prior to that, in Section 7.3.1, validity of the simulated system is confirmed through comparison against the actual system.

7.3.1 Comparison of the actual and simulated systems

The moulding in Figure 7.8 is machined by the PIMM test-rig using the controller parameters in Table 7.2. The same profile is also supplied as the input to the Simulink model. The simulated system used the same controller parameters as the actual system, together with the drive model parameters in Table 7.11. During machining, the drive friction is compensated as described in Section 4.2.4; hence the friction model is disabled in the simulated system.

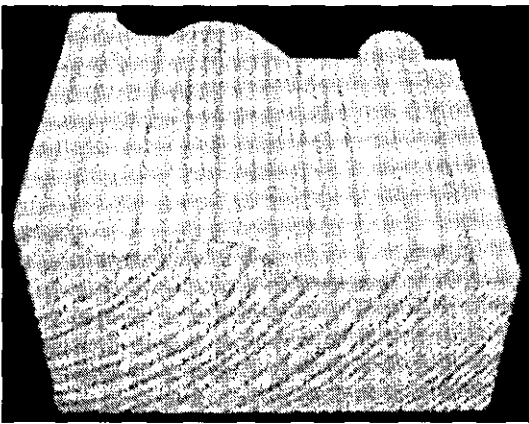


Figure 7.8 A typical moulding machined by the PIMM test-rig

parameter				horizontal drive value	vertical drive value
D/A limit				± 8192	± 8192
D/A gain	(V)	K_d		10/8192	10/8192
amplifier gain	(V/V)	K_a		2.31	2.3
current limit	(A)	I_{lim}		± 4	± 4
armature inductance	(H)	L_m		0.00012	0.00012
armature resistance	(Ohm)	R_m		0.582	0.582
motor torque constant	(Nm/A)	K_t		0.0195	0.0195
motor back-emf constant	(Vs/rad)	K_e		0.026	0.026
leadscrew gain	(m/rad)	R_s		0.000477	0.000477
equivalent inertia	(kgm ²)	J		$3.61 \cdot 10^{-6}$	$3.63 \cdot 10^{-6}$
equivalent damping coeff.	(Nms/rad)	B		$1.12 \cdot 10^{-5}$	$1.26 \cdot 10^{-5}$
carriage mass	(kg)	M		0.25	0.90
cutting force	(N)	F_c		5	5

Table 7.11 Drive model parameters

Figure 7.9 shows the experiment and simulation results for a single left-to-right pass along the width of the workpiece. The profile in Figure 7.9(a) is the compensated target for 1.6 mm cutter thickness (see Section 7.2.1). The contour error and path speed curves from the simulation (Figure 7.9(b), (d)) bear a high resemblance to the ones from the experiment (Figure 7.9(c), (e)). As mentioned previously, the velocity is estimated in the actual system by differentiating the position feedback. Therefore, the noise in the path speed curve is expected. The two sharp velocity peaks, which correspond to the midpoints of the arc segments, are due to short line segments (i.e. 1.6 mm long) that are added to the target profile for cutter thickness compensation.

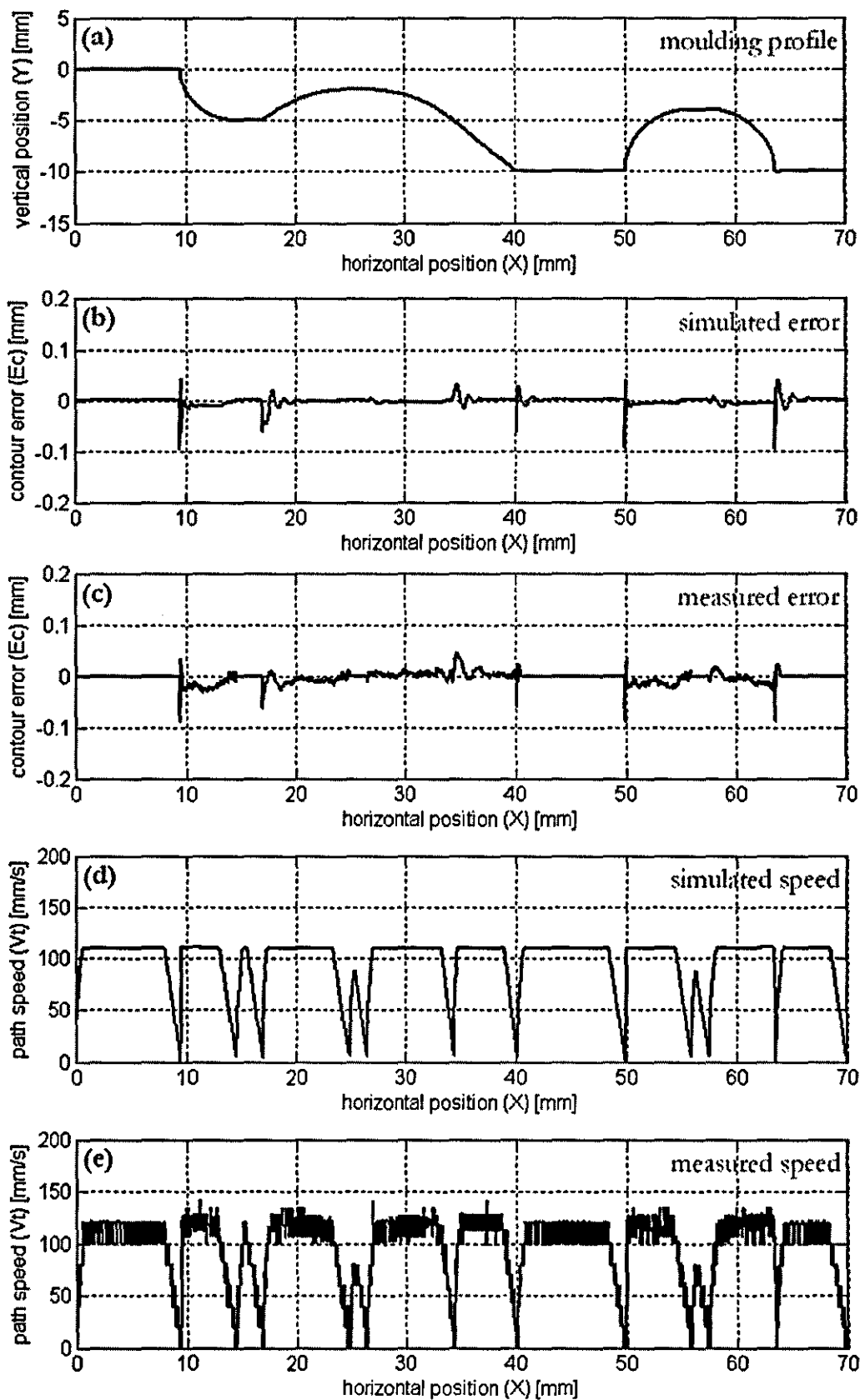


Figure 7.9 Experiment and simulation results (a) moulding profile (b) simulated error (c) measured error (d) simulated speed (e) measured speed

result		simulation	experiment
pass time (s)	t	1.135	1.137
mean path speed (mm/s)	V_{mean}	72.81	72.64
max. contour error (mm)	e_{max}	-0.09	-0.09
mean contour error (mm)	e_{mean}	0.005	0.006
IAE		12.30	13.87
ITAE		6.97	7.84

Table 7.12 Comparison of the experiment and simulation results

Table 7.12 lists the key performance measures of the experiment and simulation results. Comparison of these proves that the simulated system represents the behavior of the actual system to a high level of accuracy. Consequently, the effects of modifications on the performance can be investigated solely by software simulations. An example of this is presented in the next section, where the effect of drive weight on the performance is explored via simulations.

7.3.2 Effects of increased drive weight on the performance

The cutter assembly of the PIMM test-rig features an overhung spindle arrangement, where a 22 mm diameter, 50 W rated brushless motor directly connects to a 50.8 mm diameter cutter. This design imposes two major limitations on the overall system performance. The first one is the aforementioned (see Section 7.2.2) path speed limitation and the second one is the depth of cut limitation. Due to concentric alignment of the motor and the cutter, the maximum depth is equal to the difference between the cutter and motor radii (i.e. 14.4 mm). The limit can be improved by either using a larger diameter cutter or by placing the motor away from the cutter and using power transmission hardware. Either way results in a heavier cutter assembly. Moreover, as explored in Chapter 3, deeper cuts require more cutting power, which the system already lacks even at 10 mm depth of cut. Therefore, in a case of re-design, the first priority is the replacement of the cutter motor with the one which is at least twice as powerful; and this, also results in a heavier cutter assembly.

In order to check whether the cutting power is the only limiting factor on the path speed, the currently used cutter motor is assumed to deliver unlimited power, and the system is simulated to achieve the performance targets (i.e. speed and accuracy). Both controllers (i.e. tangential and normal) are switched to cascaded position-velocity mode and the velocity limit is set at 200 mm/s. The controller gains are tuned until the mean path speed reached within 5% to the target speed of 135 mm/s. The accuracy target, on the other hand, is not tolerated. The tuned controller parameters are given in Figure 7.10 together with the achieved simulation results.

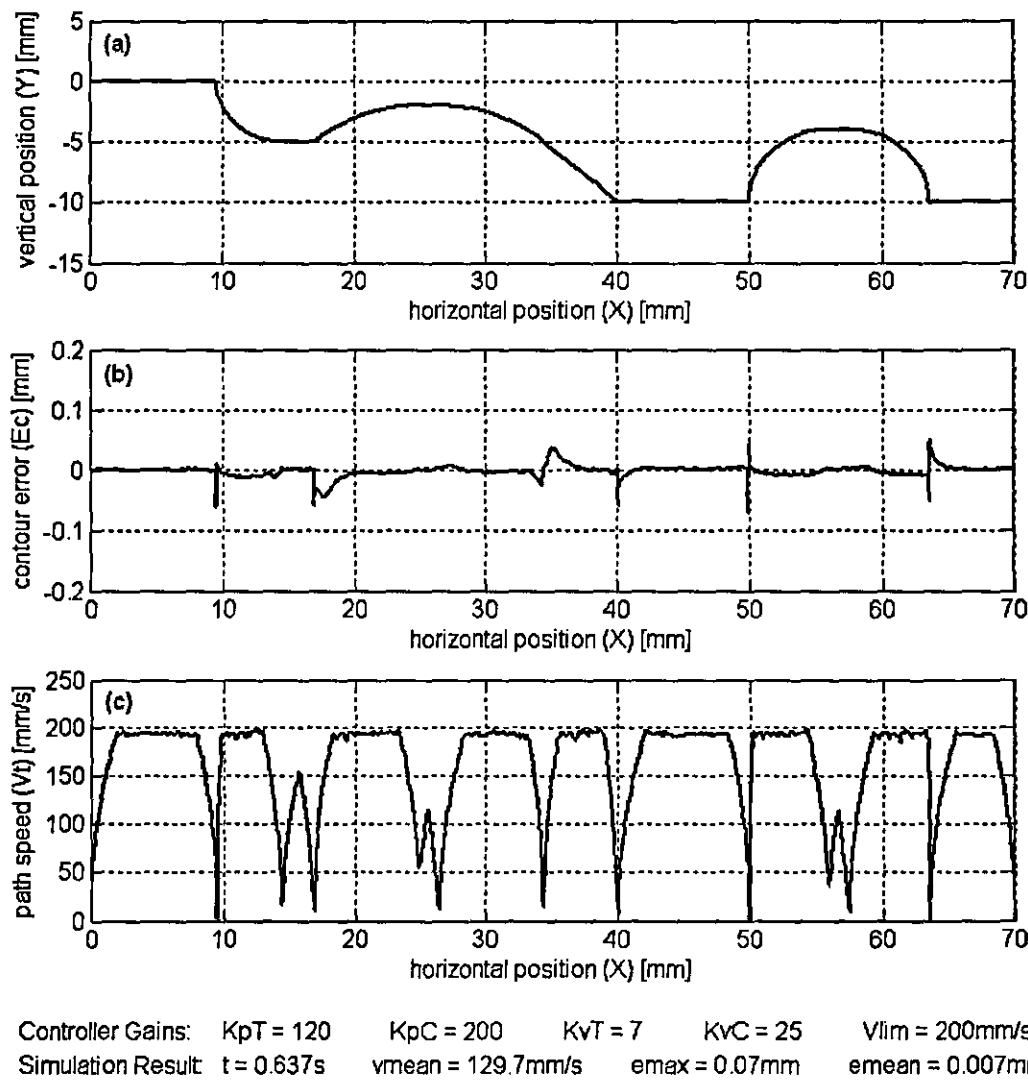


Figure 7.10 Simulation results: increased speed limit (a) profile (b) contour error vs. horizontal position (c) path speed vs. horizontal position

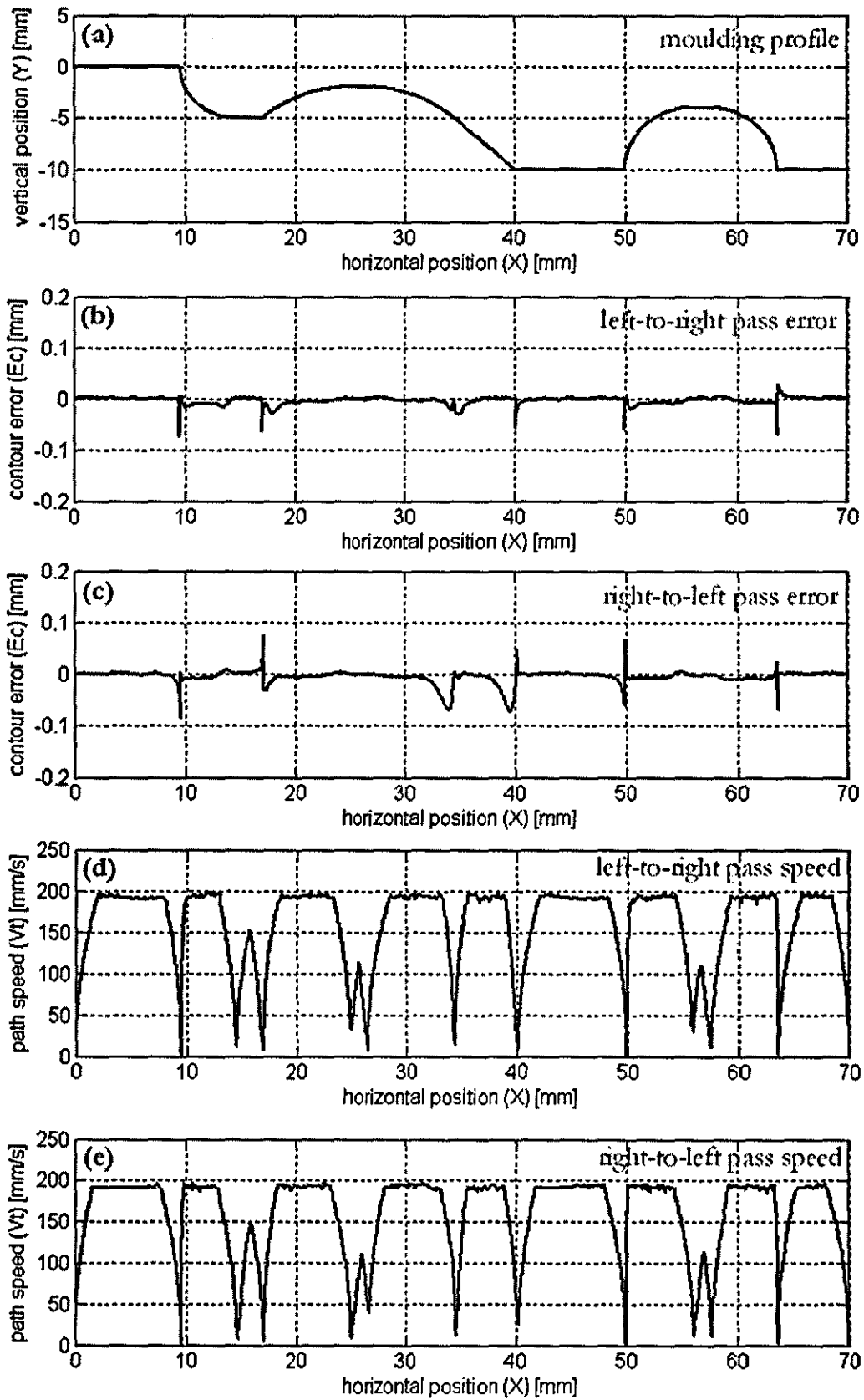


Figure 7.11 Simulation results: increased weight (a) moulding profile (b) left-to-right pass error (c) right-to-left pass error (d) left-to-right pass speed (e) right-to-left pass speed

For the second simulations, it is assumed that the cutter assembly is re-designed so that the maximum depth of cut is 25 mm, and the cutting power is sufficient to cut within the range of achievable path speeds. Consequently, the weight of the cutter assembly is increased from 0.25 kg to 0.60 kg. This increase is reflected to the carriage masses of the horizontal and vertical drives as in Table 7.13. It is also assumed that the point (0, 0) is 15 mm below the top surface of the un-machined specimen. Thus, the maximum depth of the simulated profile becomes 25 mm. The increase in the depth of cut is reflected to the simulated system as increased cutting force (Table 7.13). The simulations are performed with the same controller parameters as in the previous simulation for the both pass directions, and the results are shown in Figure 7.11 and Table 7.14.

parameter		horizontal drive		vertical drive	
		before	after	before	after
carriage mass (kg)	M	0.25	0.60	0.90	1.25
cutting force (N)	F_c	5	12.5	5	12.5

Table 7.13 Modified simulation parameters

result		left-to-right	right-to-left
pass time (s)	t	0.654	0.650
mean path speed (mm/s)	V_{mean}	126.36	126.97
max. contour error (mm)	e_{max}	-0.07	-0.09
mean contour error (mm)	e_{mean}	0.006	0.008

Table 7.14 Simulation results for left-to-right and right-to-left passes

The accuracy target is achieved on both pass directions. Increase in drive weights and cutting forces, reduced the mean path speed slightly (i.e.2.5%) compared to the previous simulation. However, the results are still close to the target by 6.4% on the left-to-right pass and 5.9% on the right-to-left pass.

As a result, the PIMM can also achieve the speed target provided that the cutting power is sufficient through the operation range of X-Y axis drives. The increased drive weights and cutting forces, due to a re-design of the cutter assembly, do not affect the tracking accuracy.

Chapter 8

Conclusions and Further Work

8.1 Conclusions

An integrated mechatronic design approach aiming at holistic development of the Profile Independent Wood-Moulding Machine (PIMM) has been presented. Investigation of the proposed machining method, as defined in the research objectives, has involved many facets of study. The key conclusions from these studies, which have been considered in detail within the main body of the thesis, are outlined as follows:

The material removal phenomena and the cutting forces occurring in the proposed machining method were explored by a series of experiments. The effects of cutting tool and machine parameters on the cutting power were identified. It was found that the cutting forces are in the order of up to 5 N, and they do not directly affect the cutter traversing speed. On the other hand, they have to be considered for the selection of the cutter motor because insufficient cutting power causes the cutter to stall. For general PIMM operation, the cutting power requirement is found to be 100 W.

An algorithm was created for extracting moulding profile geometry from CAD files in 'dxf' format. The current implementation extracts the geometry of a single face, but it can be easily modified for multiple faces.

A mathematical modeling framework has been developed for simulation of the cutter positioning on the X-Y frame. The modeling framework was used during the selection of test-rig actuators, and also for the controller design. Mathematical modeling and simulation allowed performance evaluation of various hardware and control alternatives, and enabled identification of the optimum solution for the system. The implemented motion control algorithm decouples the control efforts on the directions tangential and normal to the followed path. This allowed, within limits, independent control of pass speed and contour error.

Based on the outcome of the mathematical simulations, a PIMM test-rig was built in order to evaluate the performance of the proposed concept experimentally. In designing the test rig, a modular approach has been followed. The test rig was divided to four sub-systems as cutter assembly, horizontal drive, vertical drive, and timber feed drive which also acts as the frame of the machine. This modular design approach allowed different designs of one or more subsystems to be experimented while the rest of the test-rig remains unchanged. Small magnitudes of the forces generated in the process allowed the use of rapid prototyping plastics for various parts of the test-rig. With the help of rapid prototyping, the initial build time of the test-rig and also the modification times were considerably shortened.

After the test-rig was built, experimental system identification procedures were performed. System identification allowed compensation of the previously unknown disturbances (i.e. drive friction) in the controller. Also, the mathematical models were modified with the identified parameters to minimize the difference between simulated and actual responses. The resulting accurate models enabled exploration of the design improvements via simulation.

For experimental verification of the proposed concept, machining experiments were conducted. The results confirm the effectiveness of the PIMM. The current system is ± 0.1 mm accurate and it positions the cutter with a mean path speed of 73 mm/s. This corresponds to 0.086 m/min production of 100 mm wide mouldings with acceptable quality (i.e. surface wave pitch $p=2.5$ mm). It was shown through simulation that 0.150 m/min production rate is possible by using a more powerful cutter motor.

Further research on the system is needed to fully exploit its capabilities. A number of areas have been identified for further work and given in the next section.

8.2 Recommendations for Further Work

The suggestions listed below provide some possible directions for further work which could be carried out to extend the existing system boundaries.

8.2.1 Cutter assembly

The PIMM test-rig used an off-the-shelf slotting cutter, and dedicated cutter design has not been performed. A cutting tool, specific to the PIMM, needs to be designed for optimum performance. Cutter diameter, kerf thickness, number of teeth, and tooth geometry can be listed as the important parameters to consider for the cutting tool design.

It was explained that the test-rig could not meet the production rate target due to reduced path speed caused by the limited cutting power. The cutting power, and consequently the path speed, can be increased by replacing the cutter motor with a more powerful one. This possibly results in a re-design of the cutter assembly and may require additional power transmission hardware.

8.2.2 Timber feed mechanism

Timber feed mechanism of the PIMM test-rig was designed as a temporary solution to accommodate small test specimens during proof-of-concept investigations. Due to time limitation, methods for feeding longer workpieces could not be explored. A new mechanism needs to be designed in order to feed workpieces up to 2 m in length.

8.2.3 Surface roughness

Based on visual inspection, roughness of the surfaces produced by PIMM is adequate, but the machined specimens were not subjected to detailed measurements. Surface roughness is primarily influenced by workpiece and cutting tool properties. However, comparative measurements with conventionally machined specimens can be useful in determining the possible influence of machining method on surface roughness.

8.2.4 Cutting materials other than wood

It is foreseen that the PIMM can process materials such as plastics, stones and soft metals. Investigation of this issue is recommended to be pursued together with the cutting tool design.

8.2.5 Processing with multiple PIMMs

Multiple PIMMs can be arranged in parallel or in series. In a parallel arrangement, all the PIMMs can be controlled from the same computer and the rate of production is proportional to the number of PIMMs. Alternatively, provided that each PIMM has its own controller, different profiles can be sent to different PIMMs from a top-level control computer. In a series arrangement, a single timber feed drive can be used; one of the cutters takes a rough cut from the workpiece and the other performs the detailing.

8.2.6 Change of profile along the length

Theoretically in PIMM, profile of the moulding can be changed along its length. This is not possible in the conventional machines, and it is not known if this would be desirable in any market. The limits of profile change and the possible applications of the products require further research.

8.2.7 Processing with additional vertical spindle

An additional cutter assembly can be designed to accommodate a vertical spindle and the PIMM can be used for other machining operations such as routing, milling, engraving and drilling. Other than the hardware, this requires modification of the software and the control algorithms.

8.2.8 Portable PIMM

In this thesis, the PIMM is designed as a PC-based system. Besides many advantages, the PC limits the portability of the system. The PC can be replaced by a dedicated embedded controller and this eliminates the operating system and software dependencies of the PIMM.

Some hardware modifications are also possible in order to aid the system portability. For example, the X and Y axes can be designed to move along the Z axis so that the PIMM can be operated on vertical surfaces and ceilings. This is believed to be desirable in architectural restoration jobs.

References

-
- [1] Jackson, M. R., Parkin, R. M., Brown, N. Waves on wood. *Proceedings of the IMechE, Part B: Journal of Engineering Manufacture*, 2002, **216**, 475-497.
 - [2] Jackson, M. R. Some effects of machine characteristics on the surface quality of planed and spindle moulded wooden products. PhD Thesis, Leicester Polytechnic, 1986.
 - [3] Koch, P. *Lodgepole Pine in North America Vol III: Processes*. Forest Products Society, Madison, Wisconsin, 1996.
 - [4] Sims, W. L. *Two Hundred Years of History and Evolution of Woodworking Machinery*. 1985.
 - [5] Neumayer, R. Profile independent wood-moulding machine – dynamic model and control system. MSc. Dissertation, Loughborough University, 1999.
 - [6] Jackson, M. R., Neumayer, R. Profile independent wood-moulding machine – dynamic model and control system. In *Mechatronics 2002, The 7th Mechatronics Forum International Conference*, Atlanta, Georgia, 2000.
 - [7] Brown, N., Parkin, R. M. Improving wood surface form by modification of the rotary machining process – a mechatronic approach. *Proceedings of the IMechE, Part B: Journal of Engineering Manufacture*, 1999, **213**, 247-260.
 - [8] Hynek, P., Jackson, M., Parkin, R., Brown, N. Improving wood surface form by modification of the rotary machining process. *Proceedings of the IMechE, Part B: Journal of Engineering Manufacture*, 2004, **218**, 875-887.
 - [9] Ratnasingam, J., Ma, T. P., Perkins, M. C. Productivity in wood machining processes – a question of simple economics? *Holz als Roh- und Werkstoff*, 1999, **57**, 51-56.
 - [10] Ratnasingam, J., Reid, H., Perkins, M. C. Furniture industry: Regaining the competitive edge. *Journal of the Institute of Wood Science*, 1997, **14**, 111-120.
 - [11] Ratnasingam, J., Jusoh, M. Z. All about making the cents pay for the dollars. Extension Monograph, Agricultural University of Malaysia Press, 1996.
 - [12] Gorczyca, F. E. *Application of Metal Cutting Theory*. New York: Industrial Press Inc., 1987.
 - [13] Roland <<http://www.rolanddga.com>>
 - [14] Denford <<http://www.denford.com>>
 - [15] Waghorn, C. Numerical controlled wood moulding machine. MSc. Dissertation, Loughborough University, 1998.
 - [16] Saffert, E. Profile independent wood moulding machine – revisited. Private communication, Illmenau, Germany, 2001.
-

-
- [17] Hunt, K. H. *Mechanics and Motion*. English Universities Press, 1960.
- [18] Chen, C. Motion control and synchronization of multi-axis drive systems. PhD thesis, Loughborough University, 1994.
- [19] Koren, Y. *Computer Control of Manufacturing Systems*. New York; London: McGraw-Hill, 1983.
- [20] Koren, Y., Lo, C. C. Advanced controllers for feed drives. *Annals of the CIRP*, 1992, 41(2), 689-698.
- [21] Kakino, Y., Ihara, Y., Nakatsu, Y. The measurement of motion errors of NC machine tools and diagnosis of their origins bu using telescoping magnetic ball bar method. *Annals of the CIRP*, 1987, 36(1), 377-380.
- [22] Ibaraki, S., Kakino, Y., Lee, K., Ihara, Y., Braasch, J., Eberherr, A. Diagnosis and compensation of motion errors in NC machine tools by arbitrary shape contouring error measurement. In 5th International Conference and Exhibition on Laser Metrology, CMM and machine Tool Performance (LANDAMAP 2001), Birmingham, England, 2001.
- [23] Masory, O. Improving contouring accuracy of NC/CNC systems with additional velocity feed forward loop. *Transactions of the ASME Journal of Engineering for Industry*, 1986, 108, 227-231.
- [24] Koren, Y., Lo, C. C. Variable-gain cross-coupling controller for contouring. *Annals of the CIRP*, 1991, 40(1), 371-374.
- [25] Poo, A. N., Younkin, G. W., Bollinge, J. G. Dynamic errors in type-1 contouring systems. *IEEE Transactions on Industry Applications*, 1972, 8(4).
- [26] Astrom, K. J., Hagglund, T. The future of PID control. *Control Engineering Practise*, 2001, 9, 163-1175.
- [27] Lee, K., Kim, J. Controller gain tuning of a simultaneous multi-axis PID control system using the Taguchi method. *Control Engineering Practise*, 2000, 8, 949-958.
- [28] Park, J., Chung, W. Design of robust H_{∞} PID control for industrial manipulators. *Transactions of the ASME Journal of Dynamic Systems, Measurement, and Control*, 2000, 122, 803-812.
- [29] Liu, G. P., Daley, S. Optimal-tuning PID control for industrial systems. *Control Engineering Practise*, 2001, 9, 1185-1194.
- [30] Beaven, R. W., Wilkes, L. D., Garvey, S. D., Friswell, M. I. Application of four control strategies to high-speed independent drive systems. *Control Engineering Practice*, 1995, 3(8), 1059-1065.
- [31] Beaven, R. W., Wright, M. T., Garvey, S. D., Friswell, M. I., Seaward, D. R. The application of setpoint gain scheduling to high-speed independent drives. *Control Engineering Practice*, 1995, 3(11), 1581-1585.
-

-
- [32] Renton, D., Elbestawi, M. A. High speed servo control of multi-axis machine tools. *International Journal of Machine Tools and Manufacture*, 2000, **40**, 539-559.
- [33] Tomizuka, M. Zero phase error tracking algorithm for digital control. *Transactions of the ASME Journal of Dynamic Systems, Measurement, and Control*, 1987, **109**, 65-69.
- [34] Yeh, S. S., Hsu, P. L. An optimal and adaptive design of the feedforward motion controller. *IEEE/ASME Transactions on Mechatronics*, 1999, **4**(4), 428-439.
- [35] Tsao, T. C., Tomizuka, M. Adaptive zero phase error tracking algorithm for digital control. *Transactions of the ASME Journal of Dynamic Systems, Measurement, and Control*, 1987, **109**(4), 349-354.
- [36] Guo, L., Tomizuka, M. High-speed and high-precision motion control with an optimal hybrid feedforward controller. *IEEE/ASME Transactions on Mechatronics*, 1997, **2**(2), 110-122.
- [37] Weck, M., Ye, G. Sharp corner tracking using the IKF control strategy. *Annals of the CIRP*, 1990, **39**(1), 437-441.
- [38] Seethaler, R. J., Yellowley, I. The regulation of position error in contouring systems. *International Journal Mach. Tools Manufact.*, 1996, **36**(6), 713-728.
- [39] Yang, L., Yellowley, I. High-speed contouring using a novel dynamic interpolation mechanism. *International Journal of Machine Tools and Manufacture*, 2001, **41**, 773-794.
- [40] Niu, W., Tomizuka, M. A new approach of coordinated motion control subjected to actuator saturation. *Transactions of the ASME Journal of Dynamic Systems, Measurement, and Control*, 2001, **123**, 496-504.
- [41] Feng, F., Koren, Y., Borenstein, J. Cross-coupling motion controller for mobile robots. *IEEE Journal of Control Systems*, 1993, 35-43.
- [42] Danbury, R., Jenkinson, M. Synchronised servomechanisms – the scalar field approach. *IEE Proc. Part D Control Theory and Applications*, 1994, **141**, 261-273.
- [43] Koren, Y. Cross-coupled biaxial computer control for manufacturing systems. *Transactions of the ASME Journal of Dynamic Systems, Measurement, and Control*, 1980, **102**, 265-272.
- [44] Lo, C. C. An improved algorithm for cross-coupling control of multi-axis machine tools. *Transactions of the ASME Journal of Manufacturing Science and Engineering*, 1999, **121**, 537-540.
- [45] Zhong, Q., Shi, J. M., Huang, S. A linear cross-coupled control systems for high-speed machining. *International Journal of Advanced Manufacturing Technology*, 2002, **19**, 558-563.
- [46] Yeh, S. S., Hsu, P. L. Estimation of the contouring error vector for the cross-
-

- coupled control design. *IEEE/ASME Transactions on Mechatronics*, 2002, 7(1), 44-51.
- [47] Chen, S. L., Liu, H. L., Ting, S. C. Contouring control of biaxial systems based on polar coordinates. *IEEE/ASME Transactions on Mechatronics*, 2002, 7(3), 329-345.
- [48] Kulkarni, P. K., Srinivasan, K. Optimal contouring control of multi-axis feed drive servomechanisms. *Transactions of the ASME Journal of Engineering for Industry*, 1989, 111, 140-148.
- [49] Srinivasan, K., Kulkarni, P. K. Cross-coupled control of biaxial feed drive servomechanisms. *Transactions of the ASME Journal of Dynamic Systems, Measurement, and Control*, 1990, 112, 225-232.
- [50] Chuang, H. Y., Liu, C. H. Cross-coupled adaptive federate control for multiaxis machine tools. *Transactions of the ASME Journal of Dynamic Systems, Measurement, and Control*, 1991, 113, 451-457.
- [51] Chin, J. H., Lin, T. C. Cross-coupled precompensation method for the contouring accuracy of computer numerically controlled machine tools. *International Journal Mach. Tools Manufact.*, 1997, 37(7), 947-967.
- [52] Chen, B. C., Tilbury, D. M., Ulsoy, G. Modular control for machine tools: cross-coupling control with friction compensation. In Proceedings of the ASME-IMECE Dynamic Systems and Control Division, Anaheim, California, Nov 1998.
- [53] Shih, Y. T., Chen, C. S., Lee, A. C. A novel cross-coupling control design for bi-axis motion. *International Journal of Machine Tools and Manufacture*, 2002, 42, 1539-1548.
- [54] Lo, C. C. Three-axis contouring control based on trajectory coordinate basis. *JSME International Journal*, 1998, 41(2), 242-247.
- [55] Lo, C. C., Chung, C. Y. Tangential-contouring controller for biaxial motion control. *Trans. ASME Journal of Dynamic Systems, Measurement and Control*, 1999, 121, 126-129.
- [56] Ho, H. C., Yen, J. Y., Lu, S. S. A decoupled path-following control algorithm based upon the decomposed trajectory error. *International Journal of Machine Tools and Manufacture*, 1999, 39, 1619-1630.
- [57] Chiu, G. T. C., Tomizuka, M. Contouring control of machine tool feed drive systems: a task coordinate frame approach. *IEEE Trans. on Control Systems Technology*, 2001, 9(1), 130-139.
- [58] Kivimaa, E. Cutting force in wood working. PhD Thesis, University of Helsinki, 1986.
- [59] Walker, K. J. S. Cutting speed and cutting forces. *Wood*, 1957, 22.

-
- [60] Aguilera, A., Martin, P. Machining qualification of solid wood of *Fagus silvatica* L. and *Picea excelsa* L.: cutting forces, power requirements and surface roughness. *Holz als Roh- und Werkstoff*, 2001, **59**, 483-488.
- [61] Woodson, G. E., Koch, P. Tool forces and chip formation in orthogonal cutting of Loblolly Pine. U.S. Department of Agriculture, Forest Service Research Paper SO-52, 1970.
- [62] Costes, J. P., Larricq, P. Towards high cutting speed in wood milling. *Ann. Forest Science*, 2002, **59**, 857-865.
- [63] Huang, Y. S., Chen, S. S. Oblique wood cutting with a rotating disc cutter. *Taiwan Journal of Forest Science*, 1998, **13**(4), 301-307.
- [64] Huang, Y. S., Chen, S. S., Tang, J. L. Analysis of rotating disc cutting of wood. *Taiwan Journal of Forest Science*, 2003, **18**(4), 263-271.
- [65] Aguilera, A., Meausoone, P. J., Martin, P. Wood material influence in routing operations: the MDF case. *Holz als Roh- und Werkstoff*, 2000, **58**, 278-283.
- [66] McKenzie, W. M., Ko, P., Cvitkovic, R., Ringler, M. Towards a model predicting cutting forces and surface quality in routing layered boards. *Wood Science and Technology*, 2001, **35**, 563-569.
- [67] Eyma, F., Meausoone, P. J., Martin, P. Influence of the transitional zone of wood species on cutting forces in the router cutting process (90-0). *Holz als Roh- und Werkstoff*, 2001, **59**, 489-490.
- [68] Huang, Y. S., Chen, S. S., Hwang, G. S., Tang, J. L. Peripheral milling properties of compressed wood manufactured from planted China-fir. *Holz als Roh- und Werkstoff*, 2003, **61**, 201-205.
- [69] Schajer, G. S., Wang, S. A. Effect of workpiece interaction on circular saw cutting stability I: Theoretical background. *Holz als Roh- und Werkstoff*, 2001, **59**, 388-393.
- [70] Schajer, G. S., Wang, S. A. Effect of workpiece interaction on circular saw cutting stability II: Experimental results. *Holz als Roh- und Werkstoff*, 2002, **60**, 48-54.
- [71] Woodson, G. E. Tool forces and chip types in orthogonal cutting of southern hardwoods. U.S. Department of Agriculture, Forest Service Research Paper SO-146, 1979.
- [72] Copley Controls Corp. <<http://www.copleycontrols.com>>
- [73] Matsubara, A., Kakino, Y., Watanabe, Y. Servo performance enhancement of high speed drives by damping control. In Proceedings of the 2000 Japan-USA Flexible Automation Conference, Ann Arbor, Michigan, 23-26 July 2000.
- [74] Sato, K., Murayama, Y., Imada, S., Shimokohbe, A. Control and elimination
-

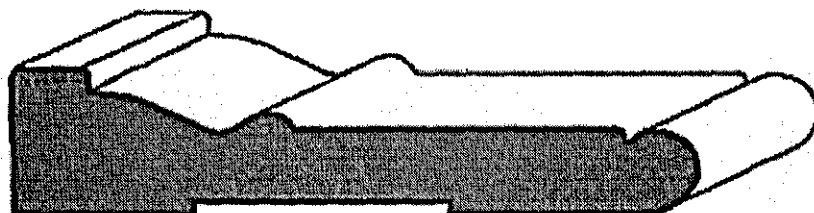
- of lead screw backlash for ultra-precision positioning. *JSME International Journal*, 1995, 38(1), 36-41.
- [75] Tachikawa, H., Fukuda, M., Shinshi, T., Sato, K., Shimokohbe, A. Precision positioning using air bearing lead screw. In International Conference on Micromechatronics for Information and Precision Equipment, Tokyo, Japan, 20-23 July 1997, pp. 238-243.
- [76] Sato, K., Shinshi, T., Abidin, Z., Shimokohbe, A. Positioning performance of a leadscrew system with six kinds of control methods - Basic positioning performance and effect of coulomb friction on the performance -. In Proceedings of China-Japan Bilateral Symposium on Advanced Manufacturing Engineering, Yellow Mountain, China, 1998, pp. 39-44.
- [77] Dorf, R. C., Bishop, R. H. *Modern Control Systems*. Massachusetts: Addison-Wesley, 1995.
- [78] Palm, W. J. *Modelling, Analysis and Control of Dynamic Systems*. New York: Wiley, 1999.
- [79] De Silva, C. W. *Mechatronics: an integrated approach*. London: CRC, 2004.
- [80] Jeong, Y. H., Cho, D. W. Estimating cutting force from rotating and stationary feed motor currents on a milling machine. *International Journal of Machine Tools and Manufacture*, 2002, 42, 1559-1566.
- [81] Erkorkmaz, K., Altintas, Y. High speed CNC system design. Part II: modeling and identification of feed drives. *International Journal of Machine Tools and Manufacture*, 2001, 41, 1487-1509.
- [82] Chen, J. S., Dwang, I. C. A ballscrew drive mechanism with piezo-electric nut for preload and motion control. *International Journal of Machine Tools and Manufacture*, 2000, 40, 513-526.
- [83] Wahyudi, M., Sato, K., Shimokohbe, A. Robustness evaluation of three friction compensation methods for point-to-point (PTP) positioning systems. *Robotics and Autonomous Systems*, 2005, 52, 247-256.
- [84] Quintero, R., Barbera, A. J. A real-time control system methodology for developing intelligent control systems. NISTIR 4936, Oct. 1992.
- [85] Dykes Lumber Company. <<http://www.dykeslumber.com>>
- [86] Rex Lumber Company. <<http://www.rexlumber.com>>
- [87] The Hardwood Company. <<http://www.thehardwoodcompany.com/>>
- [88] Forester Moulding & Lumber Inc. <<http://www.forestermoulding.com>>
- [89] Taylor's Mill Inc. <<http://www.taylorsmill.com/profiles.htm>>
- [90] Reliance Precision Limited. <<http://www.reliance.co.uk>>

-
- [91] Portescap Miniature Motors. <<http://www.portescap.com>>
- [92] Maxon Motor UK. <<http://www.maxonmotor.co.uk>>
- [93] Tung, E. D., Anwar, G., Tomizuka, M. Low velocity friction compensation and feedforward solution based on repetitive control. *Trans. ASME Journal of Dynamic Systems, Measurement and Control*, 1993, **115**, 279-284.
- [94] Sensoray (2004), Model 626 Instruction Manual – Revision F, Sensoray Co. Inc.,
- [95] <http://www.maxonmotor.com/docsx/Download/catalog_2005/Pdf/05_032_e.pdf>
- [96] Mathworks RTWT <<http://www.mathworks.com/products/rtwt/>>
- [97] Microsoft Visual Basic 6.0. <<http://msdn.microsoft.com/vbrun/>>
- [98] Sensoray (2002), Instruction Manual – Model 626 Driver for Windows, Sensoray Co. Inc.
- [99] Lacerda, H. B., Belo, E. M. A modified contour error controller for a high speed XY table. *Journal of the Brazilian Society of Mechanical Sciences*, 2000, **22**(3), 443-455.
- [100] Armstrong-Helouvry, B. *Control of Machines with Friction*. Boston, MA: Kluwer Academic Publishers, 1989.
- [101] Armstrong-Helouvry, B., Dupont, P., Canudas de Wit, C. A survey of models, analysis tools, and compensation methods for the control of machines with friction. *Automatica*, 1994, **30**(7), 1083-1138.
- [102] Haessig, D. A., Friedland, B. On the modeling and simulation of friction. *Trans. ASME Journal of Dynamic Systems, Measurement and Control*, 1991, **113**, 354-362.
- [103] Olsson, H., Astrom, K. J., Canudas de Wit, C., Gafvert, M., Lischinsky, P. Friction models and friction compensation. *European Journal of Control*, 1998, **4**, 176-195.
- [104] Karnopp, D. Computer simulation of stick-slip friction in mechanical dynamic systems. *Trans. ASME Journal of Dynamic Systems, Measurement and Control*, 1985, **107**, 100-103.
- [105] Papadopoulos, E. G., Chasparis, G. C. Analysis and model-based control of servomechanisms with friction. *Trans. ASME Journal of Dynamic Systems, Measurement and Control*, 2004, **126**, 911-915.
- [106] Hess, D. P., Soom, A. Friction at a lubricated line contact operating at oscillating sliding velocities. *Journal of Tribology*, 1990, **112**, 147-152.
-

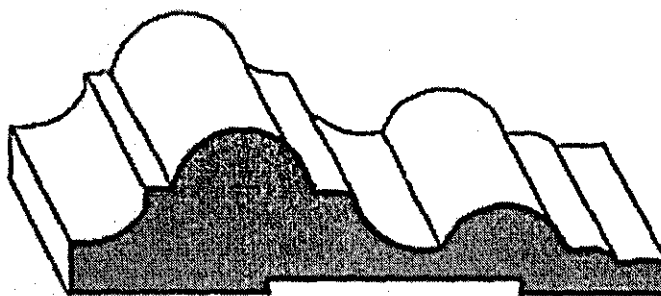
Appendices

Appendix A: Typical moulding profiles

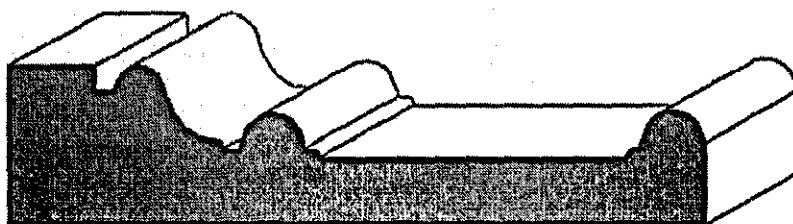
Source: The Hardwood Company (<http://www.thehardwoodcompany.com>)



(a) Not demanding for the vertical drive (long, flat horizontal surfaces)



(b) Demanding for the vertical drive



(c) Partially demanding for the vertical drive

Appendix B: Representation of geometric information in DXF script

DXF Script	Explanation
AcDbLine	Segment is a Line
10	indicator for the X ₁ coordinate
91.50	X ₁ value
20	indicator for the Y ₁ coordinate
122.30	Y ₁ value
30	indicator for the Z ₁ coordinate
0.0	Z ₁ Value
11	indicator for the X ₂ coordinate
136.20	X ₂ value
21	indicator for the Y ₂ coordinate
112.30	Y ₂ value
31	indicator for the Z ₂ coordinate
0.0	Z ₂ value

Table B.1 Line segment representation

DXF Script	Explanation
AcDbCircle	Segment is a Circle
10	indicator for the centre X coordinate (X _A)
136.20	X _A value
20	indicator for the centre Y coordinate (Y _A)
92.30	Y _A value
30	indicator for the centre Z coordinate (Z _A)
0.0	Z _A Value
40	indicator for the circle radius (R _A)
20.0	R _A value
AcDbArc	Segment is an Arc
50	indicator for the angle of the start point (θ ₁)
0.0	θ ₁ value
51	indicator for the angle of the end point (θ ₂)
90.0	θ ₂ value

Table B.2 Arc segment representation

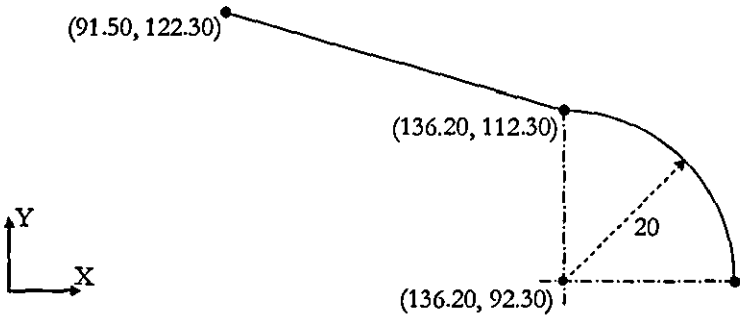


Figure B.1 Graphical representation of the above segments

Appendix C: Matlab Function “dxfread.m”

```

function P = dxfread(Filename)
global P
P=[];
fid=fopen(Filename,'r');
tline='';
n=0;

% READ SEGMENT DATA FROM DXF FILE
while strcmp(tline,'EOF')==0
    tline=fgetl(fid);
    if strcmp(tline,'AcDbLine')
        n=n+1;
        tline=fgetl(fid);
        tline=fgetl(fid); %x1
        R(1,n)=str2num(tline);
        tline=fgetl(fid);
        tline=fgetl(fid); %y1
        R(2,n)=str2num(tline);
        tline=fgetl(fid);
        tline=fgetl(fid);
        tline=fgetl(fid);
        tline=fgetl(fid); %x2
        R(3,n)=str2num(tline);
        tline=fgetl(fid);
        tline=fgetl(fid); %y2
        R(4,n)=str2num(tline);
        R(5,n)=0;
        R(6,n)=0;
        R(7,n)=0;
        R(8,n)=0;
        R(9,n)=0;
    end

    if strcmp(tline,'AcDbCircle')
        n=n+1;
        tline=fgetl(fid);
        tline=fgetl(fid); %za
        R(5,n)=str2num(tline);
        tline=fgetl(fid);
        tline=fgetl(fid); %ya
        R(6,n)=str2num(tline);
        tline=fgetl(fid);
        tline=fgetl(fid);
        tline=fgetl(fid);
        tline=fgetl(fid); %ra
        R(9,n)=str2num(tline);
        tline=fgetl(fid);
        tline=fgetl(fid);
        tline=fgetl(fid);
        tline=fgetl(fid); %th1
        R(7,n)=str2num(tline);
        tline=fgetl(fid);
        tline=fgetl(fid); %th2
        R(8,n)=str2num(tline);
    end
end
end

```

```

%FIND ARC ENDPOINTS
for i=1:n
    if R(9,i)~=0
        R(1,i)=R(9,i)*cos(R(7,i)*pi/180)+R(5,i);
        R(2,i)=R(9,i)*sin(R(7,i)*pi/180)+R(6,i);
        R(3,i)=R(9,i)*cos(R(8,i)*pi/180)+R(5,i);
        R(4,i)=R(9,i)*sin(R(8,i)*pi/180)+R(6,i);
    end
end

%CONVERT TO mm AND FORMAT
for i=1:9
    if (i==7)|(i==8)
        R(i,:)=(round(R(i,:)*1000))./1000;
    else
        R(i,:)=(round(R(i,:)*1000))./1000;
    end
end

%FIND Xmin Ymin Xmax Ymax
xmin=min(min(R(1,:)), min(R(3,:)));
xmax=max(max(R(1,:)), max(R(3,:)));
ymin=min(min(R(2,:)), min(R(4,:)));
ymax=max(max(R(2,:)), max(R(4,:)));

%FIND THE LEFT EDGE
for i=1:n
    if (R(1,i)==xmin) & (R(3,i)==xmin)
        xx=xmin;
        yy=max(R(2,i),R(4,i));
        R(:,i)=0;
        break;
    end
end

%FIND THE REST OF THE TOP PROFILE
i=0;
j=0;
while xmax > xx
    i=i+1;
    if (abs(R(1,i)-xx) < 0.01) & (abs(R(2,i)-yy) < 0.01)
        j=j+1;
        P(:,j)=R(:,i);
        R(:,i)=0;
        xx=P(3,j);
        yy=P(4,j);
        i=0;
    elseif (abs(R(3,i)-xx) < 0.01) & (abs(R(4,i)-yy) < 0.01)
        j=j+1;
        P(1,j)=R(3,i);
        P(2,j)=R(4,i);
        P(3,j)=R(1,i);
        P(4,j)=R(2,i);
        P(5,j)=R(5,i);
        P(6,j)=R(6,i);
        P(7,j)=R(8,i);
        P(8,j)=R(7,i);
        P(9,j)=R(9,i);
        R(:,i)=0;
    end
end

```

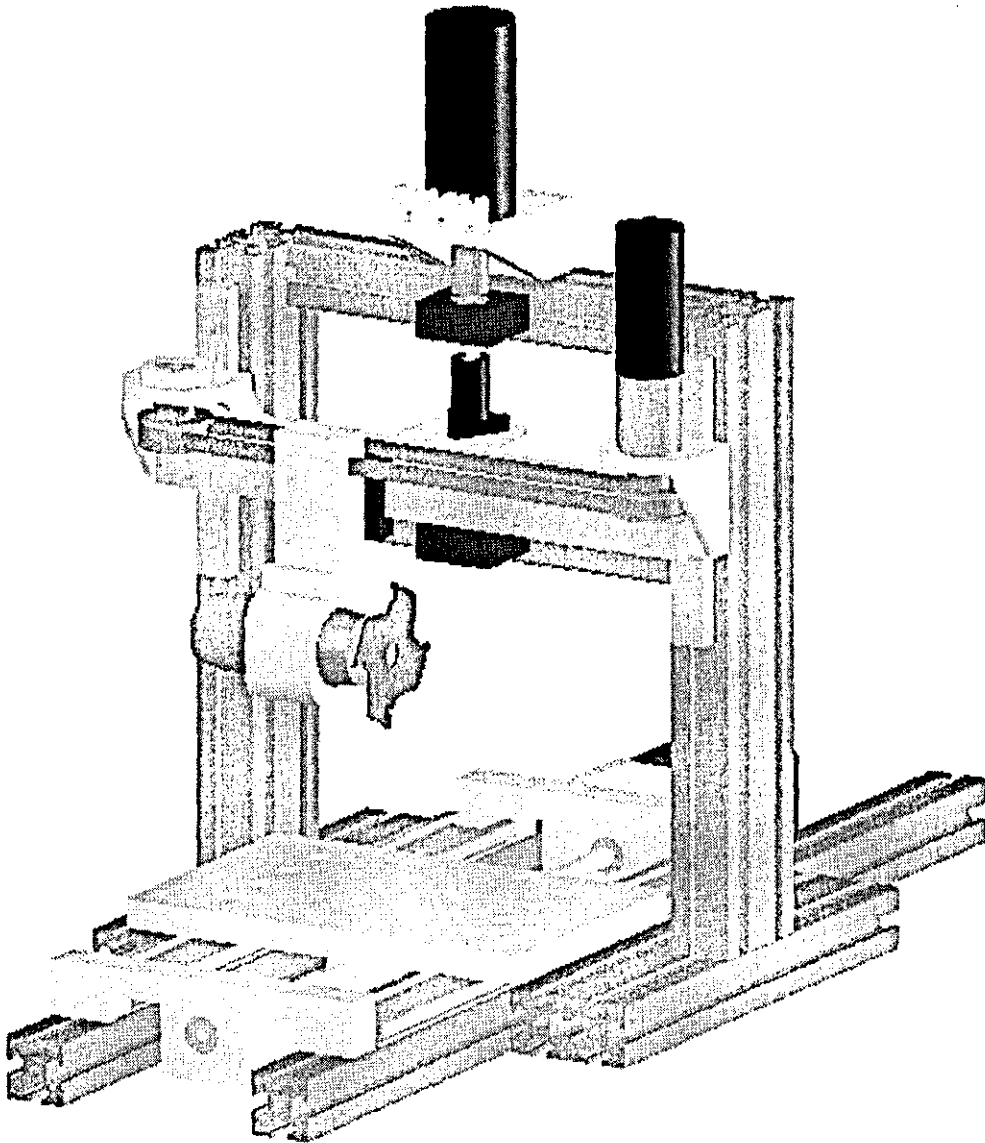
```
        xx=P(3,j);
        yy=P(4,j);
        i=0;
    end
end

%SET TOP LEFT CORNER TO (0,0)
for i=1:size(P,2)
    if P(9,i) > 0
        P(5,i)=P(5,i)-P(1,1);
        P(6,i)=P(6,i)-P(2,1);
    end
end
P(3,:)=P(3,:)-P(1,1);
P(4,:)=P(4,:)-P(2,1);
P(1,:)=P(1,:)-P(1,1);
P(2,:)=P(2,:)-P(2,1);
```

Appendix D: Previous PIMM test-rig designs

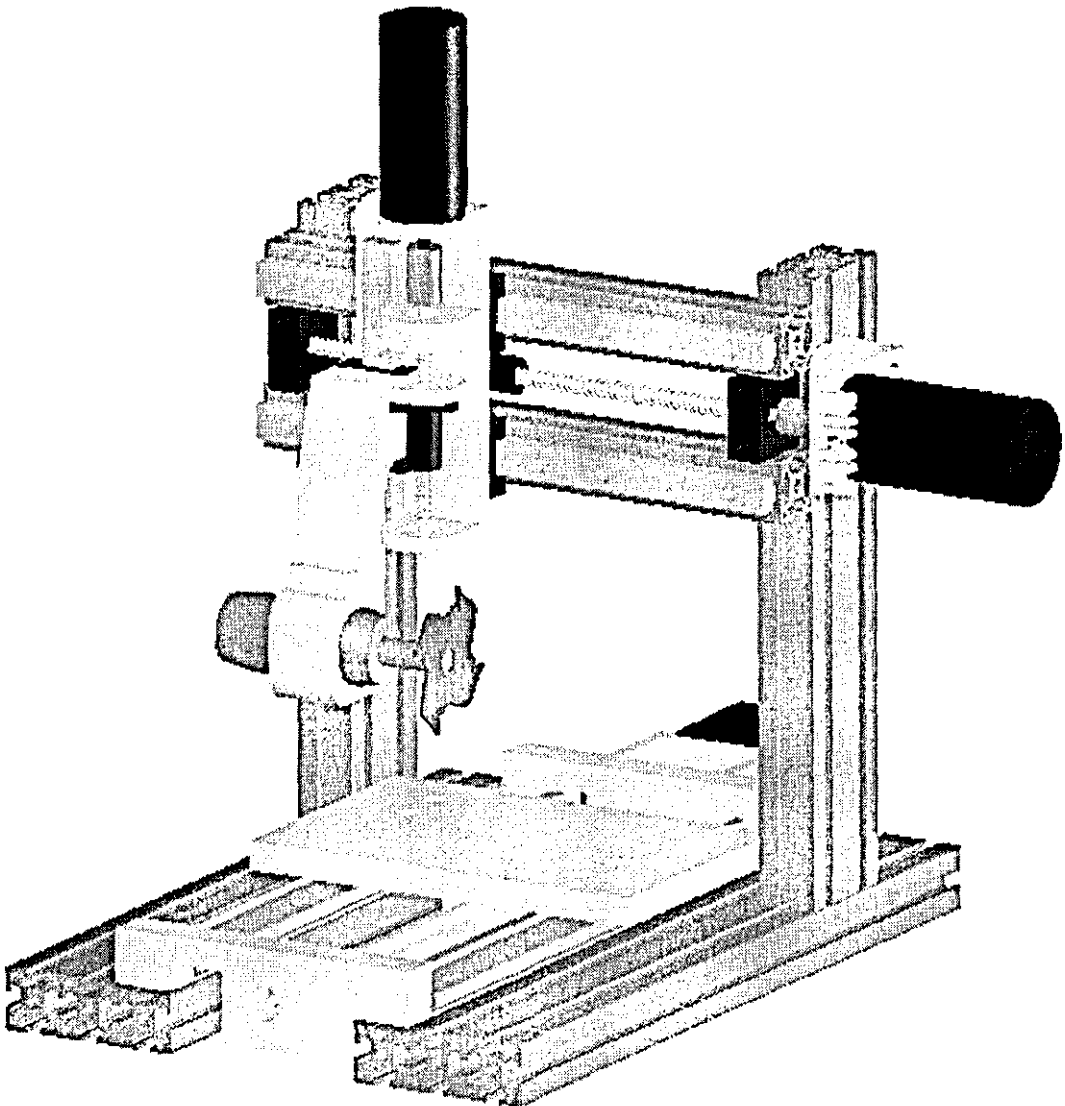
Design 1:

- ◆ Frame: Extruded aluminum
- ◆ Cutter motor: Remote Dremel AC motor + Flexible Shaft + Collet
- ◆ Horizontal axis drive: DC motor + Planetary Gearbox + Timing Belt/Pulley
- ◆ Vertical axis drive: DC motor + Leadscrew
- ◆ Timber feed drive: Stepper motor + Leadscrew



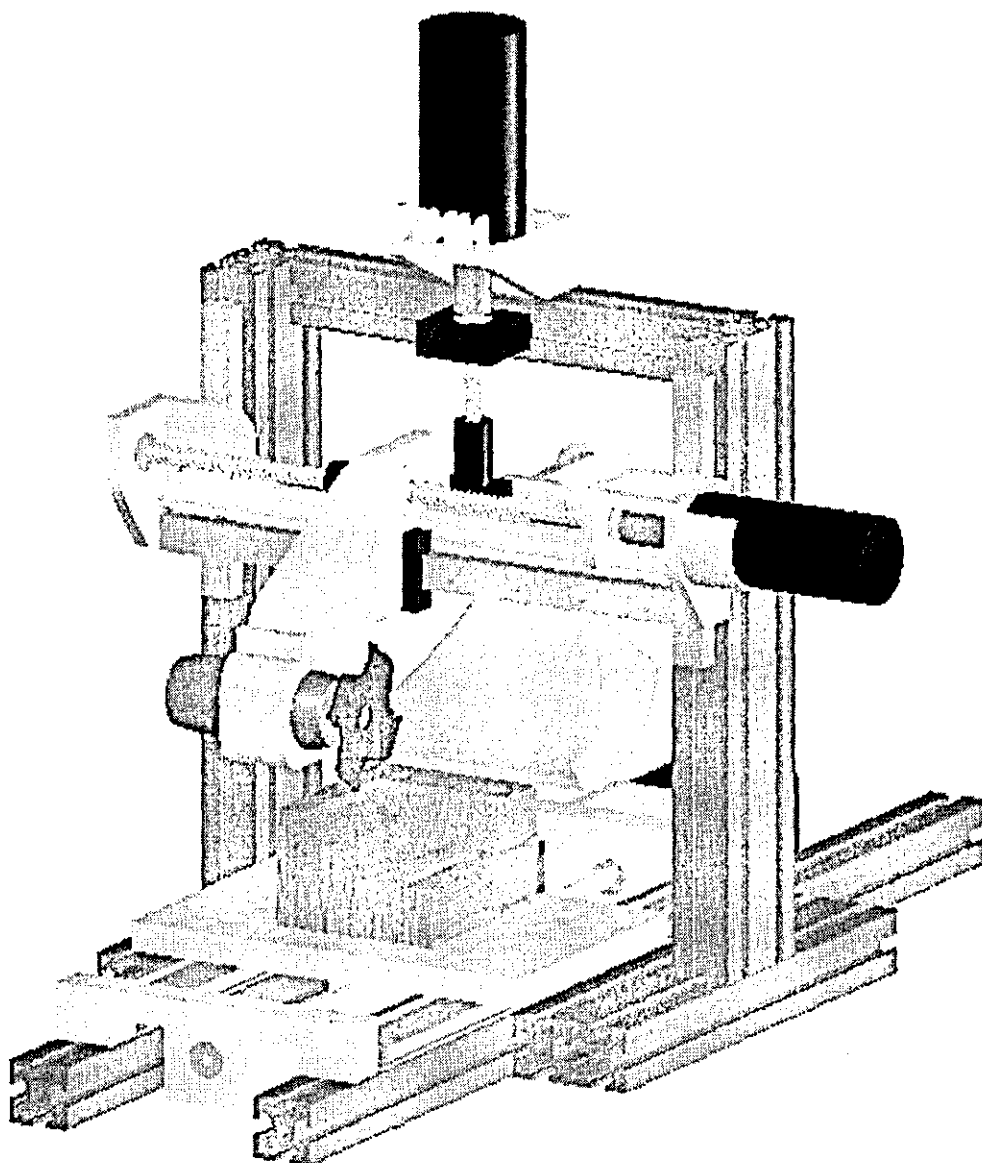
Design 2:

- ◆ Frame: Extruded aluminum
- ◆ Cutter motor: Remote Dremel AC motor + Flexible Shaft + Collet
- ◆ Vertical axis drive: DC motor + Leadscrew
- ◆ Horizontal axis drive: DC motor + Leadscrew
- ◆ Timber feed drive: Stepper motor + Leadscrew



Design 3:

- ◆ Frame: Extruded aluminum
- ◆ Cutter motor: Remote Dremel AC motor + Flexible Shaft + Collet
- ◆ Horizontal axis drive: DC motor + Leadscrew
- ◆ Vertical axis drive: DC motor + Leadscrew
- ◆ Timber feed drive: Stepper motor + Leadscrew



Appendix E: Cutter motor specifications

Maxon EC 22 Brushless Motor Datasheet

(http://www.maxonmotor.co.uk)

EC 22 Ø22 mm, brushless, 50 Watt, CE approved

maxon EC motor

A with Hall sensors

B sensorless

Connector
MKF 13268-6-0-808
Staco Elektronik GmbH

M 1:1

Stock program

Standard program

Special program (on request)

Motor Data	167130	167131	167129	167133	201049	201050	201055	201051
1 Assigned power rating	50	50	50	50	50	50	50	50
2 Nominal voltage	32.0	32.0	32.0	32.0	32.0	32.0	32.0	32.0
3 No load speed ¹⁾	30000	40700	22400	27000	38800	46700	22400	27000
4 Stall torque ¹⁾	683	575	400	332	683	575	400	332
5 Speed / torque constant ¹⁾	56	81	56	81	56	81	56	81
6 No load current ¹⁾	304	218	117	91	304	281	117	91
7 Internal resistance phase to phase	0.36	0.36	1.09	1.09	0.36	0.36	1.09	1.09
8 Max. permissible speed ²⁾	50000	50000	50000	50000	50000	50000	50000	50000
9 Max. continuous current at 10 000 rpm ¹⁾	4.00	4.00	2.80	2.80	4.00	4.90	2.80	2.80
10 Max. continuous torque at 10 000 rpm	34.0	27.6	33.6	27.8	34.0	27.6	33.6	27.6
11 Max. efficiency ³⁾	89	90	88	89	89	90	88	89
12 Torque constant	7.0	6.5	13.6	11.3	7.0	6.5	13.6	11.3
13 Speed constant	1216	1464	702	845	1216	1464	702	845
14 Mechanical time constant	2.5	2.6	2.5	2.6	2.5	2.6	2.5	2.6
15 Motor inertia	4.2	3.1	4.2	3.1	4.2	3.1	4.2	3.1
16 Internal inductance phase to phase	0.040	0.040	0.147	0.149	0.040	0.040	0.147	0.149
17 Thermal resistance housing ambient	7.0	7.0	7.0	7.0	7.0	7.0	7.0	7.0
18 Thermal resistance winding housing	1.0	1.0	1.0	1.0	1.0	1.0	1.0	1.0
19 Thermal time constant winding	5.4	5.4	5.4	5.4	5.4	5.4	5.4	5.4
20 Thermal time constant stator	323	323	323	323	323	323	323	323

1) Values determined with basic construction
2) In coordination with Encoder MFI 100, 5000 rpm

Specifications

- Axial play at axial load < 5 N: 0 mm
- Axial play at axial load > 5 N: max. 0.14 mm
- Preloaded ball bearings
- Preload strength min: 5 N
- Max. ball bearing loads:
 - axial (dynamic): 4 N
 - radial (5 mm from flange): 16 N
 - Force for press fits (static): 60 N
 - (static, shaft supported): 250 N
- Radial play ball bearing: 0.025 mm
- Ambient temperature range: -20 ... +100°C
- Max. permissible winding temperature: +125°C
- Weight of motor: 130 g
- 2 pole permanent magnet
- Values listed in the table are nominal

Connection A

brown	Motor winding 1
red	Motor winding 2
orange	Motor winding 3
yellow	V _{CC} 4.5 ... 18 VDC
green	GND
blue	Hall sensor 1*
violet	Hall sensor 2*
grey	Hall sensor 3*

Connection B (Cable AWG 24)

brown	Motor winding 1
red	Motor winding 2
orange	Motor winding 3

*Internal pull up (7 ... 13 kΩ) on pin 4

• For wiring diagram for Hall sensors, see p. 28

Operating Range

n (rpm)

50 Watt

50 Watt

167130 Motor with high resistance winding

167131 Motor with low resistance winding

Comments

Curve of constant assigned power rating

Continuous operation

In observation of above listed thermal resistances (lines 17 and 18) the maximum permissible winding temperature will be reached during continuous operation at 25°C ambient

• Thermal limit

Short term operation

The motor may be briefly overloaded (recurring)

Details on page 149

maxon Modular System

Planetary Gearhead

5222 mm

0.5 - 2.0 Nm

Details page 213

Overview on page 17 - 21

Encoder MFI 128 / 256 / 512 CPT 2 / 3 channels

Details page 237

for type B: with Resolver Res on request

Recommended Electronics:

AEC 35/3	page 262
DEC 50/5	264
DECV 50/5	265
DES 50/5	267
EDS 24/1, 24/5	271

Notes

17

Appendix F: X and Y axis drives hardware specifications

Maxon RE 30 DC Motor Datasheet

(http://www.maxonmotor.co.uk)

RE 30 Ø30 mm, Graphite Brushes, 60 Watt

maxon DC motor

Technical drawings of the Maxon RE 30 motor, including a front view showing terminal positions (1-6), a side view showing dimensions (A-H), and a rear view showing mounting holes. Dimensions are in mm.

M 1:2

	310006	310007	310008	310009
1 Assigned power rating	60	60	60	60
2 Nominal voltage	12.0	18.0	24.0	48.0
3 No load speed	8170	8590	8810	8490
4 Stall torque	844	991	1020	1020
5 Speed / torque gradient	9.74	8.71	8.70	8.33
6 No load current	270	212	154	191
7 Starting current	60.9	49.8	39.3	20.5
8 Terminal resistance	0.108	0.362	0.611	1.53
9 Max. permissible speed	8200	8200	8200	8200
10 Max. continuous current	4	4	3.81	2.42
11 Max. continuous torque	47.5	68.6	68.2	84.1
12 Max. power output at nominal voltage	177	220	233	205
13 Max. efficiency	87	87	88	88
14 Torque constant	13.0	19.9	25.9	30.8
15 Speed constant	685	479	369	240
16 Mechanical time constant	3	3	3	3
17 Motor inertia	33.5	16.7	20.9	34.5
18 Terminal inductance	0.03	0.07	0.12	0.28
19 Thermal resistance housing-ambient	6	8	8	6
20 Thermal resistance rotor-housing	1.7	1.7	1.7	1.7
21 Thermal time constant winding	16	17	16	17

Specifications

- Axial play 0.05 - 0.15 mm
- Max. ball bearing loads axial (dynamic):
 - not preloaded 5.6 N
 - preloaded 2.4 N
- radial (5 mm from flange) Force for press fit (static) 110 N (static, shaft supported) 1200 N
- Radial play ball bearing 0.025 mm
- Ambient temperature range -20 ... +100°C
- Max. rotor temperature +125°C
- Number of commutator segments 13
- Weight of motor 208 g
- 2 pole permanent magnet
- Values listed in the table are nominal. For applicable tolerances see page 43. For additional details please use the maxon selection program on the enclosed CD-ROM.

Operating Range

Graph showing the operating range of the motor. The y-axis is speed n [rpm] from 0 to 9000. The x-axis is torque M [mNm] from 0 to 12. A shaded region indicates the recommended operating range. Key points: 60 Watt, 3000 rpm, 4.0 mNm, 1.0 A.

maxon Modular System

Planetary Gearhead
20:1
0.75 - 4.5 Nm
Details page 219

Planetary Gearhead
20:1
1.0 - 6.0 Nm
Details page 220

Encoder MR
256 - 1024 CPT
3 channels
Details page 230

Recommended Electronics:

ADS 50.5	page 259
ADS_F 50.5	260
EPN 24.5	271
MIP 50	273
Notes	17

18 maxon DC motor

214

HEDS 5540 Incremental Encoder Datasheet

(<http://www.faulhaber.com>)



Encoders

Optical Encoders with Line Driver

Features:
 500 Pulses per revolution
 3 Channels + complementary outputs
 Digital output
 Line driver

Series 5540		See beginning of the Encoder Section for Ordering Information	
HEDL 5540			
Pulses per revolution	N	500	
Signal output, (quadrature)		2+1 index and complementary outputs	channels
Supply voltage	V _{cc}	4.5 to 5.5	V DC
Current consumption, typical (V _{cc} = 5 V DC)	I _{cc}	57	mA
Pulse width	P _{cc}	180 ± 35	°e
Index pulse width	P ₀	90 ± 35	°e
Phase shift, channel A to B	φ	90 ± 15	°e
Logic state width	S	90 ± 35	°e
Cycle	C	360 ± 5.5	°e
Signal rise/fall time, typical	t _{rt/ft}	0.25 / 0.25	µs
Frequency range ¹⁾	f	up to 100	kHz
Inertia of code disc	J	8.197 · 10 ⁻⁸	oz-in-sec ²
Operating temperature range		0 to 70 (32 to 158)	°C (°F)
¹⁾ Velocity (rpm) = f (Hz) x 60/N			

Ordering information			
Encoder type	number of channels	pulses per revolution	For combination with:
HEDL 5540 A	2+1	500	DC-Motors and DC-Motor-Tachos Series 2230, 2233, 2251 2338, 2342 2642, 2657, 2842 3042, 3557, 3863 brushless DC-Servomotors Series 2036, 2444, 3564

The housing dimensions of the HEDL encoder are the same as the HEDS/HEDM encoders, but there is a ribbon cable instead of plain connector pins.

Suggested Line Receivers: LT-1

Features

These incremental shaft encoders in combination with the FAULHABER DC-Motors and brushless DC-Servomotors are designed for indication and control of both, shaft velocity and direction of rotation as well as for positioning.

A LED source and lens system transmits collimated light through a low inertia metal disc to give two channels with 90° phase shift.

The index pulse is synchronized with the channel B.
 Each encoder channel provides complementary output signals.

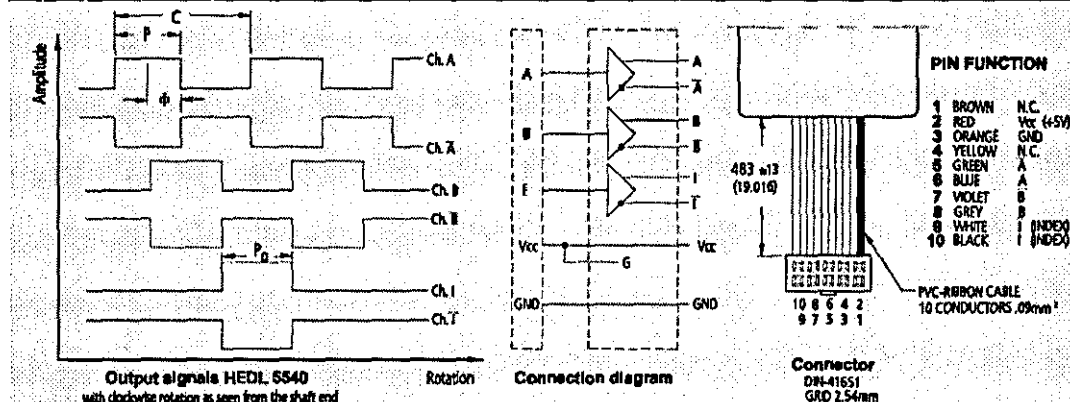
The single 5 volt supply and the digital output signals are interfaced with a connector.

The line driver offers enhanced performance when the encoder is used in noisy environments, or when it is required to drive long distances.

Motor with ball bearings are recommended for continuous operation at low and high speeds and for elevated radial shaft load.

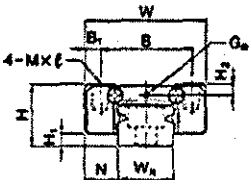
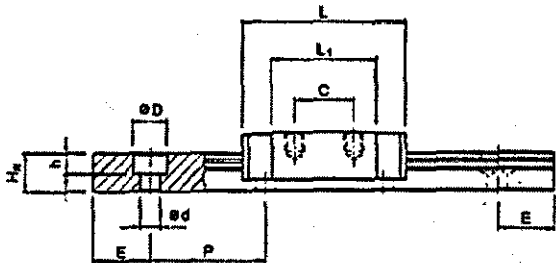
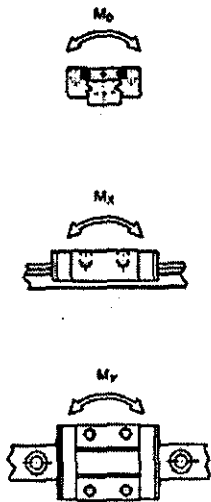
Details for the motors and suitable reduction gearheads are on separate catalog pages.

Output signals / Circuit diagram / Connector information

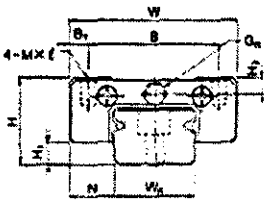
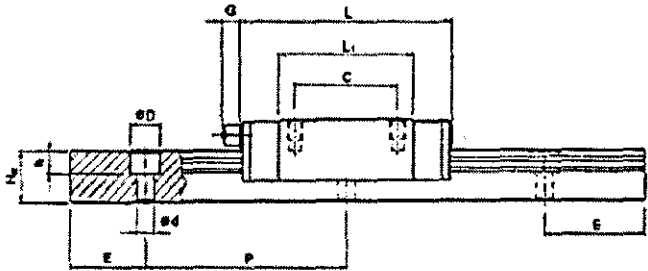


HIWIN MGN Miniature Linear Guideway Datasheet

(<http://www.hiwin.com>)



MGN 7,
MGN 9,
MGN 12



MGN 15

Model No.	Dimensions of Assembly (mm)			Dimensions of Block (mm)										Dimensions of Rail (mm)										Mounting Bolt for Rail (mm)	Basic Dynamic Load Rating C (kgf)	Basic Static Load Rating C ₀ (kgf)	Static Rated Moment			Weight	
	H	H ₁	N	W	B	B ₁	C	L	L ₁	G	G ₁	M _x (°)	H ₂	W _n	H _n	D	h	d	P	E	M ₀ (kgf·m)	M _x (kgf·m)	M _y (kgf·m)				Block (g)	Rail (kg/m)			
MGN 7C	8	1.5	5	17	12	2.5	8	13.5	22.5	-	00.8	M2x2.5	1.5	7	4.8	4.2	2.3	2.4	15	5	M2x6	100	127	0.48	0.29	0.29	10	0.22			
MGN 7H							13	21.8	30.8													140	200	0.78	0.49	0.49	15				
MGN 9C	10	2	5.5	20	15	2.5	10	18.9	28.9	-	00.8	M3x3	1.8	9	6.5	6	3.5	3.5	20	7.5	M3x8	190	260	1.2	0.75	0.75	16	0.38			
MGN 9H							16	29.9	39.9													260	410	2	1.9	1.9	26				
MGN 12C	13	3	7.5	27	20	3.5	15	21.7	34.7	-	00.8	M3x3.5	2.5	12	8	6	4.5	3.5	25	10	M3x8	290	400	2.6	1.4	1.4	34	0.65			
MGN 12H							20	32.4	45.4													380	600	3.9	3.7	3.7	54				
MGN 15C	16	4	8.5	32	25	3.5	20	26.7	42.1	4.5	GN3S	M3x4	3	15	10	6	4.5	3.5	40	15	M3x10	470	570	4.6	2.2	2.2	59	1.06			
MGN 15H							25	43.4	58.8													650	930	7.5	5.9	5.9	92				

Reliance LAF6-M030 Light-Duty Anti-Backlash Leadscrew Specifications

Source: Reliance Precision Limited (<http://www.reliance.co.uk>)

screw material	stainless steel 303
nut material	polyacetal with lubricating additive
lead type	right-hand thread
lead accuracy	0.0006mm/mm
repeatability	0.0015mm
screw diameter	6.35 mm
lead	3.0 mm
efficiency	68%
unloaded friction torque	0.004 - 0.010 Nm

Appendix G: X and Y axis drives speed, force, and inertia calculations

$$V_{\max} = \frac{\omega_{\max}}{60} \cdot \text{lead}$$

$$F_{\max} = e \cdot \frac{2\pi \cdot T_{\max}}{\text{lead}}$$

$$J_s = \frac{1}{2} \cdot M_s \cdot R_s^2$$

$$J = J_m + J_s + M \cdot \left(\frac{1}{R_t} \right)^{-2}, \quad \text{where} \quad R_t = \frac{\text{lead}}{2\pi}$$

parameter		horizontal (X) axis value	vertical (Y) axis value
max. motor speed (rpm)	ω_{\max}	8800	8800
max. continuous motor torque (mNm)	T_{\max}	86.20	86.20
motor rotor inertia (kgm ²)	J_m	$33.3 \cdot 10^{-7}$	$33.3 \cdot 10^{-7}$
leadscrew lead (mm)	lead	3	3
leadscrew efficiency	e	0.68	0.68
leadscrew mass (kg)	M_s	0.050	0.025
leadscrew radius (m)	R_s	0.0032	0.0032
carriage mass (kg)	M	0.25	0.9
maximum linear speed (mm/s)	V_{\max}	440	440
maximum continuous thrust (N)	F_{\max}	122.81	122.81
leadscrew inertia (kgm ²)	J_s	$2.52 \cdot 10^{-7}$	$1.26 \cdot 10^{-7}$
total rotating inertia (kgm ²)	J	$3.61 \cdot 10^{-6}$	$3.63 \cdot 10^{-6}$

Appendix H: Z axis drive hardware specifications

Z-axis stepper motor specifications

Source: RS Components Limited (<http://www.rswww.com>)

RS stock no	440-420
motor type	4-phase hybrid stepper motor
holding torque	70 mNm
rated current per phase	0.5 A
voltage rating	5 V (DC)
step angle	1.8°
shaft diameter	5 mm
shaft length	18.1 mm
motor length	33 mm
motor height x width	40 x 40 mm

Reliance LAF6-M100 Light-Duty Anti-Backlash Leadscrew Specifications

Source: Reliance Precision Limited (<http://www.reliance.co.uk>)

screw material	stainless steel 303
nut material	polyacetal with lubricating additive
lead type	right-hand thread
lead accuracy	0.0006mm/mm
repeatability	0.0015mm
screw diameter	6.35 mm
lead	10.0 mm
efficiency	78%
unloaded friction torque	0.004 - 0.010 Nm

Appendix I: Sensoray Model 626 PCI I/O card specifications

Source: Sensoray Co. Inc. (<http://www.sensoray.com>)

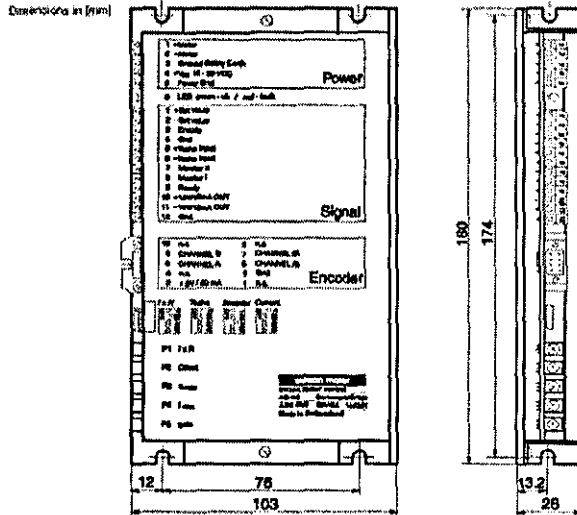
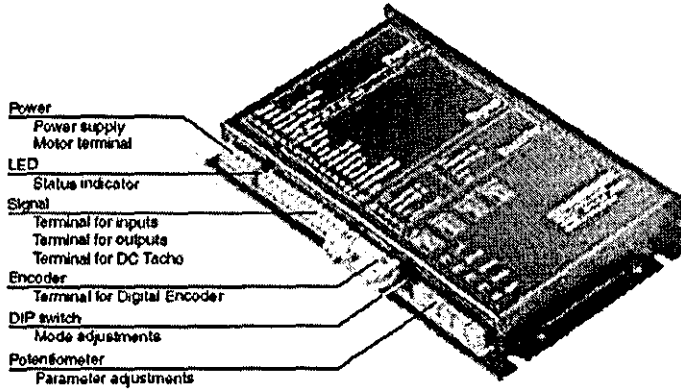
General	
Operating temperature	0 C to 70C
PC bus interface	PCI, 32-bit, 33 MHz
Input power	< 3 watts
A/D Converter	
Conversion time	20 microseconds
Number of channels	16 differential
Input resistance	100 Megohms
CMRR	100 dB minimum
Max. common mode voltage	5 volts
Resolution	16-bits
Accuracy	14-bits
Input ranges	+/-10, ± 5 V
Offset error	+/- 1/2 LSB
D/A converter	
Conversion time	20 microseconds
Resolution	14-bits
Offset error	+/- 2 bits
Output voltage	+/- 10 volts
Output resistance	87 ohms
Digital I/O	
Number of channels	48 bi-directional
Output voltage	0 to 5 V open collector
Output sink current	100 mA @1.1 V
Encoder I/O	
Number of channels	6 quadrature, 24-bit
Input voltage	TTL or RS-422
Input frequency	2 MHz w/int. clock 1 MHz w/ext. clock
Quadrature multiplier	x1, x2, x4
Watchdog Timer	
Time-out	1/8, 1/4, 1, 10 sec
Digital I/O Accessory	
18" digital cable, 50-pin	7501C
1 meter digital cable, 50-pin	7501C1
24 position relay board	720RB
24 position relay board with DIN mounting hardware	720RB-DIN
Encoder Accessory	
18" encoder cable, 26-pin	7503C
1 meter encoder cable, 26-pin	7503C1
Encoder terminal board with DIN snap rails	7503T-DIN
NiCd battery, 3.6V	

Appendix J: X and Y axis drives amplifier specifications

Maxon ADS 50/5 4-Q-DC Servoamplifier Datasheet

(<http://www.maxonmotor.co.uk>)

4-Q-DC Servoamplifier ADS in module housing



Order numbers

ADS 50/10 201593 4-Q-DC Servoamplifier POWER Version in module housing

ADS 50/5 145391 4-Q-DC Servoamplifier STANDARD Version in module housing

Accessories

235811 Shunt regulator

Electrical Data

- Supply voltage V_{DD} 12 ... 50 VDC
- Ripple $< 5\%$
- Max. output voltage $0.9 \times V_{DD}$
- Max. output current I_{max}
 - ADS 50/10 POWER 20 A
 - ADS 50/5 STANDARD 10 A
- Continuous output current I_{cont}
 - ADS 50/10 POWER 10 A
 - ADS 50/5 STANDARD 5 A
- Switching frequency of power stage 50 kHz
- Max. efficiency 95 %
- Band width current controller 2.5 kHz
- Built-in motor choke
 - ADS 50/10 POWER 75 μ H / 10 A
 - ADS 50/5 STANDARD 150 μ H / 5 A

Inputs

- Set value -10 ... +10 V ($R_i = 20\text{ k}\Omega$)
- Enable +4 ... +60 V ($R_i = 15\text{ k}\Omega$)
- DC tacho min. 2 VDC, max. 50 VDC ($R_i = 14\text{ k}\Omega$)
- Encoder signals Channel A, A', B, B' max. 100 kHz, TTL

Outputs

- Current monitor "Monitor I", short circuit protected -10 ... +10 VDC ($R_o = 100\text{ }\Omega$)
- Speed monitor "Monitor n", short circuit protected -10 ... +10 VDC ($R_o = 100\text{ }\Omega$)
- Status reading "Ready" Open collector max. 30 VDC ($I_L < 20\text{ mA}$)

Voltage outputs

- Auxiliary voltage, short circuit protected +12 VDC, +12 VDC, max. 12 mA
- Encoder supply voltage +5 VDC, max. 80 mA

Trim potentiometers

- ixR compensation
- Offset
- R_{max}
- I_{max}
- gain

LED indicator

- Bi-colour LED READY / ERROR
green = READY, red = ERROR

Ambient temperature- / humidity range

- Operation -10 ... +45°C
- Storage -40 ... +85°C
- No condensation 20 ... 80 %

Mechanical data

- Weight approx. 400 g
- Mounting plate Flange for M4-screws

Connection

- PCB-clamps (plug-in terminal clamps)
 - Power (5 poles), Signal (12 poles) 3.81 mm
- Pitch: suitable for wire cross section:
 - 0.14 ... 1 mm² multiple-stranded wire
 - 0.14 ... 1.5 mm² single wire
- Encoder Plug DIN 41661 for flat band cable with AWG 28 1.27 mm

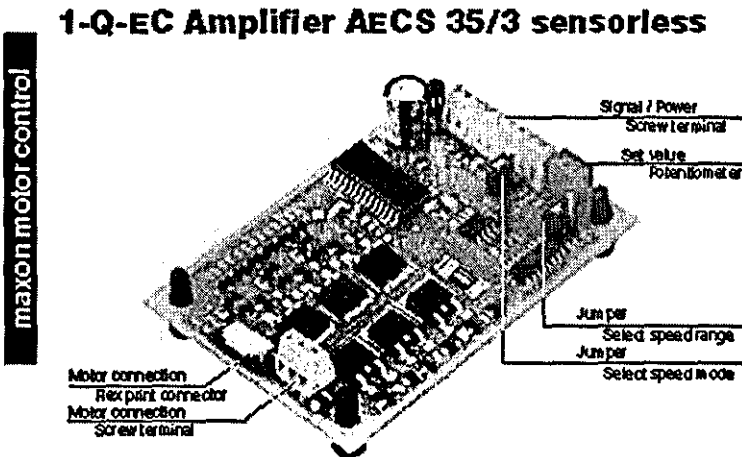
Note

General specifications on ADS 4-Q-DC servoamplifier see page 258.

Appendix K: Cutter motor amplifier specification

Maxon AECS 35/3 1-Q-EC Servoamplifier Datasheet

(<http://www.maxonmotor.co.uk>)



Advantages

- Sensorless
- Flexible
- Small design
- Different operating modes
- Significant functionality

Features

1-Q-EC Amplifier for the control of brushless EO motors without Hall sensors up to 120 Watt. With Back-EMF sensing, the actual rotor position is evaluated and the partial winding are controlled.

Wide input voltage range 8- 35 VDC. Screw terminals as well as flex print connectors (FPC) matching maxon flatmotors are provided for motor connection.

Open and compact electronic board. Easy mounting with hexagonal distance pins with inner wiring.

Simple speed control as well as pure commutation (motor speed determined via supply voltage and load) selectable with pluggable jumpers.

Direction can be set via a logic signal. The motor shaft can be either disabled or braked. The set current limitation limits the motor current to max. 5 A. The motor speed can be regulated, either with the built in potentiometer or an external analogue set value.

Electrical Data

- Supply voltage V_{DD} 8 - 35 VDC
- Max. output current I_{max} (limited internally) 5 A
- Continuous output current I_{cont} 3 A
- Speed range (to motor with 2 poles) typical 1000 ... 90 000 rpm

Inputs

- Direction logic signal (5 V) or switch against GND. Open or high level = clockwise at GND = counter-clockwise
- Brake logic signal (5 V) or switch against GND. Open or high level = motor shaft turns at GND = motor shaft stops
- Disable logic signal (5 V). Open or low level = motor shaft turns. High level = motor is separated from supply
- Set value analogue input (0.2 ... 5 V)

Outputs

- Monitor Open Collector (pull-up 22 k Ω at 5 V, 10 mA)
- Speed monitoring NCS Open Collector (pull-up 4.7 k Ω at 5 V, 10 mA)
- Control voltage OUT analogue output (0 ... 5 V)

Motor connections

- Motor winding 1
- Motor winding 2
- Motor winding 3

Ambient temperature

- Operation 0 ... +40°C
- Storage -40 ... +65°C

Humidity range

- No condensation 20 ... 90 %

Mechanical data

- Weight approx. 20 g
- Dimensions (L x W x H) 74 x 61 x 20 mm
- Position 4 distance pins hexagonal M2
- Mounting hole separation 63.2 x 40.5 mm

Connector

- Power / Signal
- Screw terminal J1 9 poles
- Pitch 2.54 mm
- AWG 26 - 20 0.14 - 0.5 mm²

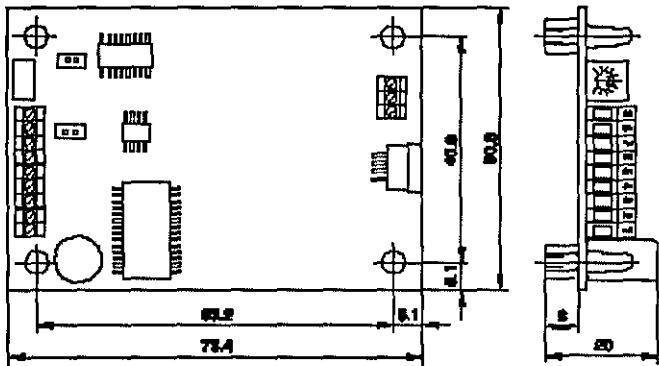
Motor connection

- Screw terminal J2 3 poles
- Pitch 2.54 mm
- AWG 26 - 20 0.14 - 0.5 mm²
- Flexprint connector J3 4 poles
- Pitch 1.0 mm

Order Number

- AECS 35/3 1-Q-EC Amplifier sensorless
- 215730

Dimensions in [mm]



Appendix L: Performance criteria (IAE, ITAE, P_{IAE}, P_{ITAE})

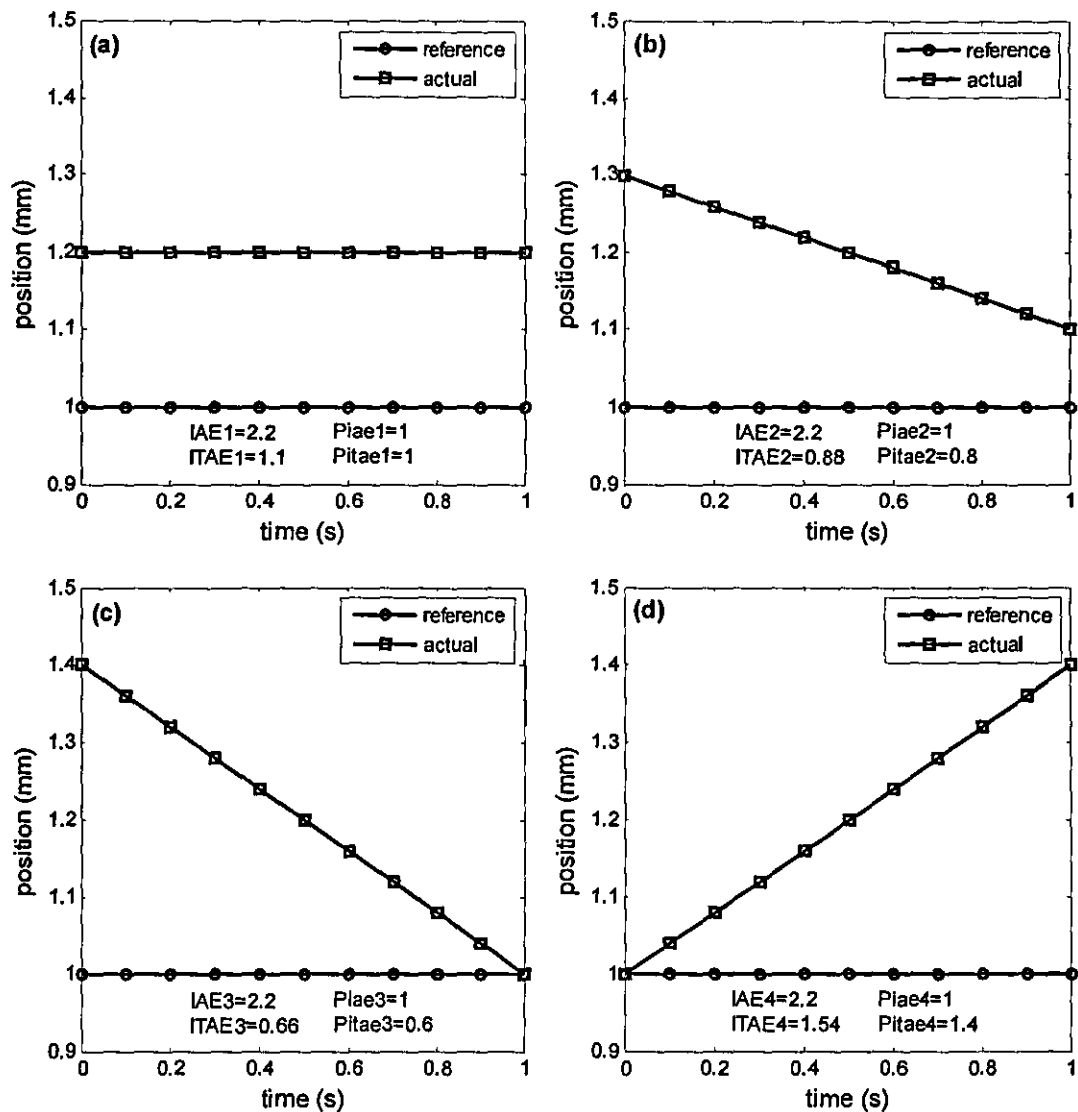


Figure M.1 Examples for performance criteria

The performance criteria *IAE* and *ITAE* are defined as:

$$IAE = \sum_i |\varepsilon_i| \quad \text{and} \quad ITAE = \sum_i t_i \cdot |\varepsilon_i|$$

where; ε_i and t_i are the error and time at the i^{th} sample respectively. In the examples of Figure M.1, the *IAE* values represent the absolute position difference between the reference and actual curves for 11 samples from $t=0$ s to $t=1$ s. Although the *IAE* describe the proximity of the two curves, responses with different characteristics may have the same *IAE* values, as in the case of Figure M.1.

The *ITAE* provide information about the error behaviour in time. Lower values indicate that the actual response approaches the reference as time progresses, and this is more desirable in contouring applications.

The performance factors P_{IAE} and P_{ITAE} describe the performance of a response relative to another. In Figure M.1, the performance factors are calculated relative to the response in Figure M.1(a) as follows:

$$P_{IAEi} = \frac{IAE_i}{IAE_1} \quad \text{and} \quad P_{ITAEi} = \frac{ITAE_i}{ITAE_1}$$

Appendix M: Accompanying CD

The accompanying CD contains the following:

- ◆ Photographs and videos of the current PIMM test-rig.
- ◆ Photographs and videos of a previous test rig (Design 3 in Appendix D).
- ◆ Source code of the Visual Basic software.

Detailed contents of the CD and instructions for viewing the video files can be found in *"Info.txt"*.

Appendix N: Design Alternatives for a Novel Wood Moulder

Paper presented at Mechatronics 2004, The 9th Mechatronics Forum International Conference, Ankara, Turkey, August 30 – September 1, 2004.

DESIGN ALTERNATIVES FOR A NOVEL WOOD MOULDER

Yigit Tascioglu, Mike R. Jackson

Loughborough University, Wolfson School of Mechanical and Manufacturing Engineering, Loughborough, UK.

email: y.tascioglu@lboro.ac.uk, m.r.jackson@lboro.ac.uk

Abstract

This paper evaluates the design alternatives for two-axis positioning system of a novel wood moulder. This new concept aims elimination of tooling and set-up costs of conventional wood moulders in short production runs. Evaluation is done by performing software simulations of different axis configurations, control algorithms and multi-axis synchronization techniques. Target performance specifications were met and the best design was identified.

1 Introduction

Wood mouldings are long narrow pieces of timber with profiled ornamental surfaces. Conventionally, wood mouldings are produced with planar/moulder machines. The fundamental principle of the conventional moulders is the separation of material from the advancing workpiece by profile-specific knives which are clamped on a rotating cutterhead as shown in Figure 1. Since the width of the knives is equal to the width of the workpiece the desired profile is achieved with a single feed. This process is characterized by high cutting tool tip velocities which are typically within the range 30-125m/s with correspondingly high workpiece feed speeds ranging from 5 to 120m/min (Jackson et al 2002).

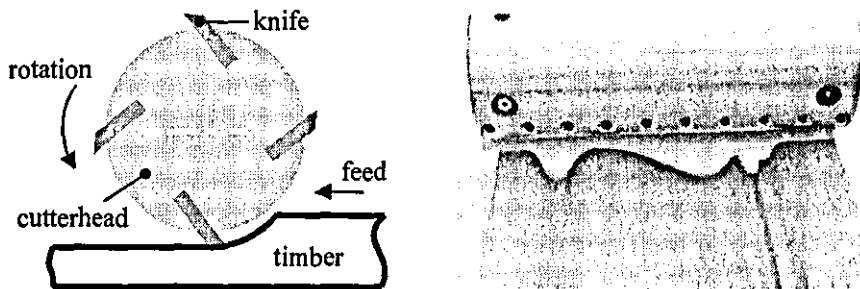


Figure 1 Conventional Moulding

High production capability of the conventional concept compensates the costs of manufacturing, mounting and maintenance of the profile-specific cutter knives as well as the downtime for machine set-up.

When batch production of a particular moulding or even a few meters of a one-off special is required, the tooling and machine set-up costs of conventional method cannot be compensated. It is intended to design a new moulding machine to minimize the above costs in short production runs. Previous work on the subject had been carried out and reported in (Waghorn 1998) and (Jackson et al 2000). This paper evaluates the design alternatives for the novel Profile Independent Wood-Moulding Machine (PIMM) by using mathematical models and simulations.

2 Profile independent moulding machine (PIMM) concept

The essential part of the proposed concept is a very thin (i.e. 1mm) cutting disc which is mounted on a two-axis positioning system (Figure 2). The moulding is produced by oscillating the rotating cutting disc along the width of the timber while following the desired profile geometry.

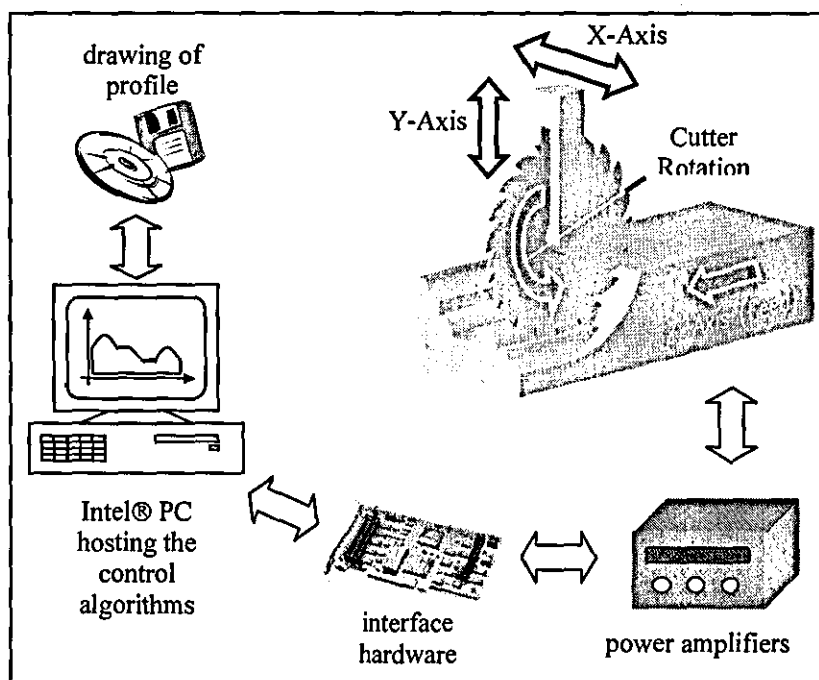


Figure 2 PIMM Concept

The input to the system is supplied directly by CAD drawings of the desired moulding profile in DXF format. The algorithms implemented on an Intel™ PC read the profile geometry and control the machine.

Being able to produce any moulding profile from CAD drawing by using the same cutting tool introduces higher manufacturing flexibility, and enables the production of wood mouldings with minimum tooling cost and virtually zero machine set-up time.

This paper concentrates only on design of the positioning system that moves the cutter on the X-Y plane. The target performance is set as 1s per pass over a 100mm-wide standard profile with a maximum contour error of 0.05mm.

3 Design alternatives

In order to find the best alternative for this multi-axis positioning system, firstly the problem was divided to three parts as follows;

- Axis configuration
- Motion control for each axis
- Multi-axis synchronization

For the first part, two main axis configurations were considered. In configuration 1 the cutter assembly (cutter and motor) is attached to the vertical drive, which is carried by the stronger horizontal drive (Figure 3a). Configuration 2 has a stronger vertical drive carrying the horizontal drive and the cutter assembly attached to it (Figure 3b).

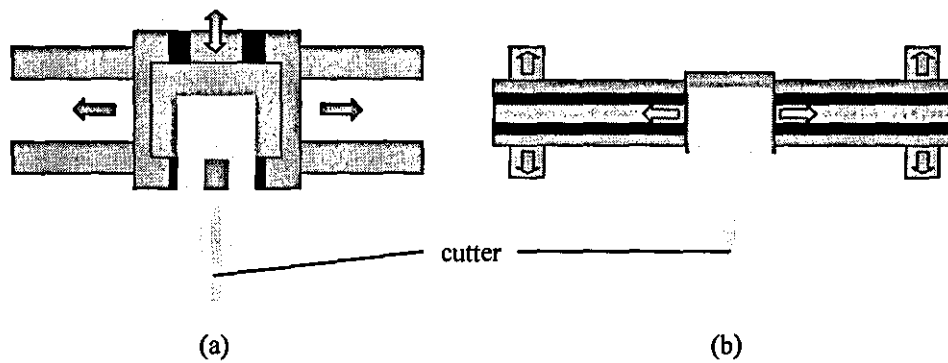


Figure 3 Axis configuration alternatives

Two conventional feedback approaches namely proportional position controller and cascaded position controller were used to control the motion of individual axes. The controller gains were tuned using the Nyquist method while tolerating 10% overshoot for the sake of fast system response.

Finally, for the synchronization of the axis motions again two methods were implemented. The first and simpler method uses the fine sampled points of the profile as the input. The horizontal drive acts as the master and the slave vertical drive gets its target input depending on the output of the master via a look-up table.

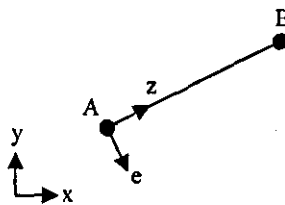


Figure 4 Vector control approach

The second synchronization method is more advanced and gives the drives an equal status. Instead of the sampled points, endpoints of the profile segments are supplied as inputs. The control coordinate system is rotated to align one axis with the motion vector while the other will be orthogonal to it. Figure 4 illustrates this concept for a motion segment from point A to point B with the control coordinate system z-e aligned to the motion vector. The z-controller will most of the time control the speed along the path while the e-controller will control the path error (Saffert 2001).

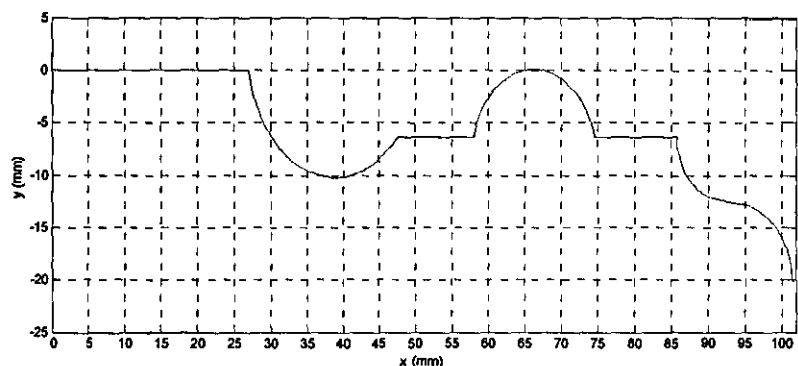


Figure 5 Test Profile

The combinations of the alternatives described above were simulated on the test profile in Figure 5.

4 Modeling of drives

Figure 6 shows the block diagram of the drives used in the simulations. Where, u : supplied voltage, L_m : motor terminal inductance, R_m : motor terminal resistance, K_t : torque constant, J_r : equivalent rotary inertia coupled to drive motor, C_r : equivalent rotary damping coupled to drive motor, K_e : back-emf constant, R : transmission ratio from motor shaft angle to carriage position (lead/2 π for leadscrew, pulley radius for timing belt), K_s : leadscrew or timing belt stiffness, M_c : carriage mass, C_c : equivalent linear damping (Matsubara et al 2000).

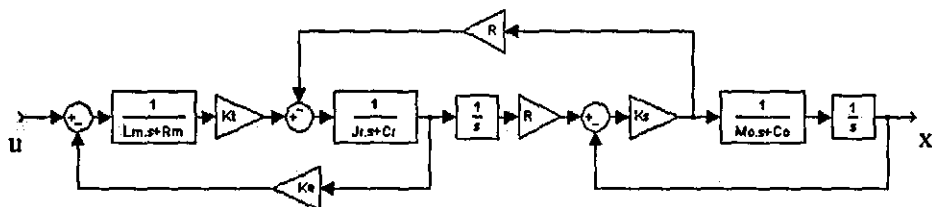


Figure 6 Drive block diagram

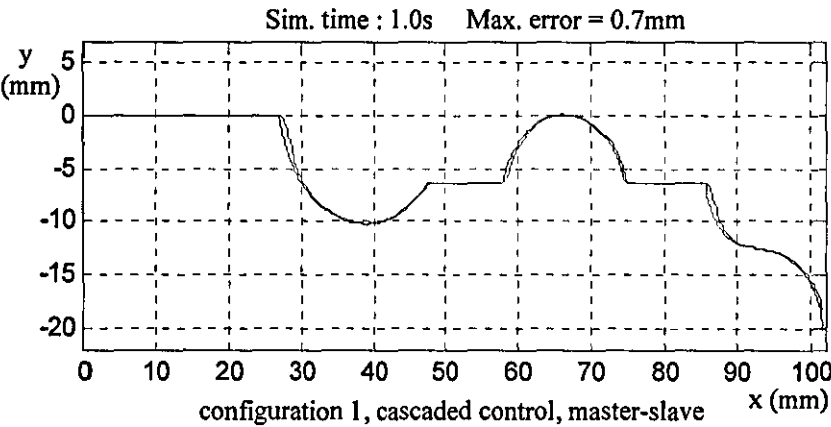
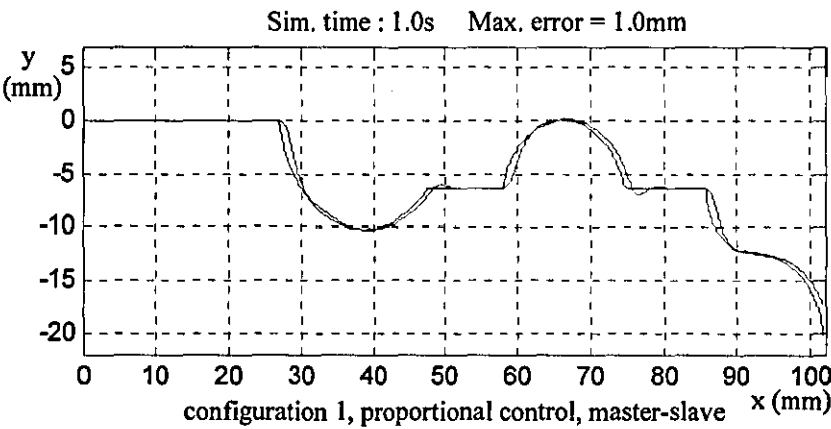
Simulation parameters for the two axis configurations described above are given in Table 1.

Parameter	Axis Configuration 1		Axis Configuration 2	
	Horizontal	Vertical	Horizontal	Vertical
Lm (H)	0.00012	0.0002	0.0002	0.00012
Rm (ohm)	0.582	2.55	2.55	0.582
Kt (Nm/A)	0.026	0.0124	0.0124	0.026
Jr (kgm2)	$3.66 \cdot 10^{-6}$	$6.13 \cdot 10^{-7}$	$6.13 \cdot 10^{-7}$	$3.66 \cdot 10^{-6}$
Cr (Nms/rad)	$2 \cdot 10^{-5}$	$1.13 \cdot 10^{-5}$	$1.13 \cdot 10^{-5}$	$2 \cdot 10^{-5}$
Ke (Vs/rad)	0.026	0.0124	0.0124	0.026
R	0.0008	0.0013	0.0013	0.0008
Mc (kg)	0.9	0.2	0.2	0.9
Cc (Ns/m)	20	20	20	20

Table 1 System Parameters

5 Simulation results

Simulations of eight different alternatives were performed in Matlab/Simulink and the results are presented in Figure 7 and Figure 8.



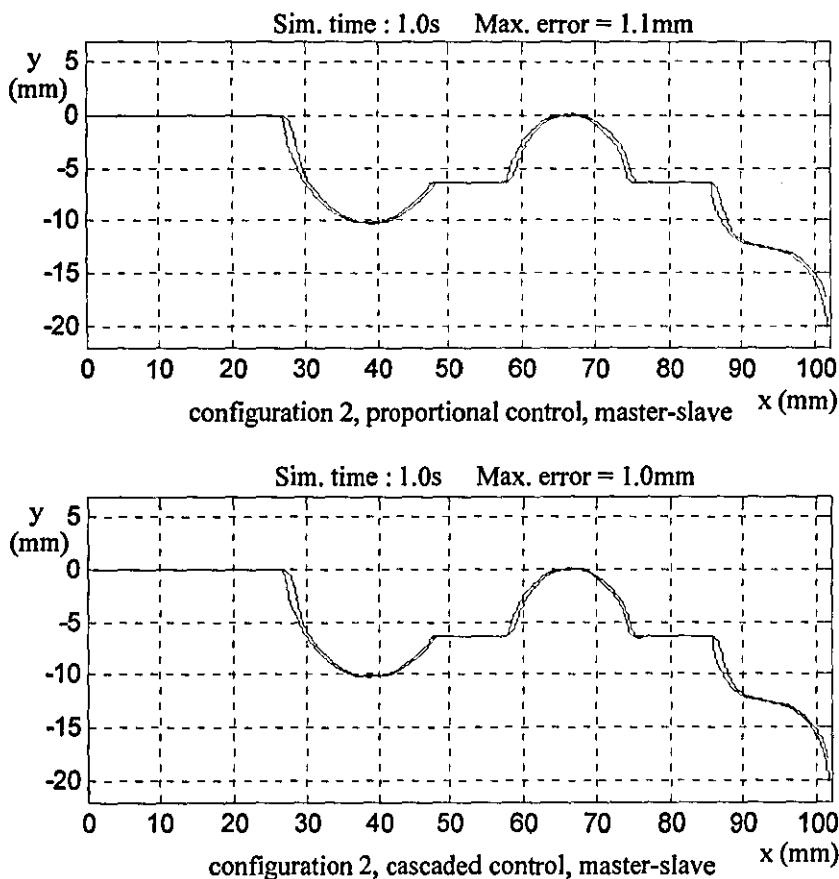
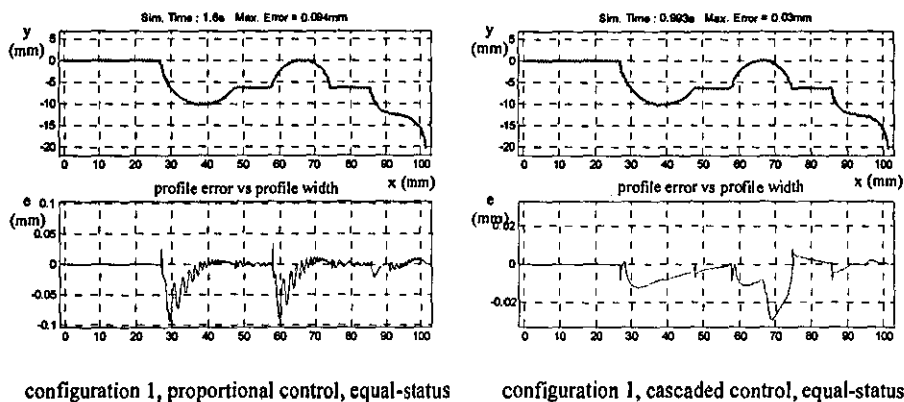


Figure 7 Master-slave simulation results

The master-slave synchronization simulations were carried out for the desired pass time of 1s. As expected, relatively better profile was achieved by axis configuration 1 than configuration 2 due to the lighter slave drive. Increased performance of cascaded control over proportional position control was identified. Nevertheless, none of the simulations achieved sharp corners and the profile accuracy with master-slave synchronization remained far behind the desired value of 0.05mm.



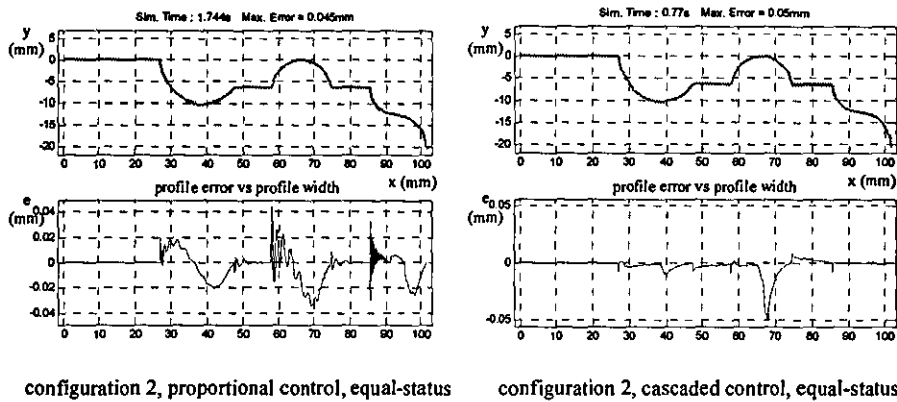


Figure 8 Equal-status simulation results

Equal-status approach reached much better results in terms overall profile accuracy and tracking sharp corners. Proportional control could not achieve the desired pass time of 1s. On the other hand, both configurations with cascaded control accomplished the desired performance. Cascaded control performed 48% faster with configuration 1 and 60% with configuration 2. Axis configuration 2 with cascaded control performed 23% faster than configuration 1.

6 Conclusions

Simulation results achieved the desired performance measures of 1s pass time and 0.05mm contouring accuracy. Stronger vertical drive which is carrying a lighter horizontal drive and the cutter assembly attained the best performance with cascaded controller and purpose designed equal-status synchronization approach, therefore proved to be the best alternative for the design.

7 References

- Jackson, M. R, Parkin, R. M. & Brown, N. (2002), Waves on wood, *Proc. Instn. Mech. Engrs. Part B: Journal of Engineering Manufacture* 216: 475-497.
- Jackson, M. R, Neumayer, R., Parkin, R. M. & Brown, N. (2000), Profile independent wood moulding machine dynamic model and control system, *Proc. of Mechatronics 2000, Georgia Inst. of Technology*, 6 - 8 September 2000.
- Matsubara, A., Kakino, Y. & Watanabe, Y. (2000), Servo performance enhancement of high speed feed drives by damping control, *Proc. of the 2000 Japan-USA Flexible Automation Conference, Ann Arbor, Michigan*, 23 - 26 July 2000.
- Saffert, E. (2001), Profile independent wood moulding machine revisited, *Personal communication, Ilmenau Technical University*.
- Waghorn, C. (1998), Numerical controlled wood moulding machine, *MSc. Thesis, Loughborough University*.

Appendix O: Mechatronic Design of a Novel Wood Moulder

Paper accepted for publication in Proceedings of the Institution of Mechanical Engineers, Part B: Journal of Engineering Manufacture.

Initial manuscript submitted on 12 January 2005.

Accepted after revision for publication on 19 January 2006.

MECHATRONIC DESIGN OF A NOVEL WOOD MOULDER

Yiğit Taşcioğlu, Mike R. Jackson

Holywell Mechatronics Research Centre,
Loughborough University, Loughborough, Leicestershire, UK
email: Y.Tascioglu@lboro.ac.uk

Abstract

This paper introduces the novel concept for a profile independent wood-moulding machine. The concept aims to eliminate tooling and set-up costs of conventional wood moulders in short production runs. The designed prototype and its expected performance in terms of production rate and product quality are outlined. The prototype is modelled and the contouring control algorithm is presented. It is shown through simulation that the target production rate and product quality can be achieved.

Keywords: wood machining, drive modelling, contouring control

NOTATION

C	equivalent damping coefficient at the motor (Nms/rad)	K_t	torque constant (Nm/A)
C_c	carriage damping coefficient (Ns)	Kp_f, Kp_e	position gains on f and e directions
C_g	gearbox damping coefficient (Nms/rad)	Kv_f, Kv_e	velocity gains on f and e directions
C_m	motor damping coefficient (Nms/rad)	L_m	motor inductance (H)
C_p	pulley bearing damping coefficient (Nms/rad)	L_s	leadscrew lead (m)
C_s	leadscrew damping coefficient (Nms/rad)	M_c	carriage mass (kg)
d	maximum depth of cut (mm)	N_g	gearbox ratio
e	unit vector perpendicular to motion	p	surface wave pitch (mm)
f	unit vector along the direction of motion	R	cutter radius (mm)
F_c	cutting force (N)	R_m	motor resistance (Ω)
F_e	external force (N)	R_p	pulley radius (m)
g	gravitational acceleration (m/s^2)	R_t	overall transmission ratio (m)
h	surface wave height (μm)	t	cycle time (s)
J	equivalent inertia coupled to the motor (kgm^2)	v_{mean}	mean contouring speed (mm/s)
J_g	gearbox inertia (kgm^2)	V_f, V_e	velocities on f and e directions (m/s)
J_m	motor inertia (kgm^2)	V_x, V_y	velocities on x and y directions (m/s)
J_p	pulley inertia (kgm^2)	w_p	profile width (mm)
J_s	leadscrew inertia (kgm^2)	$\Delta f, \Delta e$	position errors on f and e directions (m)
K_e	back-emf constant (Vs/rad)		

1 INTRODUCTION

Wood mouldings are long narrow pieces of timber with profiled ornamental surfaces. Mouldings of various profiles and wood types are used in furniture, architecture and joinery industries and typical applications include door/window frames, skirting boards and picture frames (Fig. 1).

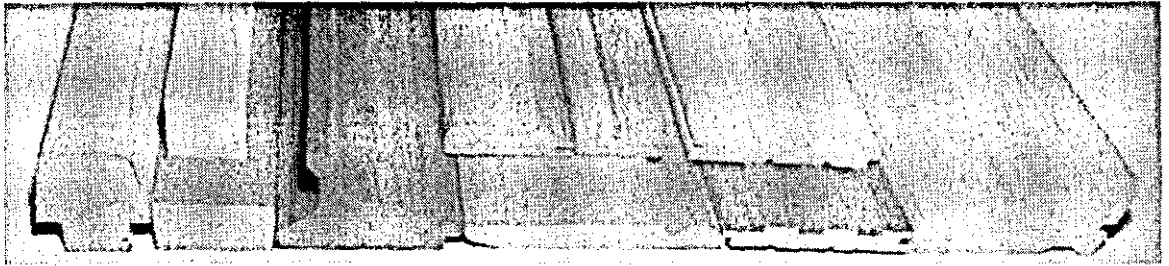


Fig. 1 Selection of wood mouldings

The general name for the process used to produce wood mouldings is rotary machining of timber. The raw material for this process is normally rough sawn timber pieces with constant nominal rectangular cross-section along the length. Dimensions typically range from 10 to 100 mm thick, 20 to 300 mm wide and 250 mm to 6 m long. Conventional moulding machines (Fig. 2) comprise a number of horizontal and vertical cutterheads configured in position and type to suit a particular market segment. Rotary machining of timber is characterised by high cutting tool tip velocities ranging from 30 to 125 m/s with correspondingly high workpiece feed speeds between 5 to 120 m/min. The material removal phenomena is similar to that of milling of metals in up-cutting mode, where a cutterhead containing cutting edges is used to sever chips from the advancing workpiece (Fig. 3). Despite being widely used, the term ‘mouldings’ is somewhat misleading since this is a material removal process and no material deformation as such takes place [1].

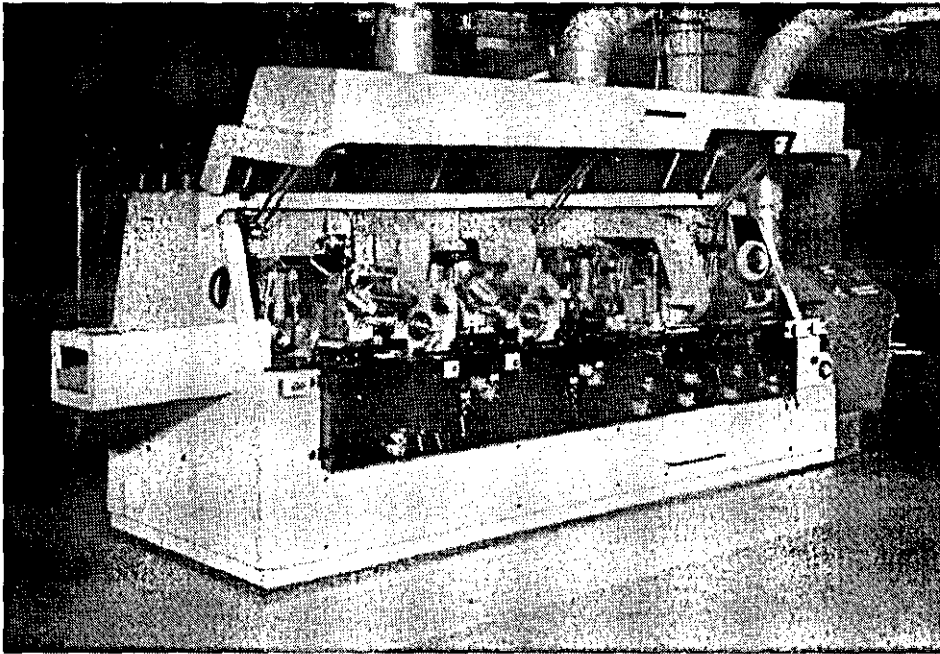


Fig. 2 Conventional planing and moulding machine

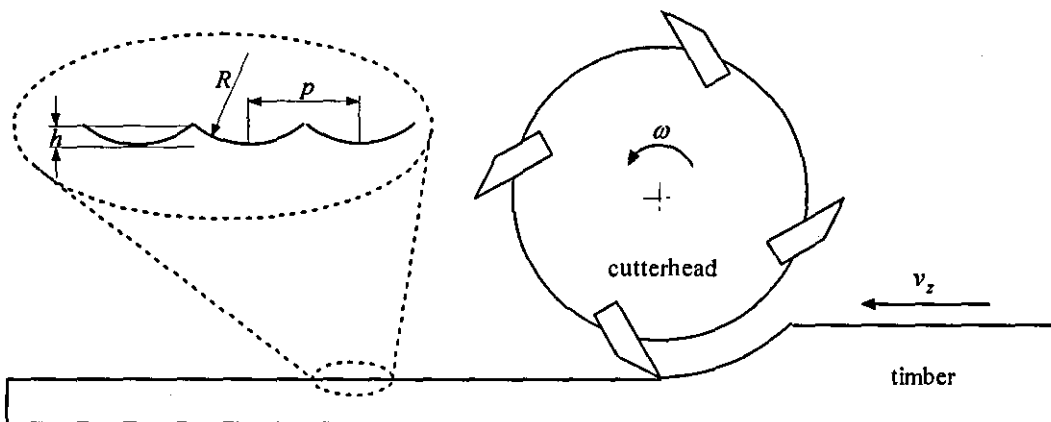


Fig. 3 Rotary machining process

For every moulding profile, cutterheads contain suitably shaped cutters (Fig.4) and the raw material is transformed into the finished product with a single feed. High production capability of the conventional concept compensates the costs of manufacturing, mounting and maintenance of the profile-specific cutters as well as the downtime for machine set-up.

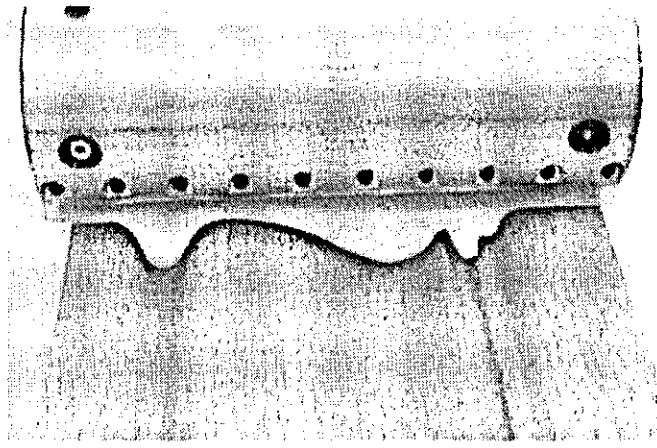


Fig. 4 Profile-specific cutter

Where just short production runs of a particular type of moulding are required or even a few meters of a one-off special is needed, the tooling and machine set-up costs of the conventional moulding machines cannot be compensated [2]. It is intended to design a new Profile Independent Moulding Machine (PIMM) for short production runs in order to minimize the tooling and machine set-up costs.

A low cost prototype of the PIMM is currently under construction. This paper introduces the idea behind the new concept, outlines the expected performance and concentrates on the mathematical modeling and simulation of the prototype. The performance evaluation of the physical prototype machine is the subject of a future paper.

2 PROFILE INDEPENDENT MOULDING MACHINE (PIMM)

The essential part of the proposed concept is a very thin (i.e. 1 mm) cutting disc, which is mounted on a two-axis positioning system (Fig. 5). The moulding is produced by oscillating the rotating cutting disc along the width of the timber while following the desired profile geometry which is supplied directly from a CAD drawing. The timber is fed in between two consecutive passes along the width.

Being able to produce any moulding profile directly from CAD drawing by using the same cutting tool results in full manufacturing flexibility, and enables the production of wood mouldings with minimum tooling cost and virtually zero machine set-up time.

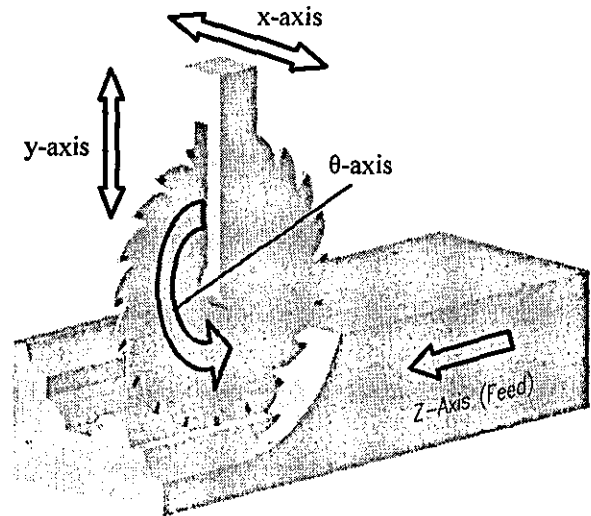


Fig. 5 PIMM Concept

The initial effort on the concept [3] was concentrated on electro-mechanical design of a two-axis positioning test rig. It was followed by a modeling and control oriented investigation [2, 4], which simulated and experimented various conventional path control methods on the previously designed hardware. Although the results show some evidence on the viability of the concept, the achieved performance of the system stayed behind the targets in terms of both speed and accuracy. The current work approaches the system as a whole and it is directed towards the holistic design of a fully functional PIMM. The evaluation of some mechanical design and control alternatives, at the initial stages of this work, is presented in [5].

The overview of the designed PC-based prototype system is shown in Fig. 6. Desired moulding profile is supplied to the system directly from CAD drawings in commonly

used DXF format. This profile information is processed in the PC and the cutter path and timber feed is controlled via the interface hardware.

The machine consists of four axes. The vertical axis (y-axis) moves along the precision linear guideways attached to the side columns of the machine and is driven from the centre by a DC-motor and a directly coupled anti-backlash leadscrew-nut assembly. It carries the horizontal axis and the cutter mechanism. The horizontal axis (x-axis) consists of a DC-motor, planetary gearbox, timing belt drive and a single linear guideway. Feedback from both axes is obtained via incremental encoders, which are attached to the rotor shafts of the drive motors. The current timber feed drive (z-axis) is only designed to perform initial tests on the positioning accuracy with small test specimens. It uses a direct drive leadscrew-stepper motor assembly. Finally, the cutter is rotated (θ -axis) by a remote high-speed AC motor via a flexible shaft. It is also intended to replace the θ -axis motor with a small air-turbine in the future in order to achieve a more compact system.

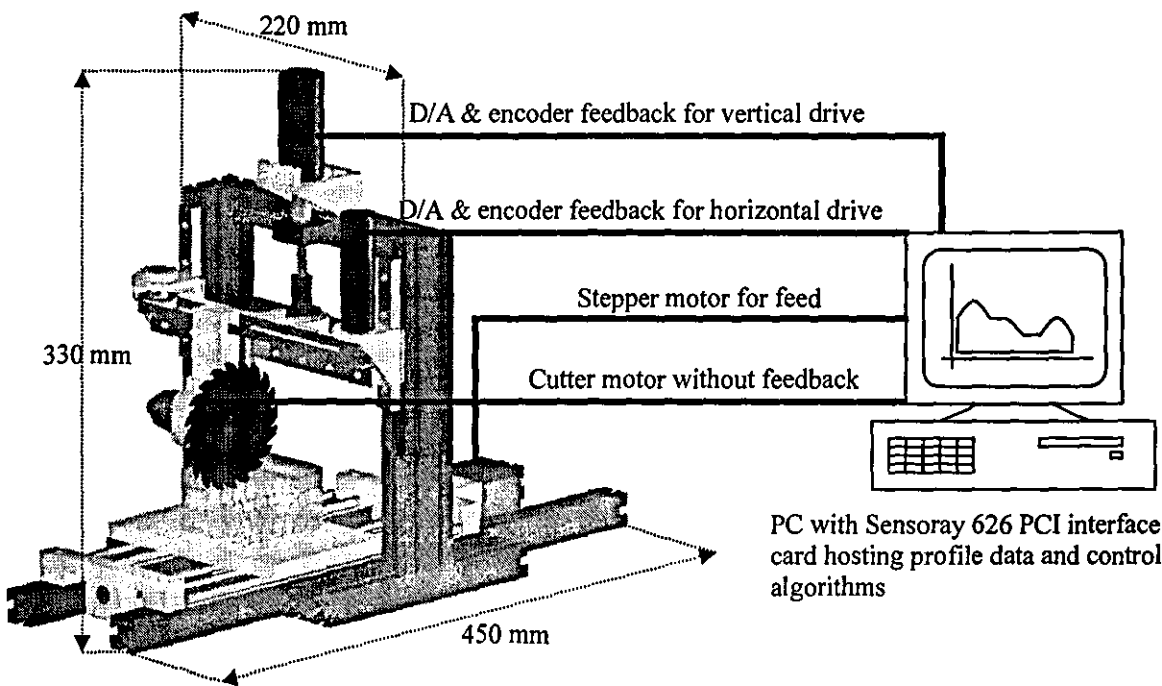


Fig. 6 Prototype PIMM system

The PIMM prototype is 330 mm high, 220 mm wide and 450 mm long, therefore, it can be considered as a ‘miniature’ moulding machine compared to the conventional machines. The maximum distances that the cutter travels in horizontal and vertical axes are 120 mm and 30 mm respectively. It is planned to use a 1 mm thick, 20-teeth circular saw with 85 mm diameter for the initial tests. The prototype allows machining of profiles having width of maximum 100 mm and height of 25 mm. This is representative of the majority of the wood profiles market. A wide range of moulding profiles can be found in manufacturers’ websites such as [6-8].

In principle, it is possible to change the profile cross section along the length of the timber thus providing the opportunity for 3-D mouldings, not currently possible on conventional planar/moulder machinery.

3 PERFORMANCE ANALYSIS AND ESTIMATIONS

Due to the operation principle, the rate of production expected from the PIMM is influenced by two parameters. The first parameter is the ‘contouring speed’ which is the time taken for the cutter to travel from one side of the timber to the other along the width while cutting. The second is the ‘profile quality’ in terms of geometric accuracy and surface waviness.

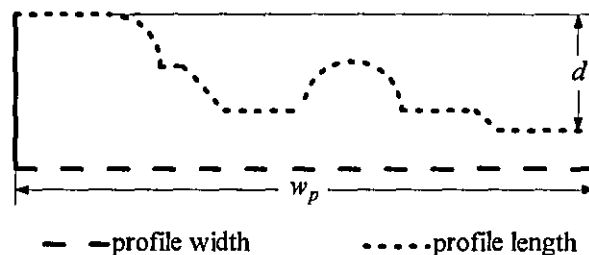


Fig. 7 Moulding dimensions

As mentioned earlier, wood mouldings can be in various shapes and sizes. Since the contouring speed is highly dependent on profile geometry, a relation between the

profile width and profile length was established and also the dimensional capabilities of the designed prototype were taken into account (Fig. 7).

The maximum dimensions for profile width w_p and depth of cut d were limited to 100 mm and 25 mm respectively, and then profile lengths of a number of commercial profiles were measured and compared with their profile widths. On average, profile lengths were found to be 20% longer than the corresponding profile widths. Therefore, the mean contouring speed v_{mean} is calculated by using the following equation

$$v_{mean} = \frac{w_p}{t} \cdot 120\% \tag{1}$$

where, w_p is the profile width and t is the cycle time. Fig.8 shows the plot of the mean contouring speed versus cycle time for 100 mm wide moulding. This shows that a fast machine with cycle time less than 1 s can be achieved with a mean speed of 120 mm/s or more.

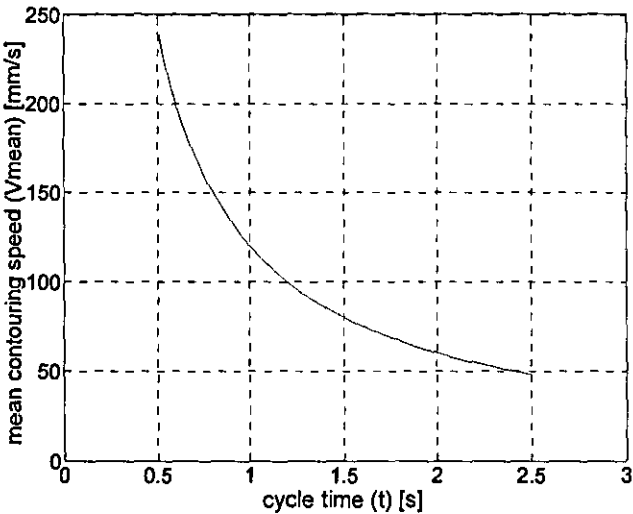


Fig. 8 Mean contouring speed vs. cycle time for 100 mm wide moulding

The second parameter ‘profile quality’ is divided into two parts as geometric accuracy and the surface waviness. The measure of geometric accuracy is the contouring error,

being the shortest distance from any point on the actual contour to the desired contour [9]. The target value for the maximum contouring error was set to be 0.05 mm.

Surface waviness is characterized by a regular series of waves that are perpendicular to the workpiece feed direction (Fig. 3). These waves are caused by the nature of the rotary machining process. In conventional planning/moulding, surface wave pitch p is primarily dependent on workpiece feed speed, cutterhead rotational speed and the number of cutting edges in the cutterhead. A good quality surface is classified by a wave pitch of typically <1.5 mm, and a lower quality surface by a wave pitch of typically >2.5 mm. The wave height of the idealized surface is described by the equation (2) and is typically 2µm for the higher-quality surfaces:

$$h = \left(R - \sqrt{R^2 - \frac{p^2}{4}} \right) \cdot 10^3 \quad (2)$$

Generally, smaller cutter radii will produce deeper cuttermarks and this is perceived as a lower quality surface. The small values of surface wave height make the waviness quality highly sensitive to displacements between cutting edges and workpiece, normal to the machined surface. Such displacements can be caused by spindle runout and excessive structural vibrations. Detailed investigation of surface waviness and influencing factors can be found in [1, 10, 11].

It is easier to work with wave pitches for timber surfaces primarily because wave pitch can be measured using vernier calipers more easily than wave height. A secondary factor is that the timber processing industry already uses wave pitch as a measure of surface quality [1].

In PIMM, the workpiece is stationary during cutting and fed in between two consecutive cycles. Hence, the wave pitch p is equal to the length of timber fed after each cycle. The equation (2) still holds for calculation of wave heights and; for 85 mm

diameter cutter the wave heights are $2.9\text{ }\mu\text{m}$ for $p = 1\text{ mm}$ and $18.3\text{ }\mu\text{m}$ for $p=2.5\text{ mm}$. Another point is that, due to the operation principle of PIMM, possible spindle runout is expected to have less influence on the surface waves than the conventional process. However, this needs to be experimentally investigated and will be addressed in the future.

The graph of production rate versus cycle time for different waviness pitches is shown in Fig. 9.

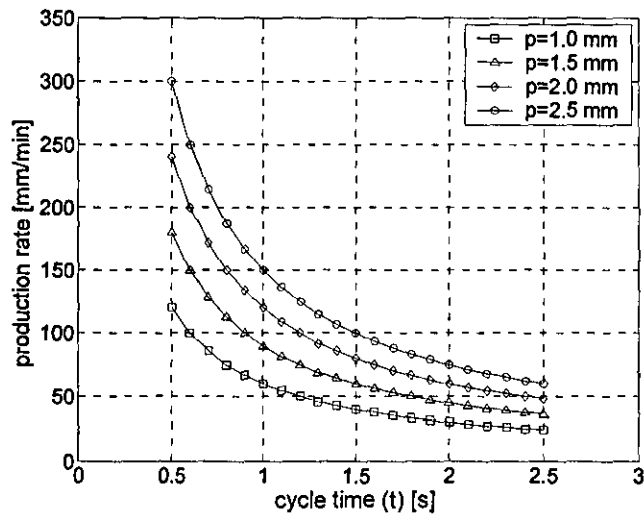


Fig. 9 Production rate vs. cycle time

A target production rate for a moderate quality (i.e. $p=2.5\text{ mm}$), 100 mm wide moulding was set as 150 mm/min. It can be achieved with 1 s cycle time (Fig. 9) and therefore the mean contouring speed should be 120 mm/s (Fig. 8).

In order to analyse and evaluate the performance of the concept prior to the detailed design, the drives were mathematically modelled and simulated. Following sections explain the modelling and simulation in Matlab/Simulink.

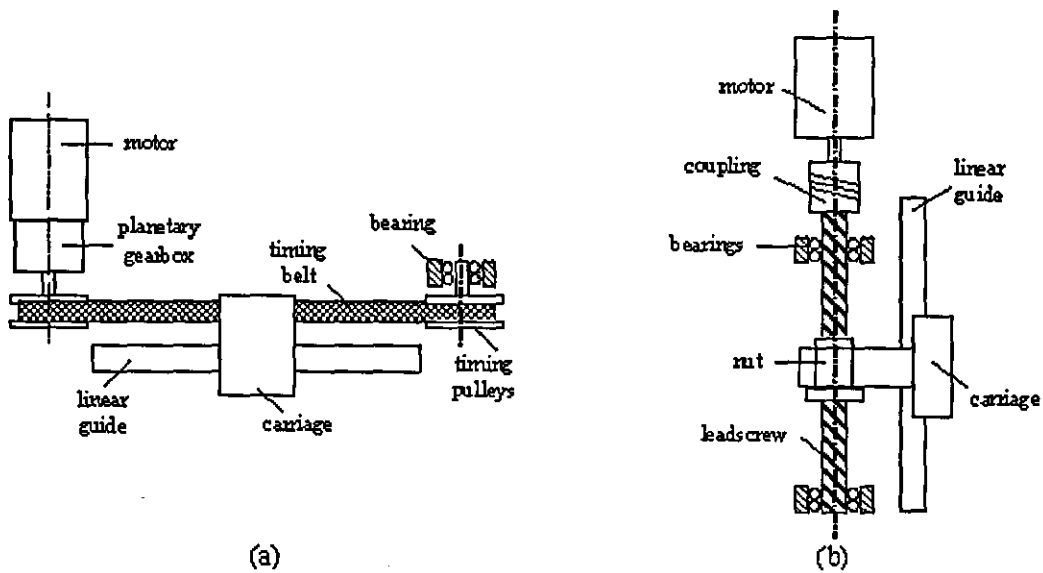


Fig. 10 Horizontal (a) and vertical (b) drive train elements

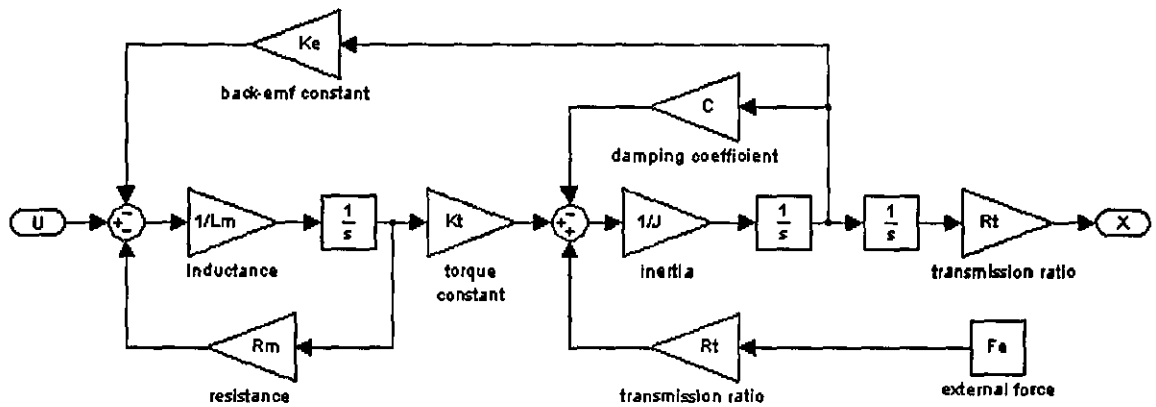


Fig. 11 Block diagram of a single drive

4 MODELING OF HORIZONTAL AND VERTICAL DRIVES

Fig. 10 shows the schematic of the horizontal and vertical drives. Generalized block diagram of a single drive is given in Fig. 11. The parameters for a particular drive are used with superscripts (^H) for horizontal and (^V) for vertical (i.e. K_t^H , L_m^V). For the sake of simplicity, ideally stiff transmission was assumed between the masses. Since the position feedback is obtained via incremental encoders, which are attached to the rotor shafts in the actual system, all the masses are referenced to the motors in the model.

If two masses are linked through a stiff transmission with ratio r ,

$$s_o = rs_i \quad \text{and} \quad v_o = rv_i \quad (3)$$

since the kinetic energy remains invariable, the input mass appears on the output as

$$M_i^o = r^{-2} M_i \quad (4)$$

This holds regardless whether M_i is a mass or inertia. It also holds for damping coefficients. If the motion is transformed from rotary to linear, then r will be the equivalent radius. Therefore, the equivalent inertia J , damping coefficient C and transmission ratio R_i for the horizontal and vertical drives were calculated as follows.

$$J^H = J_m^H + \left(J_g^H + 2 \cdot J_p^H + M_c^H \cdot \left(\frac{1}{R_p^H} \right)^{-2} \right) \cdot \left(\frac{1}{N_g^H} \right)^{-2} \quad (5)$$

$$J^V = J_m^V + J_s^V + M_c^V \cdot \left(\frac{2 \cdot \pi}{L_s^V} \right)^{-2} \quad (6)$$

$$C^H = C_m^H + \left(C_g^H + 2 \cdot C_p^H + C_c^H \cdot \left(\frac{1}{R_p^H} \right)^{-2} \right) \cdot \left(\frac{1}{N_g^H} \right)^{-2} \quad (7)$$

$$C^V = C_m^V + C_s^V + C_c^V \cdot \left(\frac{2 \cdot \pi}{L_s^V} \right)^{-2} \quad (8)$$

$$R_i^H = N_g^H \cdot R_p^H \quad (9)$$

$$R_i^V = \frac{L_s^V}{2 \cdot \pi} \quad (10)$$

Investigation of the cutting forces occurring in the PIMM process is beyond the scope of this work. However, the magnitude of F_c lies within the range of 2 – 7 N, depending on the cutting parameters. Typical forces can be found in [12]. The force acting on the horizontal drive by the workpiece is approximated as a constant force opposing the direction of motion (11). For the vertical drive, it is assumed that the cutting force is acting only when the drive is moving downwards (-y direction). The

external force on the vertical drive also includes the weight carried by the vertical carriage (12).

$$F_e^H = \begin{cases} -F_c \cdot \text{sgn } \dot{x} & \dot{x} \neq 0 \\ 0 & \dot{x} = 0 \end{cases} \quad (11)$$

$$F_e^V = \begin{cases} -M_c^V \cdot g & \dot{y} \geq 0 \\ F_c - M_c^V \cdot g & \dot{y} < 0 \end{cases} \quad (12)$$

5 SIMULATIONS

Simulation of the PIMM was performed in Matlab and Simulink. The simulated system is comprised of three main parts being *Reference Generator*, *Path Controller* and the *Motion System* (Fig. 12).

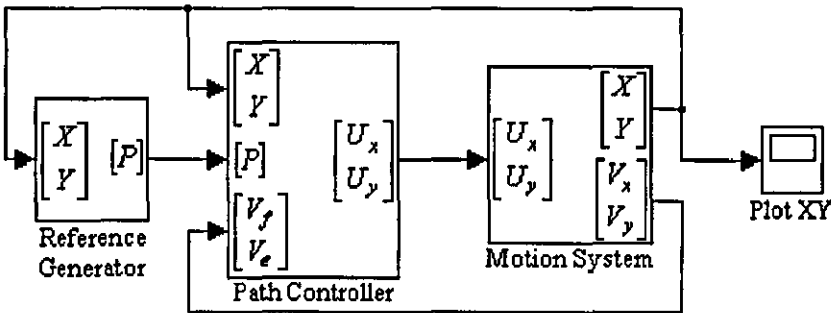


Fig. 12 Overview of simulated system

5.1 Reference Generator

Reference Generator block reads the desired moulding profile segments from a DXF file, stores them in a look-up table and supplies the segments to *Path Controller* when necessary. A segment can either be a line or an arc due to the nature of the DXF file format.

$P =$	X_{A1}	\dots	X_{Ai}	start point x coordinate
	Y_{A1}	\dots	Y_{Ai}	start point y coordinate
	X_{B1}	\dots	X_{Bi}	end point x coordinate
	Y_{B1}	\dots	Y_{Bi}	end point y coordinate
	X_{C1}	\dots	X_{Ci}	arc centre x coordinate (0 if segment is line)
	Y_{C1}	\dots	Y_{Ci}	arc centre y coordinate (0 if segment is line)
	θ_{A1}	\dots	θ_{Ai}	start point arc angle (0 if segment is line)
	θ_{B1}	\dots	θ_{Bi}	end point arc angle (0 if segment is line)
	R_1	\dots	R_i	arc radius (0 if segment is line)

Fig. 13 Profile matrix

Profile data is stored in the look-up table as $(9 \times i)$ matrix where, i is the number of segments and each column representing a single segment (Fig. 13). A function in the block initializes the left hand side of the profile to $(0, 0)$, modifies all the segment coordinates accordingly, and then fills the matrix with the segments from left to right (Fig. 14).

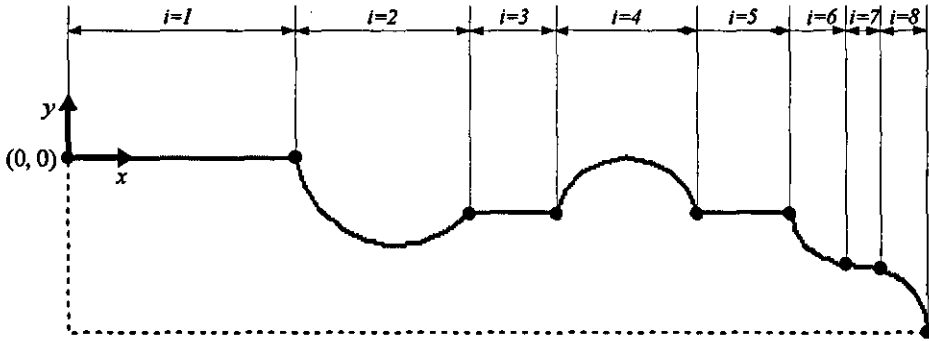


Fig. 14 Profile segments

When the simulation starts, the *Reference Generator* supplies the first segment (i.e. first column of the matrix) to the *Path Controller* and checks the distance to the end point of the segment at each sampling interval. If the distance is smaller than the position error norm (i.e. 0.05 mm) then the next segment is supplied.

5.2 Path Controller

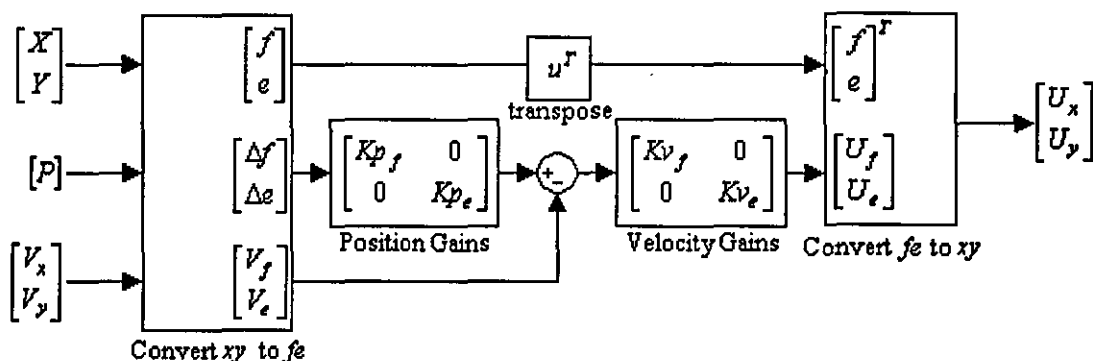


Fig.15 Path controller

The path controller shown in Fig. 15 uses a control coordinate system, which rotates to align one axis with the direction of motion while the other axis is orthogonal to it. Fig. 16 illustrates this concept both on line and arc segments for a motion from (X_A, Y_A) to (X_B, Y_B) , where f and e are unit vectors on motion and error directions respectively.

Once the position and velocity information on x - y directions are projected to f - e directions, the path controller becomes a conventional cascaded position-velocity controller, which uses proportional gains Kp_f , Kp_e for the position loop and Kv_f , Kv_e for the velocity loop. Generally, the control action on f -direction controls the speed along the path while the one on e -direction controls the contour error. After the gains are applied, the output is projected back to x - y directions before being sent to the motion system.

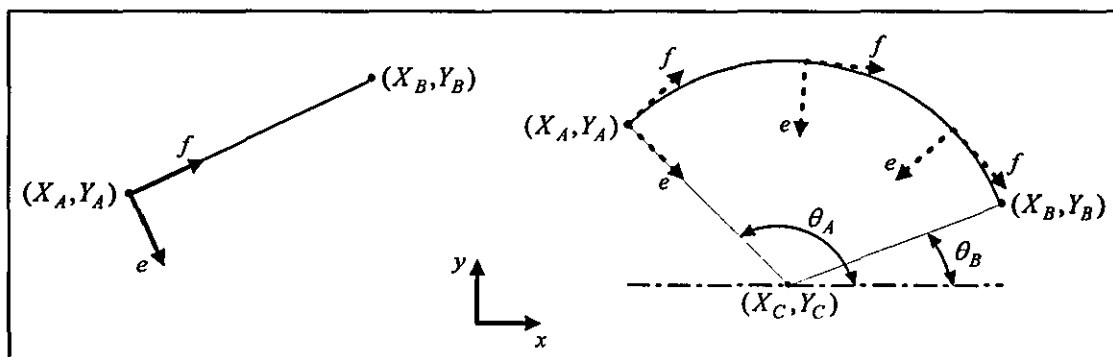


Fig. 16 Vector control approach

On a particular line segment, f and e vectors remain fixed from the start point to the end point and they are calculated by using equation (13).

$$\begin{bmatrix} f \\ e \end{bmatrix} = \begin{bmatrix} \frac{X_B - X_A}{\sqrt{(X_B - X_A)^2 + (Y_B - Y_A)^2}} & \frac{Y_B - Y_A}{\sqrt{(X_B - X_A)^2 + (Y_B - Y_A)^2}} \\ \frac{Y_A - Y_B}{\sqrt{(X_B - X_A)^2 + (Y_B - Y_A)^2}} & \frac{X_B - X_A}{\sqrt{(X_B - X_A)^2 + (Y_B - Y_A)^2}} \end{bmatrix} \quad (13)$$

Whereas on arc segments, the vectors are re-calculated at every sampling interval to ensure that the e -direction is always inline with the arc centre and the f -direction always tangent to the arc (Fig. 16). The direction of the f vector also depends on whether the arc segment is followed clockwise or anti-clockwise. Equation (14) shows the calculation of f and e vectors for an arc segment followed clockwise and (15) anti-clockwise.

$$\begin{bmatrix} f \\ e \end{bmatrix} = \begin{bmatrix} \frac{Y_c - Y}{\sqrt{(X - X_c)^2 + (Y - Y_c)^2}} & \frac{X - X_c}{\sqrt{(X - X_c)^2 + (Y - Y_c)^2}} \\ \frac{X - X_c}{\sqrt{(X - X_c)^2 + (Y - Y_c)^2}} & \frac{Y - Y_c}{\sqrt{(X - X_c)^2 + (Y - Y_c)^2}} \end{bmatrix} \quad (14)$$

$$\begin{bmatrix} f \\ e \end{bmatrix} = \begin{bmatrix} \frac{Y - Y_c}{\sqrt{(X - X_c)^2 + (Y - Y_c)^2}} & \frac{X_c - X}{\sqrt{(X - X_c)^2 + (Y - Y_c)^2}} \\ \frac{X - X_c}{\sqrt{(X - X_c)^2 + (Y - Y_c)^2}} & \frac{Y - Y_c}{\sqrt{(X - X_c)^2 + (Y - Y_c)^2}} \end{bmatrix} \quad (15)$$

Position errors Δf and Δe are calculated by using (16) for line segments and (17) for arc segments. Also the velocity feedbacks on x - y directions are projected to f - e directions by using (18).

$$\begin{bmatrix} \Delta f \\ \Delta e \end{bmatrix} = \begin{bmatrix} f \\ e \end{bmatrix} \cdot \begin{bmatrix} X_B - X \\ Y_B - Y \end{bmatrix} \quad (16)$$

$$\begin{bmatrix} \Delta f \\ \Delta e \end{bmatrix} = \begin{bmatrix} \frac{\theta_B - \arctan\left(\frac{Y - Y_C}{X - X_C}\right)}{360} \\ R - \sqrt{(X - X_C)^2 + (Y - Y_C)^2} \end{bmatrix} \quad (17)$$

$$\begin{bmatrix} V_f \\ V_e \end{bmatrix} = \begin{bmatrix} f \\ e \end{bmatrix} \cdot \begin{bmatrix} V_x \\ V_y \end{bmatrix} \quad (18)$$

The following equations show the application of controller gains (19) and projection of the output back to x - y directions (20).

$$\begin{bmatrix} U_f \\ U_e \end{bmatrix} = \begin{bmatrix} Kv_f & 0 \\ 0 & Kv_e \end{bmatrix} \times \left(\left(\begin{bmatrix} Kp_f & 0 \\ 0 & Kp_e \end{bmatrix} \times \begin{bmatrix} \Delta f \\ \Delta e \end{bmatrix} \right) - \begin{bmatrix} V_f \\ V_e \end{bmatrix} \right) \quad (19)$$

$$\begin{bmatrix} U_x \\ U_y \end{bmatrix} = \begin{bmatrix} f \\ e \end{bmatrix}^T \times \begin{bmatrix} U_f \\ U_e \end{bmatrix} \quad (20)$$

5.3 Motion System

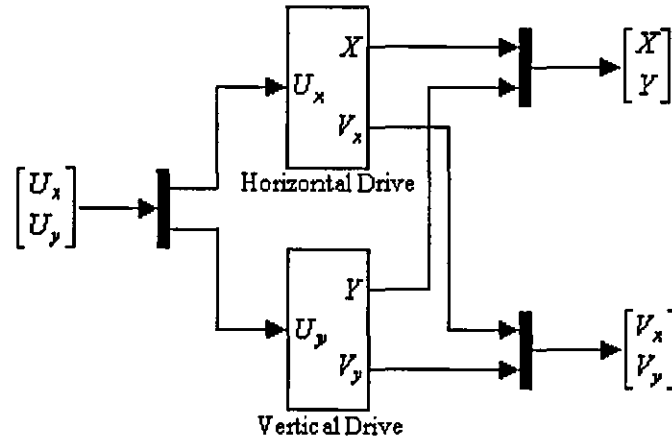


Fig. 17 Motion System

The Motion System is composed of vertical and horizontal drive models, which are described in Section 4. The input and output are treated as vectors and they are handled by multiplexer and demultiplexer blocks in Simulink (Fig. 17).

6 SIMULATION RESULTS

parameter		horizontal drive value	vertical drive value	unit
motor back-emf constant	K_e	0.0124	0.026	Vs/rad
motor torque constant	K_t	0.0124	0.026	Nm/A
motor inductance	L_m	0.0002	0.00012	H
motor resistance	R_m	2.55	0.582	Ohm
equivalent inertia	J	$7.34e-7$	$3.5e-6$	kgm^2
equivalent damping coeff.	C	$2.25e-5$	$2.46e-5$	Nms/rad
transmission ratio	R_t	$7.8e-4$	$4.8e-4$	m
carriage mass	M_c	0.2	0.9	kg
cutting force	F_c	5	5	N
position gain on f -direction	K_{p_f}		120	
position gain on e -direction	K_{p_e}		50	
velocity gain on f -direction	K_{v_f}		0.15	
velocity gain on e -direction	K_{v_e}		100	

Table 1 Simulation Parameters

Simulations have been performed for single left-to right pass along the profile width by using the parameters in Table 1. Fig. 18 shows the initial performance of the simulated system.

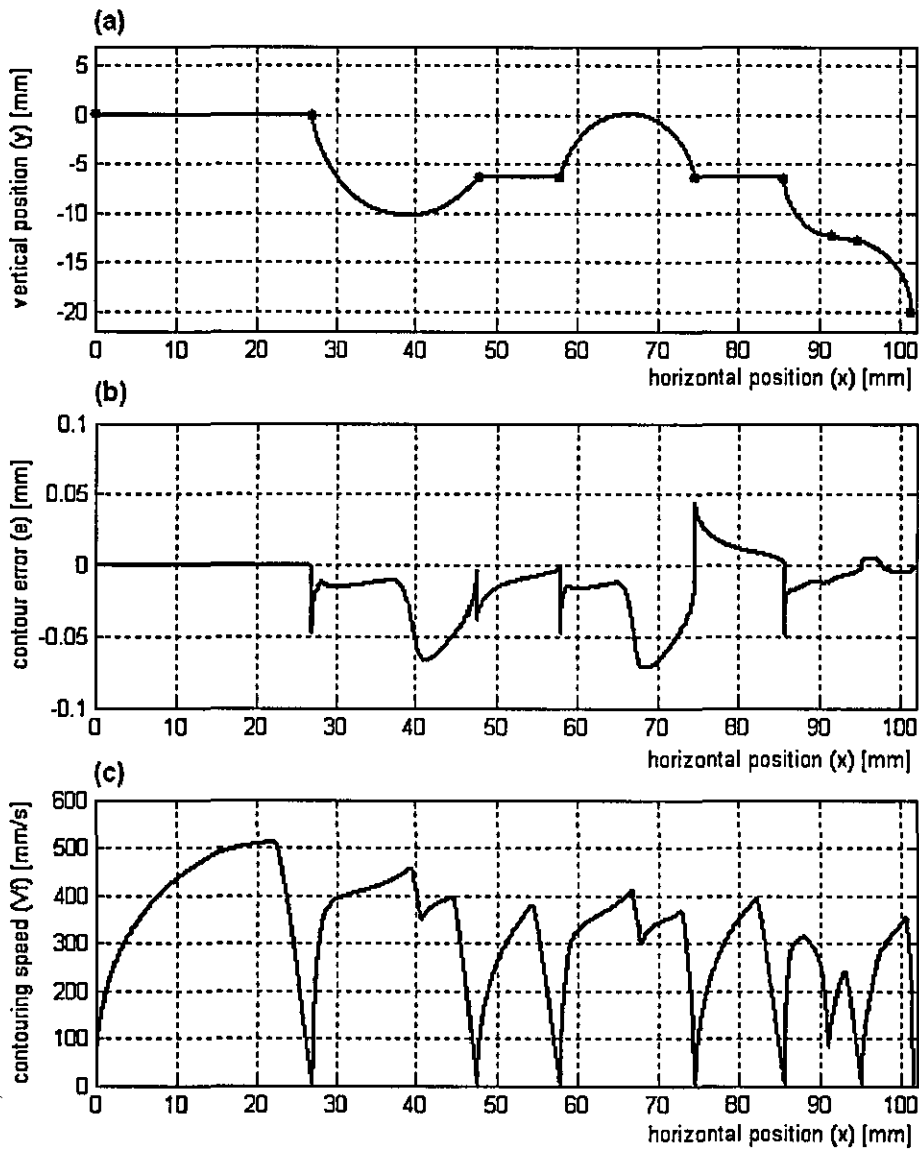


Fig. 18 Initial performance (a) moulding profile (b) contour error vs. horizontal position (c) contouring speed vs. horizontal position

The pass took only 0.716 s, which is 28% quicker than the targeted 1s. However, the maximum contouring error of 0.076 mm is 50% greater than the acceptable value. The contouring error data in Fig. 18b can be analyzed in three parts, namely, segment end-points, line segments and arc segments. The spikes represent the segment end-points where the *Reference Generator* supplies the next segment to the *Path Controller*. In terms of end-point accuracy the simulation is successful since all the spikes are below ± 0.05 mm. Also on the line segments, the contouring error values are below the maximum acceptable value. Finally, on the arc segments although the error generally

stays below the limit, problem occurs when the vertical drive is required to change direction while the horizontal keeps moving. This happens when an arc segment passes through 90° or 270°.

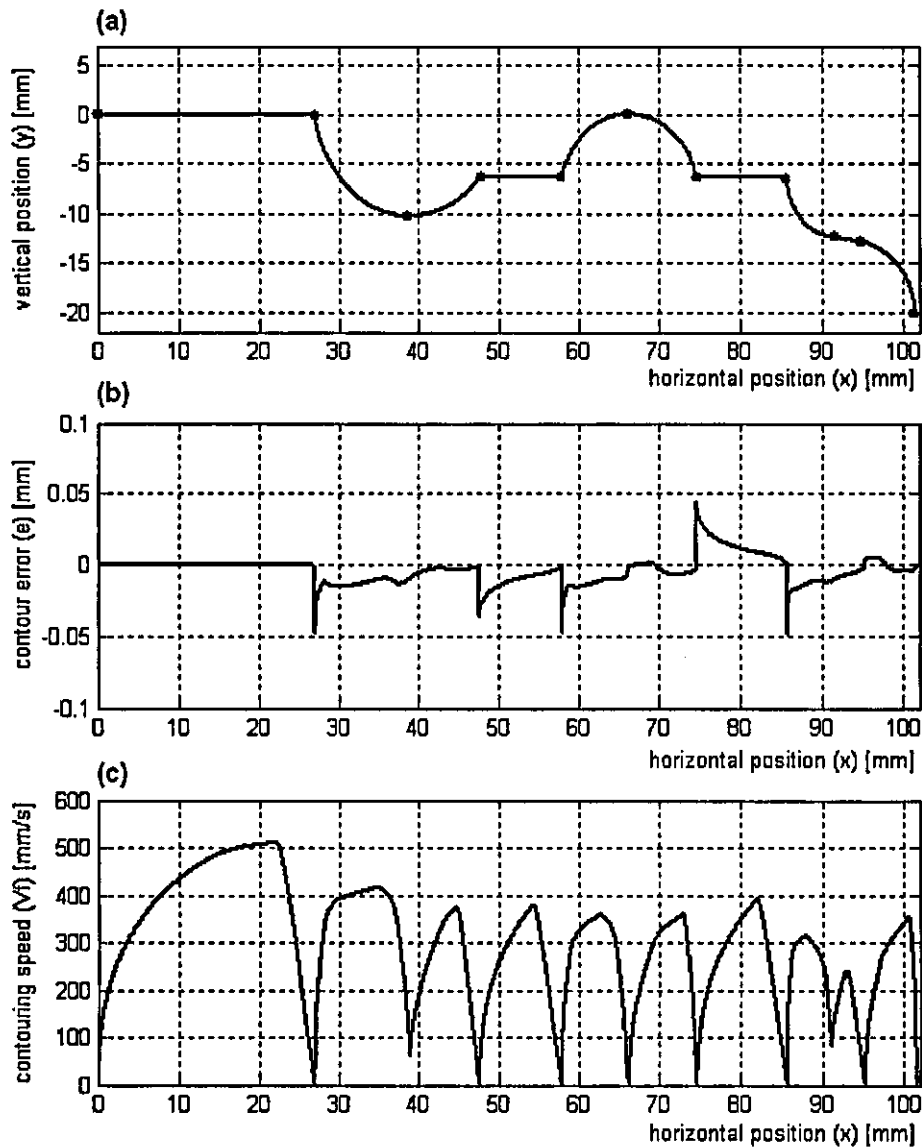


Fig. 19 Split-arc performance (a) moulding profile (b) contour error vs. horizontal position (c) contouring speed vs. horizontal position

In order to solve the problem, the arc segments that satisfy the condition in (21) were split into two segments at either 90° or 270° and the result in Fig. 19 was obtained.

$$|\theta_B - \theta_A| > 90^\circ \quad (21)$$

Since the system stops at the points connecting two consecutive segments, splitting arcs into two results in more points to stop (Fig. 19a). Therefore, the pass with the split arcs took 0.784 s. On the other hand, the problem identified in the first simulation was solved and the maximum contouring error value dropped significantly to 0.049 mm.

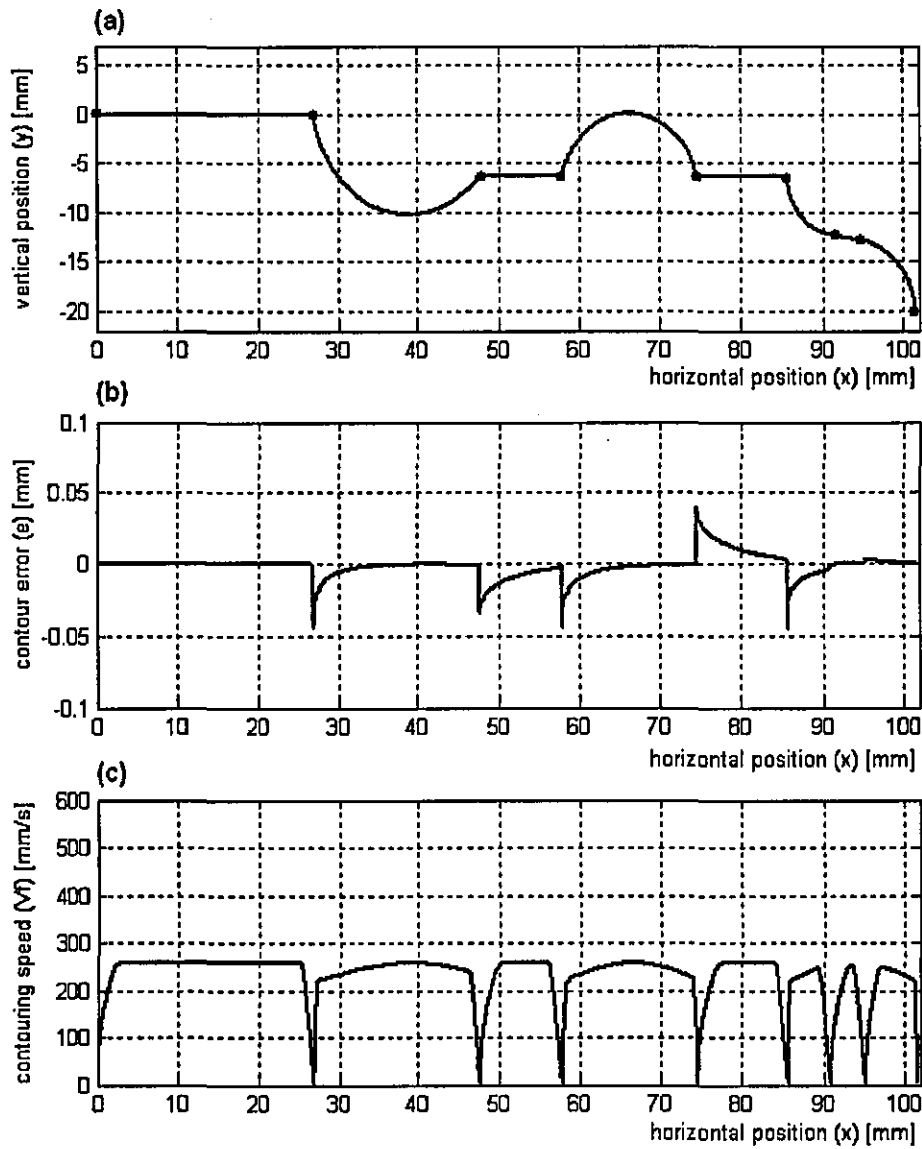


Fig. 20 Limited speed performance (a) moulding profile (b) contour error vs. horizontal position (c) contouring speed vs. horizontal position

In the first two simulations the drives were allowed to run as fast as possible and the contouring speed reached to a value of 510 mm/s. However, the mean contouring speed values remained at 161 mm/s in the first and 152 mm/s in the second case. A

final simulation was performed with a speed limit of 260 mm/s and the position gain Kp_f was increased to 170. The result is shown in Fig. 20.

A very smooth contouring performance was achieved without the need for splitting arcs. The error reached a maximum value of 0.046 mm appearing only on segment end-points. Limiting the maximum speed allowed the system to decelerate later and thus increased the mean speed to 173 mm/s, resulting in a pass time of 0.710 s.

7 CONCLUSION

The novel concept of profile independent wood moulding machine (PIMM) has been introduced. A prototype design and its expected performance were presented. The prototype has been modelled and simulated on a test profile in Matlab and Simulink.

A path controller using vector approach was explained and the simulation results were studied. It is shown that a target production rate of 150 mm/min can be achieved for moderate quality ($p=2.5\text{mm}$) 100 mm wide mouldings with a contour error less than 0.05 mm. The prototype is currently being built and further work on system identification and controller refinement is being pursued.

ACKNOWLEDGEMENTS

The authors wish to thank Mr. Eugen Saffert for his expert advice on the design of the path controller during the early stages of this project.

REFERENCES

- 1 Jackson, M. R., Parkin, R. M. and Brown, N. Waves on wood. *Proc. Instn. Mech. Engrs., Part B: J. Engineering Manufacture*, 2002, **216**(B4), 475-497.

- 2 Neumayer, R.** Profile independent wood moulding machine—dynamic model and control system. MSc. Thesis, Loughborough University, 1999.
- 3 Waghorn, C.** Numerical controlled wood moulding machine, MSc. Thesis, Loughborough University, 1998.
- 4 Jackson, M. R., Neumayer, R., Parkin, R. M. and Brown, N.** Profile independent wood moulding machine dynamic model and control system. In *Mechatronics 2000*, Georgia Inst. of Technology, USA, 2000.
- 5 Tascioglu, Y., Jackson, M. R.** Design alternatives for a novel wood moulder. In *Mechatronics 2004*, Middle East Technical University, Ankara, Turkey, 2004.
- 6** <http://www.rexlumber.com>
- 7** <http://www.forestermoulding.com>
- 8** <http://www.dykeslumber.com>
- 9 Chiu, G. T.-C., Tomizuka, M.** Coordinated position control of multi-axis mechanical systems. *Transactions of ASME Journal of Dynamic Systems Measurement and Control*, 1998, **120**, 389-393.
- 10 Hynek, P., Jackson, M. R., Parkin, R. M. and Brown, N.** Improving wood surface form by modification of the rotary machining process. *Proc. Instn. Mech. Engrs., Part B: J. Engineering Manufacture*, 2004, **218**(B8), 875-887.
- 11 Jackson, M.R.** Some Effectes of Machine Characteristics on the Surface Quality of Planed and Spindle Moulded Wooden Products. PhD Thesis, Leicester Polytechnic, 1986.
- 12 Kivimaa, E.** Cutting forces in woodworking. PhD Thesis, University of Helsinki, 1950.

Appendix P: Profile Independent Wood Moulding Machine

Paper presented at the 17th International Wood Machining Seminar, Rosenheim, Germany, 26-28 September 2005.

Profile Independent Wood Moulding Machine

Yiğit Taşcıoğlu, Dr. Mike R. Jackson

Holywell Mechatronics Research Centre,
Loughborough University, Loughborough, Leicestershire, UK

Abstract

This paper introduces the novel concept for a profile independent wood-moulding machine (PIMM). The concept aims to eliminate set-up and tooling costs of conventional wood moulders in short production runs. A PC controlled, proof-of-concept test rig of the PIMM was built in Loughborough University. The PIMM test rig is explained and its performance in terms of production rate and product quality is presented. The viability of the concept is verified and possible design improvements and modifications are discussed.

Keywords: wood moulding, machining simulation, contouring control

Introduction

Conventionally, wood mouldings are produced with planar/moulder machines. The fundamental principle of the conventional moulders is the separation of material from the advancing workpiece by profile-specific knives which are clamped on a rotating cutterhead as shown in Figure 1. Since the width of the knives is equal to the width of the workpiece the desired profile is achieved with a single feed. This process is characterized by high cutting tool tip velocities which are typically within the range 30-125m/s with correspondingly high workpiece feed speeds ranging from 5 to 120m/min [1].

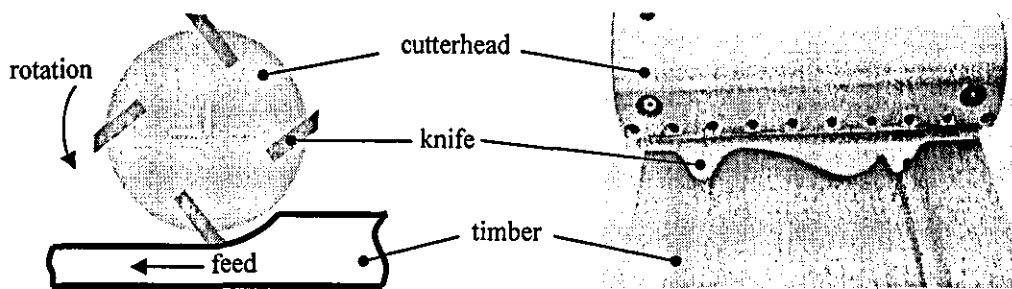


Figure 1. Conventional moulding

For every moulding profile, cutterheads contain suitably shaped cutters. High production capability of the conventional concept compensates the costs of manufacturing, mounting and

maintenance of the profile-specific cutters as well as the downtime for machine set-up. Where just short production runs of a particular type of moulding are required or even a few meters of a one-off special is needed, the tooling and machine set-up costs of the conventional moulding machines cannot be compensated [2, 3]. It is intended to design a new wood moulder for short production runs in order to minimize the tooling and machine set-up costs.

A proof-of-concept test rig of the PIMM has been constructed. This paper introduces the novel concept, explains the test rig and discusses the results of mathematical machining simulations and initial experiments.

PIMM Concept

The essential part of the proposed concept is a very thin (i.e. 1 mm) cutting disc, which is mounted on a two-axis positioning system (Figure 2). The moulding is produced by oscillating the rotating cutting disc along the width of the timber while following the desired profile geometry which is supplied directly from a CAD drawing. The timber is fed in between two consecutive passes along the width.

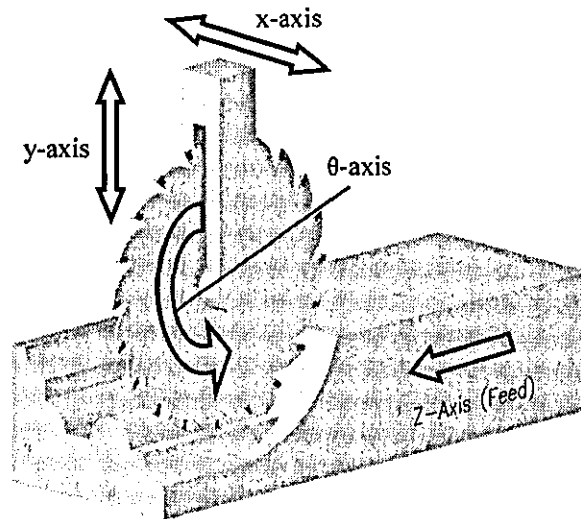


Figure 2. PIMM concept

Being able to produce any moulding profile directly from CAD drawing by using the same cutting tool results in full manufacturing flexibility, and enables the production of wood mouldings with minimum tooling cost and virtually zero machine set-up time. The PIMM concept transforms the moulding process from being hardware dependent to software oriented. Previous work on the concept can be found in [2-4].

PIMM Test Rig

The overview of the designed test rig is shown in Figure 3. Desired moulding profile is supplied to the system directly from CAD drawings in commonly used DXF format. This profile information is processed in the PC and consequently the cutter path and timber feed is controlled via the interface hardware.

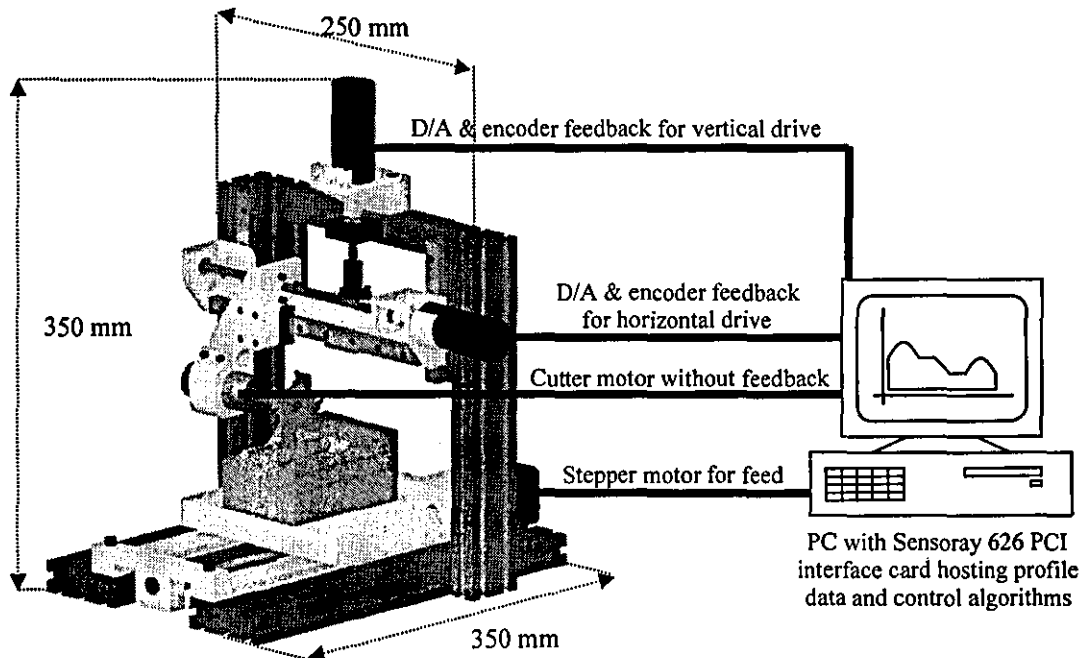


Figure 3. PIMM test rig

The machine consists of four drives. The horizontal (x-axis) and vertical (y-axis) drives move the cutter simultaneously and produce the desired geometry on the stationary workpiece. Timber feed drive (z-axis) feeds the workpiece in between two consecutive passes of the cutter along the width of the timber. The cutter drive (θ -axis) rotates the cutter.

Since the speed of the process and also the geometric accuracy of the finished product rely mostly on the performance of the X and Y axis drives, the research up to now mainly concentrated on design and control of these drives. For the other two drives, temporary solutions were utilized. The current timber feed (z-axis) mechanism is a stepper motor-leadscrew driven table with a top speed of 10mm/s and travel length of 170mm. The cutter (θ -axis) is driven by a remote AC-motor, with a top speed of 22000rpm, via a flexible shaft and collet. As the cutting disc, a 50mm diameter 4-tooth slotting cutter with 1.6mm kerf has been used.

In order to produce a single moulding, the PIMM must perform hundreds of passes. First of all, on every single pass the cutter must rigidly follow the desired geometry. Although this procedure is managed by the software mechanism and the controller, it also needs accurate drive hardware on X and Y axes. According to [1], tolerances for the geometric accuracy of the machined timber sections are between $\pm (0.5-0.1)$ mm depending of the end-usage of the product. The geometric accuracy within a single pass only affects the profile quality on the X-Y plane. On the other hand, relative position differences among the individual passes result in undesirable geometry on the X-Z and Y-Z planes. Hence it is critical to ensure that all the passes are identical and for that, the X and Y axis drives must be free from backlash and possess high repeatability. Figure 4 shows the solid model of the X and Y axis drives. Both drives move along precision linear guideways and utilize DC servomotors directly coupled to anti-backlash leadscrews. They can attain a maximum speed of 400mm/s and deliver a maximum continuous force of 200N. Feedback from both drives is obtained from incremental encoders, which are attached to the rotor shafts of the motors. The drives are controlled via Sensoray 626 PCI interface card, which provides 14bit D/As for DC motor power amplifiers and 24bit quadrature counters for the encoders.

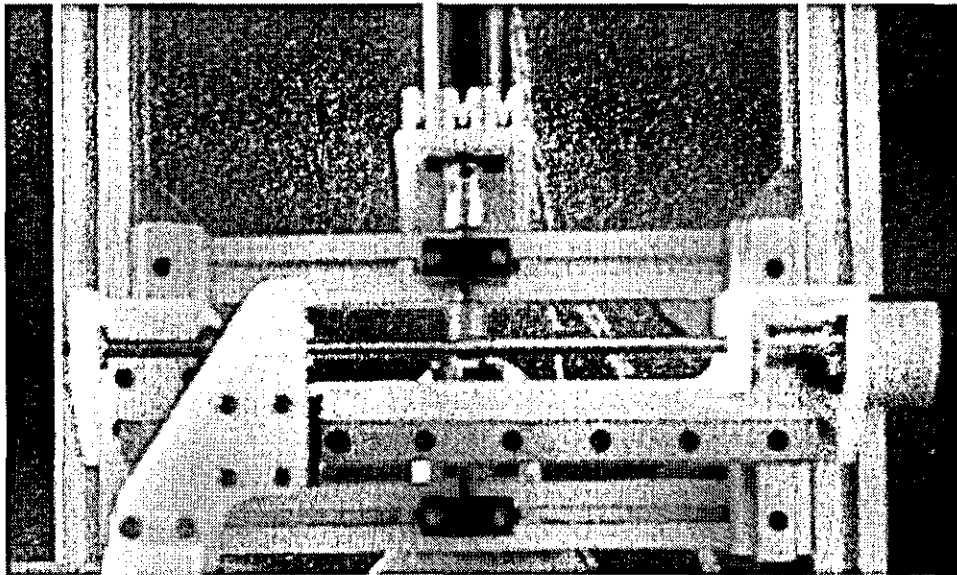


Figure 4. X and Y axis drives

The PIMM test rig is 350 mm high, 250 mm wide and 350 mm long, therefore, it can be considered as a 'miniature' moulding machine compared to the conventional machines. The maximum distances that the cutter travels in horizontal and vertical axes are 120 mm and 30 mm respectively. The rig allows machining of profiles having width of maximum 100 mm.

The maximum cutting depth is limited only by the cutter radius and can be up to 30mm. This is representative of the majority of the wood profiles market.

Target Quality and Production Rate

Product quality is determined from two parameters, the geometric accuracy and the surface waviness. The former one, as mentioned earlier, is between $\pm (0.5-0.1)$ mm depending of the end-usage of the product. The measure of the geometric accuracy is the contour error, being the shortest distance from any point on the actual contour to the desired contour. The target value for the contour error was set to be ± 0.1 mm.

Surface waviness is characterized by a regular series of waves that are perpendicular to the workpiece feed direction. These waves are caused by the nature of the rotary machining process. A good quality surface is classified by a wave pitch of typically <1.5 mm, and a lower quality surface by a wave pitch of typically >2.5 mm. The relationship between the surface waves and the machining parameters are well established for the conventional planning/moulding processes and more information can be found in [1, 5]. Whereas in PIMM, since the workpiece is stationary during cutting and fed in between two consecutive passes, the waviness pitch p is equal to the length of timber fed after each pass. The graph of production rate versus pass time for different waviness pitches is shown in Figure 5.

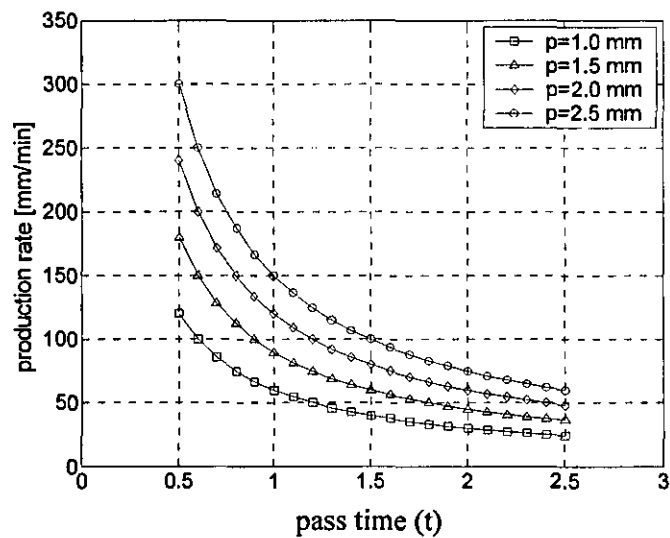


Figure 5. Production rate vs. pass time

A sensible target production rate for the initial performance of the PIMM rig was set as 150mm/min. It can be seen from Figure 5 that in order to produce a moderate quality (i.e. $p=2.5$ mm) moulding, each pass should be completed in 1s.

Simulations

Prior to the experiments, the performance of the test rig was evaluated by software simulations in Matlab and Simulink. The simulated system is comprised of three main parts being the *Reference Generator*, *Path Controller* and the *Motion System*.

The *Reference Generator* reads the moulding profile from a DXF file, identifies the face to be machined and divides the contour on this face to smaller entities suited for the *Path Controller*. Figure 6 illustrates the operation principle of the *Reference Generator*.

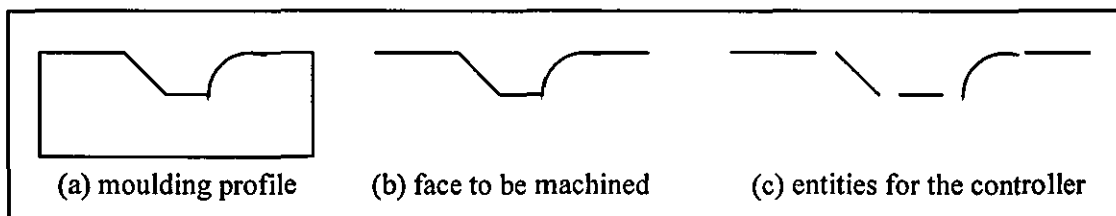


Figure 6. *Reference Generator* principle

The *Path Controller* is a custom designed, de-coupled contouring controller. It provides separate control of the contour error and path velocity. The details of the path controller are beyond the scope of this paper but can be found in [4].

Finally, the *Motion System* contains mathematical models of the X and Y axis drive hardware. For the experiments, the *Motion System* is replaced by the actual test rig via the Real Time Windows Target protocol in Simulink, while the other two parts of the simulation system are still used. Consequently, the simulations not only enable controller tuning but also identify the variations between the mathematical model and the actual system for future modifications.

A 70mm wide test profile (Figure 7) with a maximum cutting depth of 15mm was generated for the simulations. This profile enabled inspection of the machine performance on different geometries such as horizontal lines, sloped lines and arcs.

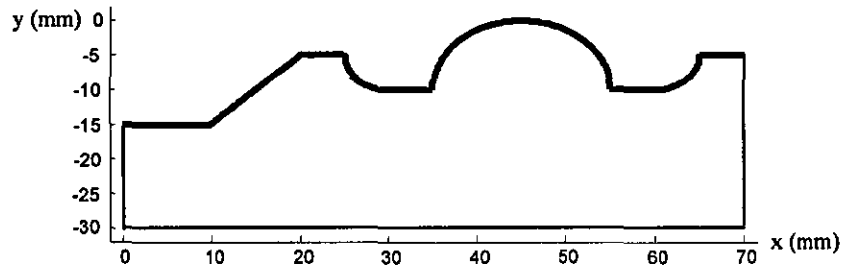


Figure 7. Test profile

Figure 8 shows the result of the simulation. The pass was completed in 1s, which was the target time. A very smooth contouring performance was achieved with a mean contour error of 0.01mm. The error spikes at the intersections of two segments are expected due to the reference generator supplying the next segment to the path controller. The maximum error was recorded to be 0.09mm which is slightly better than the target value of 0.1mm.

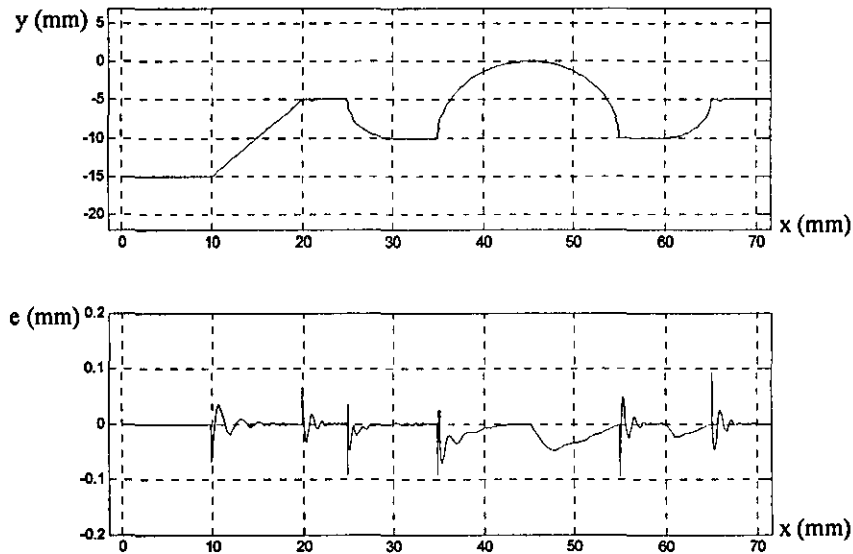


Figure 8. Simulation Result

Experiments

Two sets of experiments were carried out using the same controller parameters as in the simulation. In the first set, air cutting was performed. The result in Figure 9 shows that the pass was completed 1.21s which is slower than the simulation and the target value. The mean and maximum values for the contour error were 0.015mm and 0.13mm respectively. The maximum error occurred at the first corner due to overshooting horizontal drive.

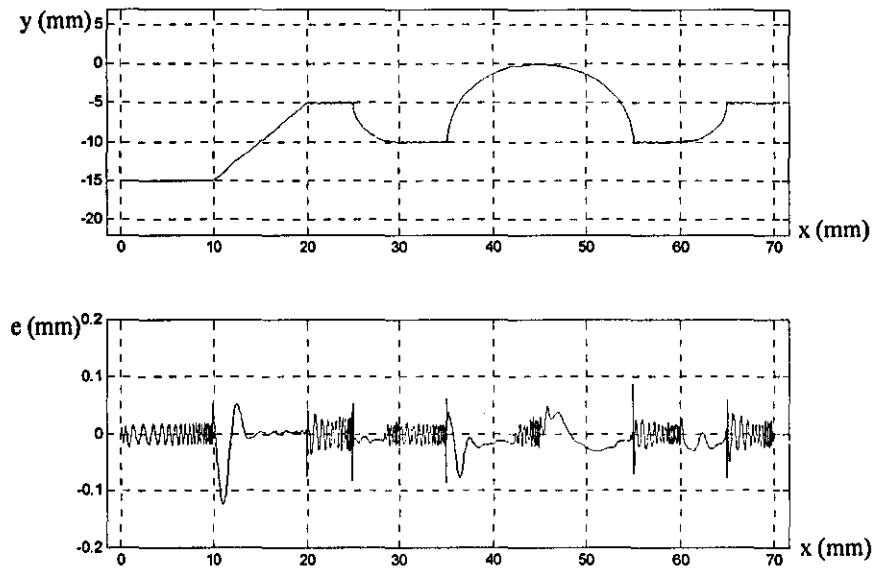


Figure 9. Experiment result (Air Cutting)

The second set of experiments was performed with a meranti specimen. The pass was completed in 1.17s (Figure 10). The resistance of the workpiece prevented overshooting at the corners and resulted in maximum contour error of 0.09mm. The mean value of error was recorded as 0.02mm.

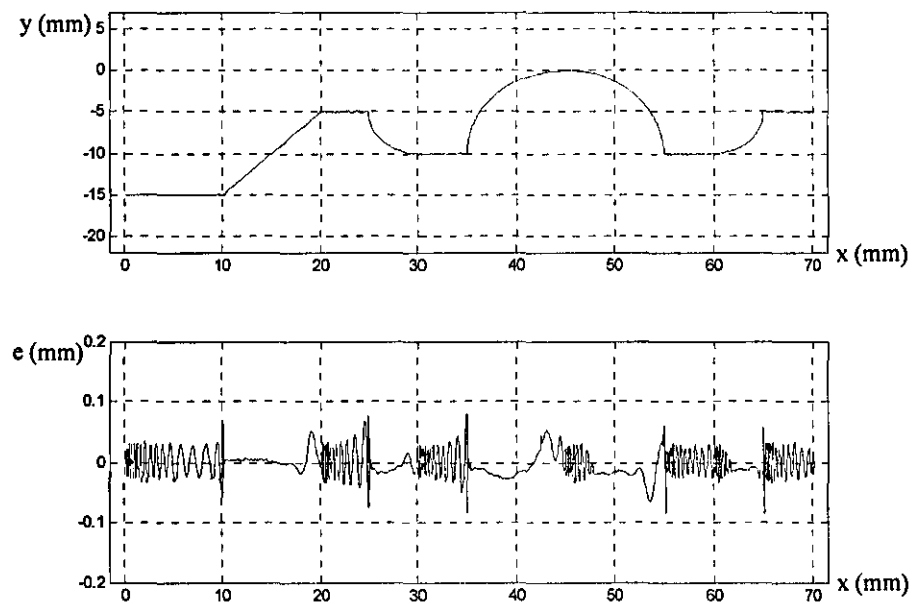


Figure 8. Experiment result (Meranti Specimen)

Conclusion

The novel concept of profile independent wood moulding machine (PIMM) has been introduced. The designed proof-of-concept test rig was explained and its expected initial performance was outlined in terms of production rate and product quality.

Software simulations as well as air cutting and wood cutting experiments clearly verified the viability of the PIMM. The result of the wood cutting experiments showed that a production rate of 128mm/min can be achieved with a maximum contour error of 0.09mm.

Currently, the work is concentrated on path controller refinement in order to achieve a faster and more robust system. The future work will be focused on designing permanent solutions for Z and θ axis drives.

References

- 1 Jackson, M. R., Parkin, R. M. and Brown, N. Waves on wood. *Proc. Instn. Mech. Engrs., Part B: J. Engineering Manufacture*, 2002, **216**(B4), 475-497.
- 2 Jackson, M. R., Neumayer, R., Parkin, R. M. and Brown, N. Profile independent wood moulding machine dynamic model and control system. In *Mechatronics 2000*, Georgia Inst. of Technology, USA, 2000.
- 3 Neumayer, R. Profile independent wood moulding machine—dynamic model and control system. MSc. Thesis, Loughborough University, 1999.
- 4 Tascioglu, Y., Jackson, M. R. Design alternatives for a novel wood moulder. In *Mechatronics 2004*, Middle East Technical University, Ankara, Turkey, 2004.
- 5 Hynek, P., Jackson, M. R., Parkin, R. M. and Brown, N. Improving wood surface form by modification of the rotary machining process. *Proc. Instn. Mech. Engrs., Part B: J. Engineering Manufacture*, 2004, **218**(B8), 875-887.

